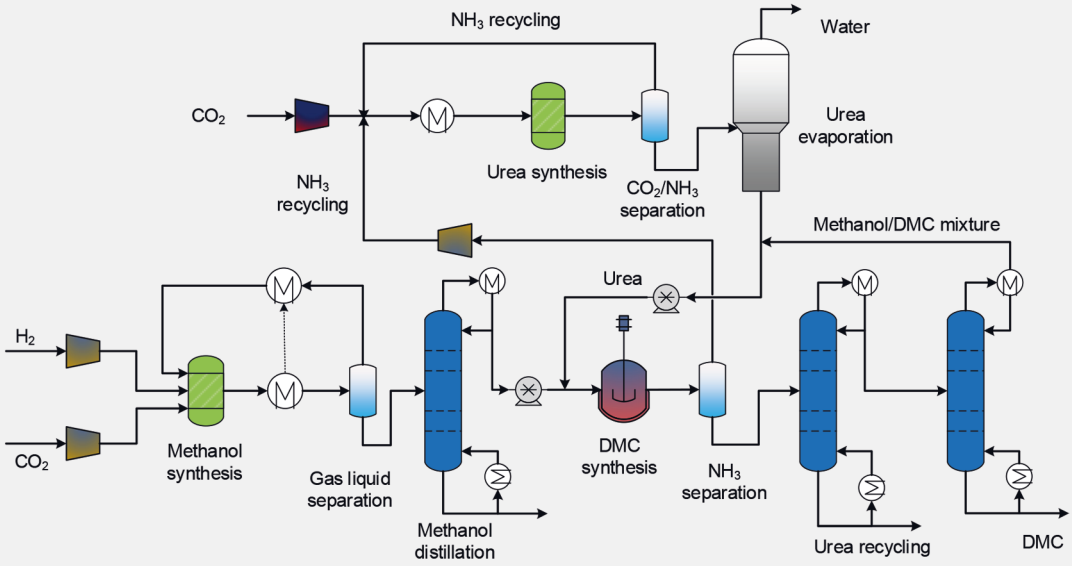

Membrane Reactor Concepts for Power-to-Fuel Processes

Hong Huang

Energie & Umwelt / Energy & Environment
Band / Volume 610
ISBN 978-3-95806-703-5

Mitglied der Helmholtz-Gemeinschaft

JÜLICH
Forschungszentrum

Schriften des Forschungszentrums Jülich
Reihe Energie & Umwelt / Energy & Environment Band / Volume 610

Forschungszentrum Jülich GmbH
Institut für Energie- und Klimaforschung (IEK)
Elektrochemische Verfahrenstechnik (IEK-14)

Membrane Reactor Concepts for Power-to-Fuel Processes

Hong Huang

Schriften des Forschungszentrums Jülich
Reihe Energie & Umwelt / Energy & Environment Band / Volume 610

ISSN 1866-1793 ISBN 978-3-95806-703-5

Bibliografische Information der Deutschen Nationalbibliothek.
Die Deutsche Nationalbibliothek verzeichnet diese Publikation in der
Deutschen Nationalbibliografie; detaillierte Bibliografische Daten
sind im Internet über http://dnb.d-nb.de abrufbar.

Herausgeber und Vertrieb:	Forschungszentrum Jülich GmbH Zentralbibliothek, Verlag 52425 Jülich Tel.: +49 2461 61-5368 Fax: +49 2461 61-6103 zb-publikation@fz-juelich.de www.fz-juelich.de/zb
Umschlaggestaltung:	Grafische Medien, Forschungszentrum Jülich GmbH
Druck:	Grafische Medien, Forschungszentrum Jülich GmbH
Copyright:	Forschungszentrum Jülich 2023

Schriften des Forschungszentrums Jülich
Reihe Energie & Umwelt / Energy & Environment, Band / Volume 610

D 82 (Diss. RWTH Aachen University, 2023)

ISSN 1866-1793
ISBN 978-3-95806-703-5

Vollständig frei verfügbar über das Publikationsportal des Forschungszentrums Jülich (JuSER)
unter www.fz-juelich.de/zb/openaccess.

Abstract

This thesis concerns the development of membrane reactor concepts in the context of Power-to-Fuel processes. Standing on the disciplines of Process Engineering and Chemical Reaction Engineering, this thesis carries out work at the process level and the equipment level, respectively.

Dimethyl carbonate and methyl formate are selected as two representative esters for their potential as electrofuels. At the process level, available production pathways are screened with respect to their technical maturities and their compliance with green chemistry principles. The selected pathways are conceptually designed starting from CO_2 and H_2, which also act as the background of membrane reactor development. The process simulations and techno-economical assessments adopt the same boundary conditions and assumptions to ensure comparability across pathways. It can be expected that these pathways can be technically realistic, energy efficient, and economically viable in the near future. It is thus with enough confidence to believe that esters will sit alongside alcohols, ethers, and hydrocarbons as a new member of the Power-to-Fuel family.

To guide membrane selection and matching, mapping relationships among reaction, membrane, and reactor concept are constructed to present an overview of possible combinations before detailed designs. Theoretical calculations are then performed to quantify the potential of each combination by correlating equilibrium constant, conversion, and the Damköhler (*Da*) number as well as the Péclet (*Pe*) number. The correlation is exemplified by the reverse water gas shift and dry reforming of methane. At the equipment level, various novel membrane reactor concepts are designed for the two reactions based on CFD simulations by receiving boundary conditions from process analysis. The trade-off among conversion, productivity, and membrane permeation is the core design aspect of the membrane reactors. The conversion enhancement is directly related to the percentage of species permeation. Concentration polarization is a phenomenon that adversely affects the species permeation and has to be minimized to fully exploit the membrane potential. Compact designs by increasing the ratio of membrane area to reactor volume are simple but effective approaches to increase conversions but maintain high productivity.

A methodological framework that starts from process analysis, over theoretical calculation, to CFD simulation can be condensed from this work. The communications among these methodologies make them an integrated part and can be applied to other processes and reactor concepts of interest.

Kurzfassung

Diese Arbeit befasst sich mit der Entwicklung von Membranreaktorkonzepten im Kontext von Power-to-FuelProzessen. Ausgehend von den Disziplinen Verfahrenstechnik und Chemische Reaktionstechnik werden in dieser Arbeit Untersuchungen auf Prozessebene bzw. Anlagenebene durchgeführt.

Dimethylcarbonat und Methylformiat werden aufgrund ihres Potenzials als Elektrokraftstoffe als zwei repräsentative Ester ausgewählt. Auf Prozessebene werden verfügbare Produktionswege hinsichtlich ihrer technischen Reife und ihrer Einhaltung von Prinzipien der Grünen Chemie überprüft. Die ausgewählten Pfade sind ausgehend von CO_2 und H_2 konzipiert, die auch als Hintergrund für die Entwicklung von Membranreaktoren dienen. Die Prozesssimulationen und techno-ökonomischen Bewertungen gehen von den gleichen Randbedingungen und Annahmen aus, um die Vergleichbarkeit über die Pfade hinweg zu gewährleisten. Es ist zu erwarten, dass diese Wege in naher Zukunft technisch realistisch, energieeffizient und wirtschaftlich realisierbar sind. Es ist daher anzunehmen, dass Ester neben Alkoholen, Ethern und Kohlenwasserstoffen als neues Mitglied der Power-to-Fuel Familie fungieren werden.

Um die Membranauswahl und -abstimmung zu leiten, werden Mapping-Beziehungen zwischen Reaktion, Membran und Reaktorkonzept erstellt, um einen Überblick über mögliche Kombinationen vor detaillierten Entwürfen zu geben. Anschließend werden theoretische Berechnungen durchgeführt, um das Potenzial jeder Kombination zu quantifizieren, indem die Gleichgewichtskonstante, der Umsatz und die Damköhler-Zahl (*Da*) sowie die Péclet-Zahl (*Pe*) korreliert werden. Die Korrelation wird durch die umgekehrte Wassergas-Shift Reaktion und die Trockenreformierung von Methan veranschaulicht. Auf apparativer Ebene werden auf Basis von CFD-Simulationen durch Einpflegen von Randbedingungen aus der Prozessanalyse verschiedene neuartige Membranreaktorkonzepte für die beiden Reaktionen ausgelegt. Der Kompromiss zwischen Umwandlung, Produktivität und Membranpermeation ist der zentrale Konstruktionsaspekt der Membranreaktoren. Die Steigerung des Umsatzes steht in direktem Zusammenhang mit dem Anteil permeierter Komponenten. Konzentrationspolarisation ist ein Phänomen, das die Stoffpermeation negativ beeinflusst und minimiert werden muss, um das Membranpotential voll auszuschöpfen. Kompakte Konstruktionen durch Erhöhen des Verhältnisses von Membranfläche zu Reaktorvolumen sind einfache, aber effektive Ansätze, um die Umwandlungen zu erhöhen, aber eine hohe Produktivität aufrechtzuerhalten.

Aus dieser Arbeit lässt sich ein methodischer Rahmen verdichten, der von der Prozessanalyse über die theoretische Berechnung bis hin zur CFD-Simulation reicht. Die Kommunikation zwischen diesen Methoden macht sie zu einem integrierten Bestandteil und kann auf andere relevante Prozesse und Reaktorkonzepte angewendet werden.

Table of contents

1 Introduction and objectives

To reach the target of being a greenhouse gas-neutral country by 2045 [1], Germany, on the one hand, has promised to close its existing nuclear power and coal-fired plant fleets by 2022 and 2038, respectively [2]; on the other hand, it is underway of *Energiewende* (energy transition) to a renewable energy system, of which renewable electricity is an important part. Yet the intermittency of renewable electricity leads to times when the power supply exceeds the demand, resulting in so-called surplus power. Long-term and large-scale storage of such surplus power is technically challenging. One emerging storage is to transform surplus power into hydrogen by water electrolysis. Hydrogen can be then used as a feedstock, along with CO_2, to produce various products for future use, which is known as the Power-to-X concept. The Power-to-X concept provides a solution that can store surplus power and reduce CO_2 emissions at the same time. The "X" can be chemicals, fuels, and heat. In particular, if end products are transport fuels, it is then specifically referred to as the Power-to-Fuel concept, and the fuels here are also known as electrofuels. By doing this, the energy and transport sectors are successfully coupled [3].

1.1 The Power-to-Fuel concept

In the Power-to-Fuel concept, three key components are water electrolysis, CO_2 supply, and fuel synthesis and separation, and the performance of a Power-to-Fuel process can be affected by any one of the components. For water electrolysis, three technology options are available: alkaline water steam electrolysis, polymer electrolyte membrane (PEM) water electrolysis, and solid oxide electrolyzer cell (SOEC) water electrolysis. Alkaline water electrolysis is the state-of-the-art (SoA) technology that has been commercialized, but its disadvantages of low partial load range, low current density, and low operating pressure have limited its wider applications [4]. To overcome these disadvantages, PEM electrolyzers are being actively studied and has also become a SoA technology. The performance of PEM water electrolysis has been comprehensively reviewed by Carmo et al. [4]. PEM electrolyzers can operate at high current densities up to 2 A/cm^2 enabled by good proton conductivities, which can lower the costs of H_2 production [4]. In addition, the quick response of proton transport across membranes has allowed a wider range of power input and highly flexible operation [4]. However, the problem of cross-permeation of H_2 and O_2 at high operating pressures would lead to safety issues, and thicker membranes would be required [4]. SOEC water electrolysis is also a

promising technology that has gained ever more attention in recent years. SOEC works at much higher temperatures than alkaline and PEM water electrolysis, ranging from 700 °C to 900 °C, and its theoretical energy efficiency can approach to 100% under thermo-neutral conditions [4]. The Sunfire GmbH is now able to build modular SOEC water electrolysis systems with a power input of 2.68 MW and a H_2 production capacity of 750 Nm^3/h, and the efficiency is up to 84% [5]. A systematic comparison of the three water electrolysis technologies in the context of the Power-to-Gas and Power-to-Liquid concepts can be found in the review by Buttler et al. [6].

In terms of CO_2 supply, CO_2 source and capture technology are two major considerations. Conventional industrial CO_2 sources include steel and iron, and fossil fuel-fired power plants. CO_2 from these sources have the advantages of large quantity and high concentration, which are beneficial to energy consumption for capture. Substantial literature reviews have been published regarding CO_2 capture from various industrial sources with different capture technologies [7, 8], so here they are not introduced in detail. However, CO_2 sources from steel and iron and fossil fuel-fired power plants will not be available in the future, since production of steel and iron will use hydrogen as the reducing agent to replace coke and Germany has decided to close its coal-fired power plants by 2038. In this setting, future options for supplying CO_2 have to be explored. CO_2 emissions from the cement industry remain unavoidable and can be considered as an option for providing CO_2 for Power-to-Fuel processes. Markewitz et al. [9] performed a techno-economic analysis for the CO_2 emissions reduction of the German cement industry. The CO_2 avoidance costs are in the range of 77 - 115 €/t-CO_2 using monoethanolamine absorption processes, and the CO_2 reduction potential was determined to be 70 - 90%. CO_2 from biogas is also a good option as a carbon source for its easy availability and high concentration. Zhang et al. [10] conducted a life cycle assessment of Power-to-Gas with biogas as the carbon source. The analysis showed that using the produced bio-methane as a transport fuel could reduce greenhouse gas emissions by 27 – 62% compared to natural gas or 41 – 70% compared to gasoline. Schorn et al. [11] presented a biogas-oxyfuel process that integrated a biogas plant into a Power-to-Methanol process. The CO_2 capture cost was determined to be 33 - 88 €/t, which is comparable with capture costs from industrial sources. A new trend is capturing CO_2 directly from the atmosphere, namely direct air capture. The characteristic of CO_2 in the atmosphere is with very low concentration of around 400 ppm, which makes separation energy consumption and costs significantly higher. Keith et al. [12] calculated the energy demand and cost of a direct air capture process based on aqueous KOH absorption. The estimated primary energy consumption was 8.81 GJ/t-CO_2, and the levelized cost was 94 – 232 $/t-$CO_2$. Solid sorbent adsorption seems a better choice for direct air capture since it is suitable for

gas separation with very low concentration. Fasihi et al. [13] comprehensively compared the direct air capture technologies of high temperature aqueous absorption and low temperature solid sorbent adsorption. It was shown that the adsorption-based technology is favorable due to lower heat supply costs and the possibility of using waste heat from other sources. It was also predicted that direct air capture costs could be reduced to 50 €/t or below by 2040 using hybrid PV-wind-battery processes. Sabatino et al. [14] compared the techno-economic performance of two absorption processes and one adsorption process. The CO_2 capture costs were all below 200 \$/t-CO_2, and the adsorption process performed better than the two absorption processes. Based on the finding of these previous investigations, more studies focused on direct air capture by adsorption processes. Kulkarni et al. [15] analyzed a direct air capture process using an amino-modified silica adsorbent, with throughput of around 1.1 t CO_2 at 88.5% purity. The total energy required was calculated to be 6.745 GJ/t-CO_2 and the capture cost was estimated to be around 100 \$/t-CO_2. Sinha et al. [16] developed an adsorption process using metal organic frameworks coated as films on monolithic contactors. The energy consumption of the process is 0.113 - 0.145 MJ/mol-CO_2, and the cost is between 60 and 190 \$/t-CO_2. Although capturing CO_2 from air is currently energy and cost expensive, it represents a promising negative emission technology that can capture CO_2 from non-point sources.

Once the water electrolysis and the CO_2 source and capture technology are determined, the next question is what are the suitable electrofuels that can be produced by Power-to-Fuel processes. Broadly, the electrofuels being discussed include hydrocarbons, alcohols, and ethers. Schemme et al. [17] summarized the property requirements of diesel fuel alternatives produced from renewable H_2 and CO_2 and gave recommendations for the choice of electrofuels. To be suitable electrofuel candidates, a first consideration is that the fuel does not require major modifications to existing transport infrastructures and engines so that market entry is easy. This requires electrofuels should be compatible with commercial gasoline, diesel, or kerosene. At this point, hydrocarbons produced by Fischer-Tropsch are an ideal choice as they hold similar properties to commercial transport fuels. Alcohols are also suitable electrofuels and have been considered for many years for their lower combustion emissions due to high oxygen contents. In addition to the frequently discussed lower alcohols such as methanol and ethanol, higher alcohols have also gained some attention for their property advantages as fuels over lower alcohols. It has been identified by Schemme at al. [18] that 1-/2-/iso-butanol and 1-octanol are most relevant for fuel replacement among available higher alcohols. Among ethers, dimethyl ether is the one that has been extensively studied for the same reason of low emissions. However, it is in the gas phase at ambient pressure and temperature, which should be pressurized to the liquid phase if it is used as a

transport fuel. Oxymethylene ether is an emerging diesel alternative for its ideal properties and has been praised by many studies [19-21].

After identifying suitable electrofuel candidates, producing them in efficient ways is an immediate question that has to be answered at the process level. Energy efficiency and production cost are two major concerns when comparing different pathways. Many previous studied have performed comparisons for various electrofuels in different pathways and will be reviewed in the next two sections.

1.1.1 Energy efficiency

As introduced above, any Power-to-Fuel process consists of three components of water electrolysis, CO_2 supply, and fuel synthesis and separation, and any of which can impact the overall energy performance of the overall process. To investigate the impacts of water electrolysis technology, Rivera-Tinoco et al. [22] compared the energy efficiencies of Power-to-Methanol processes using two water electrolysis technologies of PEM and SOEC. The energy efficiencies were 45.3% for PEM and 54.8% for SOEC. More recently, Herz et al. [23] also compared the energy efficiencies of Power-to-Liquid processes employing the mentioned two water electrolysis technologies, it was calculated that the energy efficiency of processes with SOEC was 51.3%, which was higher than 41.5% for those with PEM electrolysis. A common point of both studies is that SOEC-based Power-to-Fuel processes could exhibit higher energy efficiencies. Another aspect regarding water electrolysis is that it occupies the biggest share in total energy consumption, no matter what water electrolysis technology adopted. CO_2 source and capture technology can also influence system performance. For example, the energy efficiency of a Power-to-Methanol process using CO_2 from industrial sources could be 57.6% [24], but if CO_2 is sourced from the atmosphere, its efficiency is lowered to 50% [25]. Recently, Marchese et al. [26] designed a Fischer-Tropsch coupled with direct air capture, the energy efficiency of the process was determined to be 36.3%, which was much lower than 43.3% if using an industrial CO_2 source [27]. The influence of fuel synthesis and separation comes from different process designs that will lead to different levels of utilities demand. The utilities demand of a process can be kept at a low level if it is well designed. Process intensification and heat integration are two useful ways for designing efficient chemical processes, and there are many good methodologies, tools, and prior examples showcasing how to handle this task [28-30]. This thesis will focus on process intensification by integrated reaction and separation and will be discussed in detail in the next sections.

Maximizing the utilization of by-products can reduce waste discharge and improve energy performance. For example, the purge gas in methanol processes can be utilized to enhance methanol production. This idea was presented in a study by Agahzamin et al. [31]. In their study, the purge gas was converted into syngas by autothermal reforming and the methanol output was increased while CO_2 emissions decreased. The same idea can be also applied to Fischer-Tropsch processes, where light gases can be recycled to regenerate syngas. Schemme et al. [24] calculated that the energy efficiency of Fischer-Tropsch processes with light gas utilization was 50.6%, but the efficiency was only 43.3% without light gas recovery [27].

Although many previous studies have analyzed the impacts of each factor for various processes, one underlying problem arises: different system boundaries and assumptions are employed, so it is hard to compare results from different studies. In a bid to ensure comparability across pathways, Schemme et al. [32] performed a comprehensive study for various Power-to-Fuel processes on the bases of identical boundary conditions and assumptions.

1.1.2 Cost competitiveness

To replace fossil fuels, the capital investments and production costs of electrofuels must be competitive enough. Brynolf et al. [33] reviewed the production costs of many eletrofuels. However, the range of 10 - 3500 €/MWh is fairly broad and not informative. The authors also made their own calculations as a complement to the literature review results. The calculated production costs are between 200 - 280 €/MWh, which are much narrower than the surveyed values. It was also pointed out that the two most important factors affecting production costs of electrofuels are capital investment of the electrolyzer and the cost of hydrogen production, respectively [33]. Rivera-Tinoco et al. [22] compared the costs of Power-to-Methanol processes using PEM and SOEC electrolyzers, which were 891 and 5459 €/t, respectively, suggesting that electrolyzers have a huge impact on production cost. König et al. [34] estimated the net production cost of a Fischer-Tropsch process to be 12.41 - 21.35 $ per gallon gasoline equivalent. The water electrolyzer occupied 72.8% of the total capital investment while the H_2 generation accounted for 68.1% of the net production costs. Michailos et al. [35] calculated the net production cost of a dimethyl ether process to be 2112 €/t. The share of electrolyzer cost in the total purchased equipment costs was 35.6%, and the electricity cost for H_2 production was 85% in the total cost. In addition to H_2, CO_2 can also impact production costs. A study by Bos et al. [25] showed that, at an electricity price of 0.03 – 0.05 €/kWh, the cost of CO_2 should be 50 – 100 €/t so that produced methanol can be competitive against fossil-based methanol. Schorn et al. [36] also gave a range of CO_2 price

from 0 to 200 €/t, within which the net production costs of methanol can be limited to below 600 €/t, which is hopefully competitive against current methanol market prices of around 400 €/t in the near future.

There is also an interest in predicting cost reductions in the future. Brynolf et al. [33] predicted that the production costs of electrofuels will fall in the range of 160 - 210 €/MWh until 2030. Böhm et al. [37] employed the learning curve model to predict the cost reductions of Power-to-Gas processes considering economies of scale and spillover effects. By assuming different learning rates of process components, it was projected that a 75% reduction in the production costs would be possible if the global capacity of water electrolysis can reach 4530 GW by 2050, and the resulting production cost will drop to 150 €/MWh, which seems reasonable compared to the prediction by Brynolf et al. [33] above. The reductions in cost are mainly driven by reduced capital investments, electricity costs, and improved process efficiency. Herz et al. [23] predicted the net production costs for Power-to-Liquid processes with PEM and SOEC electrolysis. The results showed that, although Power-to-Liquid processes with PEM electrolysis are temporarily more economical, the net production costs with SOEC electrolysis will drop to 203 €/MWh by 2050, which will be lower than 262 €/MWh for those with PEM electrolysis.

1.2 Role of reactors and separators for Power-to-Fuel processes

It has been clear that the overall performance of Power-to-Fuel processes can be improved by efficient process designs. Like other chemical processes, Power-to-Fuel processes usually consist of a number of unit operations including reaction, separation, etc. The main task of designing an efficient process is to connect and couple each unit operation to form an integrated part. To guide chemical process designs, Smith [30] proposed an “onion model” that comprises general steps that a chemical process requires, which is represented by a hierarchical model, as shown in Fig. 1-1. The “onion model” has five layers, and each layer represents a unit operation of a chemical process. The most inner layer is reactor design where process designs begin. Mixtures from the reactor contain products and unreacted reactants, and unreacted reactants are then separated and recycled. So designs of separation and recovery systems follow reactor designs. Reactor and separation require heating or cooling, so the heat recovery and utility designs come next. The most outer layer is water and effluent treatment for environmental consideration.

The “onion model” provides a clear picture of process design procedures. From the model, reaction and separation can be seen as distinctive steps for their important roles in a process. In a study by Emets et al. [38], the designs of reactors were stressed in the context

of whole processes. Illustrated by an example of benzene production by hydrodealkylation of toluene, it was shown that a more economical process could be designed by modifying the reactor design so that it is well-suited to the process. Though the study only emphasized reactor designs as a distinctive step, it could be broadly interpreted that any key equipment that may significantly contribute to a process should be highlighted.

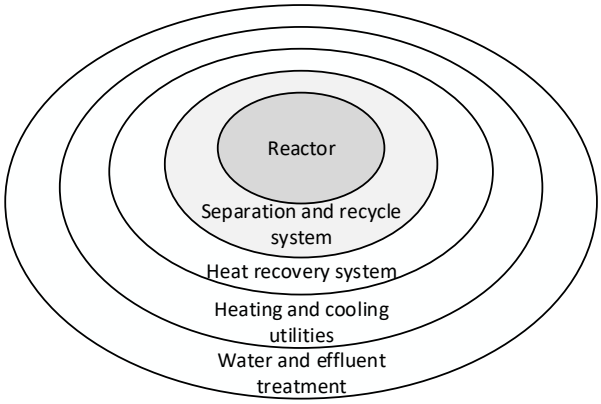

Fig. 1-1 The “onion model” by Smith for integrated chemical process designs [30].

Having recognized the importance and complexity of reactor and separator designs, the question becomes how to design reactors and separators and incorporate them into processes. Broadly, there are two connecting modes of reaction and separation. Conventional reactor and separator designs follow a sequential procedure, where reactors and separators are segregated, as shown in Fig. 1-2 (a) [39]. The segregated mode can work well for many processes but is also being challenged by some processes where reactions and separations are limited by kinetics and/or thermodynamics. Combining reactors and separators into one integrated unit may bring synergic effects, as shown in Fig. 1-2 (b) [39]. The multifunctional reactor in the integrated mode plays two roles: improving the conversions and yields of reactions while reducing product separation effort. Another benefit is that simultaneous optimization of reaction and separation can be achieved [39].

In reality, the integrated mode can be realized by membrane reactors or reactive distillation. This thesis focuses on membrane reactors for coupling of reaction and separation. Diverse models and flexible configurations of membrane reactors have enabled the possibility of meeting various needs in industrial scenarios, including conversion enhancement, reaction-reaction coupling, and reactant distribution, etc. In some areas, membrane reactors can make unique contribution and their potential has been sufficiently

proven by previous successful applications such as high-purity hydrogen production. A study by Becka [40] systematically compared several reactor concepts for methanol synthesis by CO_2 hydrogenation, including a fixed-bed reactor, a quench reactor, and a membrane reactor. The membrane reactor outperformed the other two in terms of conversion and productivity, showing the prospects of membrane reactors for Power-to-Fuel applications.

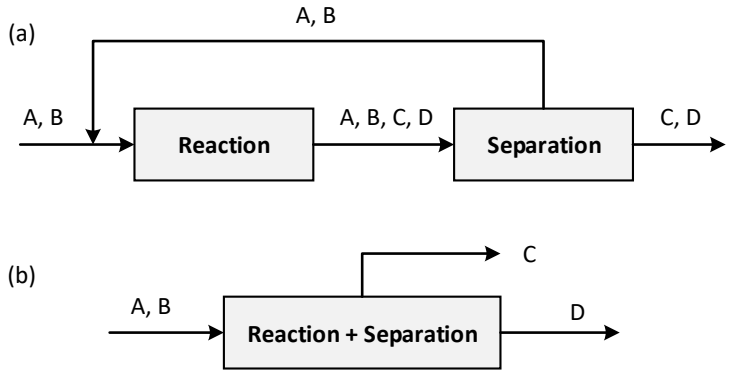

Fig. 1-2 (a) Segregated mode and (b) integrated mode of reaction and separation [39].

1.3 Research contents and framework

The overall target of this thesis is to develop membrane reactor concepts for applications in Power-to-Fuel processes. To meet this final target, the following sub-objectives are set:

- **Extension of Power-to-Fuel family to esters**
- **Guiding membrane reactor selection and matching**
- **Development of novel membrane reactor concepts**

So far, processes for alcohols, hydrocarbons, and ethers have been previously studied, so the first objective is to extend the Power-to-Fuel family to esters. Also, possible membrane application opportunities will be identified by process analysis for later detailed reactor designs. The second objective is inspired by the finding that previous studies often use a preconceived membrane for an intended reaction, which is, in fact, based on heuristics and therefore subjective. An efficient method is still lacking for selecting a suitable membrane for a reaction. In light of this, this thesis will conduct a quantified analysis in a general form that aims to help guide membrane reactor selection and matching to maximize performance under the same conditions, which also acts as a key intermediate step linking

process analysis and detailed designs. CFD has been widely used in many fields as a basic approach to help investigate fluid and particle flows, heat and mass transfer, and chemical reactor development, etc. Therefore, various reactor concepts will be developed based on computational fluid dynamics (CFD) simulation.

Having defined the objectives, the following research questions shall be answered accordingly:

- **Are dimethyl carbonate (DMC) and methyl formate (MF) production pathways technically realistic, energy efficient, and economically viable?**
- **What are the reactions suitable for membrane reactor applications?**
- **Which membrane and reactor concept should be preferentially matched with a given reaction under what conditions to achieve better performance?**
- **What is the performance of the developed membrane reactor concepts?**

To realize the objectives and answer the research questions, an integrated research framework is proposed in this thesis, as shown in Fig. 1-3. The framework consists of three parts of process analysis, theoretical calculation, and CFD simulation. The process analysis part corresponds to Chapter 4, which is used for analyzing techno-economic performance of the selected Power-to-Fuel processes and for identifying suitable reactions for membrane reactor applications. Dimethyl carbonate (DMC) and methyl formate (MF) pathways that have sound technical maturities will be first screened. After this, process design and simulation will be performed. Based on process mass and energy balances, techno-economic performance of each pathway will be analyzed and compared. From the process analysis, the reverse water gas shift reaction will be identified as a suitable membrane reactor application as it can produce syngas for some Power-to-Fuel processes where CO_2 cannot be directly used as an educt such as Fischer-Tropsch. In addition, dry reforming of methane is a similar reaction that can be seen as an alternative for syngas production, so it is also relevant to Power-to-Fuel applications. Then, suitable membranes and reactor concepts will be matched for the above two reactions. The potential of different membrane reactor concepts will be quantified by theoretical calculations, which corresponds to Chapter 5. Finally, CFD simulations will be performed to develop various novel membrane reactor concepts by receiving boundary conditions from process analyses, which corresponds to Chapter 6. The detailed reactor parameters can be sent back to process analysis for efficient process designs.

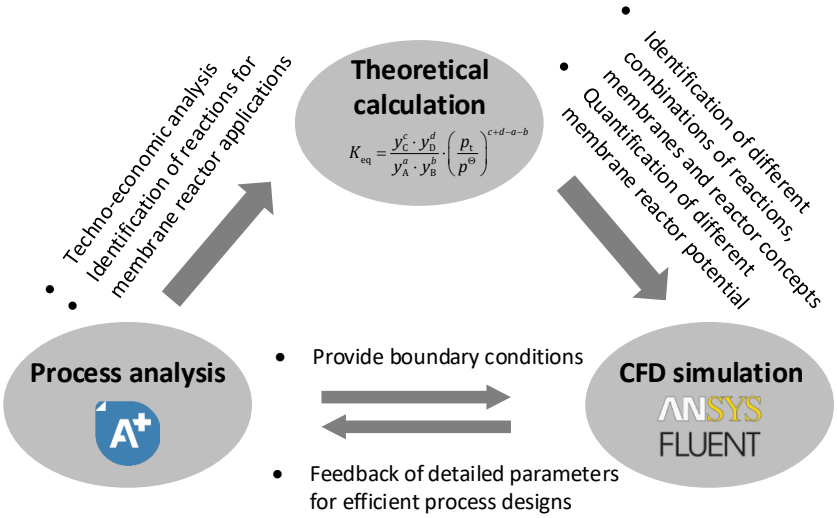

Fig. 1-3 Integrated research framework for process analysis and membrane reactor development.

1.4 Thesis structure

Based on the contents to be accomplished, the main body of this thesis has seven chapters and are structured in Fig. 1-4**.** Chapter 1 and 2 introduces the background of the thesis and literature reviews on DMC, MF, and membrane reactors. Chapter 3 introduces the theory and methods on techno-economic analysis and CFD. Chapter 4 analyzes the techno-economic performance of selected DMC and MF pathways. Chapter 5 is on the membrane reactor selection and matching by qualitative mapping relationships and quantified calculations. Chapter 6 develops several membrane reactor concepts for reverse water gas shift and dry reforming of methane by CFD simulation. The last chapter concerns general discussion and summarizes the conclusions and key findings from this work.

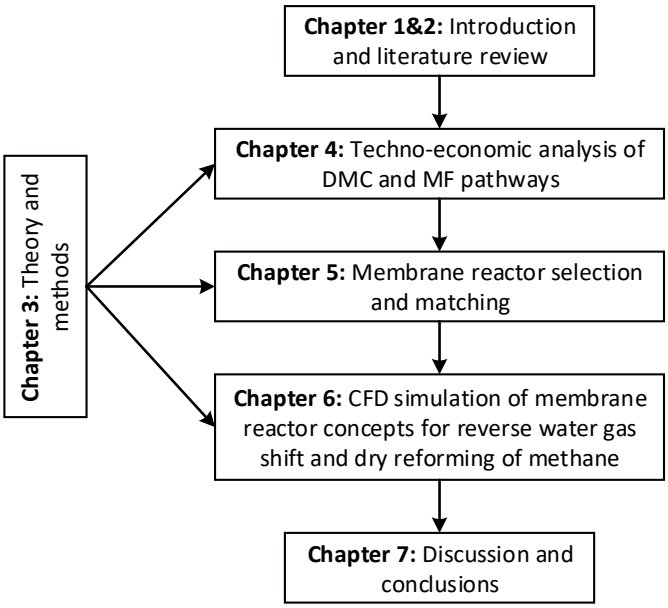

Fig. 1-4 Structure and workflow of the thesis.

2 State-of-the-art

First, this chapter introduces the properties of DMC and MF, and their production pathways are reviewed regarding catalysis, and process development and analysis. The research status of reverse water gas shift and dry reforming of methane with emphasis on reactor development will be introduced. Based on literature review, research gaps are also pointed out.

2.1 Suitability of DMC and MF as fuels

The molecular structure of DMC is symmetric while MF has one less methyl group, as shown in Fig. 2-1. DMC and MF are not new substances, and both have long been used for many applications. For DMC, its applications ranges from solvent, to methylation reagent, to electrolyte in ion-batteries [41]. For MF, it is often used as an intermediate or solvent in many organic synthesis reactions [42]. In recent years, DMC and MF have been increasingly viewed as prospective fuel alternatives due to their good properties [42-44]. Table 2-1 gives some properties that are critical for combustion. DMC and MF have the same oxygen content. High oxygen contents are beneficial to reducing combustion emissions. Both their octane numbers are very high, which are beneficial to combustion stability. However, they also have some disadvantages such as their lower heating values are lower compared to diesel, and their densities are high. Comparing the properties of both, it is seen that some of their properties are complementary such as melting point and vapor pressure. The melting point and vapor pressure of DMC are too low while those of MF are much higher, thus blending the two fuels may achieve satisfactory properties. The phase diagram of DMC-MF blends is shown in Fig. 2-2, which behaves like an ideal mixture and therefore they are well compatible.

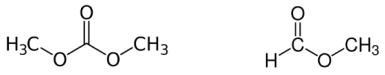

Fig. 2-1 Molecular structures of DMC and MF.

Table 2-1 Physical properties of DMC and MF [45].

Property	Unit	DMC	MF
Molecular formula	-	$C_3H_6O_3$	$C_2H_4O_2$
Molecular weight	g/mol	90	60
Density	kg/m^3	1079	957
Oxygen content	wt.%	53.3	53.3
Melting point	°C	0.5 - 4.7	-100
Boiling point	°C	90	31.5
Auto ignition temperature	°C	458	450
Vapor pressure (at 38 °C)	kPa	10.8	127.2[a]
Ignition limits	vol.%	4.2 - 12.9	2 - 20
Dynamic viscosity (at 20 °C)	mPa s	0.63	0.36
Enthalpy of vaporization	kJ/kg	418	464
Surface tension	mN/m	28.5	25
Lower heating value	MJ/kg	15.8	15.8
RON/MON[b]	-	109/102	115/114.8

[a]own calculation; [b]RON: research octane number; MON: motor octane number

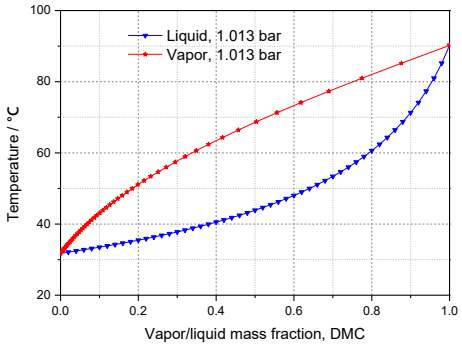

Fig. 2-2 Phase diagram of DMC-MF blends.

Some prior experimental studies had been performed to test the combustion performance of DMC and MF. Rounce et al. [46] compared the emissions of a diesel fuel and a diesel-DMC blend. It was found that the total hydrocarbons, carbon monoxide, and particulate matter emissions could be reduced by up to 50% with 4 vol.% DMC. Nevertheless, the nitrogen oxides were slightly increased, which may be due to the enhanced and more premixed combustion. In a study by Yang et al. [47], different blending levels of DMC from 5 - 30 vol.% with a diesel fuel were tested. The particulate matter reductions ranged from 30 - 78% and the carbon monoxide reductions were between 26.3% to 60.9%. However, the total hydrocarbon emissions were increased from 32.5% to 137%, which was in contrast with other studies. The authors explained that this was due to the quenching at the cylinder walls, causing the blends to disperse to the chamber without adequate combustion. In addition, the nitrogen oxides emissions were also slightly increased. This finding was consistent with that by Rounce et al. [46]. In a recent report [48], the U.S. National Center for Sustainable Transportation evaluated the viability of DMC as an alternative fuel for the transport sector. The report claimed that the particulate matter reductions could be up to 76% using a 20% DMC blend with diesel. It was also suggested that it is necessary to completely characterize the emissions before DMC can be more widely used as a fuel.

Studies on MF combustion are more limited. A study by Maier et al. [45] showed that the particulate matter emissions of MF combustion were reduced nearly two orders of magnitude less compared to gasoline. The authors also compared the combustion emissions of MF and DMC, it was shown that the particulate matter emissions of DMC achieved one order of magnitude reductions compared to gasoline, suggesting that MF is better in terms of particulate matter emissions. It should be pointed out that the experiments were carried out for pure MF rather than its blends with diesel or gasoline. More experiments regarding the combustion emissions using MF blends need to be performed.

2.2 Available production pathways of DMC

Motivated by the wider applications and excellent combustion emissions performance, various DMC production pathways are being actively developed. This section introduces available DMC production pathways and analyzes the advantages and disadvantages of each.

2.2.1 Oxidative carbonylation of methanol

Before 1980, DMC was produced by phosgenation of methanol [49]. However, phosgene is highly toxic and it was already abandoned by industry. In 1983, the ENIChem Inc.

developed and industrialized a greener DMC production process by oxidative carbonylation of methanol [49], which has been extensively employed for DMC production in industry:

$$2CH_3OH + CO + 0.5O_2 \rightarrow C_3H_6O_3 + H_2O \qquad \text{Eq. 2-1}$$

The reaction is performed in the liquid phase and catalyzed by CuCl catalysts under conditions of 20 - 40 bar and 120 - 140 ℃ [50]. It is widely acknowledged that the reaction follows a two-step redox mechanism. The first step is the oxidation of CuCl by oxygen to form $Cu(OCH_3)Cl$ [50]. As the molecule structures involved in the following reactions are more complicated, to more vividly show the chemical equations, the molecules are also demonstrated in the form of 3D balls with space filling. The copper atom is shown by the yellow color, chlorine by the green color, carbon by the black color, hydrogen by the grey color, and oxygen by the red color, as shown below:

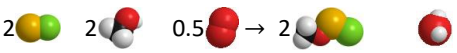

$$2CuCl + 2CH_3OH + 0.5O_2 \rightarrow 2Cu(OCH_3)Cl + H_2O \qquad \text{Eq. 2-2}$$

$Cu(OCH_3)Cl$ is then reduced by CO in the second step to regenerate CuCl [50]:

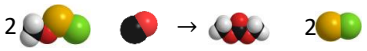

$$2Cu(OCH_3)Cl + CO \rightarrow C_3H_6O_3 + 2CuCl \qquad \text{Eq. 2-3}$$

Water formed in the first step can further reduce CuCl into element Cu with HCl formed by an undesired side reaction [50]:

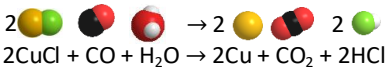

$$2CuCl + CO + H_2O \rightarrow 2Cu + CO_2 + 2HCl \qquad \text{Eq. 2-4}$$

The presence of water leads to catalyst deactivation and the formed HCl is corrosive to equipment. Therefore, the water content in the reaction system is not allowed to exceed 3 wt.%. to protect catalysts and equipment [50]. In addition, the use of oxygen may cause potential explosion risks, so the oxygen content should be limited to 4 mol.% and below [50]. In addition to CuCl catalysts, cobalt-based catalysts were also found to be active for this reaction. Delledonne et al. [51] prepared a number of cobalt complexes for this reaction. It was found that the methanol conversion was in the range of 10 - 30% and the selectivity was between 96% and 99%, with carbon dioxide being the major by-product.

Another problem of this process is that the reaction takes place in the slurry phase, which leads to a challenge in regard to the complexity of product separation and catalyst

recycling as well as energy demand. In order to avoid the separation of products and catalysts, it is possible to carry out this reaction in the gas phase. In the 1980s, the Dow Chemistry patented a gas phase oxidative carbonylation process [44]. Catalysts for the gas phase reaction are also mostly Cu-based. Tomishige et al. [52] prepared an activated carbon supported $CuCl_2$ catalyst with a Cu loading of 2.5 - 7.5 wt.%. The reaction was carried out in a fixed-bed flow reactor at temperatures of 110 - 170 ℃ and a pressure of 5 bar. The formation rate of DMC was strongly related to the Cl/Cu ratio. The by-products of carbon dioxide, MF, and dimethoxy methane, and small amount of dimethyl ether were also observed. The same by-products were also reported by Anderson et al. [53]. In order to reduce the formation of by-products and increase the selectivity, Li et al. [54] developed a highly selective CuCl/aluminium silicate catalyst. Selectivity of 100% and methanol conversions of 5 - 10%were achieved. Itoh et al. [55] developed a $CuCl_2$/NaOH/activated carbon catalyst, and the methanol conversions were in the range of 16 - 17.2% with a selectivity higher than 90%. Using bimetallic catalysts may also improve catalyst performance. Yang et al. [56] prepared a mesoporous bimetallic $PdCl_2$-$CuCl_2$ catalyst. The molar ratio of Cu/Pd was found to be a critical parameter and the optimal ratio was around 20. The highest methanol conversion was 6.4% with 100% selectivity.

However, the above mentioned catalysts all make use of chloride. There are some studies devoting to developing catalysts without chloride, which are usually based on zeolite. Richter et al. [57, 58] prepared a Cu-impregnated zeolite Y catalyst. The authors tested the catalyst's performance at atmospheric and elevated pressures. At atmospheric pressure, the methanol conversions and selectivities were around 9.0 - 11.5% and 50 - 60%, respectively, while at the elevated pressure, the methanol conversions were 5 - 12%, and the selectivities of methanol were increased to 70 - 75%. Although the gas phase oxidative carbonylation of methanol is a promising process, the selectivity and catalyst lifetime has not yet met the requirements of industrialization.

There is another gas phase carbonylation process that can avoid the separation of catalyst and products, which was developed by the UBE Industries [59]. The process splits the DMC synthesis into two steps, as shown in Fig. 2-3.

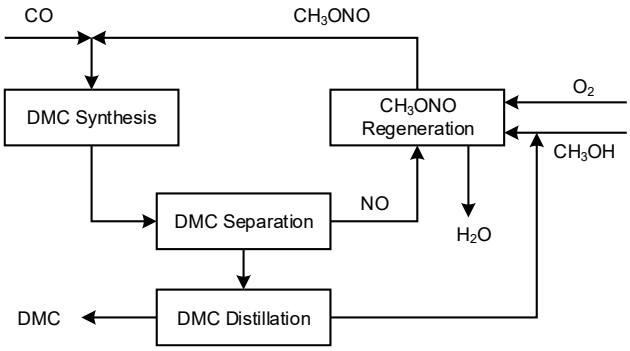

Fig. 2-3 Two-step gas phase oxidative carbonylation of methanol via methyl nitrite [59].

The first step is the synthesis of CH_3ONO from NO and O_2. NO is first oxidized by oxygen into N_2O_3, then N_2O_3 reacts with methanol to produce methyl nitrite [59]:

$$2NO + 0.5O_2 \rightarrow N_2O_3$$ Eq. 2-5

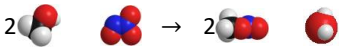

$$2CH_3OH + N_2O_3 \rightarrow 2CH_3ONO + H_2O$$ Eq. 2-6

This reaction is generally performed at around 60 ℃ in the liquid phase without catalyst [59]. The methyl nitrite from the first step is then sent to the second step together with CO for the synthesis of DMC [59]:

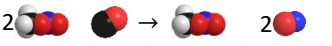

$$2CH_3ONO + CO \rightarrow C_3H_6O_3 + 2NO$$ Eq. 2-7

The above reaction is usually carried out under conditions of 80 - 150 ℃ and 2 - 5 bar [59]. The reaction is in gas phase and the product mixtures contain DMC, NO, and unreacted CO as well as methyl nitrite. The products and unreacted reactants can be separated by absorption. The unreacted reactants are sent back to the first step for methyl nitrite regeneration, and the products are then further purified to get the DMC product [59]. The reaction can be catalyzed by supported Pd-based catalysts. In order to extend catalyst lifespan, a small amount chloride compound is introduced. In addition, the anhydrous environment is beneficial to maintaining catalyst activity. The catalyst lifetime was reported to be more than one year and met the requirements of industrialization [59]. Hence, In 1993, the UBE Industries constructed a DMC plant with a capacity of 3000 t/a [59]. However, the

use of highly toxic reagents of nitrogen oxides and potential explosion risks make the process not very popular.

Studies have shown that supports have strong impacts on catalyst performance. Matsuzaki et al. [59] compared four supports for Pd-Cu-Cl catalysts. It was found that activated carbon showed the highest activity, followed by activated alumina, NaY zeolite, and silica. Despite the fact that the presence of chloride can improve the performance of Pd-based catalysts, many studies are seeking novel chloride-free catalysts. Yamamoto et al. [60] prepared a Pd/NaY catalyst for the synthesis of DMC from methyl nitrite and CO at 110 ℃. The catalyst properties were studies as a function of Pd content and calcination temperature. The selectivity was higher than 85% with respect to methyl nitrite and CO, and the catalyst remained stable after 700 h operation. Tan et al. [61] also prepared a chloride-free Pd-based catalyst. The CO conversion reached 60.1% and the selectivity toward DMC was as high as 99.9%, which were attributed to the high oxidation state of Pd. Doping Cu^{2+} in Pd/NaY catalyst could effectively promote the dispersion of Pd by shrinking the Pd species size while maintaining the high oxidation state of Pd.

2.2.2 Transesterification

DMC can be also synthesized by the transesterification reaction from methanol and ethylene carbonate:

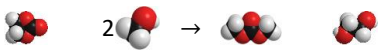

$$(CH_2O)_2CO + 2CH_3OH \rightarrow C_3H_6O_3 + (CH_2OH)_2$$ Eq. 2-8

A number of patents have been published by Texaco Company. In 1987, the Texaco patented a DMC and ethylene glycol cogeneration process from methanol and ethylene carbonate using a number of heterogeneous catalysts such as ion exchange resins, alkali and alkaline earth silicates [62]. The preferred operating temperatures of the process are 60 - 120 ℃ and operating pressures are at least 3.4 bar. Methanol to ethylene carbonate molar ratios should be between 1:2 and 1:5. Another DMC and ethylene glycol cogeneration process was subsequently patented in the same year, with the major difference being that the catalysts were changed [63]. The new process uses homogeneous metal catalysts including zirconium, titanium, and tin under similar operating conditions and is featured with higher selectivity. In 1993, the Texaco Company continued to patent a new process using a heterogeneous, phosphine-bound polymer catalyst [64]. The advantage of this process is that the optimal mass ratio of methanol to ethylene carbonate is lowered to 2 - 3 so that less

methanol has to be recycled. The lower mass ratio of methanol to ethylene carbonate is contributed by the high selectivity of the catalyst employed.

Ionic liquids are receiving ever more attention for the catalysis of this reaction. Kim et al. [65] prepared a number of immobilized ionic liquid catalysts, and the maximum ethylene conversion was 58.8 - 77% and a DMC yield of 53.9 - 69.6% was achieved. The reusability of catalysts is an important aspect for long-term industrial applications. Therefore, Kim et al. also tested the catalyst reusability for three cycles, the results showed that the ethylene carbonate conversion was decreased from 58.8% to 51.6% and the DMC yield from 53.9% to 45.0%, respectively. Yang et al. [66] developed a basic ionic liquid catalyst and tested the activity for four cycles, it was shown that the ethylene carbonate conversion and DMC yield were only slightly decreased from 90% to 88% and from 81% to 79%, respectively.

Propylene carbonate can also be used for the synthesis of DMC via transesterification, in a process that is very similar to the process via ethylene carbonate:

$$CH_3(C_2H_3O_2)CO + 2CH_3OH \rightarrow C_3H_6O_3 + CH_3CH(OH)CH_2OH$$ Eq. 2-9

Deng et al. [67] comprehensively reviewed the catalysts reported in the literature. Both homogeneous and heterogeneous catalysts are available. Homogeneous catalysts include soluble alkalis, organic non-ionic super alkalis and ionic liquids while heterogeneous catalysts include metal oxides, composite oxides, hydrotalcites, and ion exchange resins. The catalytic activity of alkoxides are usually stronger than those of inorganic alkalis, which is attributed to the strong basic strength of alkoxides [67]. Among available alkoxides, CH_3ONa is better than CH_3OLi for industrial applications due to its lower cost [67]. Although CH_3ONa is a suitable catalyst for industrial applications, it also has some disadvantages such as it is very sensitive to H_2O and CO_2 [67]. The catalyst can be deactivated even with trace amounts of CO_2 and H_2O in the reactor. Also, the formed Na_2CO_3 and CH_3OCONa are not very soluble and can block the reboiler of the reactor.

Organic non-ionic super alkalis such as verkade super alkali also show high activity at lower temperatures, but these catalysts are usually toxic and expensive [67]. 1-alkyl-3-methyl imidazolium salts are a class of representative ionic liquids, and higher temperatures and pressures are usually beneficial to catalyst activity. Ju et al. [68] investigated catalytic activity of 1-alkyl-3-methyl imidazolium salts with different alkyl groups of C_2, C_4, C_6 and C_8 and anions of Cl^-, BF_4^-, and PF_6^-. When the alkyl group increased from C_2 to C_8, the propylene carbonate conversion was decreased from 35.7% to 20.8%. In the meanwhile, the propylene

carbonate conversion was increased from 22.7% to 35.7% in the order of anions PF_6^- < BF_4^- < Cl^-. Using heterogeneous catalysts may solve the problem of CH_3ONa deactivation due to the presence of H_2O and CO_2. Oxides of metal such as Mg, Ca, Zr, Ce, and Ti are suitable candidates due to their strong basicity, abundant surface sites and simple preparation processes [67]. Bhanage et al. [69] compared four catalysts of Al_2O_3, La_2O_3, ZnO, and CaO. The CaO catalyst showed the highest DMC yield of 25.6% with 100% selectivity, followed by ZnO, La_2O_3, and Al_2O_3. In addition, using composite metal oxides may further improve catalyst performance.

Overall, homogeneous catalysts are more efficient but prone to deactivate and difficult to separate. Heterogeneous catalysts are easy to separate and have a promising future in industrial applications, but their low catalytic efficiencies remain a current challenge.

2.2.3 Direct urea methanolysis

The disadvantage of the transesterification is that equimolar ethylene glycol or propylene glycol is simultaneously produced with DMC. Urea can also be used for the synthesis of DMC by reacting with methanol, which is referred to as direct urea methanolysis:

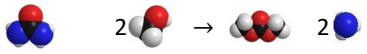

$$NH_2CONH_2 + 2CH_3OH \rightarrow C_3H_6O_3 + 2NH_3$$ Eq. 2-10

The major advantage of this pathway is that no side product is formed, and the ammonia can be easily separated and recycled. Many studies showed that the reaction follows a two-step mechanism. The first step is the formation of methyl carbamate, and it is then converted into DMC in the second:

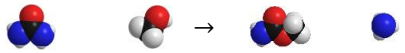

$$NH_2CONH_2 + CH_3OH \rightarrow NH_2COOCH_3 + NH_3$$ Eq. 2-11

$$NH_2COOCH_3 + CH_3OH \longrightarrow C_3H_6O_3 + NH_3$$ Eq. 2-12

The first step is thermodynamically favorable while the second step is with strong thermodynamic limitations. From the Table 2-2, we can find that the second step and the overall reaction have a positive Gibbs free energy change even at 500 K [70]. Experimental results also indicated that, in the absence of catalyst, methyl carbamate yield could reach 99%

but only trace amount of DMC can be formed at 433 K [71], showing that the second reaction is the rate-limiting step.

In order to accelerate the second step, Wang et al. [71] developed four solid base catalysts. The activity of these catalysts followed the order of CaO > La_2O_3 > MgO > ZrO_2, which was a result of the amount and strength of the basic sites. In a subsequent study, Wang et al. [72] screened ZnO as a suitable catalyst from a number of metal oxide catalysts including CaO, MgO and ZrO_2. The selected ZnO showed high DMC yield of 29% at the optimal temperature of 170 ℃. Due to the non-toxic and insoluble properties, ZnO was recommended as the model heterogeneous catalyst. The reusability test after four cycles showed that no obvious deactivation was observed, proving the stability of the catalyst. In order to further increase the DMC yield, Wang et al. [70] proposed a reactive distillation process to circumvent the thermodynamic limitations. The DMC yield was increased to 60 - 70% by in-situ removal of the DMC product, while the DMC yield of a reference batch process was only 35%. With the emergence of ammonia permeable membranes, it is now possible to integrate the reaction with an ammonia permeable membrane to shift the reaction equilibrium to the product side. Such an idea was realized in a recent study by Zeng et al. [73]. The authors employed two membranes for the synthesis and separation of DMC: a modified SAPO-34 membrane and a regular SAPO-34 one. The first membrane is for removing ammonia from the reaction system and the second for methanol permeation to get high-purity DMC. The DMC yield was increased by 139% compared a reactor without membrane.

Table 2-2 Gibbs free energy changes and equilibrium constants at different temperatures [70].

T **/K**	**Eq. 2-11**		**Eq. 2-12**		**Eq. 2-10**	
	$\Delta_r G^{\ominus}$ **/ kJ/mol**	K_{eq}	$\Delta_r G^{\ominus}$ **/ kJ/mol**	K_{eq}	$\Delta_r G^{\ominus}$ **/ kJ/mol**	K_{eq}
300	-13.26	203.88	15.41	2.08×10^{-3}	2.14	0.42
350	-13.5	120.88	15.85	4.30×10^{-3}	1.89	0.52
400	-14.82	86.07	16.41	7.20×10^{-3}	1.59	0.62
450	-15.91	70.27	17.08	1.04×10^{-2}	1.15	0.74
500	-17.21	62.74	17.84	1.37×10^{-2}	0.63	0.86
550	-18.60	58.40	18.73	1.66×10^{-2}	0.10	0.98
600	-20.23	57.65	1.72	1.2×10^{-2}	-0.51	1.11

2.2.4 Indirect urea methanolysis

The transesterification pathways produce by-products of ethylene glycol and propylene glycol. These side products can be converted back into ethylene carbonate and propylene carbonate by reacting with urea, which is referred to as indirect urea methanolysis. In fact, indirect urea methanolysis is a combination of transesterification and direct urea methanolysis. By adding one additional step of ethylene glycol or propylene glycol conversion, the DMC synthesis loop is closed. The indirect urea methanolysis is featured with no by-product formation and high conversion, as it inherits the advantages of transesterification and direct urea methanolysis.

The reaction formulas of urea with ethylene glycol and propylene glycol are shown in Eq. 2-13 and Eq. 2-14. The two reactions can be catalyzed by similar catalysts as those used for direct urea methanolysis. Bhanage et al. [74] compared a series of metal oxide catalysts and found that the ZnO catalyst exhibited higher conversion and selectivity compared to the MgO, CeO_2, La_2O_3, CaO, and ZrO_2 catalysts. Under the optimal conditions of 150 ℃ and 0.03 bar, urea was fully converted with 98% selectivity. In addition, the reusability of the ZnO catalyst was tested, and the lowest conversion of urea was 97%, suggesting the stability of the catalyst. Li et al. [75] also validated that ZnO catalysts have higher activity for the synthesis of cyclic carbonates. Acid and base properties are critical to catalyst performance. Wang et al. [76] developed an acid-base bifunctional zinc-yttrium oxide for the synthesis of ethylene carbonate, and the urea conversion and ethylene carbonate selectivity were 96% and 98%, respectively. For the synthesis of propylene carbonate, Zhao et al. [77] used a zinc acetate catalyst. The highest yield of propylene carbonate was 94% at 170 ℃ with a molar ratio of urea to propylene glycol of 2:8. Wu et al. [78] used a monolithic stirrer reactor for the synthesis of propylene carbonate with a supported zinc-chromium mixed oxide catalyst. The highest yield of propylene carbonate reached 97.8%. Overall, the yield of ethylene carbonate and propylene carbonate are both very high.

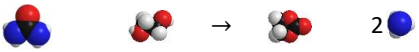

$$NH_2CONH_2 + (CH_2OH)_2 \rightarrow (CH_2O)_2CO + 2NH_3$$ Eq. 2-13

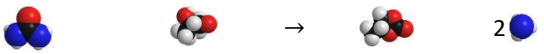

$$NH_2CONH_2 + CH_3CH(OH)CH_2OH \rightarrow CH_3(C_2H_3O_2)CO + 2NH_3$$ Eq. 2-14

2.2.5 Direct synthesis from CO_2

In the recent years, direct synthesis of DMC from CO_2 and methanol has emerged due to its short synthesis route:

$$2CH_3OH + CO_2 \rightarrow C_3H_6O_3 + H_2O \quad \text{Eq. 2-15}$$

Frequently used catalysts are based on Ce [79-83]. Other novel catalysts are also being actively developed such as ionic liquids and polymer catalysts and more details can be found in the review by Tamboli et al. [84].

However, the above is strongly thermodynamically limited. In order to achieve a high conversion, some strategies have been developed to intensify the reaction. Removing water can effectively promote methanol conversion. 2-cyanopyridine is a suitable dehydrating agent to remove water in the reaction system and has been proven efficient to increase methanol conversion and DMC yield [85-87]. Other dehydrating agents being used include benzonitrile [88], ethylene oxide [89], and butylene oxide [90]. Choi et al. [91] developed a novel circulating reaction system where molecular sieve 3A was used to remove water, and the highest yield of DMC was 27.0%. Hu et al. [89] proposed a hydration-assisted reactive distillation process using ethylene oxide as a dehydrating agent for the synthesis of DMC. The methanol conversion was increased to 99.5% compared to 10% in a fixed-bed reactor. Membrane reactors can also make contribution to the conversion. Li et al. [92] employed three hydrophilic membranes of silica inorganic membrane, polyimide-silica and polyimide-titania hybrid membranes for the water removal of direct synthesis of DMC. The highest conversion was 8.90% in the membrane reactor while the conversion in a fixed-bed reactor was 6.55%. Although direct synthesis of DMC from CO_2 and methanol is a promising pathway, it is still at an early development stage and far from practical applications.

2.2.6 Process development and analysis

Many previous studies have been devoted to the development and analysis of novel processes based on the above pathways. For direct urea methanolysis, Sánchez et al. [93] designed and analyzed a sustainable DMC process from renewable ammonia and methanol. The DMC production cost was 520 €/t, which was mainly subject to methanol price. The environmental impact analysis showed that the specific CO_2 emissions are 5.74 kg-CO_2/kg-DMC. Two studies by Vázquez et al. [94] and Javaloyes-Antón et al. [95] showed that the direct urea methanolysis pathway can be profitable if kinetic barriers could be overcome. In 2010, the Chinese Academy of Sciences built a demonstration plant for DMC production by direct urea methanolysis [96], but no scale-up of this plant was reported.

Hsu et al. [97] designed an extractive distillation for the separation of DMC and methanol for DMC production by transesterification of ethylene carbonate. Aniline was found to be an effective entrainer to enhance the relative volatility of DMC and methanol. A simple procedure was then proposed for the quick comparison of alternative entrainers before detailed process simulations. Souza et al. [98] performed a technical, economic and environmental analysis for a DMC synthesis process via transesterification of ethylene carbonate. The process uses CO_2 and ethylene oxide as raw materials to produce ethylene carbonate, and it is then used for DMC synthesis together with methanol. The analysis found that the product separation is the dominant factor to the energy performance of the process. Thus, different schemes for the separation DMC and methanol azeotrope by extractive distillation were compared. The results showed that the separation scheme using methyl isobutyl ketone as the entrainer was less energy efficient than using ethylene glycol. The economic and environmental performance of the separation scheme based on ethylene glycol is also better in terms of net present value (NPV) and equivalent CO_2 emissions. For industrial practice, in 2020, a Chinese company Zhejiang Petrochemical built a 200, 000 t/a DMC and 132, 000 t/a ethylene glycol cogeneration plant [99], which is currently the largest capacity in the world.

Holtbruegge et al. [100-104] did a series of work for the intensification of transesterification of propylene carbonate. They developed a DMC synthesis process via transesterification of propylene carbonate in a pilot-scale reactive distillation column to improve DMC yield, and the process was validated by experiments and modeling [100]. On top of the distillation column is the azeotrope of DMC and methanol. In order to separate the azeotrope energy efficiently, Holtbruegge et al. [104] proposed to use hydrophilic membranes to separate DMC and methanol mixture by vapor permeation. Based on this idea, the authors further developed a novel process combining reactive distillation and membrane separation [104]. In this process, methanol and propylene carbonate are first fed into the reactive distillation column, and the distillate from the top of the column is then separated using a membrane without condensation. The process features high DMC yield with low energy consumption for separation, which is contributed by the joint effects between reactive distillation and membrane separation. More recently, Li et al. [105] also designed a process that integrates membrane pervaporation and reactive distillation. The membrane pervaporation is also installed on top of the reactive distillation column, but one different point is that the membrane pervaporation is after distillate condensation. The process could achieve a 32% energy saving and a 42% total annual cost reduction, compared to a reactive distillation process without membrane. Huang et al. [106] designed a novel simplified process, which was also based on reactive distillation. In contrast to conventional processes with two

columns for the separation of methanol and DMC azeotrope, the simplified process employs only one column for the separation. The energy consumption of the novel process was reduced by 29.5% compared to a reference process using two columns, and the total annual cost was reduced by 31.5%.

Propylene carbonate synthesis from urea and propylene glycol is an important step for realizing indirect urea methanolysis via propylene carbonate. Shi et al. [107] published the first work on the novel process designs of indirect urea methanolysis via propylene carbonate. Different routes of propylene carbonate synthesis were considered in the process designs. Reactive distillation and distillation with internal vapor compression heat integration were found to be the economic process intensification approaches. More recently, Patraşcu et al. [108] also designed a similar process of indirect urea methanolysis via propylene carbonate. Based on rigorous process simulations, 38% and 42% reductions in heating and cooling duties were achieved by heat integration, and the resulting specific energy demand was 2.64 kWh/kg-DMC. Economic analysis showed that the production cost was 628 $/t-DMC. In 2020, the Chinese Academy of Sciences built a 50, 000 t/a demonstration DMC plant via indirect urea methanolysis of propylene glycol [109], which is a big step toward industrialization.

For direct synthesis from CO_2 and methanol, Wu et al. [110] designed and compared four direct DMC synthesis processes from CO_2 and methanol including a conventional process using continuous stirred tank reactor, an intensified process using conventional distillation with a side reactor, an intensified reactive distillation process with a side reactor, and an intensified reactive distillation process with a dehydrating agent and a side reactor. Economic analysis showed that the three intensified processes could save up to 88% total annual cost compared to the conventional process, and the CO_2 emissions were significantly reduced due to lower energy consumption. Ohno et al. [111] performed a cradle-to-gate greenhouse gas emission study for a direct DMC synthesis process from CO_2 and methanol. The process used a CeO_2 catalyst and a dehydrating agent of 2-cyanopyridine. Through process simulation and analysis, the greenhouse gas emissions were determined to be 0.39 kg-CO_2/kg-DMC, with methanol consumption being the largest contributor. Through heat exchanger network optimization, the greenhouse gas emissions were further reduced to 0.34 kg-CO_2/kg-DMC.

There are also some studies devoted to comparisons across different pathways. Garcia-Herrero et al. [112] performed an environmental assessment of a electrochemical process in comparison with an oxidative carbonylation process. The global warming potential of the electrochemical process ranged from 63.3 to 94.5 kg-CO_2/kg-DMC while that of the oxidative carbonylation process was only 3.2 kg-CO_2/kg-DMC. The high global warming potential of the

electrochemical process is caused by the low methanol conversion. If the conversion of the electrochemical process could be raised to 20%, the global warming potential of both processes will be comparable. Yu et al. [113] compared the economic performance CO_2 emissions of a direct DMC synthesis process from CO_2 and methanol and a process from CO_2 and ethylene oxide. Both economic performance and CO_2 emissions of the latter were better than those of the direct process, caused by the higher conversion of methanol. Kongpanna et al. [114] comprehensively evaluated various DMC pathways based on CO_2. In this study, different available pathways were first screened by a thermodynamic analysis. The selected processes include oxidative carbonylation of methanol, direct urea methanolysis and transesterification of ethylene carbonate. The energy performance and CO_2 emissions were then calculated and compared.

Much can be learned from these prior studies. However, no process development and analysis has been found in the context of the Power-to-Fuel, so this thesis will develop and analyze DMC production processes using CO_2 and H_2 as starting materials.

2.3 Available production pathways of MF

This section introduces available MF production pathways, and the advantages and disadvantages of each will be compared.

2.3.1 Carbonylation of methanol

Carbonylation of methanol uses CO and methanol as raw materials, which can be catalyzed by alkaline metal methoxide catalysts such as CH_3ONa [115]:

$$CH_3OH + CO \rightarrow C_2H_4O_2 \qquad \text{Eq. 2-16}$$

This process was first patented by BASF in 1925 as part of a formic acid synthesis process [115]. Typical reaction conditions are 60 - 120 ℃ and 20 - 70 bar [115]. At early stages, high-purity CO is required, later, improved processes that use dilute CO was developed so that CO from industrial sources with low purities can be used [115]. Although alkaline metal methoxide catalysts present good conversion and selectivity, the extreme sensitivity to moisture and CO_2 often deactivates catalysts. Novel catalysts that are more robust under industrial conditions are needed. Transition metal complex catalysts such as copper, ruthenium, platinum and tungsten are suitable candidates that do not need to activate the oxygen-hydrogen bond of methanol [115]. For instance, He et al. [116] developed a soluble copper nanocluster catalyst for heterogeneous carbonylation of methanol, and the prepared catalyst had better catalytic performance than CH_3ONa. Similar

to the oxidative carbonylation of methanol for DMC synthesis, another problem of carbonylation of methanol for MF synthesis is that the reaction is in the liquid phase, which leads to difficulties in separation of product and catalyst. Inspired by this idea, Rong et al. [117] proposed a vapor phase carbonylation of methanol process for MF production using nanocatalysts.

2.3.2 Dehydrogenation of methanol

MF can also be produced by methanol dehydrogenation with a side reaction of MF decomposition into syngas:

$$2CH_3OH \rightarrow C_2H_4O_2 + 2H_2 \quad \text{Eq. 2-17}$$

$$C_2H_4O_2 \rightarrow 2CO + 2H_2 \quad \text{Eq. 2-18}$$

This reaction can be carried out in the gas phase in fixed-bed reactors at 150 - 300 ℃ and atmospheric pressure. The yield of MF of this process is higher than that of carbonylation of methanol. Yet a higher MF yield is constrained by thermodynamic limitations, and membrane reactors may be applicable for this reaction to enhance conversion by removing H_2. The selectivity of the reaction toward MF is limited by the side reaction but is still up to 90% [115]. The Mitsubishi Gas Chemicals Company first industrialized this process for the purpose of producing CO by MF pyrolysis with a copper-zinc catalyst [115]. Yuan et al. [118] developed a highly stable and reusable Cu/MgO-based catalyst for this reaction. 1 wt.% doping of Pd significantly improved the activity of the catalyst. Methanol conversion of 80% with stable selectivity were achieved during 200 h operation. The basic strength of the catalyst played a key role in the catalytic performance. Since the reaction is endothermic, external heat supply is needed. The heat balance of the reaction can be realized by introducing oxygen, which is referred to as oxidative dehydrogenation of methanol. However, addition of oxygen leads to the formation of formaldehyde by partial oxidation of methanol. In addition, combustion of H_2 with oxygen generates excess heat, which reduces the energy efficiency of the process. Autothermal operation of this process could be a trade-off between heat supply and energy efficiency by controlling the amount of oxygen. Recently, a process for MF synthesis via methanol dehydrogenation by electrolysis was reported by Kishi et al. [119]. The core part of this process is a membrane electrode assembly consisting of a Pt/C electrocatalyst and a proton-exchange membrane, which may be a promising process for future development.

2.3.3 Other available pathways

Dimerization of formaldehyde to produce MF is a possible pathway but the route is longer and more complex than using methanol directly as a raw material. And more side products can be formed such as methanol and formic acid. Direct synthesis of MF from syngas is the shortest pathway, so it has received increased attention:

$$2CO + 2H_2 \rightarrow C_2H_4O_2 \qquad \text{Eq. 2-19}$$

The partial pressures of reactants are critical to the product yield. At a high partial pressure of H_2, the dominant product is methanol while at a high partial pressure of CO, the dominant product becomes MF [115]. Zhao et al. [120] prepared a catalyst comprised of Cu-Mn mixed oxides and CaO-ZrO_2 solid base, and the reaction was performed in a slurry reactor. Under the optimal reaction conditions of 160 ℃ and 30 bar, the CO conversion was 22.4% and the selectivity toward MF was 82.3%. Different Cu/Mn molar ratios were further studied, and the CO conversion and selectivity increase with Cu/Mn molar ratios. Although direct synthesis of MF from syngas represents the shortest pathway, the operating pressure is very high and the performance of current catalysts are not satisfactory enough.

MF can be also produced by CO_2 hydrogenation in the presence of methanol:

$$CO_2 + H_2 + CH_3OH \rightarrow C_2H_4O_2 + H_2O \qquad \text{Eq. 2-20}$$

Many noble metal-based catalysts can be used for the reaction. Wu et al. [121] prepared several supported gold catalysts, including Au/ZrO_2, Au/CeO_2 and Au/TiO_2. The Au/ZrO_2 catalyst was more active than the other two catalysts, and the Au/ZrO_2 catalyst with smaller Au particles showed higher activity. In order to avoid the use of noble metal catalysts, Sun et al. [122] developed a phosphine-based polymer-bound Ru catalyst. The catalyst showed high activity with a turnover number of up to 3401 at 160 ℃. There was no significant decrease in activity after seven times reuse.

2.3.4 Process development and analysis

Studies on the process development and analysis of MF production are quite limited. Scott et al. [123] developed an integrated process that combined catalytic hydrogenation and reactive distillation. The process consists of two steps. In the first step, CO_2 reacts with H_2 to form a formate-amine adduct in a heterogeneous system with *n*-decane as the catalyst phase and methanol as the product phase. In the second step, the methanol solution containing the formate-amine adduct was sent to reactive distillation for esterification and separation of MF.

1,2-Dimethyl-imidazole was identified as an effective catalyst for the integration of both steps. The purity of MF on top of the reactive distillation was 91.5% and can be further purified to obtain pure MF. Jens et al. [124] proposed a process for CO_2 capture and conversion into MF. In this process, CO_2 from raw natural gas is absorbed by methanol. The methanol solution containing CO_2 was sent to a reactor, where it was transformed into MF with addition of H_2. Compared to a segregated CO_2 capture and conversion process, the integrated process can save up to 46% operating electricity demand, leading to savings of 8% and 7% in cost and greenhouse gas emission. There is currently no study on the process development and techno-economic analysis for MF production pathways using H_2 and CO_2 as educts.

2.4 Reverse water gas shift

This section introduces the catalysis for reverse water gas shift and research status on the development of reactor concepts for this reaction.

2.4.1 Catalysis and kinetics

Reverse water gas shift transforms CO_2 and H_2 into CO and H_2O:

$$CO_2 + H_2 \leftrightarrow CO + H_2O \qquad \text{Eq. 2-21}$$

Side reactions of CO and CO_2 methanation may take place simultaneously:

$$CO_2 + 3H_2 \rightarrow CH_4 + H_2O \qquad \text{Eq. 2-22}$$

$$CO_2 + 4H_2 \rightarrow CH_4 + 2H_2O \qquad \text{Eq. 2-23}$$

The main reaction is an equimolar endothermic reaction. Thermodynamic analysis shows that the preferred temperature is in excess of 900 ℃ to increase the conversion and suppress the methanation reactions [125]. The pressure does not change the equilibrium of the main reaction, but a higher pressure can increase the productivity of CO due to faster kinetics.

Various catalysts have been developed for this reaction and have been comprehensively reviewed by Daza et al. [126], Su et al. [127], and Nielsen et al. [128]. These catalysts can be broadly classified into types of noble and non-noble metal catalysts. Although noble metal catalysts such as Pt and Rh have high activity, high costs have limited their applications. Non-noble metal catalysts are being extensively studied and used for the reaction, with Cu and Fe being two frequently used ones. For Cu-based catalysts,

introduction of Fe can elevate the activity and stability. Chen et al. [129] developed a Fe-promoted Cu/SiO_2 catalyst. By adding 0.3 wt.% Fe, the Cu/SiO_2 catalyst exhibited high and stable activity for up to 120 h. The new active species located at the interface between Cu and Fe particles are critical for enhancing the activity while remaining the reduced state of Cu. In addition to Fe, doping Cs may also improve the activity and stability of Cu-based catalysts, as shown in a study by Pastor-Pérez et al. [130]. Fe catalysts can also be used independently. Kim et al. [131] developed a Fe-oxide nanoparticle catalyst for the reaction below 600 °C. No significant sintering was observed, and the surface structure remained almost unchanged after the reaction. Ni-based catalysts also have high activity due to large oxygen exchanging capacity, but they also lead to easier CH_4 formation. Sun et al. [132] prepared a series of Ni-based catalysts supported on Ce-Zr-O by co-precipitation. The formation of the Ce-Zr-O solid solution enhanced the oxygen storage capability of the catalysts. Different Ni content was evaluated at atmospheric pressure and temperatures of 550 - 750 °C in a fixed-bed quartz reactor. A CO_2 conversion of 49.66% was reached with 3 wt.% Ni content while a selectivity of 99.65% was reached with 10 wt.% Ni. Wolf et al. [133] prepared a $Ni\text{-}Al_2O_3$ for the reaction at high temperatures. 80% CO_2 conversion was achieved at 900 °C, and long-term experiments validated the stability of the catalyst at high temperatures.

Metal oxides are also suitable candidates also thanks to large oxygen storage capacity. ZnO catalysts are frequently used due to high activity, but they are unstable at high temperatures due to reduction. Park et al. [134] found that Al_2O_3 supported ZnO catalysts with the optimal Zn/Al molar ratio of 4/1 showed good restoration resistance and stability due to the formation of $ZnAl_2O_4$ spinel phases. Other metal oxides such as In_2O_3 are also being studied [135]. In addition to single metal oxides, mixed metal oxides have even higher oxygen mobility and reducibility, especially at high temperatures [127]. Mixed metal oxides are often used in combination with chemical looping processes. For example, Daza et al. [136] prepared a $La_{1-x}Sr_xCoO_{3-\delta}$ and a $La_{0.75}Sr_{0.25}Co_{1-y}Fe_yO_3$ catalyst for a chemical looping process and found that they had high structural stability and CO productivity. Transition metal carbide catalysts are also prospective candidates for their low costs and high activity. Juneau et al. [137] developed a potassium-promoted molybdenum carbide catalyst supported on gamma alumina and investigated the viability for scale-up in the temperature range of 300 - 600 °C. The catalyst showed 44% conversion of CO_2 and 98% selectivity toward CO at 450 °C. No obvious deactivation was detected for more than ten days on stream.

Kinetics is important for the chemical reactor design and analysis. Several kinetics has been developed for different catalysts in different forms. Ernst et al. [138] proposed kinetics for Cu(110) catalysts. The activation energy was determined to be 75.3 kJ/mol. The reaction

orders of H_2 and CO_2 strongly depended on the temperature and H_2/CO_2 ratio. At very low partial pressures CO_2, the reaction order of CO_2 was around 0.6 while the order of H_2 was zero. When the partial pressure of CO_2 increased, the reaction order of CO_2 reduced to zero but the order of H_2 increased. Ginés et al. [139] developed a kinetic expression for $CuO/ZnO/Al_2O_3$ catalysts. It was also found that the reaction order of H_2 was zero at low partial pressures of CO_2. But at high partial pressures of CO_2, the orders of CO_2 and H_2 were 0.3 and 0.8, respectively. At low H_2 partial pressures, the surface coverage was very low and therefore the reaction rate was dependent on the H_2 partial pressure. At high H_2 partial pressures, the order of H_2 was reduced as abundant hydrogen can be supplied in the forms of molecule or proton. Wolf et al. [133] developed an intrinsic kinetics for $Ni\text{-}Al_2O_3$ catalysts at high temperatures. The activation energy was determined to be 82 kJ/mol. The reaction orders with respect to H_2 and CO_2 were 0.3 and 1, respectively.

2.4.2 Reactor design and simulation

There are many studies devoted to reactor modeling, simulation, and intensification. Ghodoosi et al. [140] performed a mathematical modeling study for reverse water gas shift in a fixed-bed reactor. The temperature, concentration, and pressure profiles inside the reactor were predicted, and results from the model agreed well with experimental data. Zhang et al. [141] designed and simulated a helium-heated reactor. The radial temperature gradients and the diffusion-reaction phenomenon were considered using a two-dimensional model. Significant radial temperature gradients and the resulting radial gradients of reaction rates were observed. The reactor was then optimized by the non-dominated sorting genetic algorithm to determine optimal operating parameters.

Many studies aimed to increase the conversion of CO_2 by in-situ water removal. Parra et al. [142] developed a moving-bed adsorptive reactor by using a water vapor adsorbent of zeolite 3A. The adsorbent moved slowly toward the reverse direction of reacting gases so that the reactor can be operated in steady state, and the adsorbents were regenerated in another equipment. By adsorbing produced water vapor, the reactor can work at a lower temperature with a high CO_2 conversion. The productivity of CO can be increased by an order of magnitude compared to a fixed-bed reactor under the same operating conditions. Membrane reactors can also be used to separate water vapor during reaction. To date, only one experimental study about membrane reactor application to the reverse water gas shift has been reported by Lee et al. [143]. In their study, they prepared a polyimide hollow fiber membrane for water vapor permeation and integrated it into a fixed-bed reactor. The gas permeation and long-term stability of the membrane were tested at temperatures from 200 ℃ to 300 ℃, and the reaction was then conducted employing the membrane in the

temperature range of 250 ℃ - 300 ℃. The CO yield increased by two to three times compared to a fixed-bed reactor without membrane. Dzuryk et al. [144] performed a simulation study for a packed-bed reactor equipped with a water permeable membrane. The effects of space velocity, H_2/CO_2 ratio, H_2O/H_2 perm-selectivity, and sweep gas to reacting gas pressure and flow rate ratio were comprehensively studied with co-current and counter-current flow configurations considered. Optimization was also performed to minimize reactor size, and the membrane reactor can effectively produce desired syngas for downstream fuel syntheses. One disadvantage of water vapor permeable membranes is that they can only work at low temperatures, but the reaction is preferred at high temperatures. CO_2 permeable membranes may be applicable for this reaction at temperatures up to 900 ℃, but the purpose is not conversion enhancement. By integrating CO_2 permeable membranes into this reaction, CO_2 capture and conversion can be achieved at the same time. This idea was realized in a study by Chen et al. [145], where a ceramic-carbonate dual-phase membrane is used for coupling CO_2 separation and conversion by reverse water gas shift.

Some studies were dedicated to the integration of reverse water gas shift into processes. Cui et al. [146] performed a thermodynamic analysis for methanol synthesis process from CO_2 via reverse water gas shift at moderate temperatures between 200 ℃ to 300 ℃ so that water permeable membranes are applicable. The analysis showed that using membranes could significantly improve CO_2 conversion of reverse water gas shift and subsequent methanol yield if water removal is higher than 80%. Samimi et al. [147] designed a methanol synthesis process from CO_2 via reverse water gas shift using membrane reactors. The process employed two water permeable membrane reactors, one for methanol synthesis and the other for reverse water gas shift. Based on reactor and process simulations, the process achieved a 20.8% increase in methanol production rate. Although the reaction itself is preferred at high temperatures, a study by Elsernagawy et al. [148] discussed the question if a temperature higher than 900 ℃ is necessary on a process level. It was pointed out that while running the process at a lower temperature of 450 °C demands lower energy consumption, it comes with a higher reactor cost due to lower reaction rates.

2.5 Dry reforming of methane

This section introduces the fundamental catalysis for the dry reforming of methane and the development of reactor concepts for the intensification of this reaction.

2.5.1 Catalysis and kinetics

Dry reforming of methane transforms CO_2 and CH_4 into H_2 and CO accompanied by a side reaction of reverse water gas shift:

$$CH_4 + CO_2 \rightarrow 2CO + 2H_2 \quad \text{Eq. 2-24}$$

$$CO_2 + H_2 \leftrightarrow CO + H_2O \quad \text{Eq. 2-25}$$

The main reaction is strongly endothermic and thus preferred at high temperatures to increase the conversion and reduce carbon deposition, but higher pressures can lead to lower conversions.

Developing highly active catalysts that are also resistant to carbon deposition is of particular importance to the practical applications. In general, noble catalysts are active and resistant to carbon deposition at high temperatures. Pakhare et al. [149] comprehensively reviewed the mechanism, kinetics, and deactivation of noble catalysts including Rh, Ru, Pt, and Pd. Among these metal catalysts, Rh- and Ru-based catalysts have been proven more active compared to Ni, Pd, and Pt with the same particle size and dispersion [149]. But high costs have also limited their wider applications, which motivates the developments of non-noble metal such as Ni, Fe, and Co catalysts. Among non-noble metal, Ni is the most studied and most frequently used on the industrial scale.

Carbon deposition is a major cause of catalyst deactivation, which consists of methane cracking, coke gasification, and the Boudouard reactions:

Methane cracking: $CH_4 \rightarrow C + 2H_2$ Eq. 2-26

Coke gasification: $C + H_2O \rightarrow CO + H_2$ Eq. 2-27

Boudouard: $2CO \rightarrow C + CO_2$ Eq. 2-28

When catalysts are fresh, carbon deposition is primarily due to CH_4 dissociation since CO is absent in reactants. If significant amount of CO is produced, the Boudouard reaction is also one of the primary sources of carbon deposition [149]. Many strategies have been proposed to alleviate carbon deposition and protect catalysts. A general strategy is to enhance dispersion and reduce ensemble size of active metal on the surfaces of supports [149]. It is advantageous to use supports with high surface areas, since they allow improved dispersion of active metal through structured pores and large active surface areas. But a disadvantage is that high surface area supports having small pores lead to strong diffusion limitations of reactants and products. Using supports with bimodal pores; micropores, and

macropores, may achieve a trade-off between diffusion limitations and activity [149]. To enhance the catalytic performance of Rh/Al_2O_3 catalysts by engineering catalyst pore network structure, Liu et al. [150] developed a catalyst model that considered mass, heat transfer, and reactions to optimize monodisperse and bidisperse catalyst pellets. The optimized pore diameters of the monodisperse and bidisperse catalysts were obtained. The optimal bidisperse catalyst was 56 - 175% more active with 10 - 18% less catalyst loading used compared to the optimal monodisperse catalyst with the same mesopore size, indicating the significance of introducing macroporosity into mesoporous catalyst pellets. Lin et al. [151] investigated the relationships between catalyst pore structure and catalytic activity by lattice Boltzmann simulation. A catalyst with hierarchical pore structures was modeled. To find the optimal pore structure, the effects of catalyst porosity, ratio of mesopore to macropore volume, and the ratio of average macropore to mesopore diameter on carbon deposition and catalytic performance were investigated.

Increasing the basicity of the catalysts can increase the rate of activation of mildly acidic CO_2, which assists in oxidation of surface carbon and increases the catalyst resistance to deactivation [149]. The presence of activated CO_2 on catalyst surfaces can inhibit carbon formed from CH_4 cracking. Also, increasing the oxygen conductivity of catalysts can help oxidation of carbon, and one effective way is incorporation of active metal into supports with high oxygen mobility so that carbon can be quickly gasified [149].

From a thermodynamic point of view, the reaction is preferred at low pressures to achieve a high conversion. However, high pressure is beneficial to industrial applications because of higher productivity. Nagaoka et al. [152] developed a Ru catalyst and compared the effects of several supports of SiO_2, Al_2O_3, MgO, and TiO_2 for dry reforming of methane at 20 bar and 750 °C. Although the TiO_2 supported catalyst showed the lowest activity, it featured the strongest resistance to carbon deposition, which may be attributed to the decoration of metal particle surfaces by TiO_x species, and the TiO_x species destroyed large ensemble of metal atoms that served as active sites for carbon deposition. Nagaoka et al. [153] also studied the reduction temperature on catalytic activity of a Co/TiO_2 catalyst at 20 bar. It was found that 850 °C was a critical point, below which Co/TiO_2 lost its activity completely at the beginning of the reaction caused by carbon deposition. The slow deactivation of the Co/TiO_2 was caused by the oxidation of the metallic cobalt and could be solved by addition of Ru. More recently, Kahle et al. [154] used a Pt catalyst for the reaction at 850 °C to 1000 °C and 20 bar in a pilot-plant flow reactor. A key finding was that H_2 addition can inhibit carbon deposition even better than H_2O.

In the respect of kinetic studies, there are kinetic expressions available for noble and non-noble catalysts. Richardson et al. [155] developed a kinetic model for Rh supported on y-Al_2O_3. The model includes the reactions of dry reforming of methane and reverse water gas shift, which is expressed as the classical Langmuir-type considering the adsorption of CO_2, CH_4, and H_2. The model showed good capability in predicting the conversion and product distribution and was verified by pilot-scale experiments. For Ni-based catalysts, different types of kinetics based on different mechanisms had been developed including power-law, Eley-Rideal, and Langmuir types and can be found in the review by Kathiraser et al. [156].

2.5.2 Reactor design and simulation

Currently available reactor concepts include fixed-bed reactor, solar thermochemical reactor, microreactor, and membrane reactor, and each of these has its advantages and disadvantages. Wang et al. [157] studied the effects of reactor structure and operating conditions for fixed-bed reactors. Cold spots were observed due to heat transfer limitations. Reducing the tube radius is useful to control temperature gradients, which is an important implication for reactor designs. The total pressure and CH_4/CO_2 ratio were found to be key operating parameters affecting the equilibrium conversion of CH_4. Wehinger et al. [158] focused on fixed-bed reactors with small tube-to-particle diameter ratios. A detailed model was developed that incorporated catalyst particle resolution combined with a microkinetic mechanism. This modeling approach could reduce dependencies on empiricism for the simulations of fixed-bed reactors. The model successfully determined the carbon deposition regions, which demonstrated the advantages of this modeling approach. Solar energy can be used for providing heat for this reaction. Chen et al. [159] performed a CFD simulation for a solar thermochemical reactor with a gradual foam structure in both radial and axial directions. The CH_4 conversion almost increased gradually with porosity and cell size with a uniform foam structure. The decreasing porosity and cell size either in axial or radial direction had better performance than the increasing ones. Zhang et al. [160] simulated a solar thermochemical reactor filled with structured foams. The porosity and the cell size of the foam were two important parameters affecting conversion and carbon deposition, so the optimal values of porosity and the cell size of the foam were calculated. Carbon deposition was greatly affected by incident radiation intensity. Microreactors may offer better heat and mass transport performance. Fukuda et al. [161] developed a double-layer catalytic wall-plate microreactor with a baffled channel. Compared to a tubular microreactor, the temperature gradient and carbon deposition was obviously reduced due to the excellent heat transfer. In order to further intensify the wall-plate microreactor, a void space and micro-baffle were built in the packed layer and in the blow-through channel to enhance

convective heat and mass transfer [162]. Particle-resolved CFD simulations verified the favorable effects of the microstructure on flow distribution. Experiments showed that the micro-structured wall-plate microreactor significantly outperformed the tubular microreactor with reduced carbon deposition.

Membrane reactors are able to increase conversion and selectivity by employing H_2 permeable membranes. Paturzo et al. [163] experimentally studied a Ru-based ceramic membrane reactor where the catalyst was coated on the membrane surface. Both CH_4 and CO_2 conversions greatly increased compared to a fixed-bed reactor. However, carbon deposition on the membrane surface also increased with temperature due to a higher CH_4 conversion and more H_2 removal. Haag et al. [164] used a nickel membrane reactor and found that the CH_4 and CO_2 conversions also increased and the carbon deposition was effectively suppressed. The membrane maintained a constant separation factor at 550 ℃. Leimert et al. [165] also used a nickel self-supported membrane reactor with catalyst coating on the membrane surface, which is very similar to the Ru-based ceramic membrane reactor above. The CH_4 conversion increased by 60 - 90% due to H_2 removal. However, carbon deposition on the membrane surface was also observed but could be effectively suppressed at 800 ℃ and above. Pd-based membrane reactors have been extensively studied and used for this reaction. Caravella et al. [166] performed a thermodynamic and experimental study for a Pd-Ag membrane reactor at 500 ℃. The CH_4 conversion was 26%, and the H_2 recovery was 47%. Gallucci et al. [167] compared the performance of a porous Pd-Ag membrane and a dense tubular one. The reaction temperature was in the range of 350 - 450 ℃ because a higher temperature led to the welding problem between the Pd-Ag membranes and the stainless steel tubes. The dense membrane reactor had higher CH_4 and CO_2 conversions than the porous membrane. Also, the dense membrane had stronger carbon deposition resistance compared to the porous membrane reactor. Substrates also play an important role in the membrane performance. García-García et al. [168] analyzed the performance of a Pd hollow fiber membrane reactor fabricated from an Al_2O_3 substrate. The results at 450 ℃ showed that, although the CH_4 conversion using the hollow fiber membrane reactor was almost the same as that of a tubular membrane reactor fabricated from a stainless steel substrate, the amount of Pd loading of the hollow fiber membrane reactor was much reduced. An important consideration of using membrane reactors is operating pressure, and increasing pressure can increase membrane permeation but reduce CH_4 conversion. A study found that 5 bar is a good trade-off between conversion and permeation [169].

There are also many studies for the analysis of membrane reactors for the dry reforming of methane by way of simulation. Lee et al. [170] modeled and simulated a

membrane reactor. A key conclusion was that a threshold value of H_2 flux existed to achieve effective H_2 yield enhancement. They also focused on characteristics of membrane reactor geometry by investigating the radial distance between the reactor center and the membrane. A key finding was that the H_2 yield enhancement was proportional to both the radial distance and the H_2 flux [170]. Coronel et al. [171] performed a combined experimental and modeling study for a dense Pd-Ag membrane reactor. The CH_4 conversion and H_2 flux were analysed as a function of permeation area, sweep gas flow rate, and feed composition. Co-current and counter-current configurations of the reacting gas and the sweep gas were compared. By numerical simulations, the relationship between CH_4 conversion enhancement and H_2 recovery was obtained and was in good agreement with the correlation given by Oyama et al. [172]. Bian et al. [173] simulated a H_2 permeable membrane reactor. A non-dimensionalization method was employed by introducing three dimensionless numbers of the Damköhler number, the Péclet number, and the relative permeance number. With these dimensionless numbers, the interplay between H_2 permeation and reaction was visualized and analyzed. A high H_2 flux combined with a moderate reaction rate was beneficial to the CH_4 conversion and the H_2 yield enhancement. The effect of flow configuration was investigated, and it indicated that the counter-current sweep gas configuration was more efficient.

This chapter reviews the catalysis and process developments of available DMC and MF production pathways. The catalyst and reactor concept developments are also reviewed. In the next chapter, the theory, methods, and tools for process analysis and reactor development will be introduced.

3 Theory and Methods

This chapter introduces the theory and methods involved in the Process Engineering and membrane reactor development. The methods for Process Engineering are based on techno-economic analysis, which includes aspects of technical maturity, energy efficiency, and cost estimation. The membrane reactor concepts are developed through approaches of theoretical calculations and CFD simulations. The mass, energy, and momentum conservation equations, mass transport limitations, and reaction kinetics are described and explained. The indicators for the evaluation of the developed membrane reactor concepts are also introduced.

3.1 Techno-economic analysis

This section first introduces the methods of technology readiness level (TRL) and green chemistry principles for pathway screening, and then the methods for calculating energy efficiency and costs are presented.

3.1.1 Technology readiness level

As an emerging concept, there will be inevitably some new technologies involved in the Power-to-Fuel concept. The maturity of a new technology will influence how far it is from practical applications. TRL is an assessment method that caters to the need of quantifying the maturity of a technology. It was first developed by the U.S. Department of Defense, originally known as the Technology Readiness Assessment [174]. Later, the European Commission adapted this method for the evaluation of renewable energy technologies [175], which can be readily used for Power-to-Fuel processes. The TRL is divided into nine levels. Table 3-1 gives the criteria of each TRL. TRL 1 means that a technology is at an early development stage. According to the detailed explanations by the European Commission, technologies for which only concepts, underlying barriers and applications have been identified could be assigned TRL 1 [175]. From TRL 1 to TRL 2 is a shift from fundamental principles to applied research, and possible applications of a technology can be speculated [175]. TRL 4 and 5 are technology validation phases in different settings [175]. TRL 6 and 7 are technology and system demonstration in different environments. TRL 8 is the system completion and qualification [175]. TRL 9 means that technologies have been sufficiently proven in operational environment and can be readily put into commercial operation [175]. In principle,

technologies with higher TRLs should be preferentially chosen and those with very low TRLs should be avoided such as TRL 1 or 2 that are very far from applications. TRL is a useful tool to assess the technical maturity of emerging technologies and has been extensively used in the field of CO_2 utilization. For instance, Schemme et al. [18] employed the TRL to assess conceivable production pathways of higher alcohols, and promising pathways thereof were identified. Roh et al. [176] also employed this method for evaluating emerging CO_2 utilization technologies with four demonstration cases studied. This thesis employs this method to exclude pathways of DMC and MF with TRL below 5.

Table 3-1 Criteria of TRL for renewable energy technologies by the European Commission [175].

TRL	Criteria
1	Basic principles observed
2	Technology concept formulated
3	Experimental proof of concept
4	Technology validated in lab
5	Technology validated in relevant environment
6	Technology demonstrated in relevant environment
7	System prototype demonstration in operational environment
8	System complete and qualified
9	Actual system proven in operational environment

3.1.2 Green chemistry principles

In compliance with the consensus of green production, the green chemistry principles are also used as complementary criteria for pathway screening. The green chemistry principles used here were proposed by Anastas et al. [177], which consists of twelve principles:

1. Prevention

2. Atom economy

3. Less hazardous chemical synthesis

4. Designing safer chemicals

5. Safer solvents and auxiliaries

6. Design for energy efficiency

7. Use of renewable feedstocks

8. Reduce derivatives

9. Catalysis

10. Design for degradation

11. Real-time analysis for pollution prevention

12. Inherently safer chemistry for accident prevention

The above principles can be classified into four aspects of material utilization, energy efficiency, safety, and environment protection. The green chemistry principles are used together with TRL as a preliminary step of process analysis.

3.1.3 Power-to-Fuel efficiency

Energy efficiency is basic metric that is widely used for the quantified evaluation of energy utilization level of a process. The energy efficiency is specifically termed as Power-to-Fuel efficiency and defined as follows:

$$\eta_{PtF} = \frac{\dot{m}_p \cdot LHV_p}{\frac{\dot{m}_{H_2} \cdot LHV_{H_2}}{\eta_{PEM}} + \dot{m}_{CO_2} \cdot e_{CO_2} + P_{utility}} \qquad \text{Eq. 3-1}$$

The numerator terms in the equation above represents energy outputs, which include the lower heating values of target products and by-products. The denominator is the sum of all energy input terms, including energy consumption for water electrolysis, CO_2 capture, and plant utilities. The water electrolysis technology adopted here is polymer electrolyte membrane (PEM) electrolysis, and its efficiency is assumed to be 70% [4], which is a moderate value and is realizable under current conditions. While energy demand for CO_2 capture depends on carbon sources and capture technologies, a fixed value of 1.2 MJ/kg is

used [178]. This value is typical for CO_2 capture from industrial sources by solvent absorption. The utility term accounts for energy consumption of steam, electricity, and cooling water, which is determined by process simulations and strongly depends on process designs and component properties such as phase change enthalpy and relative volatility. The forms of utilities can be steam, electricity, and cooling water, and the conditions used in calculations are shown in Table 3-2**.** Since different fuels have different lower heating values and densities, energy consumption is converted to the basis of unit liter diesel equivalent to make like-for-like comparisons.

Table 3-2 Utility forms and conditions for process simulations [32].

Utility	Condition	$\triangle T_{min}$ / K
Low-pressure steam	125 ℃, 2.3 bar	10
Medium-pressure steam	175 ℃, 8.9 bar	10
High-pressure steam	250 ℃, 39.7 bar	10
Cooling water	20 - 25 ℃	5

3.1.4 Cost estimation

This section introduces two methods for estimating capital expenditure (CAPEX): one is the method of scaling factor and the other is module costing technique. Then, cost of manufacturing (COM) and profitability analysis are shown.

Capital expenditure

The total costs required for building a plant are referred to as capital expenditure (CAPEX). CAPEX is the sum of fixed-capital investment (FCI) and working capital (WC). FCI represents the cost of purchased equipment, instrument, installation, etc, while WC represents cash flows needed to maintain plant daily operation, which usually accounts for 15% of CAPEX [179]:

$$CAPEX = FCI + WC = \frac{FCI}{0.85} \quad \text{Eq. 3-2}$$

To calculate CAPEX, the remaining task is to determine FCI. At present, there are two methods for estimating FCI: (1) method of scaling factor, which is based on the work by Peters et al. [179]; (2) module costing technique, which was given by Turton et al. [180]. In

either method, the key step is to calculate purchased equipment costs. The calculation procedures of both methods are specifically shown below.

Method of scaling factor

The method of scaling factor is based on the economies of scale [179]:

$$C_a = C_b \left(\frac{S_a}{S_b} \right)^{sf} \quad \text{Eq. 3-3}$$

In above equation, C_a represents the purchased cost of equipment to be calculated. C_b represents the purchased cost of reference equipment, which can be found in literature. S_a and S_b represent characteristic size, respectively. The characteristic size can be power consumption for compressors and pumps and areas for heat exchangers. Finding a reference equipment cost and calculating the characteristic size of the equipment to be calculated are the two main tasks. *sf* represents the scaling factor. In reality, the scaling factor varies with equipment type and size. In the absence of more information, the scaling factor can be 0.6 and therefore this method is also called the six-tenths rule [179]. In general, the scaling factor should be less than 1. The larger the equipment is, the lower the cost of equipment per unit of capacity is, which is a benefit of economies of scale [179]. One underlying assumption of using this method is that the related equipment only differs in size, while other aspects, like operating conditions and construction materials, cannot be reflected. Another constraint is that the size of both equipment should be in the same order of magnitude, otherwise the accuracy will be unacceptable [179]. Despite these limitations, this method is widely used for estimating equipment or even total process costs for its quick estimation ability.

After calculating purchased equipment costs, FCI can be estimated by ratio factors because all other costs are directly or indirectly related to purchased equipment costs. Peters et al. [179] gave a table that shows the ratio factor of each contributing cost item. It can be found that the FCI is further divided into direct costs and indirect costs. Direct costs include those used for equipment purchase and related costs while indirect costs include those used for serving plant construction. By summing up each cost item, the FCI and CAPEX can be determined. Peters et al. [179] roughly classified chemical plants into three types: solid processing, solid-fluid processing and fluid processing. From the table, it is found that the CAPEX is around 4.5 to 6 times the purchased equipment costs, with the type of fluid processing being the highest. For Power-to-Fuel processes, the fluid processing type is applicable. In summary, there are two major steps for calculating CAPEX: the first step is

calculating purchased equipment costs using Eq. 3-3 and the second one is calculating CAPEX with Table 3-3.

Table 3-3 Ratio factors for calculating FCI and CAPEX based on purchased equipment cost [179].

Item	**Percentage of purchased equipment cost**		
	Solid	**Solid-fluid**	**Fluid**
Direct costs			
Purchased equipment delivered	100	100	100
Purchased equipment installation	45	39	47
Instrumentation and controls (installed)	18	26	36
Piping (installed)	16	31	68
Electrical systems (installed)	10	10	11
Buildings (including services)	25	29	18
Yard improvements	15	12	10
Service facilities (installed)	40	55	70
Total direct plant cost	269	302	360
Indirect costs			
Engineering and supervision	33	32	33
Construction expenses	39	34	41
Legal expenses	4	4	4
Contractor's fee	17	19	22
Contingency	35	37	44
Total indirect plant cost	128	126	144
FCI	**397**	**428**	**504**
WC (15% of CAPEX)	**70**	**75**	**89**
CAPEX	**467**	**503**	**593**

Module costing technique

In addition to the disadvantage of low accuracy, another disadvantage of the scaling factor method is that if a totally new plant is to be designed, there is no equipment available for reference, and then this method fails. On this occasion, the module costing technique is an alternative. In contrast to the scaling factor method, the module costing technique uses a general correlation is to calculate purchased equipment costs [180]:

$$\log_{10} C_{p,0} = K_1 + K_2 \log_{10} A + K_3 \left(\log_{10} A\right)^2 \quad \text{Eq. 3-4}$$

where K_1 K_2, and K_3 are the cost coefficients and they were defined by Turton et al. [180]. For conventional chemical process equipment such as pumps, heat exchanger, tank, etc. A is the characteristic size, which has been explained above in the scaling factor method. After calculating purchased cost of each equipment, the next step is to calculate the bare module cost [180]:

$$C_{BM} = C_{p,0} F_{BM} \quad \text{Eq. 3-5}$$

where $C_{p,0}$ is bare module cost under base conditions, and F_{BM} is bare module factor, which accounts for direct and indirect cost items. The F_{BM} is similar to the ratio factors in the table above**,** but it contains more aspects of material and pressure factors, calculated by [180]:

$$F_{BM} = B_1 + B_2 F_p F_M \quad \text{Eq. 3-6}$$

where B_1 and B_2 are equipment-dependent, F_p and F_M are the pressure and material factors. F_p is calculated through the correlation below [180]:

$$\log_{10} F_p = C_1 + C_2 \log_{10} p + C_3 \left(\log_{10} p\right)^2 \quad \text{Eq. 3-7}$$

where C_1, C_2, and C_3 are the pressure correction coefficients. Note that the above relationship is only applicable when the pressure is higher than 5 bar, and F_p=1 otherwise. The next step is to calculate grass root cost of each equipment, which consists of two parts. The first term below represents contingency and fee costs, and the second term represents auxiliary facilities costs [179]:

$$C_{GR} = 1.18 \sum_{i=1}^{n} C_{BM,i} + 0.5 \sum_{i=1}^{n} C_{BM,i}^0 \quad \text{Eq. 3-8}$$

$$C_{BM,i}^0 = C_{p,0} \left(B_1 + B_2\right) \quad \text{Eq. 3-9}$$

FCI can be obtained by summing up the grass root costs of all equipment. From the calculation procedures, it is found that the module costing technique may be more accurate than the method of scaling factor because the former method considers more factors including the impacts of pressure and materials, but it also requires more information of equipment, which can be realized with the help of process simulations. One disadvantage of this method is that coefficients for calculating $C_{p,0}$ are only available for conventional equipment. Coefficients for unconventional equipment such as water electrolyzers are still missing. In this circumstance, the two methods can be used in a hybrid mode to overcome the disadvantages of each other. Therefore, in this thesis, both methods will be applied.

Cost of manufacturing

Determination of COM is through a breakdown approach. Total costs are the sum of a number of sub-items. The sub-items can be divided into two categories: one is material costs and the other is operating costs, as shown in Table 3-4. Material costs include raw material and utility, etc. Operating costs contain many miscellaneous items such as labor costs, maintenance, depreciation, etc. From the table, it can also be seen that some items are interdependent. For example, maintenance and repair work as well as taxes and insurance costs are related to FCI, and patent and license fees depend on COM. By adding all the cost items, the formula for calculating COM is obtained [180, 181].

Table 3-4 Cost items for the calculation of COM [180, 181].

Cost	Item	Calculation
Material costs	Raw materials and utilities	$C_R + C_U$
	Overhead costs: transport, storage, etc.	$0.708 \cdot C_p + 0.036 \cdot FCI$
Operating costs	Manufacturing staff	C_p
	Surveillance and office staff	$0.18 \cdot C_p$
	Maintenance and repair work	$0.06 \cdot FCI$
	Consumables	$0.009 \cdot FCI$
	Labor costs	$0.15 \cdot C_p$
	Patent and license fees	$0.03 \cdot COM$
	Taxes and insurance	$0.032 \cdot FCI$
	Depreciation	$FCI \cdot i(1+i)^t / \left((1+i)^t - 1\right)$

$$COM = 0.141FCI + 2.1C_p + 1.03\left(C_R + C_U\right) + FCI \cdot \frac{i\left(1+i\right)^t}{\left(1+i\right)^t - 1} \quad \text{Eq. 3-10}$$

Net present value and minimum selling price

CAPEX and COM reflect how much money should be paid to build and operate a chemical plant, but it remains unknown if the plant is profitable. Therefore, it is necessary to perform profitability analysis. The profitability of a process, one the one hand, depends on COM, on the other hand, depends on selling prices of products. Therefore, a higher COM of a process does not necessarily mean that it is less profitable. There are many indicators which can be used to quantify profitability such as return on investment, payback period, net present value (NPV), and minimum selling price (MSP), etc. This thesis selects NPV and MSP as the indicators for profitability analysis. NPV represents the total absolute revenues over the whole lifetime of a plant [182, 183]:

$$NPV = \sum_{t=1}^{n} \frac{C_i - C_o}{\left(1+i\right)^t} \quad \text{Eq. 3-11}$$

where C_i and C_o are cash inflow and outflow, and their difference mean net profits of each fiscal year. i interest rate. C_i is determined by selling prices of products, and C_i is cash outflow that depends on COM, and i is interest rate, which reflects the time value of money. For simplicity, the i is fixed at 8% as it is a relatively stable value. NPV>0 suggests that a process is profitable. Changes of the above three parameters can lead to different NPV values. Particularly, the selling price of products that leads to zero NPV is referred to as MSP [182, 184]:

$$\sum_{t=1}^{n} \frac{\left(MSP - COM\right) \cdot \dot{m}_p}{\left(1+i\right)^t} = 0 \quad \text{Eq. 3-12}$$

If the market selling price is higher than the MSP, then the plant can be seen as profitable. It should be noted that although market prices vary with time and region, the purpose is to provide a breakeven point to determine the profitability of a plant. In further analysis, sensitivity will be performed to study the impacts of market uncertainties.

The assumptions for calculating COM are given in Table 3-5. These values are taken from relevant studies in the literature and previous studies of IEK-14, and their validity is as such confirmed. Since the prices of the ducts and products can change from time to time,

these values are only indicative prices, and the impacts of price fluctuations are reflected by sensitivity analysis.

Table 3-5 Assumptions used in the cost calculations.

Assumption	Value	Reference
H_2 price	4.6 €/kg	[185]
CO_2 price	70 €/t	[33]
O_2 price	80 €/t	[186]
Low-pressure steam	0.0146 €/MJ	[24]
Medium-pressure steam	0.0158 €/MJ	
High-pressure steam	0.0187 €/MJ	
Operating electricity	0.0976 €/kWh	
Cooling water	0.1 €/t	
Plant lifetime	20 years	[187]
Interest rate	8%	[188]
DMC selling price	1000 €/t	[189]
MF selling price	1000 €/t	[190]

3.2 Computational fluid dynamics modeling

This section introduces the mass, heat and momentum conservation equations, which are presented in differential forms. Reaction kinetics and mass transport limitations are also introduced and incorporated into the mass balance equations.

3.2.1 Mass balance

The mass balance of a chemical reactor can be generally expressed in a differential form [191]:

$$\frac{\partial \rho}{\partial t} + \nabla \cdot \left(\rho \overset{\mathrm{r}}{v} \right) = S_m \qquad \text{Eq. 3-13}$$

where ρ is fluid density and $\vec{v}$ is velocity. The first term on the left side represents accumulation or loss of mass in the system; the second term is mass flux by fluid flow. S_m stands for external source terms such as adsorption or membrane permeation. The above equation is applicable for incompressible and compressible flows. For 2D axisymmetric geometries, the continuity equation is adapted to the following coordinate form [191]:

$$\frac{\partial \rho}{\partial t}+\frac{\partial}{\partial x}\left(\rho v_x\right)+\frac{\partial}{\partial r}\left(\rho v_r\right)+\frac{\rho v_r}{r}=S_m \qquad \text{Eq. 3-14}$$

where v_x is velocity in axial direction, and v_r is velocity in radial direction. If chemical reactions are present in the system, the continuity equation is more specifically written as follows [191]:

$$\frac{\partial}{\partial t}\left(\rho Y_i\right)+\nabla\cdot\left(\rho \vec{v} Y_i\right)=-\nabla\cdot\vec{J}_i+\eta_o r_i+S_i \qquad \text{Eq. 3-15}$$

where Y_i is the species local mass fraction. $\vec{J}_i$ is mass diffusion of species caused by concentration and temperature gradient, which accounts for mass transport by natural convection. r_i is consumption or production rate of species by chemical reactions, and η_o is catalyst overall effectiveness factor, which accounts for the mass transport limitations to reactions and will be explained in detail in the following sections.

3.2.2 Heat balance

The heat balance equation is also composed of several terms [191]:

$$\frac{\partial}{\partial t}\left(\rho E\right)+\nabla\cdot\left(\vec{v}\left(\rho E+p\right)\right)=\nabla\cdot\left(k_{eff}\nabla T-\sum_j h_j\vec{J}_j+\left(\overline{\overline{\tau}}_{eff}\cdot\vec{v}\right)\right)+S_h \qquad \text{Eq. 3-16}$$

$$E=h-\frac{p}{\rho}+\frac{v^2}{2} \qquad \text{Eq. 3-17}$$

where E is energy, p is static pressure, k_{eff} is the effective conductivity, and $\overline{\overline{\tau}}_{eff}$ is the stress tensor. The first three terms on the right side represent heat transfer due to conduction, species diffusion, and viscous dissipation, respectively.

3.2.3 Momentum balance

The momentum balance equation is written as follows [191]:

$$\frac{\partial}{\partial t}\left(\rho \vec{v}\right)+\nabla\cdot\left(\rho \vec{v}\vec{v}\right)=-\nabla p+\nabla\cdot\left(\bar{\bar{\tau}}\right)+\rho\vec{g}+\vec{F} \qquad \text{Eq. 3-18}$$

where $\rho\vec{g}$ and $\vec{F}$ are the gravitational body and external body forces such as those arise from interaction with the dispersed phase, respectively. $\vec{F}$ also contains other model-dependent source terms such as porous media, which can be used for calculating pressure drop.

Pressure drop is an important aspect in designing chemical reactors. Low pressure drop is desired because less energy is then required for compression of feedstock. As mentioned above, pressure drop of catalyst bed can be solved by the term of $\vec{F}$ in the above equation. In reality, pressure drop is subject to many factors such as porosity, fluid velocity catalyst particle shape and size, etc. Detailed calculations of pressure drop requires resolution of catalyst particles and is beyond the scope of this thesis. An alternative way of calculating pressure drop is to simplify catalyst beds as porous media model. Porous media model significantly reduces the complexity of pressure drop calculations while still capturing the main characteristics of catalyst beds. A widely used model for pressure drop estimation was proposed by Ergun [192], which was derived from packed columns :

$$\Delta p=\frac{150\mu L}{d_p^2}\frac{\left(1-\varepsilon_b\right)^2}{\varepsilon_b^3}v_s+\frac{1.75\rho L}{d_p}\frac{\left(1-\varepsilon_b\right)}{\varepsilon_b^3}v_s^2 \qquad \text{Eq. 3-19}$$

where μ is fluid viscosity, d_p is catalyst diameter, and ε_b is porosity of catalyst bed. v_s is superficial velocity. The above equation is then incorporated into Eq. 3-18 as part of the momentum balance. In this thesis, only the pressure drop in the axial direction is considered. The Ergun equation can be solved by the ANSYS Fluent program by defining the intrinsic permeance α and inertial resistance β [193]:

$$\alpha=\frac{\varepsilon_b^3 d_p^2}{150\left(1-\varepsilon_b\right)^2} \qquad \text{Eq. 3-20}$$

$$\beta=\frac{3.5\left(1-\varepsilon_b\right)}{\varepsilon_b^3 d_p} \qquad \text{Eq. 3-21}$$

3.2.4 Reaction kinetics and mass transport limitations

As mentioned in the mass balance equations, the kinetics of a reaction is inevitably slowed by mass transport limitations. The limitations are caused by concentration gradients

of reactants inside and outside of catalyst. In the bulk stream, reactants pass through the boundary layer surrounding the catalyst to reach the particle surface, and then they continue to diffuse through catalyst pores to reach active sites. As a result, the concentration of reactants at active sites is much lower than in the bulk stream, leading to much reduced reaction rates. The external and internal mass transport limitations can be quantified by external and internal effectiveness factors. The internal effectiveness factor is defined as the ratio of the reaction rate using reactant concentration within catalyst to the reaction rate with concentration on catalyst surfaces [194]:

$$\eta_{int,i} = \frac{r_{i,obs}}{r_{i,surf}} = \frac{\int_0^{V_p} r_i\left(C_i\right) dV}{V_p r_i\left(C_{i,s}\right)} \qquad \text{Eq. 3-22}$$

where V_p is the volume of catalyst, $r_{i,obs}$ is the observed reaction rate, which is calculated based on the species concentrations within catalyst particles and $r_{i,surf}$ is the surface reaction rate on the catalyst surface using species surface concentrations. To calculate the internal effectiveness factor, the internal and surface concentration of reactants should be known. However, it is difficult to obtain internal and surface concentrations. Thiele modulus can be used to calculate the internal effectiveness factor according to [194, 195]:

$$\eta_{int,i} = \frac{1}{\phi_{TM}}\left(\frac{1}{\tanh 3\phi_{TM}} - \frac{1}{3\phi_{TM}}\right) \qquad \text{Eq. 3-23}$$

$$\phi_{TM} = \frac{V_p}{S_p}\sqrt{\frac{n+1}{2}\frac{k_{i,s}C_{i,s}^{n-1}\left(1+K_{eq}\right)}{D_{mi}^e K_{eq}}} \quad n > -1 \qquad \text{Eq. 3-24}$$

where ϕ_{TM} is Thiele modulus, V_p and S_p are catalyst volume and surface area, K_{eq} is reaction equilibrium constant, $k_{i,s}$ is surface kinetic factor, D_{mi}^e is the effective pore diffusion of component *i*, which encompasses molecular diffusion and Knudsen diffusion [195]:

$$\frac{1}{D_{mi}} = \frac{1}{D_{ki}} + \sum_{\substack{j=1 \\ j\neq i}}^{N} \frac{x_j}{D_{i,j}} \qquad \text{Eq. 3-25}$$

$$D_{mi}^e = \frac{\varepsilon}{\tau} D_{mi} \qquad \text{Eq. 3-26}$$

where D_{ki} and $D_{i,j}$ are Knudsen and binary diffusion coefficients; respectively. ε and τ are catalyst porosity and tortuosity, respectively. Knudsen and molecular diffusion can be estimated by [195, 196]:

$$D_{ki} = 97 r_{pore} \sqrt{\frac{T}{M_i}} \quad \text{Eq. 3-27}$$

$$D_{i,j} = \frac{10^{-7} T^{1.75}}{p\left[\left(\sum V_i\right)^{1/3} + \left(\sum V_j\right)^{1/3}\right]} \sqrt{\frac{1}{M_i} + \frac{1}{M_j}} \quad \text{Eq. 3-28}$$

where r_{pore} is catalyst pore radius, which is usually from a few nanometers to tens of nanometers; M_i and M_j are molecular weight; V_i and V_j are atomic diffusion volume.

In practice, Eq. 3-24 is only used for first order reactions as surface concentration is unknown for higher order reactions. For reactions with higher orders, linearization should be performed so that surface concentration is not needed. Before linearization, a key component that has a higher reaction order should be selected as it has stronger effects on reaction rates [197]. Then the linearized reaction rates can be expressed as:

$$r_i = k_{i,s}\left(C_i - C_{i,eq}\right) \quad \text{Eq. 3-29}$$

The external effectiveness factor of a reaction can be calculated using the second-order Damköhler number [193]:

$$\eta_{ext,i} = \frac{r_{i,surf}}{r_{i,bulk}} = \frac{k_{i,s} C^n_{i,s}}{k_{i,s} C^n_{i,b}} = \frac{1}{1 + Da_{II}} \quad \text{Eq. 3-30}$$

The second order Damköhler number is defined as the ratio of reaction rates to mass transport rates:

$$Da_{II} = \frac{k_{i,s}}{A_{ext}\beta_i} \quad \text{Eq. 3-31}$$

where A_{ext} and β_i are specific external catalyst surface area and mass transport area, respectively. β_i is calculated based on the Sherwood, Reynolds, and Schmidt numbers [133]:

$$\beta_i = \frac{Sh_b D^e_{mi}}{d_p} \quad \text{Eq. 3-32}$$

$$Sh_b = \left(1 + 1.5\left(1 - \varepsilon_b\right)\right) Sh_p \quad \text{Eq. 3-33}$$

$$Sh_p = 2 + 0.69\sqrt{Re_p}\sqrt[3]{Sc} \quad \text{Eq. 3-34}$$

$$Re_p = \frac{u_s d_p}{\varepsilon_b \mu_i}$$ Eq. 3-35

$$Sc = \frac{\mu_i}{D_{mi}^e}$$ Eq. 3-36

With internal and external effectiveness factors, observed reaction rates are calculated as:

$$r_{i,obs} = \eta_{int,i}\eta_{ext,i} r_i$$ Eq. 3-37

The intrinsic kinetics for reverse water gas shift is taken from Wolf et al. [133]. The reaction order with respect to H_2 is 0.3 using Ni-based catalysts, suggesting that it is less influential to the reaction rate:

$$r_1 = k_1 \left(c_{CO_2} c_{H_2}^{0.3} - \frac{c_{CO} c_{H_2O}}{K_{eq1} c_{H_2}^{0.7}} \right) \quad mol/(kg\,s)$$ Eq. 3-38

$$k_1 = 3100 \exp(-82000/RT)$$ Eq. 3-39

The intrinsic kinetics for dry reforming of methane is from Richardson et al. [155]. The reaction mechanism of dry reforming of methane consists of two reactions, and the kinetics is based on Rh catalysts:

$$r_2 = \frac{k_2 K_{CO_2 1} K_{CH_4} p_{CO_2} p_{CH_4}}{\left(1 + K_{CO_2 1} p_{CO_2} + K_{CH_4} p_{CH_4}\right)^2} \left(1 - \frac{p_{CO}^2 p_{H_2}^2}{K_{eq2} p_{CO_2} p_{CH_4}} \right)$$ Eq. 3-40

$$k_2 = 1290 \exp(-102065/RT) \quad mol/(g_{cat}\,s)$$ Eq. 3-41

$$K_{CO_2 1} = 0.0261 \exp(37641/RT) \quad atm^{-1}$$ Eq. 3-42

$$K_{CH_4} = 0.026 \exp(40684/RT) \quad atm^{-1}$$ Eq. 3-43

$$r_3 = \frac{k_3 K_{CO_2 2} K_{H_2} p_{CO_2} p_{H_2}}{\left(1 + K_{CO_2 2} p_{CO_2} + K_{H_2} p_{H_2}\right)^2} \left(1 - \frac{p_{CO} p_{H_2}}{K_{eq3} p_{CO_2} p_{H_2}} \right)$$ Eq. 3-44

$$k_3 = 350 \exp(-81030/RT) \quad mol/(g_{cat}\,s)$$ Eq. 3-45

$$K_{CO_2 2} = 0.5771 \exp(9262/RT) \quad atm^{-1}$$ Eq. 3-46

$$K_{H_2} = 1.494\exp(6025/RT) \quad atm^{-1}$$ Eq. 3-47

3.3 Membrane permeation and modeling

This section introduces different types of membranes for water, carbon dioxide, and hydrogen permeation that will be used for the reactions of reverse water gas shift and dry reforming of methane. In parallel, available membrane reactor concepts are introduced. To model membrane reactors, the mechanisms of different permeation processes are described. Then, mathematical models for membranes are formulated and incorporated into CFD models via user-defined functions (UDFs). Finally, this section introduces two dimensionless numbers for guiding membrane reactor selection and matching.

3.3.1 Zeolite membranes for water separation

The motivations of using water permeable membranes are to increase the conversion and protect catalysts. To date, various water permeable membranes are available. Polymer membranes such as polyvinylidene fluoride hollow fiber membranes are being extensively used for water separation due to their high fluxes and stability. However, the applications of polymer membranes are limited to temperatures below 200 ℃. In addition, polymer membranes are meso- or macro-porous, which have low selectivities for separating small molecules [198]. For many fuel synthesis reactions by CO_2 hydrogenation, operating temperatures are typically in the range of 200 – 300 ℃. Therefore, water permeable membranes that can work at temperatures higher than 200 ℃ are required. As a kind of inorganic membranes, zeolite membranes can meet this requirement, which are capable of working at high temperatures with high thermal stability. Zeolite membranes are made of crystalline microporous aluminosilicates composed of TO_4 tetrahedra, where T can be Al, P, Si, etc [198]. The general chemical formula of zeolites can be expressed as $M_{2/n}OAl_2O_3{\cdot}xSiO_2{\cdot}yH_2O$, where the cation M has valence n, x is 2 or more, and y is the moles of water in the voids [199]. The advantages of zeolite membranes include uniform structure, structural diversity, excellent stability, and adjustable hydrophilicity. To date, various types of zeolite membranes have been developed including Linde type A (LTA), chabazite (CHA), ZSM-5, faujasite (FAU), mordenite (MOR), etc. These membranes are characterized by different pore size and structures, as shown in Fig. 3-1. Table 3-6 summarizes selected zeolite membrane parameters.

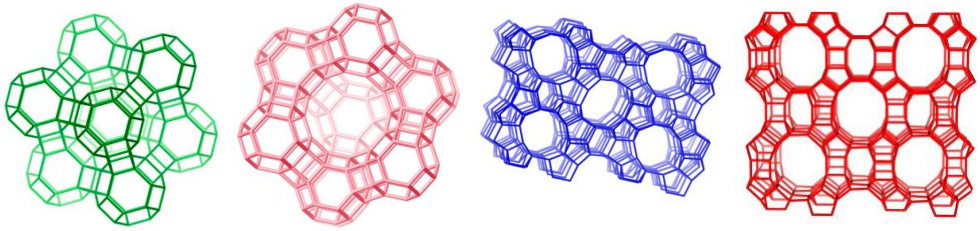

(a) (b) (c) (d)

Fig. 3-1 Structures of selected zeolite: (a) LTA; (b) FAU; (c) MFI; (d) MOR [200, 201].

Table 3-6 Structure and pore size of some zeolite membranes [202].

Structure type	**LTA**	**FAU**	**MFI**	**MOR**
Si/Al ratio	1	2.3	8 ~ ∞	4
Cation	Na	Na, Ca	Na	Na
Pore size	0.41 nm × 0.41 nm	0.74 nm × 0.74 nm	0.51 nm × 0.55 nm 0.53 nm × 0.56 nm	0.65 nm × 0.70 nm 0.34 nm × 0.48 nm 0.26 nm × 0.57 nm
Channel network	3D	3D	3D	1D

There are three possible separation mechanisms of zeolite membranes: preferential adsorption, diffusion, and molecular sieving [203], shown in Fig. 3-2. In the mechanism of preferential adsorption, water molecule is preferentially adsorbed on the pore surfaces, whereas other molecules are rejected. In the mechanism of diffusion, molecules with faster diffusion rates can pass through the membrane pore tunnels, and the diffusion can be molecular or Knudsen diffusion. In the mechanism of molecular sieving, the passage of molecules strongly depends on pore size, but trade-offs must be made between flux and selectivity.

No matter what kind of mechanisms, the performance of zeolite membranes can be improved by both external and internal factors.

The temperature is a critical external factor that affects the amount of water adsorbed. Higher temperatures make water adsorption weaker, leading to blocking effects reduced and diffusion rates of other molecules increased [198]. As a result, the separation factor is reduced. Another potential problem at high temperatures is that cracks may be formed in the absence of water due to the shrinkage of zeolite grains in dry gases. In terms of pressure,

Gorbe et al. [204] found that water vapor/gas separations at high pressures could cause a significant drop in separation factor, although water fluxes could be much increased. This is because the diffusion of other molecules becomes much faster at a higher pressure difference between feed and permeate sides, suggesting that operating pressure should also be balanced.

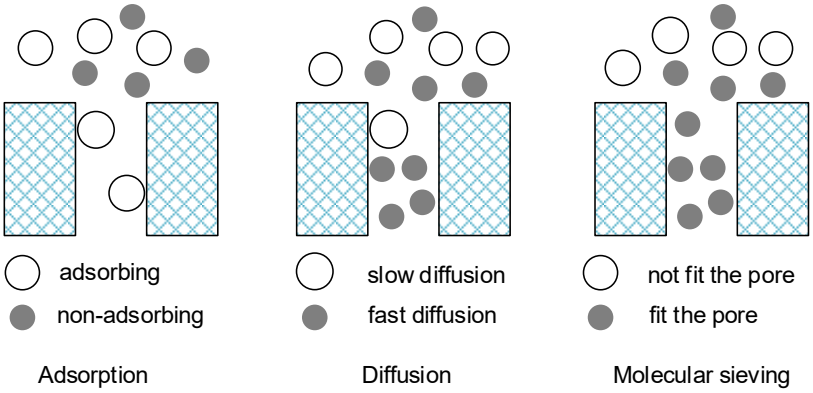

Fig. 3-2 Separation mechanisms of zeolite membranes [203].

Internal factors include pore size, hydrophilicity, and defects. The matching between zeolite pore and molecule size is critical to membrane performance. Table 3-7 gives the kinetic diameters of selected molecules. H_2O has the smallest diameter, which is the basis of separating it from light gases. Ion-exchange method is an effective way to get stronger hydrophilicity. Ion-exchange using Na^+ cation can significantly increase the affinity toward polar molecules such as water, which can provide more active sites for water adsorption [198]. The Si/Al ratio is an important parameter to zeolite membrane performance. More Al contents can accommodate more cations, leading to stronger hydrophilicity, but high Al contents also make membranes unstable [198]. In addition, defects within zeolites can also reduce the resistance of zeolite membranes, resulting in leakage of undesired molecules [198]. Defects of zeolite pore structures can be controlled by the preparation method. Secondary growth is an effective approach to prepare defect-free polycrystalline membranes. In this method, nanosized seeds are prepared and deposited onto a support by dip-coating and spin-coating, which then provide nucleation sites for sequential growth of crystals. Also, the removal of template during preparation processes could lead to the formation of non-zeolitic voids, which could be avoided by using template-free methods [198].

Table 3-7 Kinetic diameters of selected molecules [205].

Molecule	H_2	CO	CO_2	H_2O	CH_4	N_2
Kinetic diameter / Å	2.89	3.76	3.30	2.65	3.80	3.64

There are some prior examples applying zeolite membranes for fuel synthesis reactions at high temperatures. Raso et al. [206] prepared a number of zeolite membranes including LTA, MOR, zeolite T, CHA-Al, and CHA-Ti and tested their performance for separation of $H_2O/H_2/CO_2$ mixtures at high temperatures between 160 ℃ and 260 ℃. For the LTA membrane, the separation factors for H_2O/CO_2 and H_2O/H_2 increased with temperature below 200 ℃, above which the separation factor decreased with temperature due to less amount of water adsorbed but its permeance always increased with temperature. The separation factors of the MOR were much lower compared to the LTA membrane. The H_2O/H_2 separation factor of the MOR was below 1, suggesting that H_2 moves faster than H_2O. The performance of the zeolite T membrane was better than the MOR membrane but still lower than the LTA membrane. Both the CHA-Al and CHA-Ti membranes were also inferior to the LTA membrane in terms of separation factor. Based on the membrane performance, the LTA membrane was then applied to the methanol synthesis reaction. The results showed that the CO_2 conversion and methanol yield were significantly increased by removing water. These results suggested that the LTA membrane may be more suitable for fuel synthesis reactions at high temperatures. Gallucci et al. [207] also conducted an experimental study on methanol synthesis between 210 ℃ and 250 ℃ using an LTA membrane reactor. The CO_2 conversion in the membrane reactor was more than doubled and the methanol yield was more than tripled compared to a conventional fixed-bed reactor. A later theoretical analysis also by Gallucci et al. [208] confirmed that it is possible to achieve a higher CO_2 conversion and selectivity simultaneously. Becka [40] developed a membrane reactor concept for methanol by CO_2 hydrogenation. The CO_2 conversion was increased by 75% compared to a fixed-bed reactor but the methanol productivity was decreased due to a lower space velocity. Diban et al. [209] performed a study for dimethyl ether synthesis by methanol dehydration using a zeolite membrane. It was shown that the dimethyl ether yield enhancement was strongly related to the selectivity of the zeolite membrane. A low selectivity could not lead to a higher dimethyl ether yield due to the loss of methanol. Also, removal of water did not only enhance the dimethyl ether yield, but the hydrocarbons were increased. Rohde et al. [210] prepared a hydroxy sodalite zeolite (H-SOD) membrane with high water fluxes and selectivities. The membrane can work at high temperatures up to 200 ℃ and therefore could be used for Fischer-Tropsch synthesis and other fuel synthesis reactions. It was pointed out

that the permeance should be higher than 1×10^{-7} mol/(m^2 Pa s), and selectivity should be higher than 75, which are realizable for current zeolite membranes.

3.3.2 Ceramic-carbonate dual-phase membranes for CO_2 separation

Compared to polymer and inorganic microporous membranes, ceramic-carbonate dual-phase membranes can separate CO_2 from high-temperature streams without cooling, which can capture CO_2 more efficiently. At this point, ceramic-carbonate dual-phase membranes present a unique competence against their counterparts. The first dual-phase membrane was developed by Chung et al. [211], which was composed of a metal phase and a carbonate one. The permeance of the dual-phase membrane was very low with pure CO_2 and N_2 and was increased by mixing O_2 in the feed gases. Eliminating the need of O_2 had stimulated the development of ceramic-carbonate dual-phase membranes, where the metal phase is replaced with an ion-conducting (ceramic) phase. The working principle of ceramic-carbonate dual-phase membranes is presented in Fig. 3-3. Clearly, there are two separate channels that represent two different phases. The ionic conducting phase is for conducting oxygen ions, which can be composed of yttria-doped zirconia (YSZ), gadolinia-doped ceria (CGO), and samaria-doped ceria (SDC), etc. The molten carbonate phase is for transporting carbonate, which is usually a eutectic mixture of Li_2CO_3, Na_2CO_3, and K_2CO_3 [212]. By using two separate phases, the passage of different species is not crowded and fluxes can be much higher. On the lower side of the membrane surface, CO_2 in the stream combines with oxygen ions to generate carbonate, and the generated carbonate passes through the molten carbonate phase to the upper surface, where it decomposes into CO_2 and oxygen ions. The oxygen ions then come back to the lower surface through the ion conducting phase. To confirm the ion transport mechanism, Wade et al. [213] used a YSZ dual-phase membrane and a CGO one for CO_2 separation. Using a non-ion conducting solid oxide of Al_2O_3 did not result in strong CO_2 permeance or selectivity, which supported the mechanism above. In addition, the presence of water on the upper surface can promote CO_2 fluxes by reacting with carbonate and water can be removed in this way [145]. This feature is helpful for reactions where CO_2 is needed and water is to be removed such as reverse water gas shift.

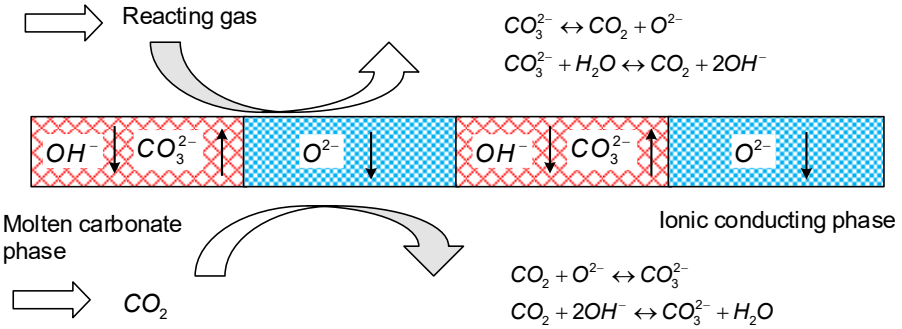

Fig. 3-3 Transport mechanism of ceramic-carbonate dual-phase membranes [145, 213].

Previous studies have developed various ceramic-carbonate dual-phase membranes. Anderson et al. [214] developed a dual-phase membrane from a porous $La_{0.6}Sr_{0.4}Co_{0.8}Fe_{0.2}O_{3-\delta}$ (LSCF) support infiltrated with a $Li_2CO_3/Na_2CO_3/K_2CO_3$ mixture. The CO_2 permeance was in the range of 2.01 – 4.77×10^{-8} mol/(m^2 Pa s) at 900 ℃, with a CO_2/Ar separation factor of at least 225. And the activation energy of the membrane was 86.4 – 89.9 kJ/mol, depending on the membrane thickness. A membrane permeation model was also developed, based on which the oxygen ion conduction was determined to be the rate-limiting step with confirmation by the experimental data. Pore structures of support have strong effects on CO_2 permeation. Ortiz-Landeros et al. [215] studied the effects of support pore structure of LSCF membranes by preparing various support pore structures. The CO_2 permeance of the membrane was affected by the carbonate and oxygen ion conductivities as well as the carbonate or solid fraction to tortuosity ratio. Dong et al. [216] developed an asymmetric dual-phase membrane. The membrane was characterized by a tubular design with a high area-to-volume ratio. The inner support layer was made of SDC while the outer layer of SDC and $Bi_{1.5}Y_{0.3}Sm_{0.2}$ $O_{3-\delta}$ (BYS) mixture. As the microstructures of SDC and BYS are very similar, the BYS was well compatible with the SDC. At 900 ℃, the CO_2 permeance was 2.33×10^{-7} mol/(m^2 Pa s), which is nearly one order of magnitude higher that of the above-mentioned LSFC membrane. The authors continued to improve the membrane performance by optimizing the pore size, porosity, and tortuosity of the asymmetric membrane and the CO_2 permeance reached 3.16×10^{-7} mol/(m^2 Pa s) at the same temperature [217]. Chemical stability of ceramic-carbonate dual-phase membranes is a critical issue for the performance. Norton et al. [218] examined the stability of an LSCF-carbonate membrane at temperatures between 800 and 900 ℃. A drastic decrease in CO_2 permeance was detected after 60 h exposure to CO_2/N_2, which was caused by a surface reaction between CO_2 and the support. Introducing oxygen could improve the stability of the ceramic phase, and the CO_2 permeance

could be raised by almost two orders of magnitude. In another study, Norton et al. [219] tested the stability of an SDC membrane in the range of 700 – 900 ℃ at atmospheric and an elevated pressure of 5 bar. The membrane exhibited long-term stability for up to 35 days. Even in the presence of H_2, only a slight decomposition of the ceramic phase was observed.

Some studies explored possible applications of ceramic-carbonate dual-phase membranes for chemical reactions. Reverse water gas shift and dry reforming of methane are two suitable reactions, where ceramic-carbonate dual-phase membranes can be used for providing CO_2. Anderson et al. [220] performed dry reforming of methane in a LSCF-carbonate membrane reactor. At 850 ℃, the CO_2 and CH_4 conversions were 88.5% and 8.1%, respectively, and the H_2/CO ratio was close to one, which may be attributed to the distributed feeding of CO_2. Chen et al. [145] developed a $LaNiO_3$/SDC-carbonate dual-phase membrane used it for coupling of CO_2 separation and reverse water gas shift. The presence of the reaction increased the CO_2 flux by four times, and the CO_2 conversion was 56.8% at 750 ℃. Novel applications include H_2 production by water gas shift and steam reforming of methane, where CO_2 can be removed by dual-phase membranes instead of H_2 permeable membranes. These applications have been studied by Dong et al. [221], Meng et al. [222], and Wu et al. [223] by means of experimental and numerical studies.

3.3.3 Pd-membranes for H_2 separation

To date, several types of membranes for H_2 separation have been developed. Broadly, H_2 separation membranes can be classified into organic and inorganic membranes. Organic membranes refer to polymer membranes and inorganic membranes include metallic, carbon, and ceramic ones. According to pore size, these membranes can be also categorized into porous membranes and dense membranes. Table 3-8 provides an overview of properties of different membranes.

The main advantages of polymer membranes are low pressure drop and costs, but they have low H_2 fluxes and selectivities. Also, their applications are limited to temperatures below 100 ℃ [224]. For carbon and ceramic membranes, they have either high H_2 fluxes or selectivities but do not have both properties together [224]. Metallic membranes made of Pd are the membranes that show both high H_2 fluxes and selectivities [224]. Therefore, this thesis focuses on Pd-based membranes for H_2 separation.

Table 3-8 Properties of selected H_2 separation membranes [224].

Membrane	**Dense polymer**	**Microporous ceramic**	**Dense metallic**	**Porous carbon**	**Dense ceramic**
Temperature range / ℃	< 100	200 - 600	300 - 600	500 - 900	600 - 900
H_2 selectivity	Low	5 - 139	> 1000	4 - 20	> 1000
H_2 flux* / $\times 10^3$ mol/(m^2 s)	Low	60 - 300	60 - 300	10 - 200	6 - 80
Stability issue	Swelling, compaction	Stability in H_2O	Phase transition	Brittle	Stability in CO_2
Poisoning issue	HCl, SO_x	-	H_2S, HCl, CO	Strong adsorbing vapor	H_2S
Material	Polymers	Silica, alumina, zirconia, titania, zeolites	Palladium and alloys	Carbon	Proton-conducting ceramics
Transport mechanism	Solution-diffusion	Molecular sieving	Solution-diffusion	Surface diffusion, molecular sieving	Solution-diffusion

*pressure difference of 1 bar

Although Pd membranes have excellent H_2 fluxes and selectivities, a critical problem is that below the critical temperature of 298 ℃, pure Pd produces two different phases of α and β in H_2 atmosphere [225]. The two phases are characterized by different lattice size, 0.3895 nm for the α-phase and 0.410 nm for the β-phase. The difference in volume size will cause internal stress, crystalline structure distortion and ultimately, mechanical failure [225]. The left figure of Fig. 3-4 presents the phase diagram of Pd-H_2 systems. It can be seen that the α-phase is obtained at low H/Pd atomic ratios and high temperatures while the β-phase is formed at high H/Pd atomic ratios and coexists with the α-phase below the critical temperature [225]. Another problem of Pd metal is the loss of ductility due to exposure to H_2, which is known as H_2 embrittlement.

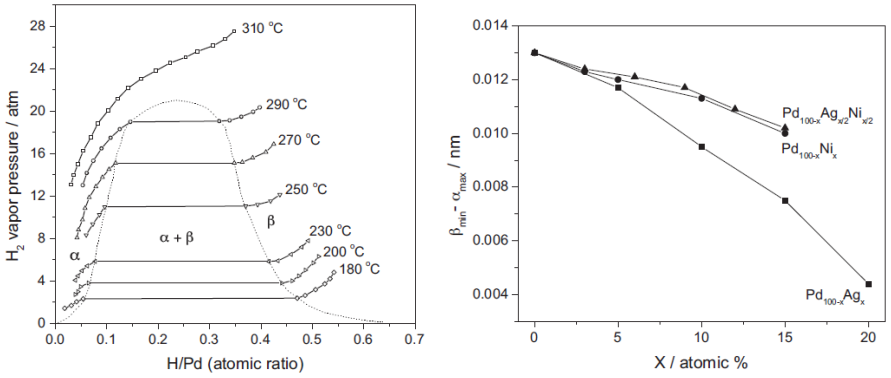

Fig. 3-4 Phase diagram of Pd/H_2 systems (left figure) and size difference of different phases (right figure) [225].

There are currently two approaches available to prevent the above problems. The first approach is using nanometer-sized Pd grains to increase H_2 concentration on grain surfaces, which can reduce stress and strain caused by α/β-phase transition according to the left figure of Fig. 3-4 [225]. The second one is to alloy Pd with one or more other metal elements such as Ag, Cu, Fe, Ni, Pt, and Y, etc. Pd alloys could offer several benefits compared to pure Pd metal. First, Pd alloys can significantly reduce the critical temperature to around room temperature so that phase transition can be effectively suppressed [225]. Second, the H_2 embrittlement problem can be overcome, as the difference in lattice size of the two phases becomes smaller, with Pd-Ag being the lowest, as shown in the right figure of Fig. 3-4 [225]. Third, the permeance of Pd alloys can be higher [225]. Table 3-9 provides the permeance of various Pd alloys. Except for Pd-Cu, other Pd alloys have higher permeance compared to pure Pd. The permeance of Pd alloys is related to the average bond distance, which explains the lower permeance of Pd-Cu [225]. Rare-earth elements such as Y and Ce have larger atomic size and therefore higher permeance, but high costs have limited their wider applications. Binary and ternary Pd alloys with Ag are suitable candidates that feature both high H_2 permeance and lower costs. For binary Pd-Ag alloys, adding Ag increases the H_2 solubility but reduces H_2 diffusivity, so there exists an optimal Ag content of 20 - 40 wt.% [225]. Currently, commercialized Pd membranes are $Pd_{77}Ag_{23}$.

Table 3-9 Average bond distance and permance ratio of Pd alloys [225].

Pd alloy	Mass fraction of alloy	Average bond distance / nm	Alloy/Pd Permeance ratio
Pd	0	0.275	1.0
Pd-Y	6.6	0.281	3.5
Pd-Y	10	0.284	3.8
Pd-Ag	23	0.278	1.7
Pd-Ce	7.7	0.280	1.6
Pd-Cu	10	0.272	0.48
Pd-Au	5	0.275	1.1
Pd-Ru-In	0.5, 6	0.278	2.8
Pd-Ru-Ru	30, 2	0.279	2.0
Pd-Ru-Ru	19, 1	0.278	2.6

It is widely acknowledged that Pd alloy membranes follow a solution-diffusion mechanism, as shown in Fig. 3-5. The mechanism includes seven steps: (a) diffusion of H_2 from bulk stream to the membrane surface; (b) disassociation of H_2 into protons on the membrane surface; (c) dissolution of protons into the membrane layer; (d) diffusion of protons through the membrane layer; (e) association of protons into molecular H_2 on the membrane surface; (f) desorption of molecular H_2 from the membrane surface; (g) diffusion of molecular H_2 from the membrane surface to bulk stream [225].

Based on this mechanism, a theoretical model for H_2 permeation can be derived. The diffusion of H_2 through Pd alloy membranes follows the Fick's law [226]:

$$J_{H_2} = D_{H_2} \nabla C_{H_2} \qquad \text{Eq. 3-48}$$

The concentration of H_2 is depends on its solubility coefficient and partial pressure of H_2 [226]:

$$C_{H_2} = S_{H_2} p_{H_2}^n \qquad \text{Eq. 3-49}$$

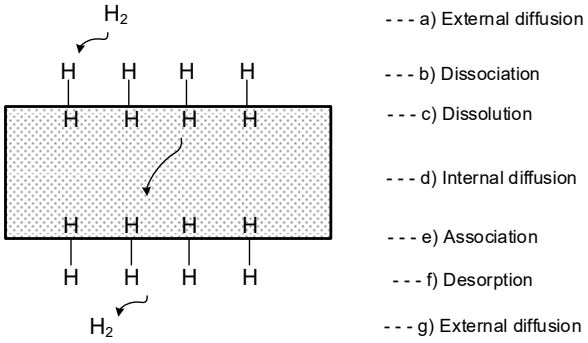

Fig. 3-5 Solution-diffusion mechanism of Pd alloy membranes [225]

Inserting the above relationship into Eq. 3-48, it can be shown that [226]:

$$J_{H_2} = \frac{D_{H_2} S_{H_2}}{L}\left(p_{H_2,f}^{n} - p_{H_2,s}^{n}\right) \qquad \text{Eq. 3-50}$$

In the above equation, the pressure exponent *n* is 0.5 if the rate-limiting step, according to the Sievert's law, is bulk diffusion through the Pd layer. However, this may not always the be case for all membranes. In literature, *n* values of 0.5 – 0.8 have been reported, depending on surface activity, defect, and mass transport mechanism [225]. Guazzone et al. [227] studied the pressure exponents of several Pd membranes. At temperatures lower than 350 ℃, the pressure exponents were higher than 0.6 and approached to 0.5 when temperatures were above 400 ℃. The activation of membrane surfaces in hot air gave rise to lower pressure exponents due to the contribution of surface reactions. For Pd membranes with selectivities below 400, a high pressure exponent of 0.75 were obtained due to the Knudsen diffusion and viscous flow.

The product of H_2 diffusion and solubility coefficient in Eq. 3-50 is referred to as permeability [226]:

$$P_e = D_{H_2} S_{H_2} \qquad \text{Eq. 3-51}$$

Permeability is temperature-dependent and given by the Arrhenius-type relationship [226]:

$$P_e = P_{e0} \exp\left(\frac{-E_a}{RT}\right) \qquad \text{Eq. 3-52}$$

where P_{e0} is the permeability at a reference temperature, and E_a is activation energy.

If a Pd membrane is used for a reaction system, its H_2 flux may be compromised by the presence of other species. Israni et al. [228] studied the inhibition of reacting species on H_2 flux of a methanol steam reforming system using a $Pd_{77}Ag_{23}$ membrane. A drastic decrease in H_2 flux was observed. Among all species, CO was determined to be the species with the strongest inhibiting effect on H_2 flux. A adsorption mechanism model was developed, with which fractional surface coverage could be quantified. Later, Patrascu et al. [229] adapted the above model and applied it to a methane steam reforming reaction system. The inhibition factor was determined to be 0.18 for the system, suggesting strong inhibiting effects of non-hydrogen species. Another important insight from the model is that increasing operating pressure may not always lead to higher H_2 permeation due to competitive adsorption. Boon et al. [230] systematically investigated the inhibition of other species on H_2 permeation. CO and H_2O could inhibit H_2 permeation due to high surface coverage while CO_2 had no significant inhibiting effect. And a constriction resistance model that correlated surface coverage and H_2 permeation was proposed. In addition, membrane thickness was also found to be influential on H_2 permeation because of lateral diffusion and an optimal minimum thickness existed, which was a balanced result between intrinsic permeance and inhibition.

3.3.4 Membrane reactor concept

Corresponding to different membrane types, there are also many membrane reactor concepts available. Seidel-Morgenstern [231] classified the available membrane reactor concepts into six types, as shown in Fig. 3-6. The first concept is catalyst retainment, where the membrane is for the separation of products and homogeneous catalysts. The second concept is membrane contactor, where reactants are fed into the reactor from different sides of the membrane. The membrane provides a place for the reactions take place. The third concept is more well-known and extensively used. In this concept, one of the products is to be removed by the membrane to enhance the conversion. The fourth concept is coupling of reactions, and the feature of this concept is that two different reactions take place simultaneously on the both sides of the membrane with both heat and mass transfer through the membrane. A typical application is coupling of dehydrogenation and hydrogenation reactions. The fifth concept is removal of intermediates. This concept is widely used for reactions in series. By removing one of the intermediates, the yield of target products can be increased. The last concept is reactant dosing. The purpose is to distribute one of the reactants to control the concentration to increase the yield of an intermediate.

This concept was originally developed for partial oxidation reactions to avoid deep oxidation. Now it finds novel applications such as integrated CO_2 capture and conversion.

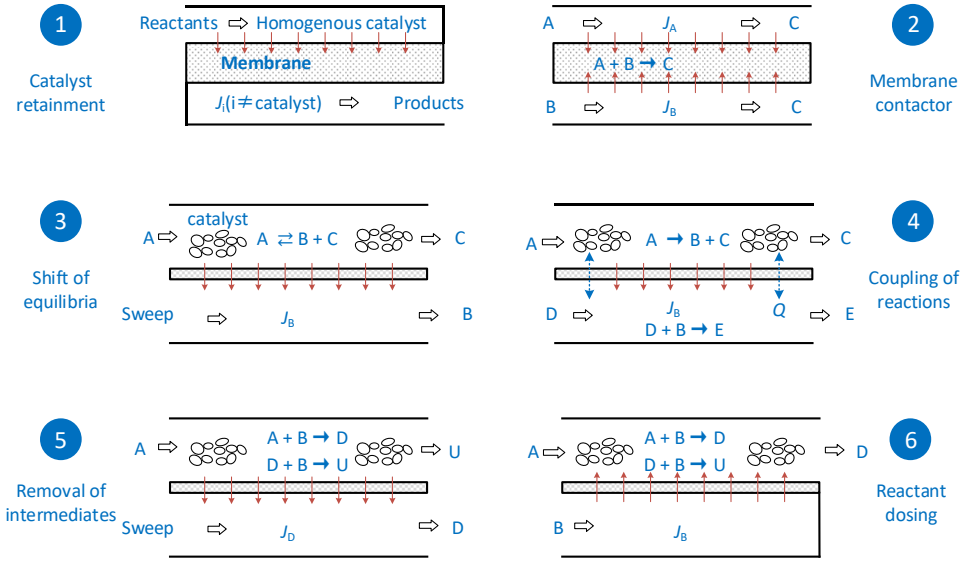

Fig. 3-6 Available membrane reactor concepts [231].

In addition to different membrane reactor concepts, there are also two different coupling modes of membrane and catalyst, namely segregated and integrated modes, as shown in Fig. 3-7. The former mode is also known as fixed-bed membrane reactors while the latter one is known as catalytic membrane reactors. For fixed-bed membrane reactors, catalysts and membranes are placed at different locations, and membranes are inert. For catalytic membrane reactors, catalyst is coated on the surfaces of membranes, and reactions and membrane separation take place in the same place. The two membrane reactor concepts are characterized by different reaction and mass transport mechanisms. For fixed-bed membrane reactors, the reaction mechanism is volumetric with both external and internal mass transport limitations. Internal limitations exist between catalyst surfaces and internal active sites. External limitations exist in the course of mass transport from bulk steam to catalyst surfaces and from catalyst surfaces to membrane surfaces. For catalytic membrane reactors, the mechanism is surface reaction, so internal mass transport limitations can be neglected.

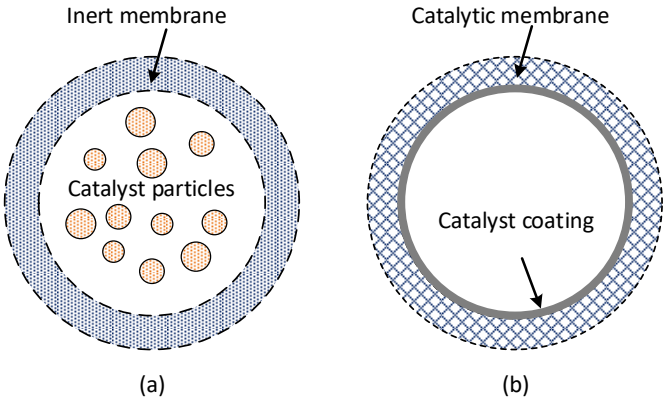

Fig. 3-7 Cross-sectional view of fixed-bed membrane reactor and catalytic membrane reactor concepts [232].

Mengers et al. [233] performed a general analysis for the comparison of the performance of fixed-bed and catalytic membrane reactors. The analysis considered the multi-component mass transfer behavior by employing the Maxwell-Stefan equation. For reactions with low or moderate equilibrium constants, catalytic membrane reactors outperform fixed-bed membrane reactors, which are attributed to large membrane area-to-volume ratios, long residence time, and high membrane permeance. But for reactions with large equilibrium constants, fixed-bed membrane reactors are superior. Bhatia et al. [234] compared the performance of several reactor concepts for oxidative coupling of methane, including a fixed-bed reactor, a fixed-bed membrane reactor, and a catalytic membrane reactor. The catalytic membrane reactor performed the best in terms of C_{2+} yield due to large surface areas.

3.3.5 Membrane permeation modeling

The first step of membrane modeling is the abstraction of permeation processes, and the second step is modeling those processes by CFD. As indicated by the mass balance in Eq. 3-14, membrane permeation can be seen as a source term, where the feed side is a negative source while the sweep side is a positive one. For CFD simulations in the ANSYS Fluent, since there is no model readily available for simulating membrane permeation processes, it is therefore necessary to develop customized models by user defined functions (UDFs). As the ANSYS Fluent solver is based on the finite volume method, membrane permeation fluxes are converted from area-specific to volume-specific:

$$S_i = \begin{cases} -\dfrac{J_i \cdot A_{c0}}{V_{c0}} & \text{Feed side} \\ +\dfrac{J_i \cdot A_{c1}}{V_{c1}} & \text{Sweep side} \end{cases} \qquad \text{Eq. 3-53}$$

In the above equation, A_{c0}, A_{c1}, V_{c0}, and V_{c1} are the areas and volumes of neighbouring cells of the membrane wall, which can be indexed by the built-in functions of *F_C0* and *F_C1*, as shown below:

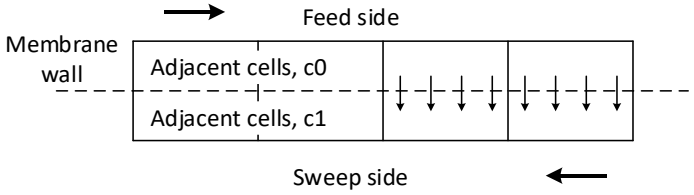

Fig. 3-8 Abstraction of membrane permeation processes.

For the water separation, a H-SOD zeolite membrane is used, and its flux can be expressed below [210]:

$$J_{H_2O} = Q_{H_2O}\left(p_{H_2O,f} - p_{H_2O,s}\right). \qquad \text{Eq. 3-54}$$

where Q_{H_2O} is the permeance of the zeolite membrane. According to a study by Rohde et al. [210], the value of Q_{H_2O} is in the range of 1×10^{-7} - 1×10^{-6} mol/(m^2 Pa s). $p_{H_2O,f}$ and $p_{H_2O,s}$ are the partial pressures of water in adjacent cells, indicating that the flux of water is proportional to its partial pressure difference. The H_2O/H_2 selectivity of the zeolite membrane is assumed to be 200 [210].

For the CO_2 separation, a YSZ ceramic-carbonate dual-phase membrane is employed [213]:

$$J_{CO_2} = \frac{RT}{4LF^2}\left(\frac{\varepsilon\sigma_C(1-\varepsilon)\sigma_V}{\varepsilon\sigma_C + (1-\varepsilon)\sigma_V}\right)\ln\left(\frac{p_{CO_2,f}}{p_{CO_2,s}}\right) \qquad \text{Eq. 3-55}$$

where L is membrane thickness, 300 μm, F is the Faraday's constant, 96485 C, ε is membrane porosity, 0.34, σ_C, and σ_V are the conductivities of CO_3^{2-} and O^{2-}, 3.5 and 0.106

S/cm at 900 °C, respectively. The permeation flux of CO_2 is proportional to temperature, but it is a logarithmic function of pressure, indicating that it is not influential to the CO_2 flux.

For the H_2 separation, a commercial Pd membrane by Johnson Matthey is employed [235]:

$$J_{H_2} = k_{H_2} \exp\left(\frac{-E_{H_2}}{RT}\right)\left(P_{H_2,f}^{0.5} - P_{H_2,s}^{0.5}\right) \quad \text{Eq. 3-56}$$

where k_{H_2} is the preexponential factor, 0.4 mol/(m^2 bar$^{0.5}$ s), E_{H_2} is the activation energy, 6.6 kJ/mol. The total flux of H_2 is related to the difference of the square roots of H_2 partial pressures.

3.3.6 Dimensionless numbers for membrane reactors

Dimensionless analysis is a powerful tool for quickly determining characteristic time and length scale of a system, for this reason, it is widely used in the fields of chemical engineering, fluid dynamics and heat and mass transfer. In membrane reactor designs, there are two dimensionless numbers dedicated to membrane reactor designs - namely the Damköhler and Péclet numbers. The Damköhler number is defined as the ratio of reaction rates to flowrates of reactants and the Péclet number is the ratio of flowrates of reactants to membrane permeation fluxes according to Bernstein et al. [236], Moon et al. [237], and Dixon [238]:

$$Da = \frac{r_i \cdot W_{\text{cat}}}{F_i} \quad \text{Eq. 3-57}$$

$$Pe = \frac{F_i}{J_i} \quad \text{Eq. 3-58}$$

where r_i represents reaction rate, W_{cat} is the catalyst weight, F_i is flowrate of reactant, and J_i is membrane flux. The definition of the Péclet number here is a little different from its conventional definition, so in some literature, it is also referred to as the permeation number [239, 240]. With these two numbers, one can further derive a dimensionless number group of *DaPe*[236-238]:

$$DaPe = \frac{r_i \cdot W_{\text{cat}}}{J_i} \quad \text{Eq. 3-59}$$

DaPe represents the ratio of reaction rates to membrane permeation rates, in which the flowrate of reactant is eliminated. *DaPe* is a very useful indicator to evaluate the relative magnitude of the reaction and membrane permeation rates. It can be used for determining the kinetic compatibility between membranes and reactions. In general, a lower *DaPe* is preferred to obtain higher conversion enhancement for a reaction as the removal of a product can be higher.

Some previous studies have employed the *Da* and *Pe* separately or *DaPe* together to help the designs of membrane reactors for various reaction systems. Tsuru et al. [240] applied the *Da* and *Pe* for steam reforming of methane to study the dependency of membrane performance on operating conditions. A major finding was that the *Da* had similar effects to H_2 permselectivity on the methane conversion. Li et al. [239] used the two numbers for ammonia decomposition. They found that the ammonia conversion, H_2 yield and purity all increased with *Da*. Battersby et al. [241] analyzed the relationship between *DaPe* and conversion for the dehydrogenation of cyclohexane to benzene. It was found that the cyclohexane conversion increased from 3% to 20% as the *DaPe* reduced from 80 to 1. Boutikos et al. [242] used the *Da* and *Pe* for water gas shift reaction. The maximum CO conversion enhancement was obtained when *Da* is equal to *Pe*, as the reaction and the permeation rates were comparable. Choi et al. [243] used the two numbers to determine desired "operating window" for propane dehydrogenation. A higher *Da* and a lower *Pe* were beneficial to the reaction, and the H_2 permselectivity was more critical to the reaction than the H_2 flux. The reciprocal of *DaPe* – 1/*DaPe* has a clearer physical meaning: the percentage of a product removed by membrane permeation. Oyama et al. [172] referred to 1/*DaPe* as operability level coefficient and employed it to analyze some reforming reactions, finding that obvious conversion enhancement could be obtained when the values of operability level coefficient fall between 0.03 and 0.78.

In addition to the *Da* and *Pe* numbers, another way to judge the kinetical compatibility of reaction and membrane is by comparing space-time yield (STY) and areal time yield. The space-time yield of a reaction should be on the order of 1 - 10 mol/(m^3 s) [244], and the corresponding areal time yield is 10^{-2} - 10^{-1} mol/(m^2 s), which is determined according to currently achievable membrane permeation fluxes, which are typically on the order of 10^{-2} - 10^{-1} mol/(m^2 s). The above range acts as a complementary criterion that can help determine the suitability of a membrane for a reaction.

3.4 Indicators for membrane reactor evaluation

The evaluation of membrane reactors is from the perspectives of conversion and productivity. Conversion is a widely used indicator for chemical reactions, which is defined as the ratio of converted moles of a reactant to its initial moles:

$$X_i = \frac{\Delta n_i}{n_{i,0}} \qquad \text{Eq. 3-60}$$

The conversion of a reaction depends on many factors. Fundamentally, reaction conversions are constrained by thermodynamic limitations. External factors like temperature, pressure, and space time can also affect conversions. Thermodynamic limitations can be circumvented by many approaches, from which the use of membrane reactors is the focus of this thesis. To quantify the contribution by applying membranes, conversion enhancement is defined as follows:

$$\Delta X_i = \frac{X_{i,m} - X_{i,FBR}}{X_{i,FBR}} \qquad \text{Eq. 3-61}$$

where $X_{i,m}$ and $X_{i,FBR}$ stands for conversions in membrane reactors and fixed-bed reactors, respectively.

To evaluate the productivity of membrane reactors, STY is an indicator that is defined as the ratio of produced moles of a product in the reactor within space time:

$$\mathrm{STY} = \frac{\Delta n_p}{t_S V_R} \qquad \text{Eq. 3-62}$$

On many occasions, a high conversion and productivity cannot be achieved at the same time. A high conversion requires higher space time, which, in turn, leads to low productivity. From an economic point of view, the single-pass conversion should be close to the equilibrium conversion to avoid large recycling streams.

This chapter introduces the methodologies for techno-economic analysis, CFD modeling of reactors and membrane permeation processes. Chapter 4 will employ the techno-economic analysis for the assessment of production pathways of DMC and MF. In chapter 6, various membrane reactor concepts will be developed based on CFD simulations.

4 Process analysis of DMC and MF

In this chapter, the techno-economic performance of DMC and MF production pathways are to be analyzed. A preliminary screening is first performed to find out suitable pathways with respect their levels of technical maturity and their compliance with green chemistry principles. After determining the pathways, thermodynamic analysis is followed to deliver insights for process design and simulation. Based on simulation results, techno-economic analysis is then performed to identify energy and economic drivers and competence of each pathway. In addition, possible opportunities for membrane reactor applications are identified.

4.1 Process analysis of DMC production pathways

As highlighted in Chapter 2, there are currently seven pathways for DMC production. In this section, four greener pathways are screened for their high TRLs. Thermodynamic analyses of the each selected pathway concern Gibbs energy change and vapor-liquid equilibrium as these are critical to synthesis reactions and product separations. The process simulations are based on the Aspen Plus© software to calculate the mass and energy balances, and the techno-economic analysis is based on the methods introduced in section 3.1. Parts of the contents was published in the pre-publication "Greener production of dimethyl carbonate by Power-to-Fuel concept: A comparative techno-economic analysis" in the journal of Green Chemistry. DOI: 10.1039/D0GC03865B. [245]

4.1.1 Process screening of DMC production pathways

In order to facilitate process screening, the available processes are classified into three categories: oxidative carbonylation, urea-based, and direct synthesis. The threshold value of TRL is set to 5, below which a process will be excluded. The TRLs and their compliance with green chemistry principles of each process are listed in Table 4-1. The liquid phase oxidative carbonylation of methanol process has already been industrialized by the ENIChem [49], so its TRL is SoA. No green chemistry principle is violated and it is therefore selected. For the gas phase process, the TRL is constrained by the lifetime of catalysts, and no industrial or pilot plant has been reported. Considering the similarity between this process and the liquid phase process, its TRL is estimated at 5. Although the two-step via methyl nitrite process has been practiced in industry by the UBE Industries [59], this process involves toxic reagent of NOx,

which is a violation of the green chemistry principle of “Safer solvents and Auxiliaries”. As such, this process is not considered. For urea-based processes, it should be first noted that transesterification processes by ethylene carbonate or propylene carbonate are not included in the process screening, as they can be part of corresponding indirect urea processes, so they are not viewed as independent processes. Another reason of not selecting the transesterification processes is that they do not obey the principle of “Atom Economy”, as equimolar by-products of ethylene glycol or propylene glycol are associated. In 2010, the Chinese Academy of Sciences built a small-scale pilot plant [96], but no further scale-up has been reported, and therefore its TRL is estimated to be 7. For indirect urea methanolysis via ethylene carbonate, although the whole process has not yet been industrialized, the core step of DMC synthesis by transesterification of ethylene carbonate is already mature, so the TRL can be 7. For indirect urea methanolysis via PC, the Chinese Academy of Sciences built a demonstration plant with a capacity of 50, 000 kt/a in 2020 [109], which is nearly ready for production at scale. Therefore, its TRL is 8 or even higher. All of the urea-based processes are well-developed and are in good accord with green chemistry principles, so they are all selected for process analysis. Although the direct DMC synthesis from CO_2 and methanol features the shortest route, its conversion is still very low and the TRL is only 3, so it is excluded from candidates for further analysis.

Table 4-1 Process screening of DMC pathways.

Category	**Process**	**TRL**	**Comply with green chemistry principles?**	**Selection?**
Oxidative carbonylation of methanol	Liquid/gas phase	SoA/5	Yes	Yes
	Two-step via methyl nitrite	SoA	No	No
Urea-based	Direct urea methanolysis	6	Yes	Yes
	Indirect urea methanolysis via EC	7	Yes	Yes
	Indirect urea methanolysis via PC	8	Yes	Yes
Direct synthesis	Direct CO_2 and methanol	3	Yes	No

4.1.2 Thermodynamic analysis of the selected pathways

This section analyzes the Gibbs free energy changes of the selected pathways and the phase equilibria of components involved in the reaction systems to deliver insights for the syntheses of separation sequences.

Gibbs free energy change

The standard Gibbs free energy change of a reaction is useful to determine the spontaneity and ease of the reaction. A negative value of standard Gibbs free energy change of a reaction indicates that the reaction can take place spontaneously. Table 4-2 presents the standard Gibbs free energy and reaction enthalpy changes of the selected reactions under the conditions of standard pressure of 1 bar and 25 ℃. Among the four reactions, the $\Delta_r G^{\Theta}_{25\,^{\circ}C}$ of the oxidative carbonylation of methanol is the lowest, suggesting that it is a thermodynamically favorable reaction. The standard reaction enthalpy is also negative, and therefore the reaction temperature should not be very high. The direct urea methanolysis is a two-step reaction, where the first step is much easier than the second. The first step is exothermic while the second is endothermic, but higher temperatures are beneficial to the overall reaction. For both the indirect urea methanolysis pathways based on transesterification, the Gibbs free energy change of the route via ethylene carbonate is negative while the route via propylene carbonate is positive, but both reactions are endothermic and increasing temperature is effective to shift the chemical equilibria.

Table 4-2 Standard Gibbs free energy changes of DMC synthesis reactions [70].

Pathway	Reaction	$\Delta_r G^{\Theta}_{25^{\circ}C}$ / kJ/mol	$\Delta_r H^{\Theta}_{25^{\circ}C}$ / kJ/mol
Oxidative carbonylation of methanol	Eq. 2-1	-233.1	-300.4
Transesterification via ethylene carbonate	Eq. 2-8	-14.9	27.5
Transesterification via propylene carbonate	Eq. 2-9	35.1	22.8
Direct urea methanolysis	Eq. 2-11	-13.2	-10.3
	Eq. 2-12	15.4	13.1
Direct synthesis from CO_2	Eq. 2-15	29.6	-15.2

Vapor-liquid equilibrium

In all of the selected processes above, methanol is one of the reactants in the reaction system. It is necessary to examine the vapor-liquid equilibrium to deliver insights for distillation process designs. Fig. 4-1 (a) is the vapor-liquid phase diagram of methanol-DMC binary mixture at different pressures using the UNIQUAC model. At atmospheric pressure, an azeotrope is formed. The azeotropic composition is 70 wt.% methanol and 30 wt.% DMC, with a minimum boiling point of 63.8 ℃. According to the phase equilibrium, at least two columns are needed to get high-purity DMC, by either extractive or pressure swing distillation. The vapor-liquid phase diagram at high pressure of 10.13 bar is also plotted. It can be found that the azeotropic composition is shifted to 89 wt.% methanol and 11 wt.% DMC. It is noticeable that the default binary interaction parameter of the methanol-DMC pair in the Aspen Plus databank cannot predict the formation of azeotrope at elevated pressures, so the values given by Hsu et al. [97] are used. The experimental data of azeotropic composition of methanol and DMC is provided in Table 4-3. The predicted values by simulations are in good agreement with the experimental results. In the oxidative carbonylation of methanol, water is also present in the products and can form a heterogeneous azeotrope with 13.8 wt.% water and 86.2 wt.% DMC, with a minimum boiling point of 79.3 ℃, as shown in Fig. 4-1 (b). To separate the heterogeneous mixture, two columns are needed with a decanter between them. Particularly, if the ternary components are present simultaneously in the products, the synthesis of distillation sequences can be very complex and challenging.

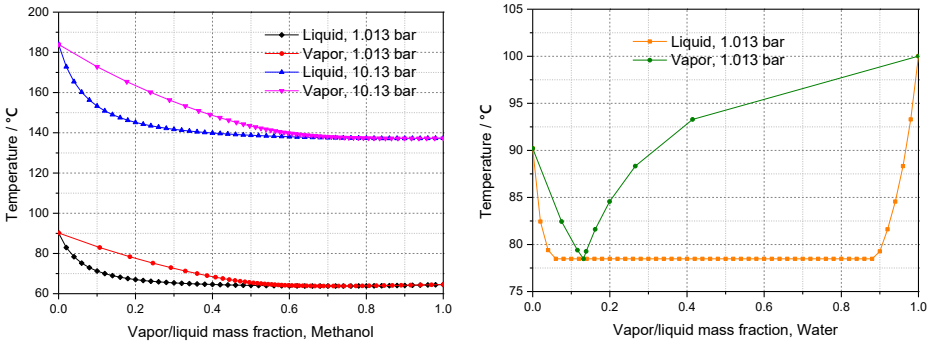

Fig. 4-1 Vapor-liquid phase diagrams of binary mixtures: (a) methanol and DMC; (b) water and DMC.

Table 4-3 Experimental and simulated temperature and composition of methanol-DMC azeotropes at various pressures.

p / bar	*T* / ℃		$w_{Methanol}$ / wt.%	
	Experimental [106]	Simulation	Experimental [106]	Simulation
1.013	64.2	63.8	70.00	70
4.052	104	104.2	79.29	80
6.078	118	118.1	82.49	84
10.13	138	137.2	87.61	89
15.195	155	153.8	93.00	95

4.1.3 Process design and simulation

This part introduces the process designs and simulation techniques of the selected processes. Each process consists of a number of production sections and the process designs follow a sequential procedure from educts to products. In addition, there are some common sections shared by different processes such as methanol synthesis and urea synthesis, so they are described once only for the sake of brevity. Pure CO_2 is used as one of the starting educts where sulfur contents are removed by upstream plants and H_2 is generated by water electrolysis. Both gas streams are supplied by pipelines. All processes are designed to be continuous and storage of raw materials is not considered.

Oxidative carbonylation of methanol

The oxidative carbonylation of methanol process consists of three sections: methanol synthesis, reverse water gas shift, and DMC synthesis and separation, where the first two sections are for the provision of methanol and CO for DMC synthesis. Since the only difference between the gas and the liquid phase oxidative carbonylation of methanol is the reaction phase, they are not distinguished in the following analysis and their process designs are merged. The process flowsheet is shown in Fig. 4-2. Methanol synthesis is the front end section of all of the processes. In this section, CO_2 and H_2 are fed into the methanol synthesis reactor after being compressed from 30 to 80 bar. Methanol synthesis is composed of the reactions of CO hydrogenation, CO_2 hydrogenation, and reverse water gas shift. Catalysts for methanol synthesis are generally Cu-based for their high activity and selectivity for both syngas-based and CO_2-based methanol synthesis. Here, a $Cu/ZnO/Al_2O_3$ catalyst is adopted

[246]. The reaction is exothermic and is operated adiabatically, with the temperature increasing along the reactor axis. The high temperature outlet stream is first used for heating the recycling stream by a heat exchanger. The remaining heat is then recovered by generating low-pressure steam for heating distillation columns where needed. This stream is then flashed for gas-liquid separation after being cooled to 40 ℃ by cooling water. The vapor phase of the flash tank is the unconverted educts and is sent back to mix with the fresh educts. The liquid phase is the mixture of methanol and water, which is pumped to the distillation column to get the methanol product with purity higher than 99 wt.%.

In parallel with the methanol synthesis is the reverse water gas shift that transforms CO_2 and H_2 into CO and H_2O, as shown in Eq. 2-21. A Ni-Al_2O_3 catalyst is used for this reaction for its long-term stability at high temperatures [133]. As described in section 2.4, the reverse water gas shift is an equimolar reaction and the operating pressure does not change the equilibrium conversion. However, higher pressure is preferred in order to achieve high productivity. Here, the operating pressure is set to 30 bar. This reaction is endothermic and faces thermodynamic limitations, to achieve a high conversion and suppress CO/CO_2 methanation reactions, the operating temperature is as high as 900 ℃, and the heat demand is supplied by electrical heating. The high temperature outlet stream of the reactor is also used for heating the inlet stream, and it is then cooled to 40 ℃ by cooling water for water condensation in a flash tank. Part of the unconverted CO_2 in the gas phase goes back to the reactor for recycling, and the remaining part goes to the section of CO_2 scrubbing by solvent absorption, where CO_2 in the products is removed and high purity CO is obtained. To avoid high temperature operation, it is possible to use water permeable membrane reactors for this reaction to increase the conversion. Detailed membrane reactor concepts will be designed and simulated by CFD simulations in Chapter 6.

The produced methanol and CO are then sent to the DMC synthesis reactor alongside O_2. The reaction temperature and pressure are 150 ℃ and 20 bar and is catalyzed by a CuCl catalyst [49]. The mixture leaving the reactor contains DMC, water, and unconverted methanol. The separation process is made of three distillation columns, as shown in the lower right corner of Fig. 4-2. As previously analyzed, the ternary mixture of DMC, water and unconverted methanol forms two azeotropes: a homogeneous DMC-methanol azeotrope and a heterogeneous DMC-water one. In the first column of the separation process, the mixture is split into two groups and each has only two components. As a result, the separation complexity are reduced. One group is obtained on top of the column that contains DMC and methanol, and the other is obtained at the bottom that contains DMC and water. The first mixture group directly returns to the reactor inlet without further purification. By doing this, one less column can be saved as the reactor plays a key role in assisting the

product separation. At this point, the reactor becomes a part of the separation process. The other mixture group is separated to get the DMC product via a typical process for separating heterogeneous azeotropes by using two columns and a decanter. In the first column, the waste water is discharged from the bottom stream. The distillate on the top is then sent to the decanter for phase separation and the water phase is pumped back to the first column as reflux. The organic phase goes to the second column, where the DMC product is obtained at the bottom of the column.

For methanol synthesis simulation in Aspen Plus® software, the SRK property method is selected for the reaction, as it is widely used for hydrocarbon processing applications. The reaction is close to chemical equilibrium, so the RGibbs model that is based on the Gibbs free energy minimization method is used to simulate the reactor. The heat recovery for steam generation is simplified as the Heater model. In order to facilitate simulation convergence, the heat exchange between the inlet and outlet streams are realized by two Heater models so that the two streams are not tightly coupled. For the same reason, a small amount of H_2 and CO_2 dissolved in the liquid is removed by the Sep model before entering the methanol distillation column. The methanol distillation is simulated using the RadFrac model based on the UNIQ-RK property method considering the non-ideal phase behaviors of methanol and water. The SRK property method and the RGibbs model are also used for the reverse water gas shift. For the DMC synthesis reactor and distillation columns, the property method is also the UNIQ-RK. The reactor is simulated by the RStoic model by specifying the methanol conversion to 70% [114].

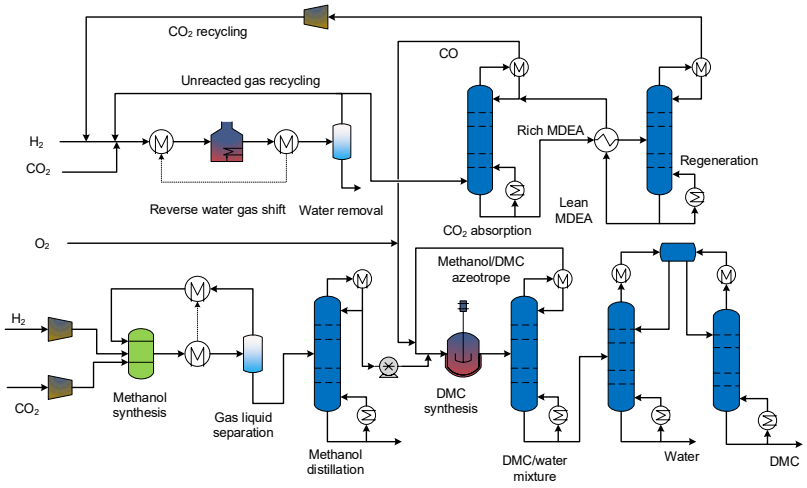

Fig. 4-2 Process flowsheet of the oxidative carbonylation of methanol for DMC production.

Direct urea methanolysis

The direct urea methanolysis process consists of methanol synthesis, urea synthesis, and DMC synthesis and separation, where methanol synthesis has already been described above and is not repeated here. The process flowsheet is shown in Fig. 4-3. Urea synthesis is also one of the front end segments of the direct urea methanolysis. Urea production from CO_2 and NH_3 has been practiced by industry for many years, which includes sub-steps of synthesis, evaporation, and granulation, and here the granulation is not needed. Urea synthesis is usually conducted at pressures higher than 100 bar. In this process, the operating pressure is brought to 138 bar by a multi-stage compressor [246]. Urea synthesis is a two-step equilibrium reaction with ammonium carbamate as the intermediate. In this process, only one overall reaction is considered. The unconverted ammonia in the reactor outlet stream is recycled, and the urea solution is then evaporated. The produced urea then reacts with methanol to form DMC and ammonia using a ZnO catalyst [71, 72]. The generated ammonia circulates between the urea and DMC synthesis loops. The solution of urea, methanol, and DMC is separated using two columns. The first column is used for separating urea from methanol while DMC and urea is obtained at the bottom of the column, and the methanol and DMC mixture on the top is further separated in the second column, whereas the unconverted methanol is recycled to the reactor inlet. The DMC product is with purity higher than 99 wt.%.

In the Aspen Plus simulation, to accurately describe the strongly non-ideal phase and chemical equilibrium at high pressures, the SR-POLAR thermodynamic model is recommended for this reaction system [247]. The urea synthesis reactor is modeled with the RStoic model by specifying the ammonia conversion of 70%. The urea evaporation is abstracted as a distillation column using the RadFrac model. The DMC synthesis is also simulated by a RStoic model with the methanol conversion of 65%. The reaction temperature and pressure are 160 ℃ and 12 bar, respectively [70].

Indirect urea methanolysis

The indirect urea methanol processes are the combination of transesterification and direct urea methanolysis. The process designs of the indirect urea methanolysis via ethylene carbonate and propylene carbonate routes are the same, so they are described together, as shown in Fig. 4-4. Ethylene carbonate and propylene carbonate syntheses are important intermediate steps that connect urea and DMC synthesis loops. For the both routes, urea is changed from reacting with methanol to reacting with ethylene glycol or propylene glycol. The synthesis of ethylene carbonate or propylene carbonate from urea and ethylene glycol or

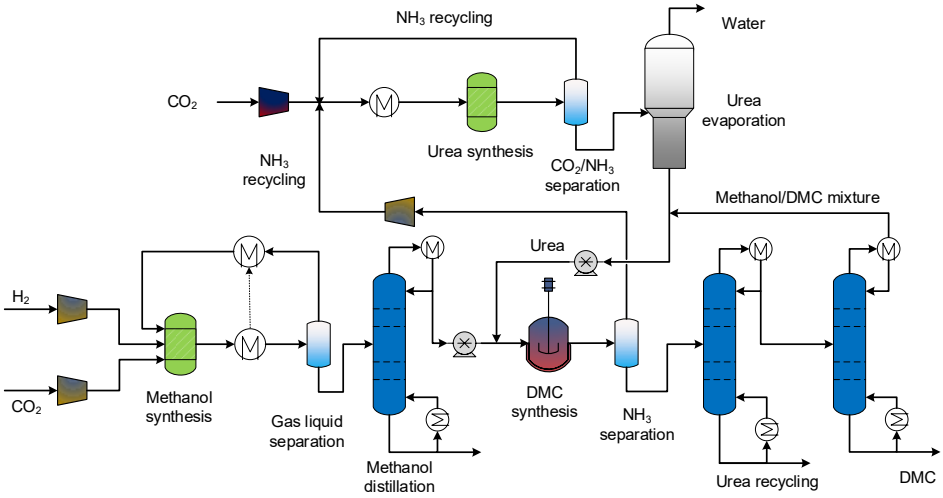

Fig. 4-3 Process flowsheet of the direct urea methanolysis for DMC production

propylene glycol is preferred at low pressures. The operating pressure is reduced to 0.03 bar to achieve high equilibrium conversions [74]. The generated ammonia returns to the urea synthesis for recycling while the produced ethylene carbonate or propylene carbonate is sent to the DMC synthesis reactor. An ion exchange resin catalyst is used for the DMC synthesis via ethylene carbonate and a CH_3ONa catalyst for the DMC synthesis via propylene carbonate. The outlet stream contains methanol, DMC, ethylene carbonate and ethylene glycol/ropylene carbonate and propylene glycol, respectively. The difference of boiling points of the above mixture is very large and this feature is fully leveraged in the designs of separation processes. Here, the separation processes use three columns, where the first column serves as a sharp split and the other two are for fine separations. At the bottom of the first column is the binary mixture group of ethylene carbonate and ethylene glycol/propylene carbonate and propylene glycol, respectively. They are separated and recycled for full conversion. On top of the first column is the binary mixture group of methanol and DMC and they are further separated in another column to recycle the unconverted methanol and get the DMC product.

In the Aspen Plus simulation, the ethylene carbonate and propylene carbonate synthesis reactors are based on the UNIQ-RK property method and the RStoic model, with the urea conversions of 100% and 97.8%, respectively [74, 78]. The DMC synthesis reactors of both routes adopt the same property method and reactor model, with the methanol

conversions of 79.2% and 66.6%, respectively [100, 103, 114]. Since there are different property methods and many recycling streams involved in the processes, in order to guarantee consistency in simulation and facilitate convergence, each sub-step is simulated separately.

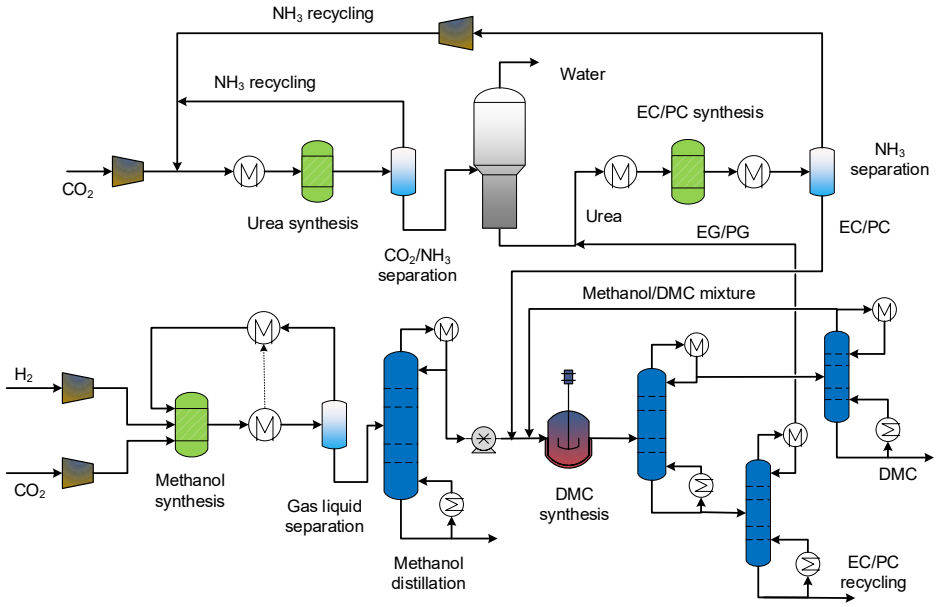

Fig. 4-4 Process flowsheet of the indirect urea methanolysis for DMC production.

4.1.4 Techno-economic performance

This part analyzes the techno-economic performance of the four processes based on the simulation results and the indicators introduced in section 3.1.

Material and energy balances

Table 4-4 illustrates the educt demand and Power-to-Fuel efficiency of each process. The production scale of each process is 300 MW. All of the processes require a similar quantity of CO_2 as it is the only carbon source of all of the processes. However, the oxidative carbonylation of methanol consumes 15.7% more H_2 than the other three urea-based processes. The former process requires additional H_2 in the reverse water gas shift to generate CO, and hydrogen is lost by forming water. The direct urea methanolysis exhibits the highest Power-to-Fuel efficiency, primarily contributed by the short route and less energy

consumption for product separations, which will be more specifically analyzed in the next section. The efficiency of the oxidative carbonylation is only lower than that of the direct urea methanolysis, ranking the second together with the indirect urea methanolysis via ethylene carbonate, despite its higher H_2 demand. The efficiency of the indirect urea methanolysis via propylene carbonate is the lowest for its longer route and lower conversion.

Table 4-4 Educt demand and energy efficiency of each process for DMC production.

Item	Oxidative carbonylation of methanol	Direct urea methanolysis	Indirect urea methanolysis via ethylene carbonate	Indirect urea methanolysis via propylene carbonate
CO_2 consumption / kg/l_{DE}	3.52	3.50	3.52	3.52
H_2 consumption / kg/l_{DE}	0.38	0.33	0.33	0.33
CO_2 consumption / kg/kg_{DMC}	1.54	1.54	1.54	1.54
H_2 consumption / kg/kg_{DMC}	0.167	0.144	0.144	0.144
DMC output / l_{DE}/h	31291.1	31409.5	31308.3	31280.3
Power-to-Fuel efficiency*	46.5%	48.5%	46.5%	46.0%

*The efficiency is calculated based on Eq. 3-1. The assumed PEM water electrolysis is 70% [4] and specific energy consumption for CO_2 capture is 1.2 MJ/kg [178].

Specific energy consumption

In order to clearly reveal the contributing factor of specific energy consumption of each process, the forms of energy consumed in each process are shown in Fig. 4-5. To assist understanding, the energy consumption of each section is provided in Table A-1 in the Appendix. Higher energy efficiencies correspond to lower energy consumption. The direct urea methanolysis has the lowest energy consumption, followed by the oxidative carbonylation of methanol and indirect urea methanolysis via ethylene carbonate, with the indirect urea methanolysis via propylene carbonate having the highest. Obviously, water electrolysis is the overwhelmingly largest contributor of energy consumption in all processes. In particular, the share of water electrolysis in the oxidative carbonylation of methanol pathway is up to 84.4%, which represents the largest portion among the four processes.

Other forms of energy consumption differ from process to process. Below, each process will be analyzed one by one.

In the oxidative carbonylation of methanol, the energy consumption for CO_2 capture consists of two parts: one part is caused by the supply of educt CO_2 and the other is from the capture of unconverted CO_2 in the reverse water gas shift. Although the regeneration of the CO_2 absorbent adds some energy costs on top of the reverse water gas shift, in the total energy consumption, its share is not large. Low-pressure steam in this process is used for methanol distillation and DMC product separation. Although the reaction heat is recovered for heating the recycling stream, a small amount of low-pressure steam is needed for methanol distillation. Yet, external steam may not be needed if the process heating and cooling are optimally integrated. The DMC synthesis reactor generates low-pressure steam that can be used for the above separations, but the reactor itself also needs medium-pressure steam for heating the reactor inlet stream. No high-pressure stream is required in this process as no component is with high boiling points. The operating electricity is for the purposes of pumps, compressors, and heating the reverse water gas shift reactor. Overall, the shares of CO_2 capture, steam, and electricity are uniformly distributed.

In the three urea-based processes, the energy consumption for CO_2 capture is equal. Another common point of the three processes is that the medium-pressure steam is the primary source of utility consumption, which comes from urea and DMC syntheses. As with methanol synthesis, urea synthesis is the section that all the urea-based processes have in common. Urea synthesis generates low-pressure steam by the reactor but requires medium-pressure steam for evaporation. In the direct urea methanolysis, low-pressure steam consumption comes from methanol distillation and DMC-methanol separation, which is only partly covered by the urea synthesis. The direct urea methanolysis is an endothermic reaction and it requires medium-pressure steam for heating the reactor. Comparing the oxidative carbonylation of methanol and the direct urea methanolysis, although the former process has no urea synthesis and evaporation, this still cannot compensate the energy consumption caused by more H_2 use compared to the latter. The operating electricity in the three urea-based processes is lower, as it is only used for pumps and compressors.

The distribution of the utility consumption of the two indirect urea methanolysis is fairly different. The indirect urea methanolysis via ethylene carbonate route has a small amount of surplus low-pressure steam, which is from the heat recovery of DMC synthesis. However, the indirect urea methanolysis via propylene carbonate route requires low-pressure steam, as the temperature of the reactor outlet stream is not high enough to generate low-pressure steam. Both routes need medium-pressure steam as the heating

source for the transesterification reactions for DMC synthesis. The reaction enthalpy change of the indirect urea methanolysis via ethylene carbonate is larger than that via propylene carbonate, leading to the higher medium-pressure steam demand in the former route. Both routes need high-pressure steam for the separation of ethylene glycol and propylene glycol due to their high boiling points. Yet the indirect urea methanolysis via propylene carbonate consumes more high-pressure steam than the ethylene carbonate route, which is explained by the larger flowrates of recycling streams due to the lower conversion. Overall, the total utility consumption in both indirect urea methanolysis is always higher than that of the other two processes, so there exists optimization potential to improve their energy performance.

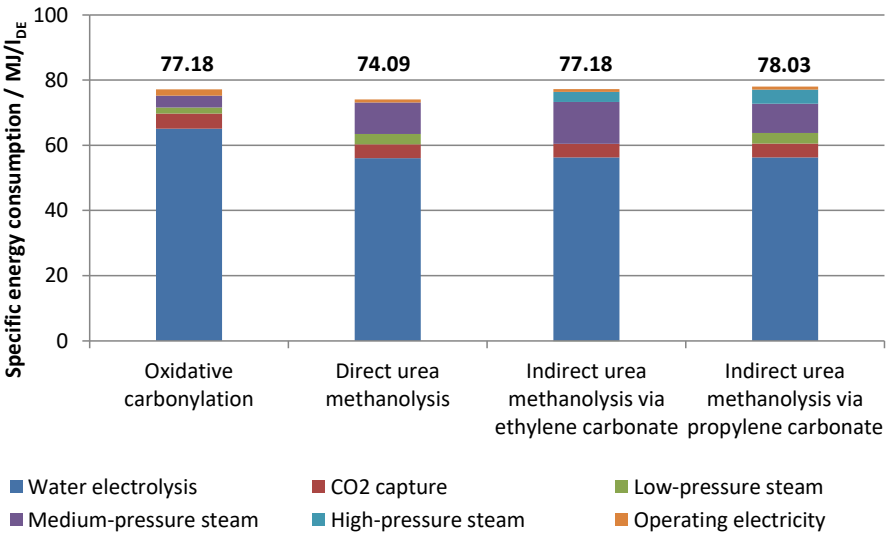

Fig. 4-5 Specific energy consumption of each process for DMC production.

Capital expenditure and cost of manufacturing

As explained in section 3.1.4, the calculations of CAPEX is through a hybrid approach. For example, the methanol synthesis in DMC and MF pathways only differs in production scale, so only one methanol synthesis is calculated using the module costing technique to get higher accuracy, and other processes are calculated with the scaling factor method for quick calculations. The results of CAPEX of each process is presented in Fig. 4-6. The process that has the lowest CAPEX is the direct urea methanolysis, and the CAPEX ranking the second is the oxidative carbonylation of methanol. Both the indirect urea methanolysis represent the highest CAPEX of 108.5 and 108.8 million Euros, respectively. Again, the FCI of methanol

synthesis of each processes is identical for the same process design and plant size. Of the contributing factors to the total CAPEX, methanol synthesis is the largest part. According to the module costing technique, the capital costs of equipment are primarily subject to equipment size and operating pressure. On the one hand, methanol synthesis is the forefront section of the processes, the flowrates of educts and recycling streams are large, and the reaction rates of CO_2 and H_2 to form CH_3OH are very slow. Both factors lead to large reactor sizes. On the other hand, the operating pressure of the reactor is up to 80 bar, which requires high-strength materials for reactor construction. The costs of equipment at 80 bar can be twenty times higher than those at atmospheric pressure, suggesting that reducing operating pressure is an effective way to drive down equipment costs. The same reasons can be used for explaining the high cost of the heat exchanger between the reactor inlet and outlet. The large heat exchanger area is caused by the large heat duty and low gas to gas heat transfer coefficient. Also, the pressure between the both sides of the heat exchanger is also very high. The total costs of the reverse water gas shift plus CO_2 absorption are an important part of CAPEX. The reverse water gas shift is a unique section of the oxidative carbonylation, to calculate the cost of the reactor, it is seen as an industrial furnace. The reactor size is small compared to the methanol synthesis reactor for its fast kinetics and short residence time. However, high temperature operation requires high-grade heat sources, complex reactor design and accessory equipment, necessitating the development of new catalysts and novel reactor concepts to lower the temperature without sacrificing the fast kinetics. For the oxidative carbonylation of methanol, as gases are present in the reactor, the reactor is pressurized to reduce volume, which, in turn, brings an increased reactor cost compared to the three urea-based reactors. The separation cost is also higher, because it is difficult to separate the azeotropic mixture of methanol, DMC, and water.

In the three urea-based processes, the urea synthesis contributes significantly to the CAPEX as the methanol synthesis does. The FCI of urea and methanol syntheses accounts for the two largest parts of the CAPEX of the three processes, and they are identified as the bottlenecks for lowering CAPEX. There are some commonalities between the urea and methanol syntheses. The urea synthesis also operates at a high pressure of 138 bar and the urea evaporation is similar to methanol distillation. These inherent commonalities predetermine their similarity in cost. Although the direct urea methanolysis has the largest reactor volume, its reactor cost is lower than that of the carbonylation reactor due to the lower operating pressure. The two indirect urea methanolysis reactors are similar in size and cost. Since no azeotrope is formed, the DMC product separations are less complex in design. Both indirect urea methanolysis processes have additional steps of ethylene carbonate and

propylene carbonate syntheses, respectively, moreover, the high conversions and low operating pressures make their cost contribution quite small.

Fig. 4-7 compares the cost of manufacturing of each process. The direct urea methanolysis represents the lowest COM of 2.19 €/l_{DE}, which echoes its highest energy efficiency. The COMs of oxidative carbonylation and indirect urea metanolysis via propylene carbonate are quite close to each other, both representing the highest COMs among the four processes. Like the specific energy consumption, the H_2 cost is the dominant economic driver of the COM of all processes. Although CO_2 is one of the educts, its impact on the COM is not significant as it is much more cheaply available compared to H_2. CO_2 is still the second COM contributor in the oxidative carbonylation of methanol and direct urea methanolysis. However, the former process outperforms the latter at the point of steam consumption. If one contrasts the specific energy consumption and COM, one finds that the COM of the indirect urea methanolysis via ethylene carbonate route is lower than that of the oxidative carbonylation of methanol, despite the fact that they have the same energy efficiency. Higher H_2 demand in the carbonylation process is the primary cause of the above finding. Unlike the above two processes, the second biggest COM contributor of the both indirect urea methanolysis processes changes to steam, especially in the route via propylene carbonate, which comes from the more complex distillation sequences and large reflux ratios. The cost of process cooling also has some impacts but can be further compressed if air cooling is employed where possible. The contribution of CAPEX to the COM is reflected in depreciation and in all processes it is only around 5%. Other impacts such as operating electricity and labor are included in the OPEX.

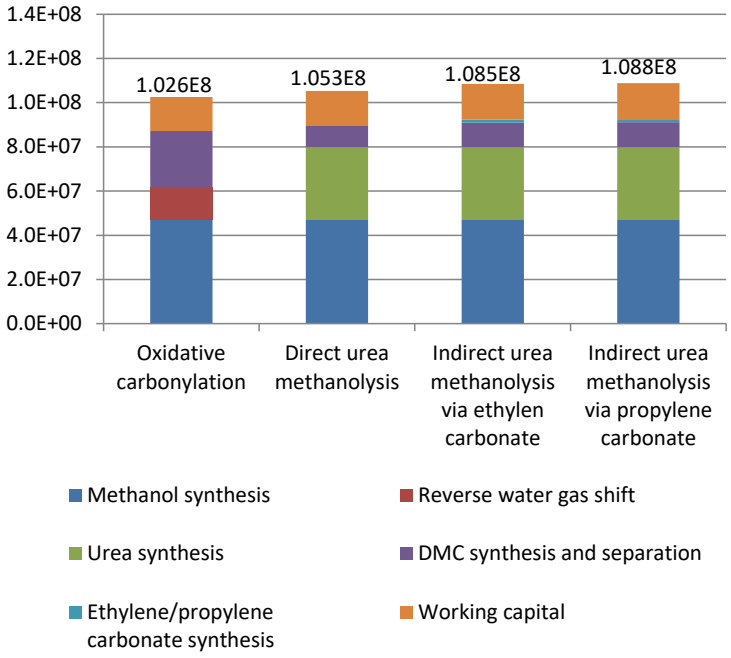

Fig. 4-6 CAPEX of each process for DMC production.

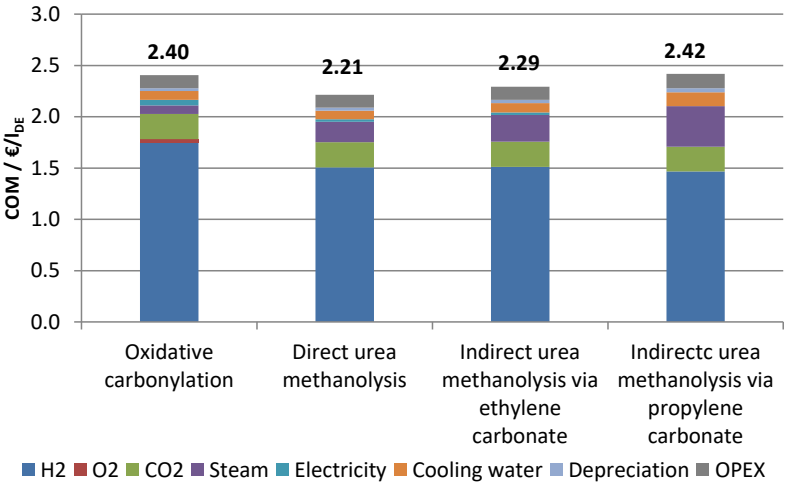

Fig. 4-7 COM of each process for DMC production.

Sensitivity analysis

In order to further analyze the impacts of technological and economic drivers on the COM in broader ranges, sensitivity analysis is also performed. Accordingly, some suggestions are put forward for COM reductions.

The sensitivity is carried out by way of univariate analysis. Specifically, when analyzing the impact of the H_2 price, other variables are kept constant, and each variable is analyzed one by one in this way. From the contributing factors to the COMs, the variables considered include educts, utilities, and capital costs. Since the price difference of different levels of steam is small, they are grouped together and assume that their prices are increased or decreased simultaneously. The results are presented via tornado diagrams in Fig. 4-8. As discussed above for the COM calculations based on the assumed values in Table 3-5, the H_2 price is the most influential variable. Therefore, the H_2 price is analyzed in a larger range from -50% to +50% whereas the other variables are changed from -25% to +25%. The oxidative carbonylation of methanol in Fig. 4-8 (a) is taken as the illustrative process and the remaining processes are not repeated as they show similar trends. At the assumed upper limit H_2 price of 6.9 €/kg, the COM reaches 3.40 €/l_{DE} while at lower limit H_2 price of 2.3 €/kg, the COM is as low as 1.60 €/l_{DE}.

As for CO_2, it is much less influential to the COM. Note that the CO_2 price considered here is from industrial sources by solvent absorption. If CO_2 is supplied by direct air capture, the share of CO_2 in COM is higher and the fluctuation range of COM from -25% to +25% can be much larger; or if it is obtained from biogas, the range can be smaller, as suggested in a study by Schorn et al. [9]. For the both indirect urea methanolysis pathway, the impact of steam is stronger than that of CO_2, and it can be lowered together with cooling water by heat integration. The impact of FCI is not significant and can be further lowered by leveraging economies of scale. The impact of operating electricity is the least significant. Overall, the reductions in COM heavily rely on the lower H_2 price, which can be achieved by advancing water electrolysis efficiency and by lowering electrolyzer costs in the future. Other processes shown in Fig. 4-8 (b) (c) (d) present similar trends.

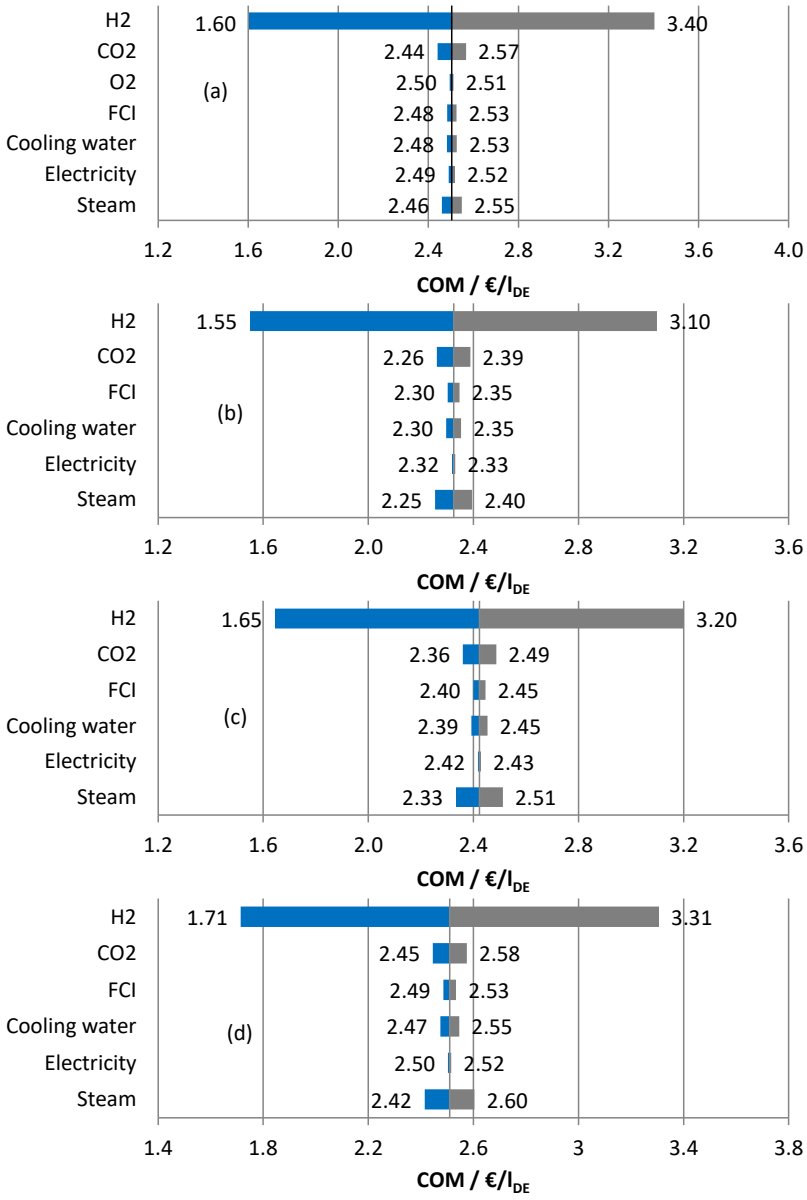

Fig. 4-8 Sensitivity analysis of each process for DMC production; (a) oxidative carbonylation of methanol, (b) direct urea methanolysis, (c) indirect urea methanolysis via ethylene carbonate, (d) indirect urea methanolysis via propylene carbonate.

Net present value and minimum selling price

Based on the COMs and a surveyed DMC selling price of 1000 €/t [189], the NPVs of the processes are calculated. At the given input values, only the NPV of the direct urea methanolysis shown in Table 4-5 is positive, suggesting that this process is slightly profitable with the assumed inputs in Table 3-5. Accordingly, it has the lowest MSP of 992.3 €/t. All other three processes represent negative NPVs, with the indirect urea methanolysis via propylene carbonate being the lowest, representing -373 million Euros. The NPVs of the oxidative carbonylation of methanol and indirect urea methanolysis via ethylene carbonate are -361 and -135 million Euros, respectively.

Table 4-5 NPV and MSP of each pathway under base conditions.

Pathway	NPV / M€	MSP / €/t
Oxidative carbonylation of methanol	-361	1075.3
Direct urea methanolysis	37.3	992.3
Indirect urea methanolysis via ethylene carbonate	-135	1028.2
Indirect urea methanolysis via propylene carbonate	-373	1079.6

The impacts of selling price of DMC and H_2 price on NPV are also analyzed. In contrast to the univariate analysis in the sensitivity analysis, the NPV of each process is presented with a number of combinations of DMC and H_2 prices and is visualized by color maps, shown in Fig. 4-9. In this way, the joint effects of both variables can be reflected. The analysis range of H_2 price is from 2.0 to 6.0 €/kg and the DMC price range is from 800 to 1200 €/t. In each color map, there is a solid line with two end points that discriminates negative and positive NPV regions, and the coordinates of the end points are also marked. The upper left region is positive while the lower right is negative. The ordinates of the solid lines are, in fact, the MSPs at corresponding H_2 price of these processes. Looking at all results together, It is seen that, except for the direct urea methanolysis, the other three processes cannot achieve positive NPV values at the highest H_2 price of 6.0 €/kg. This is also the case under base conditions, which is denoted by a symbol of black star in each color map. To facilitate analysis, the four processes are divided into two groups for comparisons, with the oxidative carbonylation of methanol and direct urea methanolysis in first group and the two indirect

urea methanolysis in the second. In the first group, for both lower and upper end points, the oxidative carbonylation of methanol requires lower H_2 prices or higher DMC selling prices compared to the direct urea methanolysis to achieve the same NPV values, suggesting that the latter process can resist to larger market fluctuations. For the second group, when both processes have the same DMC selling prices of 800 or 1200 €/t, the indirect urea methanolysis via propylene carbonate requires lower H_2 prices, and therefore it is less resilient to market uncertainties. Comparing the changing rates of the solid lines, it is found that the slope of the oxidative carbonylation of methanol is the largest, showing that this process is more sensitive to H_2 price. In the future, when the H_2 price is as low as 2.56 €/kg, the oxidative carbonylation of methanol would be superior to the indirect urea methanolysis via ethylene carbonate, exhibiting its competence at low H_2 prices. The other three slopes are nearly the same and their rankings do not change with H_2 price.

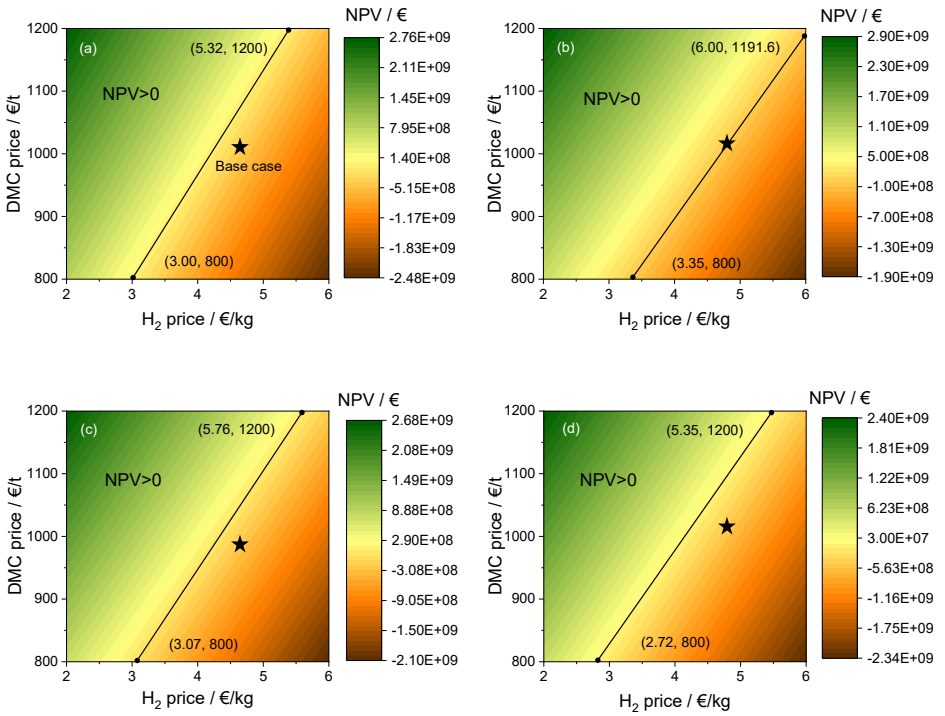

Fig. 4-9 NPV map of each process for DMC production; (a) oxidative carbonylation of methanol, (b) direct urea methanolysis, (c) indirect urea methanolysis via ethylene carbonate, (d) indirect urea methanolysis via propylene carbonate.

4.2 Process analysis of MF production pathways

Following the same procedures for DMC, the process analysis for MF also starts from process screening to thermodynamic analysis and finalized by techno-economic analysis.

4.2.1 Process screening of MF production pathways

The overview of TRL and compliance with green chemistry principles for MF production pathways are shown in Table 4-6. None of the processes violate the green chemistry principles, so at this point, no process can be excluded. TRL is the criteria that can screen the suitable processes for analysis. To date, MF production by carbonylation and dehydrogenation of methanol have been industrialized, as the two processes can achieve high conversions and selectivities, so the above two processes are selected. The oxidative dehydrogenation of methanol process is featured with low energy efficiency, as the hydrogen is consumed to supply heat for the reaction. The dimerization of formaldehyde is much more complex than other processes, as formaldehyde must be produced from methanol first. Since the oxidative dehydrogenation of methanol and dimerization of formaldehyde are not attractive, only proof-of-concept has been achieved by limited studies in the literature and their TRLs are estimated to be 3. The direct synthesis from syngas and hydrogenation of carbon dioxide with methanol represent the future directions of development, intensive studies make their technical maturities higher, but high pressure operations remain a major disadvantage of this process, and so its TRL is around 4. Since the threshold value of TRL is set to 5, only the first two processes are selected.

Table 4-6 Process screening for the MF production pathways

Process	TRL	Comply with green chemistry principles?	Selection?
Carbonylation of methanol	SoA	Yes	Yes
Dehydrogenation of methanol	SoA	Yes	Yes
Oxidative dehydrogenation of methanol	3	Yes	No
Dimerization of formaldehyde	3	Yes	No
Direct synthesis from syngas	4	Yes	No
Hydrogenation of carbon dioxide with methanol	4	Yes	No

4.2.2 Thermodynamic analysis of the selected pathways

This section analyzes the Gibbs free energy changes of the selected pathways and the phase equilibria of components involved in the reaction systems to help design distillation processes.

Gibbs free energy change

The standard Gibbs free energy and reaction enthalpy changes of the two selected processes are presented in Table 4-7. The standard Gibbs free energy of the both reactions are positive. The standard Gibbs free energy of the dehydrogenation of methanol in the gas phase is larger than that of the carbonylation of methanol, so the equilibrium conversion of the latter reaction is lower. But in the liquid phase, the standard Gibbs free energy of the carbonylation of methanol changes to +65.2 kJ/mol, leading to a lower equilibrium conversion of this reaction. The reaction enthalpy changes of the two reaction are different, negative for the carbonylation of methanol and positive for the dehydrogenation of methanol. To reach a higher conversion, the reaction temperature of the dehydrogenation of methanol would be higher.

Table 4-7 Standard Gibbs free energy changes of MF synthesis reactions.

Pathway	Reaction	$\Delta_r G^{\Theta}_{25°C}$ / kJ/mol	$\Delta_r H^{\Theta}_{25°C}$ / kJ/mol
Carbonylation of methanol	Eq. 2-16	+65.2	-37.2
Dehydrogenation of methanol	Eq. 2-17	+29.6	+49.5

Vapor-liquid equilibrium

The vapor liquid equilibrium of the methanol and MF is displayed in Fig. 4-10. The binary mixture does not form any azeotrope and their separation can be realized by only one column. Key information from the figure is that the gap between the bubble point line and the dew point one becomes narrower at high MF purity, so more stages are required above the feeding stage of the distillation column.

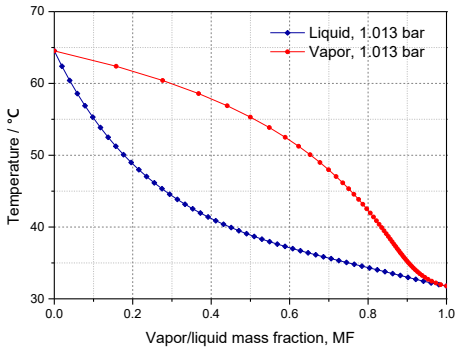

Fig. 4-10 Vapor-liquid equilibrium of methanol and MF.

4.2.3 Process design and simulation

Carbonylation of methanol

Similar to the oxidative carbonylation of methanol for DMC synthesis, the carbonylation of methanol for MF production also consists of three sections of methanol synthesis, reverse water gas shift, and MF synthesis and separation. The first two sections have the identical process designs with the only difference of production scale, so these two sections are not described again.

The process flowsheet of the carbonylation of methanol is shown in Fig. 4-11. The CO from the reverse water gas shift is compressed to the MF synthesis reactor together with methanol. The carbonylation of methanol takes place in the liquid phase catalyzed by homogeneous CH_3ONa [117]. In order to increase the equilibrium conversion, the reaction pressure is elevated to 40 bar and the temperature is set to 80 ℃ [117]. The MF product and unconverted methanol are separated in a distillation column. Methanol in the bottom stream is the recycled to the reactor, and the MF product is obtained on top of the column with purity higher than 99 wt.%.

In the Aspen Plus simulations, the UNIQ-RK is the global property method for the MF synthesis and distillation. The reactor is modeled with the RStoic model with 30% conversion of methanol [117].

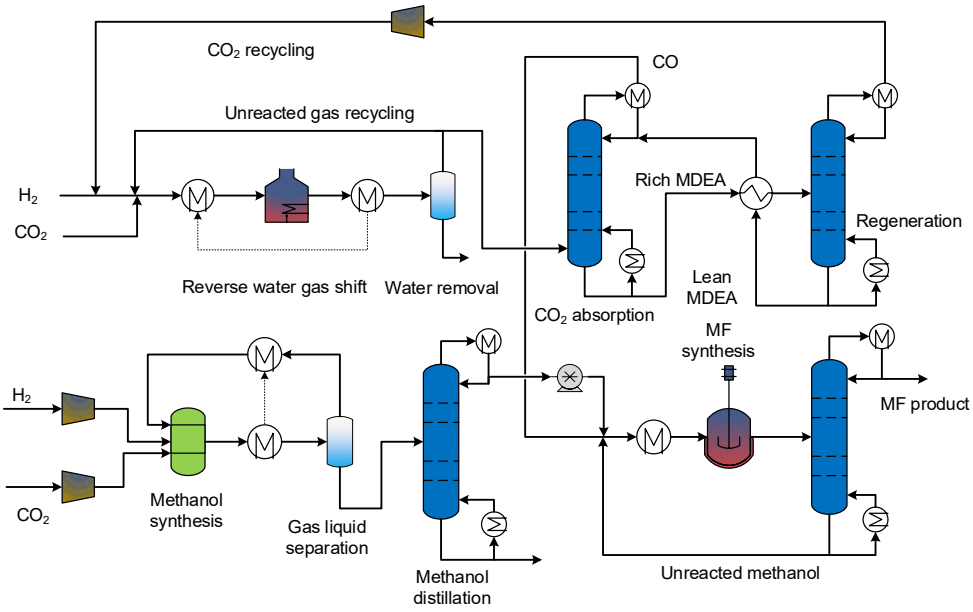

Fig. 4-11 Process flowsheet of MF production by carbonylation of methanol.

Dehydrogenation of methanol

The dehydrogenation of methanol process has only two sections of methanol synthesis, and MF synthesis and separation. The process flowsheet of the dehydrogenation of methanol is shown in Fig. 4-12**.** To produce the same amount of MF as the carbonylation of methanol, the methanol required in this process is doubled according to the reaction stoichiometry. The produced methanol is then sent to the MF synthesis reactor. The dehydrogenation of methanol takes place in the gas phase at 1 bar catalyzed by Cu-Zn-Zr/Al_2O_3. In order to vaporize methanol, the reactor inlet stream is increased to 250 ℃ [117]. The high-temperature stream of the reactor outlet is first used for low-pressure steam generation that can be later used for the product separation. After further cooling, the unconverted methanol and MF are condensed, and H_2 in the gas phase is recycled for methanol synthesis. The liquid mixture of methanol and MF is separated in the distillation column.

In the Aspen Plus simulations, the UNIQ-RK property method is used for the MF synthesis and distillation. The reactor is modeled with the RStoic model with 58.5% conversion of methanol [117].

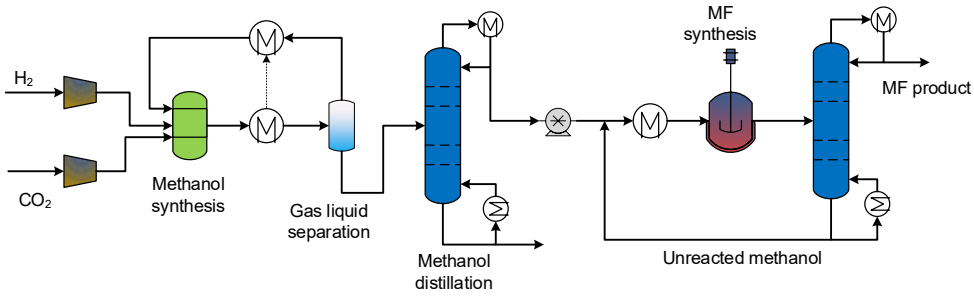

Fig. 4-12 Process flowsheet of MF production by dehydrogenation of methanol.

4.2.4 Techno-economic performance

The following sections analyze and compare the energy and economic performance of both MF production processes.

Material and energy balances

Based on the process simulation results, the material and energy balances are achieved. The synthesis scale of MF is set to 300 MW, which translates into MF output of 70 t/h, and both processes consume the same amount of H_2. The educt demand and energy efficiencies of both processes are presented in Table 4-8 . Both processes consume nearly the same amount of CO_2 and H_2. Although the carbonylation of methanol has more sections, it represents a higher Power-to-Fuel efficiency calculated by Eq. 3-1. In the dehydrogenation process, the amount of methanol required for MF synthesis is doubled, which lead to more energy demand for methanol distillation. In addition, the methanol decomposes into H_2, and it has to be recovered to synthesize methanol again. Tracking the flow of hydrogen in the process, it can be found that it undergoes the process of synthesis-decomposition-synthesis. Part of the hydrogen does not turn into MF but this increases the throughput and energy burden of the process, with a lower Power-to-Fuel efficiency as a result.

Table 4-8 Educt demand and energy efficiency of each process for MF production.

Item	Carbonylation of methanol	Dehydrogenation of methanol
CO_2 consumption / kg/l_{DE}	3.42	3.37
H_2 consumption / kg/l_{DE}	0.32	0.32
CO_2 consumption / kg/kg_{MF}	1.54	1.52
H_2 consumption / kg/kg_{MF}	0.144	0.144
MF output / l_{DE}/h	31878.7	31877.6
Power-to-Fuel efficiency*	52.5%	48.6%

*The efficiency is calculated based on Eq. 3-1. The assumed PEM water electrolysis is 70% [4] and specific energy consumption for CO_2 capture is 1.2 MJ/kg [178].

Specific energy consumption

The specific energy consumption of both processes is presented in Fig. 4-13. The energy consumption of each section of the both processes is also provided in Table A-2 in the Appendix. In consistent with the Power-to-Fuel efficiency, the carbonylation of methanol has lower specific energy consumption. Again, the water electrolysis accounts for the largest part in each process, 80.1% for the carbonylation of methanol and 75.8% for the dehydrogenation of methanol, respectively. In the carbonylation of methanol, the low-pressure steam is the second contributor to the specific energy consumption rather than CO_2 capture, which is used for methanol distillation and MF product separation. Although the CO_2 demand in both processes is nearly the same, the CO_2 recycling in the carbonylation of methanol adds additional energy burden. No medium- and high-pressure steam is needed in the carbonylation of methanol. The reverse water gas shift also requires additional electricity for reactor heating. Yet the reaction enthalpy change is only +42.1 kJ/mol, so the electricity demand for heating is not significant, accounting for only 3.2% of the total energy demand. The share of low-pressure steam in the dehydrogenation of methanol is 6.1%, which is less significant than the value of 9.8% in the carbonylation of methanol, contributed by its higher conversion. Instead, high-pressure steam is the unique energy form in this process, which is used for vaporization of reactants for MF synthesis. In addition, the sequence of vaporization-condensation-vaporization in the synthesis loop inevitably causes more energy loss, which is the culprit of the higher total energy consumption.

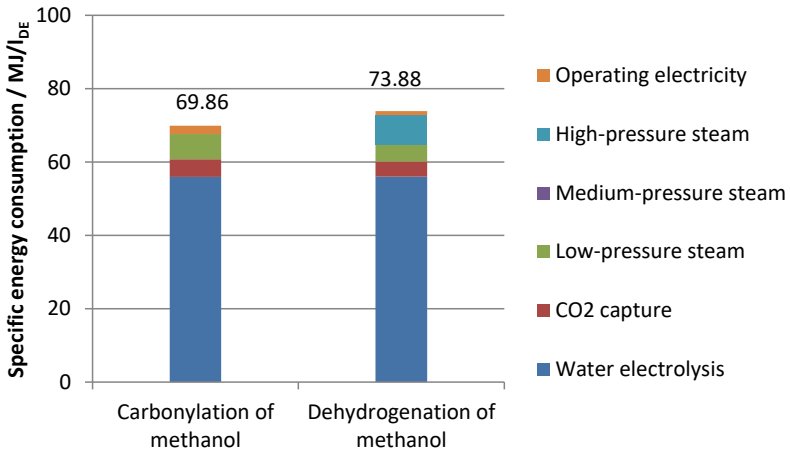

Fig. 4-13 Specific energy consumption of each process for MF production.

Capital expenditure and cost of manufacturing

The breakdowns of CAPEX of the both processes are presented in Fig. 4-14. The CAPEX of the carbonylation of methanol and dehydrogenation of methanol is 87.0 and 82.4 million Euros, respectively. In the carbonylation of methanol, methanol synthesis is the dominant contributor to the CAPEX, which accounts for nearly 50% of the total FCI. As already explained in the DMC processes, the high operating pressure and large reactor size are the main causes for its high FCI. Of the remaining 50% FCI, reverse water gas shift and MF synthesis are the two primary contributors with similar shares. The FCI of the reverse water gas shift is determined by the reactor cost while the FCI of the MF synthesis and separation is mainly caused the reactor and distillation columns. In the dehydrogenation of methanol, the methanol synthesis plays a decisive role, accounting for 84.7% of the total FCI. Although the methanol output of the dehydrogenation process is twice that of the carbonylation of methanol, its FCI only increases by 53%, which is contributed by the economies of scale. It is very interesting that the total FCI of methanol synthesis, reverse water gas shift and CO_2 scrubbing is nearly equivalent to the FCI of the methanol synthesis in the dehydrogenation of methanol, suggesting that the front end sections in both processes are not the source of the difference in CAPEX. Instead, the MF synthesis reactors are the origin for that difference. For dehydrogenation of methanol, the gas phase operation at ambient pressure requires a large reactor volume. Although the carbonylation reaction in the liquid phase can reduce reactor size, the larger recycling stream of unconverted methanol due to the lower conversion leads to the increase in the reactor volume. Overall, the carbonylation reactor is only a little

smaller than the dehydrogenation reactor, but the pressurized operation leads to an increased capital cost. The MF distillation in both processes has only one column and their costs are similar.

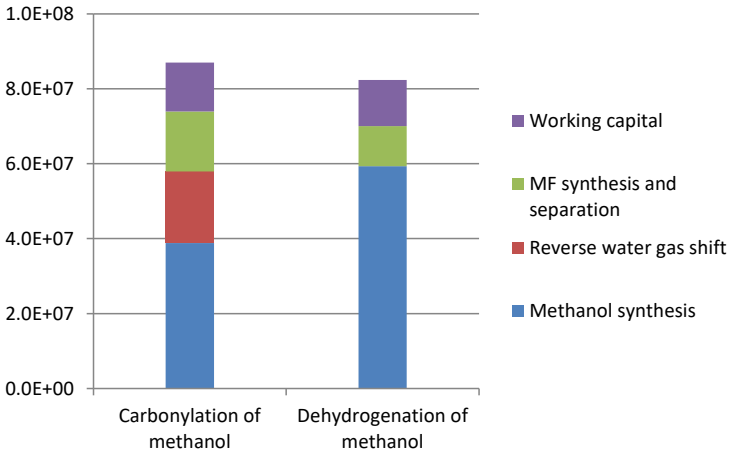

Fig. 4-14 CAPEX of each process for MF production.

The COMs of the carbonylation of methanol and dehydrogenation of methanol are 2.11 and 2.22 €/l_{DE}, respectively. The breakdowns of both processes are detailed in Fig. 4-15. Although the CAPEX of the carbonylation of methanol is higher, its COM is lower as the weight of CAPEX in the COM is not large. In both processes, the contribution of H_2 and CO_2 is nearly the same as they have similar educt demand. The difference in COM comes from the steam demand, which is in consistent with the specific energy consumption, as displayed by the green color blocks. In the carbonylation of methanol, the low-pressure steam demand is higher than in the dehydrogenation of methanol as part of low-pressure steam demand is satisfied by the heat recovery of the dehydrogenation reactor. However, the carbonylation of methanol does not require medium- and high-pressure steam. But for the dehydrogenation of methanol, it requires much high-pressure steam to vaporize the methanol educt and the recycling stream. The phase change enthalpy of methanol and MF is 35.2 and 27.9 kJ/mol, which is considerable energy expenditure in this process. More steam demand in the dehydrogenation of methanol also requires more process cooling for removing waste heat that cannot be utilized for low-pressure steam generation. The OPEX comprises the costs of taxes, overhead and labor costs, etc; and its share is between those from steam and process cooling.

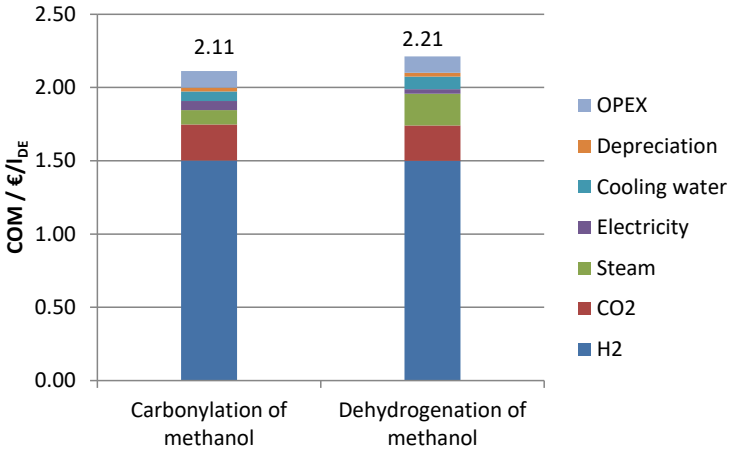

Fig. 4-15 COM of each process for MF production.

Sensitivity analysis

Following the same procedure as in DMC, the impact of each contributing factor to the COM is analyzed by univariate analysis in Fig. 4-16. For the carbonylation of methanol, when the H_2 price is varied from 2.3 to 6.9 €/kg, the COM of the process is located between 1.34 €/l_{DE} and 2.89 €/l_{DE} accordingly. CO_2 and steam contribute equally to the COM. Other variables like FCI, cooling water and operating electricity have even smaller impact. The reduction of the COM should still resort to lower H_2 and CO_2 cost reductions and less steam demand. The impacts of other variables show nearly the same trend.

Net present value and minimum selling price

In the same way, the joint effects of H_2 and MF prices on the NPVs are displayed in Fig. 4-17. The green colors in both maps represent positive NPV regions. Overall, the positive NPV region of the carbonylation of methanol has a larger area compared to the dehydrogenation of methanol, suggesting that it has more operational space. Comparing the end points of the solid lines in each map, we find that, for both upper end points with the same H_2 price of 6.0 €/kg, the MF selling price of the carbonylation of methanol to achieve a positive NPV is lower; for the lower end points with the same MF selling price of 800 €/t, the dehydrogenation requires a lower H_2 price. These figures suggest that, under same market conditions, the carbonylation of methanol is more profitable. The slopes of the two lines are the same, which means that the carbonylation of methanol is always superior to the dehydrogenation

of methanol, no matter what the H_2 price is. Applying the maps to the base cases, it is seen that although both processes represent positive NPVs, they are close to the boundary lines and are still in risky regions.

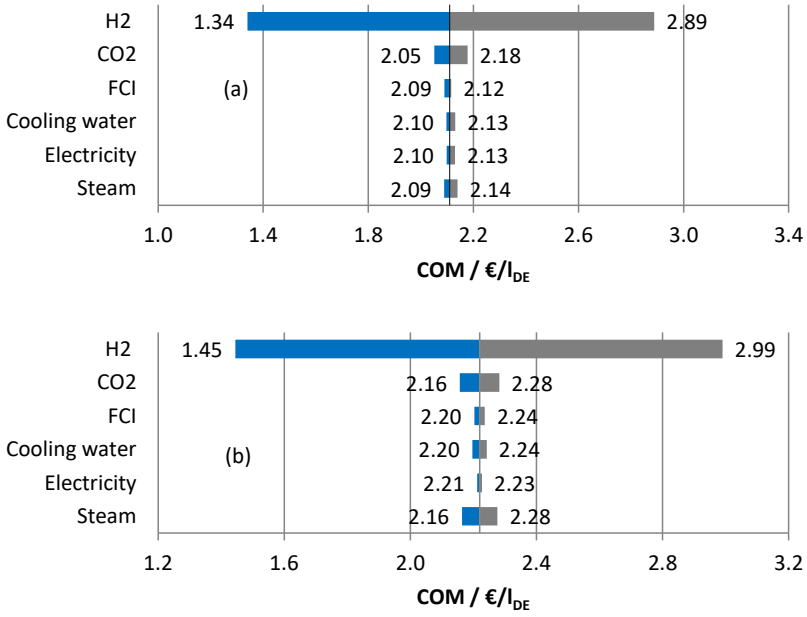

Fig. 4-16 Sensitivity analysis of each process for MF production; (a) carbonylation of methanol, (b) dehydrogenation of methanol.

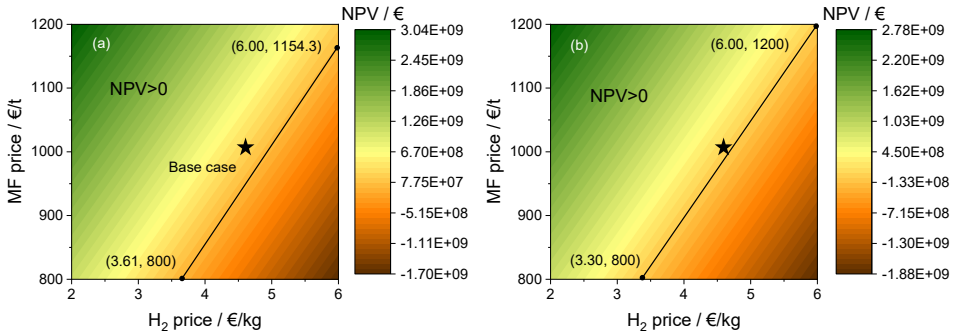

Fig. 4-17 NPV map of each process for MF production; (a) carbonylation of methanol, (b) dehydrogenation of methanol.

4.3 Cross-pathway comparison

In this chapter, the suitable pathways of each product have been techno-economically analyzed based on the same systems boundaries, assumptions, and evaluation indicators. In terms of energy performance, the two MF production processes have higher energy efficiencies and lower specific energy consumption than the four DMC production processes. Fundamentally, the performance of a chemical process is determined by the thermodynamic barriers of synthesis reactions and separation difficulties. Thermodynamic barriers determine the conversions of reactions, which will also affect product separations. Separation difficulties are subject to many factors such as number of components, relative volatility, and formation of azeotropes. More components and processing steps are involved in the DMC production processes and azeotropes are formed. All of these lead to lower energy efficiencies. Process intensification and heat integration are two effective approaches to realize more energy efficient processes. A common point of these processes is that the water electrolysis is the biggest contributor to energy consumption. Water electrolyzers are critical equipment in electrolysis-based processes that need intensive research and development.

The economic performance of the processes are closely related to energy performance. The two MF production processes are also better in terms of process efficiency and production cost due to simpler synthesis routes. Methanol synthesis is the common processing step for both DMC and MF production. A key finding is that methanol synthesis is the biggest contributor to CAPEX instead of the product syntheses themselves. High pressure operation is responsible for the high CAPEX and an implication here is that low pressure condition is preferred at the point of capital cost. The H_2 price is the dominant economic driver of the production costs of DMC and MF. With the assumed H_2 and product selling prices, both DMC and MF are not far from profitability.

Overall, DMC and MF are suitable candidates of electrofuels and can be produced from CO_2 and H_2 through processes that are technically realistic, energy efficient, and economically viable. The esters will sit alongside alcohols, ethers, and hydrocarbons as extension to Power-to-Fuel family. In addition, they are both downstream products of methanol and can be seen an addition to methanol-based pathways.

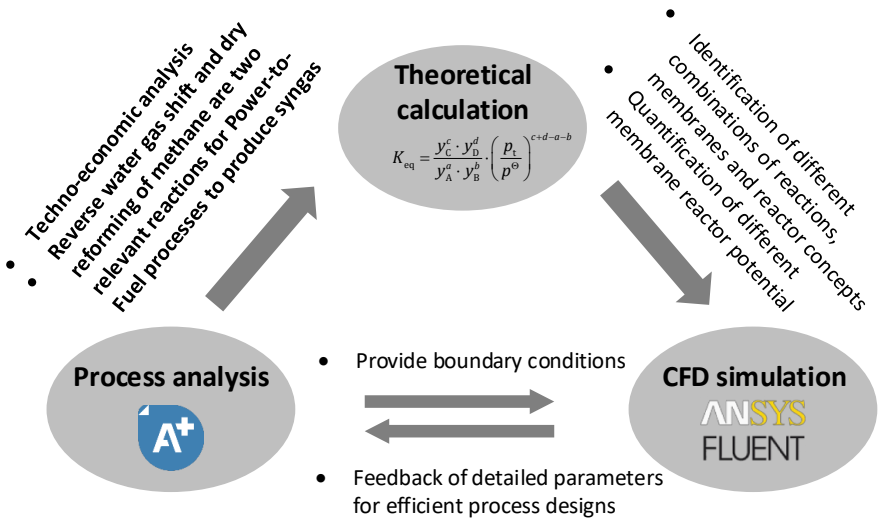

Fig. 4-18 Schematic representation of the link between chapter 4 and chapter 5.

As shown in Fig. 1-3, one of the tasks of process analysis is to identify the suitable reactions for membrane reactor applications in Power-to-Fuel processes. In this chapter, it has been shown that CO is necessary for the syntheses of DMC and MF. Also, for the Fischer-tropsch processes, syngas is needed as the educt. Therefore, producing CO and syngas from CO_2 and H_2 is an important intermediate step for Power-to-Fuel applications. Reverse water gas shift is such an reaction that can produce syngas or CO from CO_2 and H_2. However, reverse water gas shift is a thermodynamically limited reaction and can impact the techno-economic performance of the whole processes. Membrane reactors will be considered to intensify the reaction. In parallel, dry reforming of methane, as an alternative to reverse water gas shift for producing syngas, will also be considered as well. As there are many different membranes and reactor concepts available now, different combinations of reactions, membranes, and reactor concepts will be first identified. The potential of each combination will be quantified by theoretical calculations in a general way in the next chapter, as shown in Fig. 4-18.

.

5 Membrane reactor selection and matching

In the process analysis of DMC and MF, the possible applications of membrane reactors to the reverse water gas shift and dry reforming of methane have been identified. This chapter deals with the question posed in the Chapter 1.4: which membrane and reactor concept should be preferentially matched with a given reaction under what conditions to achieve better conversion enhancement. To address this question, the mapping relationships of reaction, membrane, and reactor concept are first set-up. The contribution of membrane reactors to the given reactions is then quantified by theoretical calculations. This chapter paves the way for the development of membrane reactors by CFD simulations in Chapter **6**. The results in section 5.2 have been published in the journal of Chemical Engineering Science. DOI: 10.1016/j.ces.2021.117284 [248].

5.1 Mapping of reaction-membrane-reactor concept

Depending on the purposes of applications, a reaction can be matched with different reactor concepts through different membranes. Fig. 5-1 presents mapping relationships that start from the two selected reactions of the reverse water gas shift and dry reforming of methane, over possible membrane materials, to the reactor concept 3 of “shift of equilibria”, concept 5 of “removal of intermediates”, and concept 6 of “reactant dosing” in Fig. 3-6. A total of five combinations have been identified based on the reactor concepts. For the reverse water gas shift, to increase the equilibrium conversion, the concept 3 of “shift of equilibria” is well suited to this purpose, which can be realized by water permeable membranes. This reaction can be also matched with concept 6 for distributed feeding through carbon dioxide permeable membranes, but the purpose is changed from conversion improvement to feed distribution. Compared to water permeable membranes, carbon dioxide membranes are capable of working at high temperatures, which is matched with the preferred reaction temperature of reverse water gas shift. In particular, this combination can realize integrated carbon dioxide capture and utilization, which is a very attractive application for Power-to-Fuel processes. The reactor concept 6 and carbon dioxide membranes are also applicable for dry reforming of methane for the same reasons. Since H_2 is an intermediate of this reaction, it is natural that hydrogen permeable membranes can be used together with concept 5 of “removal of intermediates”, but in fact, the equilibrium is also shifted by removing H_2, so matching with concept 3 is another option. Therefore, using a hydrogen permeable membrane can increase the selectivity and conversion at the same time. Although the mapping relationships are developed based on the selected

reactions relevant to this thesis, it can be extended to any other reactions in the same way.

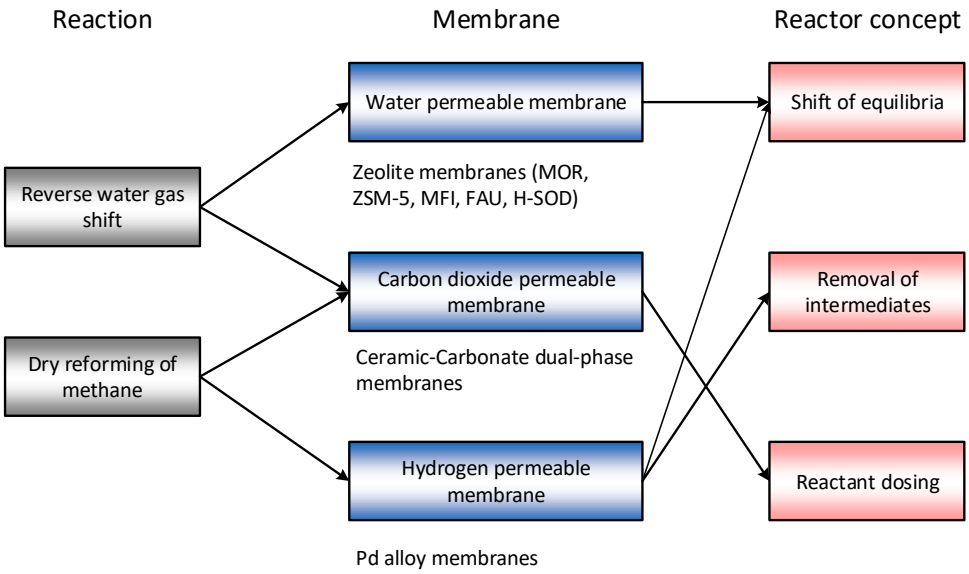

Fig. 5-1 Mapping relationship of the reactions, membranes, and reactor concept 3 of "shift of equilibria", concept 5 of "removal of intermediates", and concept 6 of "reactant dosing".

5.2 Theoretical calculations for quantified analysis

The previous section presented a guiding principle for qualitatively selecting possible membranes and reactor concepts for a reaction, but it remains unknown how effective the selected membrane and the reactor concept contribute to a reaction. Clarifying this question needs an analysis that is quantified but general. The quantified analysis can be performed through theoretical calculations based on the dimensionless number group of *DaPe*. The mapping relationships, together with the quantified calculations, form an integrated framework that could help guide the selection and matching of membrane reactors.

To make the analysis general, the reaction is expressed in a following general form:

$$a\,A + b\,B \leftrightarrow c\,C + d\,D \qquad \text{Eq. 5-1}$$

If the above reaction takes place in a conventional fixed-bed reactor, its equilibrium constant is written as:

$$K_{\mathrm{eq}} = \frac{\left(\frac{p_{\mathrm{C}}}{p^{\Theta}}\right)^{c} \cdot \left(\frac{p_{\mathrm{D}}}{p^{\Theta}}\right)^{d}}{\left(\frac{p_{\mathrm{A}}}{p^{\Theta}}\right)^{a} \cdot \left(\frac{p_{\mathrm{B}}}{p^{\Theta}}\right)^{b}} = \frac{y_{\mathrm{C}}^{c} \cdot y_{\mathrm{D}}^{d}}{y_{\mathrm{A}}^{a} \cdot y_{\mathrm{B}}^{b}} \cdot \left(\frac{p_{\mathrm{t}}}{p^{\Theta}}\right)^{c+d-a-b} \qquad \text{Eq. 5-2}$$

where p_i is the partial pressure of species i, y_i is the molar fraction, p_t is total pressure, and p^{Θ} is the standard pressure of 1 bar. Although the above equation is implicitly assumed to be in the gas phase, it is easy to adapt the above expression for reactions in the liquid phase by replacing the partial pressure with activity. If operating conditions and initial feed are given, the equilibrium composition can be calculated.

The next step is to develop the expression for the reaction taking place in a membrane reactor with one product removed by membrane permeation. The derivation of the expression is achieved by a stoichiometric table. The stoichiometric table provides a functional form that clearly shows the mole changes of reactants and products before and after the reaction. Before starting, the product that is to be removed by membrane permeation has to be designated. In principle, any species on the product side can be used, so product C is selected here for the following calculations. Assuming the initial feed of A and B are $n_a = n_b$ and the reaction extent is ξ, the following table is prepared.

Table 5-1 Stoichiometric table for the calculation of mole balances in membrane reactors.

	A	**B**	**C**	**D**	**Total moles**
Initial moles	n_a	n_b	0	0	$n_a + n_b$
Moles reacted	$-a\xi$	$-b\xi$	$c\xi\left(1-1/DaPe\right)$	$d\xi$	$c\xi\left(1-1/DaPe\right)$ $+d\xi - a\xi - b\xi$
Equilibrium moles	$n_a - a\xi$	$n_b - b\xi$	$c\xi\left(1-1/DaPe\right)$	$d\xi$	$c\xi\left(1-1/DaPe\right)+n_a+$ $n_b + d\xi - a\xi - b\xi = \mathrm{sum}$
Molar fraction	$\frac{n_a - a\xi}{\mathrm{sum}}$	$\frac{n_b - b\xi}{\mathrm{sum}}$	$\frac{c\xi\left(1-1/DaPe\right)}{\mathrm{sum}}$	$\frac{d\xi}{\mathrm{sum}}$	-

With the above table, the expression for reactions in membrane reactors is obtained, of which the variable of *DaPe* has been included:

$$K_{\mathrm{eq}}=\frac{\left(\dfrac{c\xi\left(1-1/DaPe\right)}{\mathrm{sum}}\right)^{c}\cdot\left(\dfrac{d\xi}{\mathrm{sum}}\right)^{d}}{\left(\dfrac{n_a-a\xi}{\mathrm{sum}}\right)^{a}\cdot\left(\dfrac{n_b-b\xi}{\mathrm{sum}}\right)^{b}}\cdot\left(\frac{p_{\mathrm{t}}}{p^{\Theta}}\right)^{c+d-a-b} \qquad \text{Eq. 5-3}$$

The above equation can be used for the membrane concepts of catalyst retainment, shift of equilibria, coupling of reactions, and removal of intermediates, where one of the products is to be removed for conversion enhancement, but it does not apply to the concepts of membrane contactor and reactant dosing. The simplest case by the above equation is $a = b = c = d = 1$, $K_{\mathrm{eq}} = 1$, and $n_{\mathrm{a}} = n_{\mathrm{b}} = 1$. Fig. 5-2 depicts this simplest case and compares it with the equilibrium conversion. The conversion of A or B is always higher than the equilibrium conversion but drops quickly with increasing *DaPe* in the beginning and nearly vanishes at large *DaPe*. It is also found that the *DaPe* has to be larger than a threshold value so that conversion enhancement is meaningful.

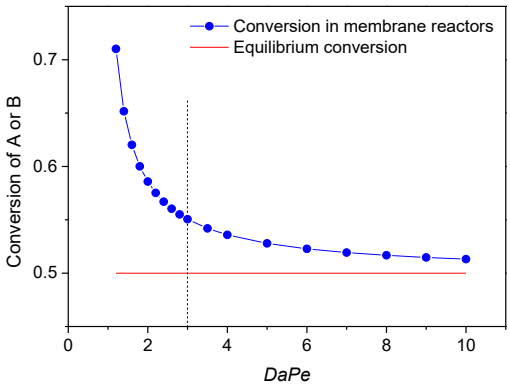

Fig. 5-2 Conversion of A or B at different *DaPe* by Eq. 5-3, $a = b = c = d = 1$, $K_{\mathrm{eq}} = 1$, and $n_{\mathrm{a}} = n_{\mathrm{b}} = 1$

5.2.1 Exemplification

The above relationship is further applied to two reactions for exemplification. It is easy to show the following equations for the dry reforming of methane and reverse water gas shift by giving initial moles of reactants. For the reverse water gas shift, the initial moles of

CO_2 and H_2 are 1 and n_{H_2} mol. For the dry reforming of methane, the initial moles of CH_4 is 1 mol while CO_2 is n_{CO_2} mol. The ξ_1 in the equations is the reaction extent of Eq. 2-21, ξ_2 and ξ_3 are the reaction extent of Eq. 2-24 and Eq. 2-25, respectively. As the dry reforming of methane also contains a side reaction of reverse water gas shift, to avoid confusion, the single reverse water gas shift reaction is referred to as independent reverse water gas shift in the following analyses.

Independent reverse water gas shift:

$$0 = K_{\mathrm{eq,RWGS}} - \frac{\left(\frac{\xi_1\left(1-1/DaPe\right)}{1+n_{H_2}-\xi_1/DaPe}\right)\cdot\left(\frac{\xi_1}{1+n_{H_2}-\xi_1/DaPe}\right)}{\left(\frac{1-\xi_1}{1+n_{H_2}-\xi_1/DaPe}\right)\cdot\left(\frac{n_{H_2}-\xi_1}{1+n_{H_2}-\xi_1/DaPe}\right)} \qquad \text{Eq. 5-4}$$

Dry reforming of methane:

$$0 = K_{\mathrm{eq,DRM}} - \frac{\left(\frac{\left(2\xi_2-\xi_3\right)\cdot\left(1-1/DaPe\right)}{1+n_{CO_2}+2\xi_2-\left(2\xi_2-\xi_3\right)/DaPe}\right)^2\cdot\left(\frac{2\xi_2+\xi_3}{1+n_{CO_2}+2\xi_2-\left(2\xi_2-\xi_3\right)/DaPe}\right)^2}{\left(\frac{1-\xi_2}{1+n_{CO_2}+2\xi_2-\left(2\xi_2-\xi_3\right)/DaPe}\right)\cdot\left(\frac{n_{CO_2}-\xi_2-\xi_3}{1+n_{CO_2}+2\xi_2-\left(2\xi_2-\xi_3\right)/DaPe}\right)}\cdot\left(\frac{p_t}{p^{\Theta}}\right)^2 \qquad \text{Eq. 5-5}$$

$$0 = K_{\mathrm{eq,RWGS}} - \frac{\left(\frac{2\xi_2+\xi_3}{1+n_{CO_2}+2\xi_2-\left(2\xi_2-\xi_3\right)/DaPe}\right)\cdot\left(\frac{\xi_3}{1+n_{CO_2}+2\xi_2-\left(2\xi_2-\xi_3\right)/DaPe}\right)}{\left(\frac{\left(2\xi_2-\xi_3\right)\cdot\left(1-1/DaPe\right)}{1+n_{CO_2}+2\xi_2-\left(2\xi_2-\xi_3\right)/DaPe}\right)\cdot\left(\frac{n_{CO_2}-\xi_2-\xi_3}{1+n_{CO_2}+2\xi_2-\left(2\xi_2-\xi_3\right)/DaPe}\right)} \qquad \text{Eq. 5-6}$$

The above nonlinear equations can be solved to get the values of ξ_1, ξ_2, and ξ_3 when the operating conditions and initial feed composition are specified.

The conversion and the corresponding conversion enhancement of the reverse water gas shift are depicted in Fig. 5-3. The impacts of temperature and feed ratio are studied. As the reaction is equimolar, the pressure has no effect on the equilibrium conversion, so it is not analyzed. The base case conditions are set at 250 °C, 30 bar, and H_2:CO_2 = 1:1, which are realistic for current zeolite membranes [206, 210]. The range of *DaPe* is from 1.2 to 10.0,

which translates into water removal from 83.3% to 10%. The conversions of CO_2 and H_2 are calculated according to $X_{H_2} = \xi_1 / n_{H_2}$ and $X_{CO_2} = \xi_1$. When the feed composition is stoichiometric, the conversions of H_2 and CO_2 and their enhancement are the same. In Fig. 5-3 (a), the conversion is reduced from 21.5% to 10.6% over the entire range of *DaPe*. Under the base case conditions, the equilibrium conversion is 10.1%. And the conversion enhancement varies between 113.7% and 4.8%. If 20% is set as the threshold of "effective enhancement", then the critical value of *DaPe* is determined to be 3.0, below which higher conversion and enhancement can be achieved. The *DaPe* of 3.0 is a moderate value that will not impose a harsh requirement for current membranes. When the feed composition of H_2:CO_2 is changed to 3:1, the conversion of CO_2 is three times that of H_2, which varies between 35.7% and 18.0% for CO_2 and 11.9% to 6.0% for H_2. The conversion enhancement remains almost the same and just a little lower compared to the stoichiometric feed. The conversions at 200 ℃ with stoichiometric feed are lower compared to those at 250 ℃ with stoichiometric feed because the reaction is endothermic, decreasing from 15.0% to 7.1%. But the conversion enhancement is higher. The critical values of *DaPe* for the "effective enhancement" in Fig. 5-3 (b) and (c) are also around 3.0 for these cases, suggesting that the contribution of membranes remains stable despite the operating conditions being changed.

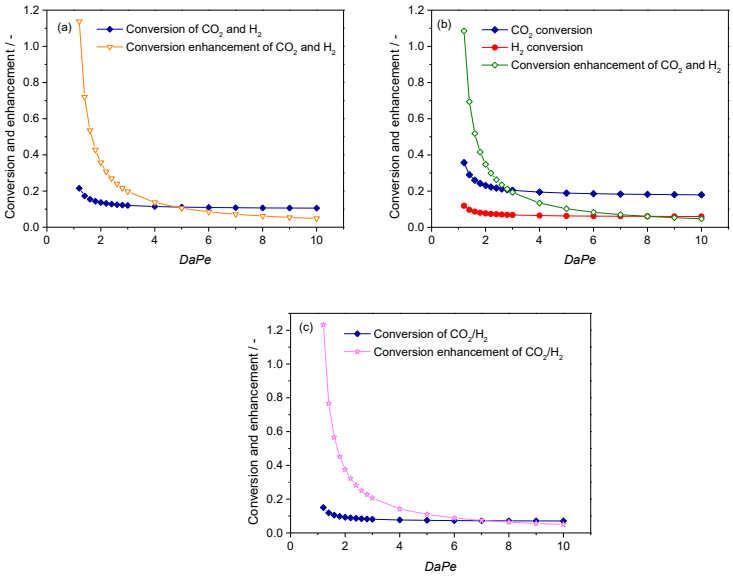

Fig. 5-3 H_2 and CO_2 conversions of reverse water gas shift and their enhancement in membrane reactors: (a) T = 250 ℃, p_t = 30 bar and H_2:CO_2 = 1:1; (b) T = 250 ℃, p_t = 30 bar and H_2:CO_2 = 3:1; (c) T = 200 ℃, p_t = 30 bar and H_2:CO_2 = 1:1.

Similarly, the results for the dry reforming of methane are shown in Fig. 5-4. The effects of temperature, pressure, and feed composition are considered. The base case conditions are 450 ℃, 20 bar, and CH_4:CO_2 = 1:1. The conversions of CH_4 and CO_2 are calculated by $X_{CH_4} = \xi_2$ and $X_{CO_2} = (\xi_2 + \xi_3) / n_{CO_2}$. Again, the range of *DaPe* is from 1.2 to 10.0, which translates into H_2 removal from 83.3% to 10%. At the lowest *DaPe* of 1.2, the conversions of CH_4 and CO_2 are 4.0% and 5.4%, respectively, as shown in Fig. 5-4 (a), which represents the smallest gap in conversion. Both conversions decrease with *DaPe* and their gap becomes ever more significant. The conversion enhancement changes from 89.6% to 2.5% for CH_4 and from 12.7% to 0.12% for CO_2, but the gap in conversion enhancement becomes ever smaller with *DaPe*. Based on these results, it is found that removing H_2 from the reaction system has stronger impacts on CH_4 than on CO_2. H_2 is a product of the main reaction but is a reactant of the side reaction, so removing it shifts the equilibrium of the main reaction but suppresses the equilibrium of the side reaction. Overall, the conversion of CO_2 is increased but much limited. To meet the standard of "effective enhancement", the critical value of *DaPe* should be higher 2.1. This value is smaller than that of the reverse water gas shift, which poses a higher requirement for H_2 permeation, and the operating window becomes smaller.

Raising the temperature to 500 ℃ increases both the CO_2 and CH_4 conversions. From the Fig. 5-4 (b), the absolute values of the conversion differences are larger than those at 450 ℃, but the conversion ratios of X_{CH_4} / X_{CO_2} at 500 ℃ are larger, which vary between 0.78 and 0.48 while those at 450 ℃ range from 0.74 to 0.45. Although increasing the temperature raises the conversions of the main reaction and the side reaction, both reactions have different sensitivities to temperature. The equilibrium constants of the main reaction increase from 1.2×10^{-4} to 1.92×10^{-3} from 450 ℃ to 500 ℃, which is an increase of more than an order of magnitude. But for the side reaction, the equilibrium constants are only from 0.13 to 0.19. Thus, a higher temperatures benefits more to the main reaction. Also, membrane permeation is higher at higher temperatures. The conversion enhancement is a little higher and shows a very similar trend to that at 450 ℃, and the critical value of *DaPe* is 2.2.

Reducing the pressure to 5 bar also helps increase the conversions of CH_4 and CO_2, shown in Fig. 5-4 (c). A lower pressure does not change the equilibrium of the side reaction but moves the equilibrium of the main reaction to the product side. Likewise, the CH_4 and CO_2 conversions are both boosted, and the conversion ratios of X_{CH_4} / X_{CO_2} are decreased from 0.83 to 0.51 with *DaPe*, suggesting that reducing pressure is an effective way to increase the conversions and selectivities. Further reducing the pressure will make the conversions and selectivities even higher, but according to a study by Lee et al. [161],

pressures are a factor that has to be balanced between conversion and membrane permeation. It was concluded that 5 bar is a good trade-off, so the pressure is not reduced to an even lower value.

In the above cases, although the conversion gap between CH_4 and CO_2 can be narrowed by changing the temperature and pressure, the CH_4 conversion cannot exceed the CO_2 conversion. To make the best use of CH_4, excess CO_2 is fed to make the CH_4 conversion higher. Here, the CH_4/CO_2 ratio is set to 1:2. In Fig. 5-4 (d), the gap between the conversions is much smaller at large *DaPe* values. When *DaPe* is lower than 2.0, the CH_4 conversion is even higher than the CO_2 conversion, which is a joint contribution of the higher feed ratio and membrane permeation, but the conversion enhancement is compromised by doing this.

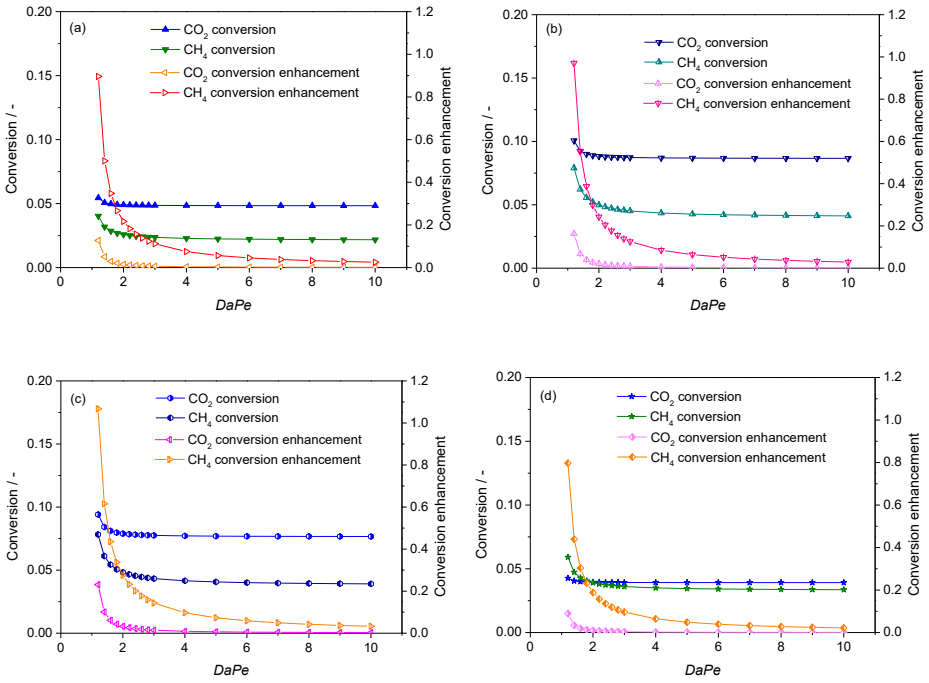

Fig. 5-4 CH_4 and CO_2 conversions of dry reforming of methane and their enhancement in membrane reactors: (a) T = 450 ℃, p_t = 20 bar, and CH_4:CO_2 = 1:1; (b) T = 500 ℃, p_t = 20 bar, and CH_4:CO_2 = 1:1; (c) T = 450 ℃, p_t = 5 bar, and CH_4:CO_2 = 1:1; (d) T = 450 ℃, p_t = 20 bar and CH_4:CO_2 = 1:2.

5.2.2 Effect of stoichiometric coefficient

As mentioned in the last section, stoichiometric coefficient also plays a vital role in conversion enhancement. The following analysis will be also based on the general reaction form to make findings generally applicable. Looking back at the expression of equilibrium constant in Eq. 5-2, stoichiometric coefficient corresponds to the partial pressure exponent of each species. A higher stoichiometric coefficient will have a stronger impact on equilibrium composition of products, according to the mathematical characteristics of power-law functions. As such, if the species to be removed by membrane permeation is with a higher stoichiometric coefficient, the conversion enhancement can be more significant with same product removal. Since the contribution of stoichiometric coefficient is implicit, Fig. 5-5 provides visualization by color maps for facile comparisons. Reactions with very low equilibrium constants of 0.001 and moderate ones of 10 are considered, which represent highly and slightly limited reactions, respectively. In each map, the highest conversion enhancement is obtained at the lower right corners, where the stoichiometric coefficient of the removed product C is the highest while the *DaPe* is the lowest. For a given *DaPe*, conversion enhancement always increases with stoichiometric coefficient, and a higher stoichiometric coefficient allows a larger *DaPe* so that the requirement for membrane permeation does not need to be that high. In addition, the unfeasible regions that do not meet the "effective enhancement" of 20% are marked in gray color. The unfeasible region area in the right map is larger, so its operating window is smaller. In the right map, the "effective enhancement" can never be met when the stoichiometric coefficient is only one, even with the lowest *DaPe*. On this occasion, a higher stoichiometric coefficient is critical to meet the standard of "effective enhancement" and its role is highlighted. This finding is helpful for guiding membrane reactor selection and matching by quantified calculations instead of by relying on heuristics.

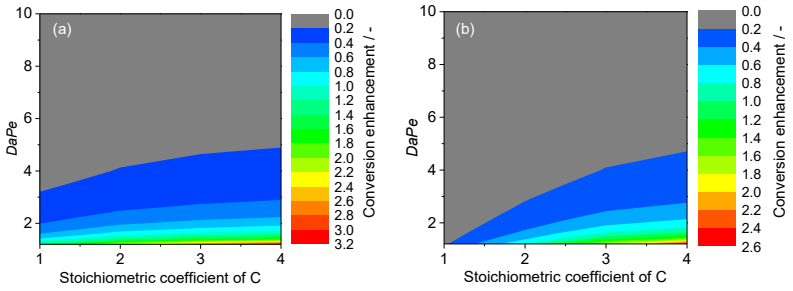

Fig. 5-5 *DaPe*-stoichiometric coefficient plot for the conversion enhancement analysis at different equilibrium constants: (a) K_{eq} = 0.001; and (b) K_{eq} = 10.

In summary, this chapter first presents mapping relationships among reaction, membrane, and reactor concepts for helping membrane reactor selection and matching. To deliver deeper insights for above purpose, a dimensionless number group of *DaPe* is introduced for quantified calculations, based on which the general relationship for membrane reactors is derived. This relationship is successfully applied to the reactions of reverse water gas shift and dry reforming of methane. A key finding is that species of a reaction with a higher stoichiometric coefficient should be preferentially removed under the same operating conditions to get higher conversion enhancement.

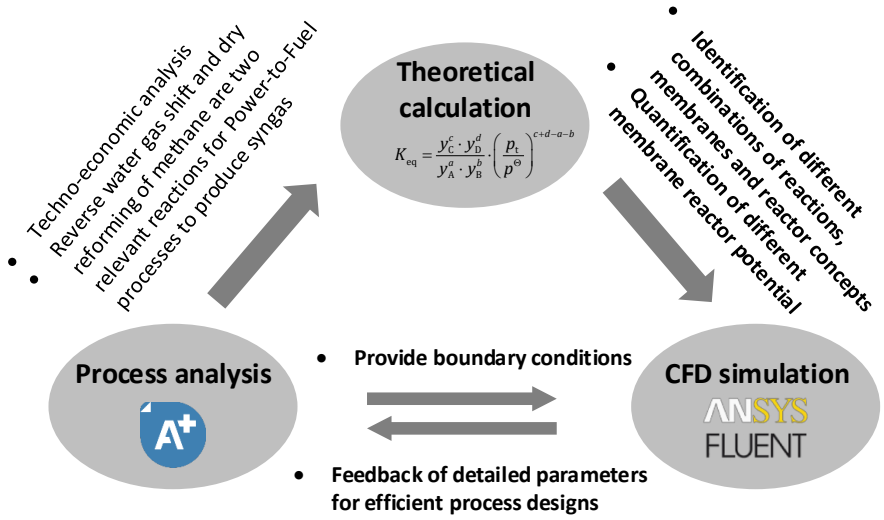

Fig. 5-6 Schematic representation of the link between chapter 5 and chapter 6.

The identified possible combinations of reactions, membranes, and reactions and their potential also provide valuable information for the designs of membrane reactor concepts for CFD simulations in the next chapter. The boundary conditions obtained by process analysis is also necessary for CFD simulations, as shown Fig. 5-6. In chapter 6, various membrane reactor concepts will be investigated based on CFD simulations with the help of the inputs from chapter 4 and 5, and the detailed design parameters of membrane reactors will be determined and can be used for guiding practical applications of membrane reactors and for helping design more efficient processes.

6 Development of membrane reactor concepts

In Chapter 5, the selection and matching of suitable membranes and reactor concepts have been discussed by qualitative analysis and quantified calculations. This chapter continues to develop membrane reactor concepts for the reverse water gas shift and dry reforming of methane based on CFD simulations.

A water permeable H-SOD zeolite membrane and a CO_2 permeable YSZ dual-phase membrane are developed for the reverse water gas shift. The water permeable membrane reactor concept is for the purpose of conversion enhancement, which is based on the concept 3 of "Shift of equilibria". The CO_2 permeable aims at capturing and converting CO_2 simultaneously based on the concept 6 of "Reactant dosing" in Fig. 3-6.

For dry reforming of methane, only an H_2 permeable Pd membrane is considered as the educts of CO_2 and CH_4 are already a mixture coming from biogas, so CO_2 permeable membranes are not applicable in this setting. A fixed-bed membrane reactor concept with an inert membrane and a catalytic membrane reactor concept without additional catalysts are developed and compared. These two membrane reactor concepts are developed on the basis of the concept 5 of "Removal of intermediates" in Fig. 3-6. The two membrane reactor concepts are characterized by different mass transport and reaction mechanisms.

The effects of various operating parameters and geometry characteristics for the above mentioned membrane reactor concepts will be comprehensively analyzed and compared using a set of indicators defined in section 3.4.

6.1 Model geometry and meshing

The generalized geometry of the membrane reactor consists of two tubes with a concentric design, as shown in Fig. 6-1. The outer tube is with radius of 25 mm while the radius of the inner tube is 7 mm, and the membrane is between the two tubes. The length of the reactor is 400 mm. All the membrane reactors share the same model geometry.

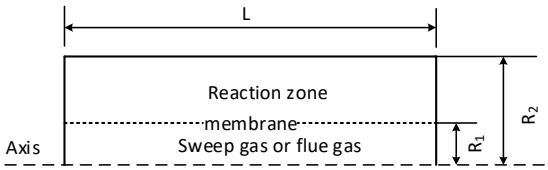

Fig. 6-1 Model geometry of the membrane reactor and the fixed-bed reactor, R_1 = 7mm, R_2 = 25 mm, and L = 400 mm. Dimensions taken from [249].

Based on the above generalized reactor geometry, the configurations of the developed membrane reactor concepts are specifically shown in Fig. 6-2. For the water permeable membrane reactor concept in Fig. 6-2 (a), the outer tube is for reacting gases of H_2 and CO_2 and the inner tube is for the sweep gas of N_2. The reacting and sweep gases are in counter-current flow to obtain a larger mean driving force for species permeation. For the CO_2 permeable membrane reactor concept in Fig. 6-2 (b), the outer tube is for pure H_2 while the inner tube is for flue gas to supply CO_2 by the membrane. The catalyst is coated on the membrane surface where the reactions take place. Another distinctive aspect of this membrane reactor concept is that the flow pattern is changed from counter-current to co-current. And no external sweep gas is needed because the H_2 itself acts as the sweep gas. The membrane reactor concepts for dry reforming of methane are shown in Fig. 6-2 (c) and (d). Both reactor concepts employ a Pd membrane for H_2 removal. The fixed-bed membrane reactor concept uses an inert membrane and the catalyst is filled in the reaction channel, and the catalytic membrane reactor concept uses a catalytic membrane with catalyst coatings on its surface. Since the membrane reactor concepts in Fig. 6-2 (a) (c) (d) are for the purpose of conversion enhancement, to calculate the relative conversion enhancement compared to conventional reactors, a fixed-bed reactor without membrane is used as the reference model for each membrane reactor concept, as shown in Fig. 6-2 (e). The volume of the fixed-bed reactor is the same as that of the membrane reactor concepts.

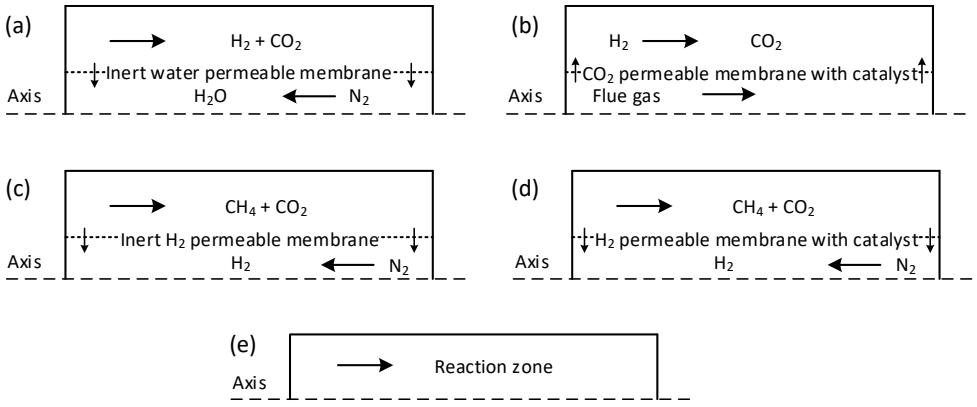

Fig. 6-2 Detailed configurations of the developed membrane reactor concepts: (a) water permeable reactor concept for reverse water gas shift; (b) CO_2 permeable reactor concept for reverse water gas shift; (c) fixed-bed membrane reactor concept for dry reforming of methane; (d) catalytic membrane reactor concept for dry reforming of methane; (e) fixed-bed reactor for reference.

The geometry is constructed with the DesignModeler in ANSYS Workbench, which is reduced from 3D cylinders to 2D rectangles through axial symmetry. This simplification is beneficial to computation time while it still captures important characteristics of the model. Then the geometry is discretized by generating meshes. The meshing is by cutting parallel edges into equal numbers of divisions. In order to account for the large gradients of heat and mass transfer within boundary layers, inflation layers are also added, so the meshes close to boundaries are denser than those in inner regions. To investigate the grid dependency, different number of meshes are generated, as shown in Fig. 6-3. H_2 flux is selected as the observed variable, as it is the lightest gas in the reaction system, so it is most sensitive to mass balance, and H_2 is the species that is to be removed by membrane and it directly influences the conversion. With the increase of meshes, the H_2 flux drops quickly and then becomes stable. A total of 23,469 cell elements are determined as a trade-off between computation effort and solution accuracy. The final meshes are displayed in Fig. 6-4. The maximum skewness is nearly zero and the quality of the meshes are thus very high.

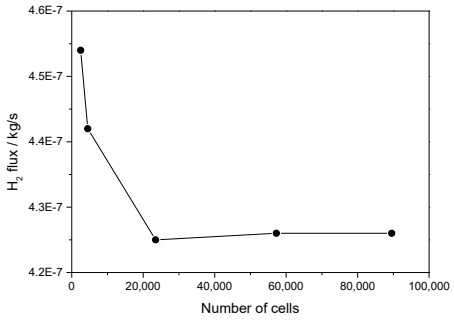

Fig. 6-3 Study of grid dependency.

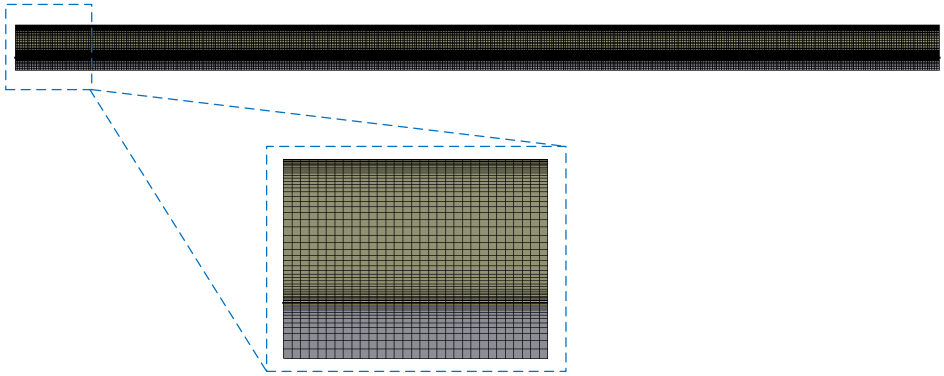

Fig. 6-4 Meshing of the membrane reactor geometry.

6.2 Setups in ANSYS Fluent

To implement CFD simulations, a number of preprocessing steps have to be done. This section introduces the physical models, setups and solution strategies in ANSYS Fluent.

6.2.1 Physical models and material properties

All the simulations are performed at steady state with pressure-based solver and the gravity is considered. The energy model is turned on to solve the energy equations. For turbulence modeling, the realizable *k*-epsilon model is chosen with the model parameters kept default. The realizable *k*-epsilon model is suitable for general turbulent flows with robust turbulence modeling capability. To model mass transport and chemical reactions, the species transport model is selected with diffusion energy source, full multicomponent diffusion, and thermal diffusion enabled. The reaction mechanism for the fixed-bed

membrane reactor concepts is “volumetric” while for the catalytic membrane reactor concepts it is “wall surface”. No turbulence-chemistry interaction is opted. A total of seven gases are involved in the reactions to be studied, including CO_2, H_2, CO, H_2O, CH_4, O_2 and N_2. These gases are extracted from the Fluent database and form a mixture package. The density of the mixture is calculated by the ideal gas method and the heat capacity by the mixing law. The thermal conductivity and viscosity are calculated by the mass-weighted mixing laws. The mass diffusivity and thermal diffusion coefficients are based on the kinetic theory. The solid material has also to be specified for the membrane and the reactor wall, but the material has no influence on simulations because the thickness is idealized to zero. Here, the default material of aluminum is used.

6.2.2 Cell zone and boundary conditions

The implementation of reaction kinetics is through the macro of DEFINE_VR_RATE or DEFINE_SR_RATE. The membrane permeation process is abstracted as a source term, which is realized by using the macro of DEFINE_SOURCE via UDFs. It should be noted species generation or disappearance is always accompanied by energy transfer. Therefore, turbulent kinetic energy, turbulent dissipation rate, energy and momentum should be calculated together. To calculate the pressure drop through catalyst beds, the porous zone option is selected. The reverse water gas shift uses a spherical Ni-based catalyst with a diameter of 6 mm and bed porosity of 0.4 [125], and the viscous and inertial resistance are calculated to be 2.34×10^7 and 5468.75 m^{-1}, respectively. The dry reforming of methane uses a [155] Rh-based catalyst with a diameter of 3.2 mm , and the resulting parameters are 8.24×10^7 and 10253.9 m^{-1}, respectively.

The boundary conditions for the water and H_2 permeable membrane reactor concepts are summarized in Table 6-1. Two H_2 to CO_2 feed molar ratios of 1:1 and 3:1 are considered for the reverse water gas shift. Note that the composition of the reactor inlet comes from process analysis by Aspen Plus, which is the stream composition after recycling rather than fresh educts. The process analysis details are given in Figure A-1 in the Appendix. The inlet velocities will be determined based on the trade-off among conversion, productivity and membrane permeation by sensitivity analysis. The highest operating temperature is limited to 250 ℃, which is constrained by the maximum allowable working temperature of current zeolite membranes. The operating pressures are elevated to 30 bar to get higher productivity and permeation fluxes.

Similar to the water permeable membrane reactor, different GHSVs of feed gas are considered by changing the inlet velocity for the H_2 permeable membrane reactor concepts.

Model composition of biogas that only consists of CH_4 and CO_2 is used, with two CO_2 to CH_4 feed molar ratios of 1:1 and 2:1 considered. The settings of inlet temperature depend on the operating temperature of the reactions. Pure N_2 is used as the sweep gas with sufficiently large inlet velocity to reduce the resistance to species permeation. The outlet conditions are kept at default values. The membrane is heat coupled for conjugate heat transfer between the two regions while the reactor wall is with a constant temperature for isothermal operation. The base case operating temperature for both membrane reactor concepts is set to 450 ℃, as a higher temperature may lead to welding problems [167]. However, a higher temperature is beneficial to this reaction and membrane permeation and 500 ℃ is possible for the Pd membrane and has been reported in the literature [166], so in the simulations, a higher temperature of 500 ℃ is also considered. The operating pressure is increased to 20 bar to reach high productivity based on the previous studies on high pressure operations [152-154]. The operating pressures at the both sides of the membranes are the same to avoid stress on membranes. For the catalytic membrane reactor concept, since the catalyst is coated on the membrane surface, the reaction option is enabled for the membrane wall.

Table 6-1 Boundary conditions for the water permeable membrane reactor simulations.

Boundary	**Location**	**Type and value**	
		Water permeable membrane reactor	**H_2 permeable membrane reactor**
Inlets	Feed gas	Velocity inlet: by sensitivity analysis Temperature: 200 ℃ Molar fraction: (H_2:CO_2=1:1): CO_2: 0.4835, H_2: 0.4835, CO: 0.033 (H_2:CO_2=3:1): CO_2: 0.23, H_2: 0.742, CO: 0.028	Velocity inlet: by sensitivity analysis Temperature: 300 ℃ Molar fraction: (CO_2:CH_4=1:1): CO_2: 0.5, CH_4: 0.5 (CO_2:CH_4=2:1): CO_2: 0.6667, CH_4: 0.3333,
	Sweep gas	Velocity inlet: 4 m/s Pure N_2	
Outlets	Feed gas	Gauge pressure: 0 bar Backflow turbulent intensity: 5% Backflow turbulent viscosity ratio: 10%	
	Sweep gas		
Walls	Membrane	Heat coupled	
	Reactor wall	Temperature: 200, 250 ℃	Temperature: 450, 500 ℃

The boundary conditions for the CO_2 permeable membrane reactor are detailed in Table 6-2. The reaction zone is fed with pure H_2 to react with permeated CO_2 and the sweep zone is fed with flue gas from a cement plant, which is relevant to Power-to-Fuel processes. The inlet velocities will be determined according to CO_2 capture rate and conversion by sensitivity analysis. To reduce thermal stress within the membrane, the inlet temperatures of H_2 and flue gas are both 500 ℃. The outlet boundary conditions are kept default. Unlike the water permeable membrane reactor, the operating temperature of the YSZ dual-phase membrane reactor can be up to 900 ℃, which is both favorable for the membrane permeation and the reaction, so the effects of operating temperature are analyzed by setting two temperatures of 800 ℃ and 900 ℃. Similar to the catalytic membrane reactor concept for the dry reforming of methane, the surface reactions are also enabled on the membrane surface for this membrane reactor.

Table 6-2 Boundary conditions for the CO_2 permeable membrane reactor simulations.

Boundary	Location	Type and value
Inlets	Feed gas	Velocity inlet: by sensitivity analysis Temperature: 500 ℃ Pure H_2
	Flue gas	Velocity inlet: by sensitivity analysis Temperature: 500 ℃ Molar fraction: CO_2: 0.178, H_2O: 0.182, N_2: 0.565, O_2: 0.075 [248]
Outlets	Feed gas	Gauge pressure: 0 bar Backflow turbulent intensity: 5% Backflow turbulent viscosity ratio: 10%
	Flue gas	
Walls	Membrane	Heat coupled, reaction enabled
	Reactor wall	Temperature: 800, 900 ℃

6.2.3 Solution strategy and convergence

To ensure better convergence, the *Coupled* instead of the default *SIMPLE* algorithm is used for pressure-velocity coupling. The discretization schemes for species and energy are both *second order upwind*, which are more accurate than the *first order upwind* scheme. The Courant number for the *Coupled* algorithm is 200 and the under-relaxation factors for species and energy are reduced from 1.0 to 0.8, which is a trade-off between convergence stability

and calculation time. The convergence criteria for continuity, energy, and species are lowered from default values to 1×10^{-5}, 1×10^{-8}, and 1×10^{-7}, and other values are kept default.

6.3 Water permeable membrane reactor concept for reverse water gas shift

Based on the established reactor geometry and numerical setups, different cases are simulated for the water membrane reactor concept that has been illustrated in Fig. 6-2 (a). In the simulations, the intrinsic kinetics of the reaction is first calculated using Eq. 3-38. and Eq. 3-39 and then the external and internal effectiveness factors are calculated using the methods introduced in section 3.2.4, and the final reaction rates are calculated by Eq. 3-37. The realization of kinetic calculations are through integrating UDFs into the main program of ANSYS Fluent.

The first step is to validate the model by comparing with literature. Then the effects of operating conditions and geometry characteristics are then analyzed.

6.3.1 Model validation with the reference fixed-bed reactor

In order to validate the models, a number of cases is simulated for the fixed-bed reactor. The observed variables are the H_2 and CO_2 conversions and reaction rates. Since there is no experimental data available under the same conditions, the data used for comparisons comes from Aspen Plus simulations and other numerical simulation results in the literature.

The CO_2 and H_2 conversions at different GHSVs and H_2 to CO_2 molar ratios are presented in Table 6-3. It can be seen that, for both cases of H_2:CO_2=1:1 and H_2:CO_2=3:1, the reaction reaches equilibrium at 270 h^{-1}. The H_2 and CO_2 equilibrium conversions calculated by Aspen Plus simulations are a little lower than those by CFD simulations. The discrepancies in equilibrium conversion between CFD simulations and Aspen Plus simulations are primarily caused by the different calculation methods employed. The equilibrium conversions by CFD simulations are determined by the equilibrium constants while the equilibrium conversions by Aspen Plus are based on Gibbs free energy minimization. Overall, the results by both simulations are close to each other and the CFD model is therefore valid.

The model is also validated from a kinetic perspective. The reaction rates are also compared in Table 6-4. The values in the table are the maximum rates in the reactor at 270 h^{-1}. The rates at H_2 to CO_2 ratios of 1:1 and 3:1 are 17.61 and 9.60 mol/(m^3 s), suggesting that the reaction rates are not fast. The reaction rates of the CO and CO_2 methanation reactions are fairly slow and can be neglected. The reaction rates by Dzuryk et al. [144] used for

comparisons were the initial rates of the reaction by numerical simulations. It is found that the reaction rates in this thesis are higher than those in the literature. The discrepancy can be explained by the following aspects: First, the pressure and temperature in the literature are 1 atm and 230 ℃, which are lower than the 30 bar and 250 ℃ used in the CFD simulations. Second, recycled educts are used in this thesis, but fresh educts are used in the literature. Also, the mass transport limitations are considered using an effectiveness factor of 0.25, but this is not considered in the simulation in the literature. Overall, the reaction rates in this thesis qualitatively agree with literature results.

Table 6-3 H_2 and CO_2 conversions of reverse water gas shift in the fixed-bed reactor at 250 ℃ and 30 bar.

GHSV / h^{-1}	**H_2:CO_2 = 1:1**		**H_2:CO_2 = 3:1**	
	H_2 conversion	**CO_2 conversion**	**H_2 conversion**	**CO_2 conversion**
90	7.4%	7.4%	13.0%	4.0%
270	7.3%	7.3%	12.3%	3.8%
900	5.2%	5.2%	6.9%	2.1%
Equilibrium conversion by Aspen Plus	6.9%	6.9%	12.2%	3.8%

Table 6-4 Reaction rates in the fixed-bed reactors at different H_2 to CO_2 ratios at 250 ℃ and 30 bar and comparisons with literature data at 230 ℃ and 1 atm.

Reaction rate / mol/(m^3 s)	**H_2:CO_2 = 1:1**		**H_2:CO_2 = 3:1**	
	This thesis	**Dzuryk et al. [143]**	**This thesis**	**Dzuryk et al. [143]**
Reverse water gas shift	17.61	11.74	9.60	8.85

6.3.2 Evaluation of the water permeable membrane reactor

After validating the reactor model, the effects of operating parameters and geometry characteristics for the membrane reactor are examined in this section. For membrane permeation modeling, as shown in Fig. 3-8, the water permeation fluxes in the adjacent cells of the membrane wall are determined according to Eq. 3-54. A moderate water permeance

of 5×10^{-7} mol/(m^2 Pa s) of the H-SOD membrane is adopted in the simulations [210]. The calculated water fluxes of the adjacent cells are stored in the user-defined memories and then read by the macro of DEFINE_SOURCE. Different cases of the water permeable membrane reactor are simulated with respect to operating temperature, H_2 to CO_2 ratio, and GHSV.

Conversion and space-time yield

As mentioned in the boundary conditions in section 6.2.2 and Table 6-1, two operating temperatures of 200 and 250 ℃ are considered for the zeolite membrane and the operating pressure is fixed at 30 bar, which is preferred for industrial operation. The analysis range of GHSV is from 90 to 900 h^{-1}, which is determined based on the trade-off of the following three aspects: first, as found in the model validation, the reaction reaches equilibrium at 270 h^{-1}, so the reaction can be performed below or beyond the reaction equilibrium point to analyze the conversion enhancement at different scenarios; second, the corresponding space time ranges from 4 to 40 s, which matches the permeation time and fluxes of the membrane; third, as conversion and productivity are the two aspects that show opposing trends with space velocity, too high or too low space velocities will lead to very low conversions or productivity, so the above range is a balanced result of the two aspects. It will be shown that, within the analyzed GHSV range, both low and high conversions and productivity can be covered to identify the operating window. The simulation results are discussed below.

Comparing the effects of H_2 to CO_2 ratio in Fig. 6-5 (a), it is seen the CO_2 conversion is always higher at the higher ratio of 3:1, no matter what the GHSV is, which can be explained by the Le Chatelier's principle. The higher H_2 molar fraction in the case of H_2:CO_2=3:1 shifts the chemical equilibrium to the product side and the higher CO_2 conversions are at the expense of lower H_2 conversions. As a result, the H_2 conversions in the case of H_2:CO_2=3:1 are lower than those in the case of in the case of H_2:CO_2=1:1. Looking at the effects of GHSV at both ratios, the CO_2 conversion decreases significantly when the GHSV is increased from 90 to 900 h^{-1}, as the permeation time is reduced from 40 to 4 s, leading to much less water removed.

The conversion enhancement compared to the fixed-bed reactor is also calculated according to Eq. 3-61 and the corresponding conversions in the fixed-bed reactor have been presented in Table 6-3. The results are displayed in Fig. 6-5 (b). Although CO_2 conversions are higher at the H_2 to CO_2 ratio of 3:1, the corresponding conversion enhancement is lower, so the stoichiometric feed is better at the point of conversion enhancement. For the considered GHSVs, only at 90 h^{-1} the conversion enhancement satisfies the “effective enhancement”

threshold of 20%, and it is largely reduced at 270 h^{-1} and nearly vanished at 900 h^{-1}, suggesting that the conversion enhancement is very sensitive to the space velocity.

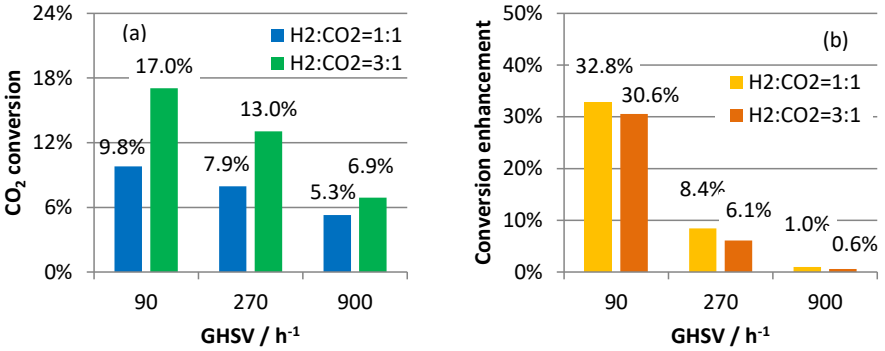

Fig. 6-5 (a) CO_2 conversion and (b) conversion enhancement of the membrane reactor at 250 ℃ and 30 bar.

The conversion and enhancement at a lower temperature of 200 ℃ are also calculated to investigate the impacts of temperature, shown in Fig. 6-6**.** The CO_2 conversions at the reduced temperature are much lower and the enhancement is all below 20%. A lower temperature is bad for the reaction and membrane, so in the following only the cases at 250 ℃ will be discussed.

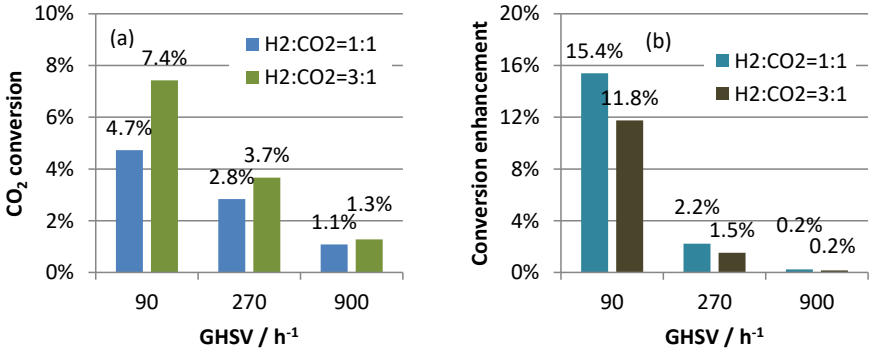

Fig. 6-6 (a) CO_2 conversion and (b) conversion enhancement of the membrane reactor at 200 ℃ and 30 bar.

Moreover, the space-time yield of CO STY and the enhancement by using the membrane reactor are shown in Table 6-5. A first finding is that the CO STY increases with GHSV as the throughput of the reactor is larger. The CO STY with H_2 to CO_2 of 1:1 ratio is higher, which is different from the trend of the CO_2 conversions. This is because the reaction rates at higher H_2 to CO_2 ratios are slower, caused by the lower reaction order with respect to H_2. It is also seen that only at 90 h^{-1} can the STY enhancement be higher than 20%. But according to the suggested operating window of 1.0 - 10 mol/(m^3 s) by Graaf et al. [244], the CO STY at 90 h^{-1} is below 1.0 mol/(m^3 s). As found in the model validation with the fixed-bed reactor, the reaction reaches equilibrium at 270 h^{-1}, in order to achieve satisfactory conversion enhancement, the space velocity should be lowered and the reaction has to be operated below the equilibrium point. This means the STY is to be sacrificed to obtain higher conversion enhancement. All these findings indicate that the limiting factor to the conversion enhancement is the membrane permeation flux instead of the reaction kinetics. Although reducing the GHSV can further increase the conversion enhancement, the productivity will be sacrificed correspondingly, which has to be considered as well. In the following sections, it will be shown how the conversion can be increased by modifying the geometry characteristics rather than by purely changing the operating conditions.

Table 6-5 CO STY and its enhancement of the membrane reactor at 250 ℃ and 30 bar.

GHSV / h^{-1}	**CO STY / mol/(m^3 s)**		**CO STY enhancement**	
	H_2:CO_2 = 1:1	**H_2:CO_2 = 3:1**	**H_2:CO_2 = 1:1**	**H_2:CO_2 = 3:1**
90	0.90	0.75	32.8%	30.5%
270	2.20	1.72	8.4%	6.1%
900	4.88	3.03	1.0%	0.6%

Water distribution and permeation flux

The CO_2 conversion and CO STY are directly related to the water permeation, so a detailed analysis of the water fraction and flux is required and can provide deeper insights for the membrane reactor design. The distribution of molar fraction of water in the membrane reactor for H_2 to CO_2 = 1:1 are shown in Fig. 6-7. In all cases, there exists a boundary layer neighboring the membrane, which is known as concentration polarization. Although the concentration gradients can trick natural convection, molecular diffusion remains the dominant mass transport mechanism in the radial direction. The formation of

boundary must be minimized, otherwise the membrane potential cannot be fully utilized. At the low GHSV of 90 h^{-1}, the thickness of the boundary layer is the largest as more water is permeated, and at the high GHSV of 900 h^{-1}, it becomes very thin, but the water removal is very limited. So there exists a contradiction between the formation of boundary layer and permeation time. There are some approaches to reconcile this contradiction. One approach is increasing the turbulence within the reactor by placing spacers and a second approach is to employ a fluidized bed membrane reactor that may offer better mass transport performance. The water distribution for H_2 to CO_2 = 3:1 is similar and is not repeated.

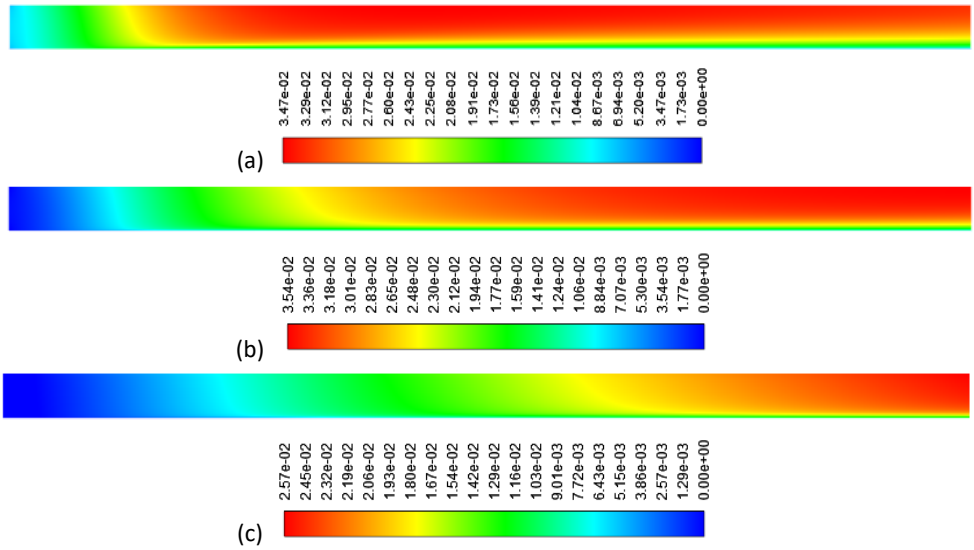

Fig. 6-7 Contours of water molar fraction: (a) 90 h^{-1}; (b) 270 h^{-1}; and (c) 900 h^{-1}. Only the results of reaction channel are shown, the flow direction of the reactants is from left to right, and the lower surface of each figure is the membrane.

The water permeation flux along the membrane surface is quantified in the Fig. 6-8. Overall, the water fluxes at various GHSVs show different trends. For H_2:CO_2 = 1:1 in the left figure, the water flux at 90 h^{-1} first increases very fast at the reactor inlet. After experiencing a maximum value, it decreases towards the rear end of the reactor, as the flow pattern of the reacting gases and the sweep gas is counter-current and the water partial pressures at the rear end of the feed side are low. At 270 h^{-1}, the water flux also increases at first but remains stable afterwards. The water production rate is higher and the concentration polarization is less significant at 900 h^{-1}, so the water flux always increases along the membrane surface. For H_2:CO_2 = 3:1 in the right figure, the water fluxes at 90 and 900 h^{-1} show similar trends to those at H_2:CO_2 = 1:1 at the same GHSVs, but at 270 h^{-1}, the water flux still increases along

the membrane surface. According to the permeation equation in Eq. 3-54, the water flux is a function of the partial pressure difference of water between the both sides of the membrane. Since the sweep gas is at a sufficiently high velocity, the resistance at the sweep side is nearly zero and therefore the partial pressure difference of water is approximately equal to the partial pressure at the feed side. So, increasing the water partial pressure on the feed side is the way to boost the water fluxes rather than by increasing the sweep gas velocity. It can be also inferred that the partial pressure or concentration of water on the membrane surface show the identical trends to the water fluxes.

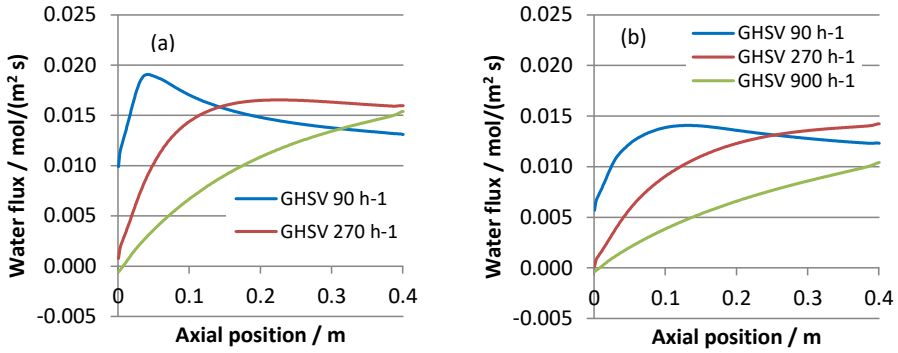

Fig. 6-8 Water flux along the membrane surface: (a) H_2:CO_2=1:1; and (b) H_2:CO_2=3:1.

The average water fluxes along the membrane and water removal rates are also calculated and provided in Table 6-6. The permeation fluxes of water are on the order of 10^{-2} mol/(m^2 s), which are below their theoretically maximum values. The average water flux at both H_2 to CO_2 ratios decrease with GHSV, and the average water fluxes at H_2:CO_2 = 1:1 are higher than those at H_2:CO_2 = 3:1, because the water production rates of the former are faster. The water removal rate also decreases with GHSV and the water removal at both feed ratios is very close.

Table 6-6 Average water flux and water removal.

GHSV / h^{-1}	Average water flux / mol/(m^2 s)		Water removal rate	
	H_2:CO_2=1:1	H_2:CO_2=3:1	H_2:CO_2=1:1	H_2:CO_2=3:1
90	0.0151	0.0128	40.7%	41.5%
270	0.0144	0.0108	16.0%	15.3%
900	0.00975	0.0061	4.9%	4.9%

Effect of the reactor geometry characteristic

As found above, increasing the CO_2 conversion by reducing the GHSVs is at the expense of reduced space-time yield of CO. The main reason is caused by the concentration gradients that cause much-reduced water fluxes, leading to reactor space not sufficiently utilized. In this section, the effects of the area to volume ratio *A/V* will be studied. The major benefit of doing this is that the conversion enhancement can be much raised and the productivity can be maintained.

Neglecting the thickness of the membrane, the *A/V* is mathematically expressed as $A/V = 2r_1/\left(r_2^2 - r_1^2\right)$, where r_1 and r_2 are the radius of the reactor geometry**.** The *A/V* has an important feature that it only contains radius and is irrelevant to the reactor's length. It can be changed by adjusting r_1 or r_2 or both. Here, changing the *A/V* is realized by reducing the dimension of r_2 in Fig. 6-1 from 25 to 15 mm so that the membrane area is not changed but the reactor volume is reduced, and the resulting *A/V* is increased from 24.3 to 79.5.

The CO_2 conversion, CO STY, and their enhancement with the higher *A/V* are presented in Fig. 6-9 and Table 6-7, which are obtained under the identical operating conditions to the base cases above. It can be seen that the CO_2 conversion and the corresponding conversion enhancement are significantly improved in comparison with the original *A/V* of 24.3. Another benefit of increasing the *A/V* is that it can also increase the CO STY at the same time, regardless of the smaller reactor volume, which is a result of more efficiently utilized reactor space. Notably, the conversion enhancement of both cases is more than three times compared to that with original *A/V* of 24.3 and the CO STY is increased to higher than 1.0 mol/(m^3 s), which falls into the suggested operating window of 1.0 - 10 mol/(m^3 s) by Graaf et al. [250]. The primary reason for these benefits is that the design of the membrane reactor is more compact and the concentration gradients of water are significantly reduced. All these findings indicate that increasing the *A/V* is a very effective way to improve the conversions of the membrane reactor but maintain high productivity. So it should be emphasized that the geometry design of membrane reactors is also an important aspect to achieve better performance.

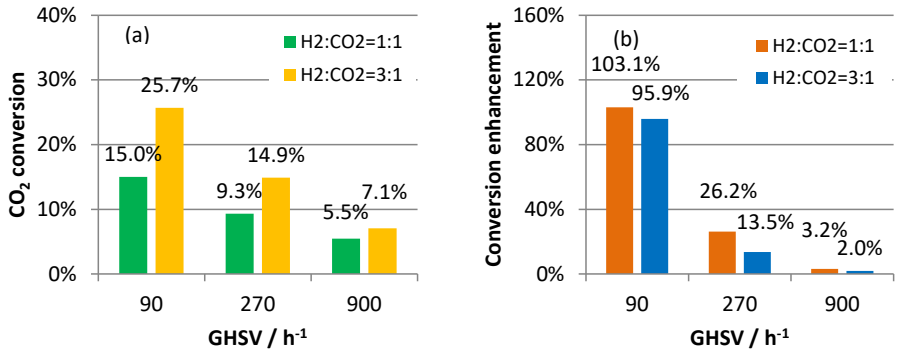

Fig. 6-9 (a) CO_2 conversion; and (b) conversion enhancement with *A/V* = 79.5, 250 ℃, and 30 bar.

Table 6-7 CO STY and its enhancement of the membrane reactor with *A/V* = 79.5, 250 ℃, and 30 bar.

GHSV / h^{-1}	CO STY / mol/(m^3 s)		CO STY enhancement	
	H_2:CO_2 = 1:1	H_2:CO_2 = 3:1	H_2:CO_2 = 1:1	H_2:CO_2 = 3:1
90	1.39	1.13	103.0%	95.7%
270	2.58	1.96	26.8%	20.1%
900	5.04	3.11	3.2%	2.0%

To avoid overlapping analysis, the water distribution contours and water flux along the membrane surface are not discussed again and only the average water fluxes and water removal rates are shown in Table 6-8. Comparing the water fluxes with the results with the original *A/V*, it can be seen that although the average water fluxes of the membrane with the larger *A/V* are lower due to the consequence of more water permeated, its water removal performance is nearly doubled compared to the base cases. As the radius of the reactor is reduced, the mass transport distance from the bulk stream to the membrane surface becomes shorter, so the generated water can be removed in time.

Table 6-8 Average water flux and water removal with *A/V*=79.5.

GHSV / h^{-1}	Average water flux / mol/(m^2 s)		Water removal rate	
	H_2:CO_2 = 1:1	H_2:CO_2 = 3:1	H_2:CO_2 = 1:1	H_2:CO_2 = 3:1
90	0.0133	0.0111	76.3%	78.1%
270	0.0137	0.0106	42.2%	43.0%
900	0.0092	0.0060	14.6%	15.3%

6.4 CO_2 permeable membrane reactor concept for reverse water gas shift

This section analyzes the results for the CO_2 permeable membrane reactor concept for the reverse water gas shift. As introduced in Fig. 6-2 (b), the membrane reactor concept is developed for integrated CO_2 capture and conversion, which uses a YSZ ceramic-carbonate dual-phase membrane. The kinetics for this membrane reactor concept is also based on Eq. 3-38 and Eq. 3-39. The permeation fluxes of the YSZ membrane is calculated by Eq. 3-55. The results in this section have been published in the publication: “CFD modeling of a membrane reactor concept for integrated CO2 capture and conversion” in the journal of Reaction Chemistry & Engineering. DOI: 10.1039/d2re00282e.

6.4.1 Conversion and space-time yield

The boundary conditions have been detailed in section 6.2.2 and Table 6-2. One different point is that the analyzed range of GHSV is from 360 to 900 h^{-1}, which is determined based on the capture rates of CO_2. It will be shown, at the lowest space velocity of 360 h^{-1}, the CO_2 capture rates can be over 90%, so further lowering the space velocity is not necessary.

The CO_2 and H_2 conversions at 900 ℃ are first analyzed and presented in Fig. 6-10**.** In the left figure, the CO_2 conversions are very high in all cases simulated. This is not only because of the high reaction temperature. The equilibrium conversion of CO_2 at 900 ℃ with stoichimetric feed is only 52.9%. So the excess amount of H_2 also leads to its high conversions. In other words, the high CO_2 conversions are partly at the expense of the H_2 conversions, as indicated by the low H_2 conversions in the right figure. Reducing the flow rates of H_2 or recycling the unreacted H_2 can increase the H_2 conversions. In the left figure, it is also found that the CO_2 conversions are mainly affected by the H_2 flow rates rather than the flue gas flow rates. Although more H_2 input can shift the chemical equilibrium and increase the CO_2

conversions, in this memebrane reactor concept, H_2, in fact, also acts as the sweep gas in addition to as a reactant, so more CO_2 is taken away from the reactor without being reacted at higher H_2 flow rates, leading to the lower CO_2 conversions.

The CO_2 conversions at 800 ℃ are slightly lower than those at 900 ℃ but are still very high, as shown in Fig. 6-11. The H_2 conversions are even lower. A higher temperature is both beneficial to the reaction conversion and CO_2 permeation, so the following analyses only concern the results at 900 ℃.

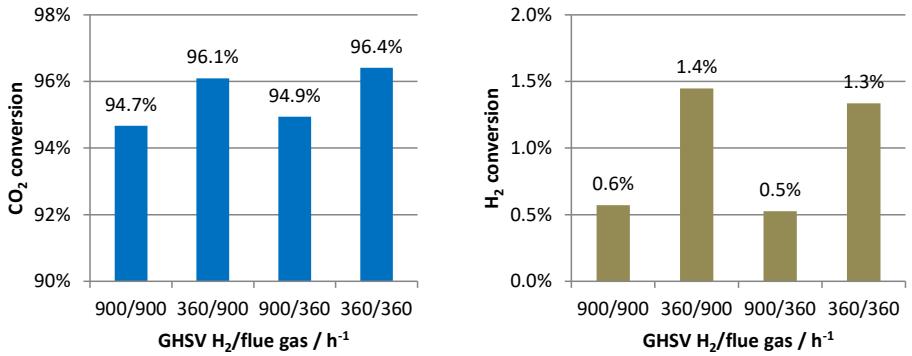

Fig. 6-10 CO_2 and H_2 conversions of the CO_2 permeable membrane reactor at 900 ℃ and 30 bar.

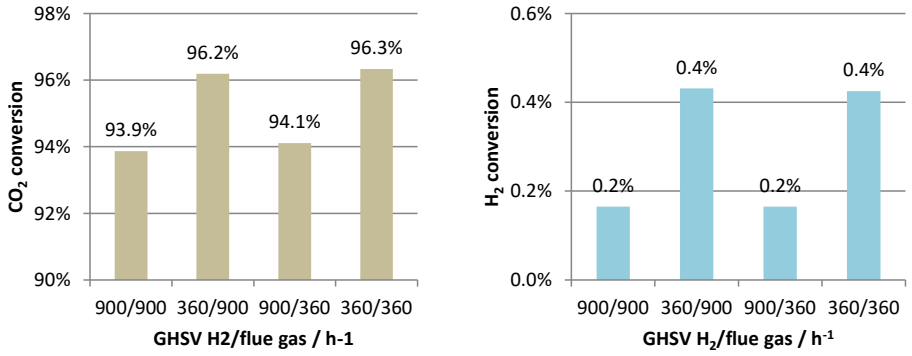

Fig. 6-11 CO_2 and H_2 conversions of the CO_2 permeable membrane reactor at 800 ℃ and 30 bar.

The calculation results of the CO STY are provided in Table 6-9**.** Comparing the water permeable and the CO_2 permeable membrane reactor concepts, although the CO_2 conversions of the CO_2 permeable membrane reactor concept are around three times that of the maximum conversion of 32.8% of the water permeable membrane reactor in Fig. 6-5, the CO STY of all cases remains stable and is only around one eighth that of the maximum CO STY in Table 6-5. As the CO_2 conversions of all the cases approach to completion, the CO STY is determined by the amount of permeated CO_2. At the low flue gas flow rate, the CO_2 permeation flux is lower due to the lowered CO_2 concentration in the flue gas.

As one of the purposes of this membrane reactor concept is to capture CO_2 from industrial sources for *in-situ* conversion, another important aspect is the percentage of CO_2 captured by membrane permeation. As shown in Table 6-9. The captured CO_2 is inversely proportional to the GHSV of flue gas. At the high flue gas GHSVs, nearly 40% CO_2 can be captured through the membrane permeation. When the GHSV is reduced to 360 h^{-1}, the CO_2 capture is raised to more than 90%, suggesting that this membrane reactor concept has the potential of efficient CO_2 capture.

In contrast to the linear relationship between the water flux and the partial pressure difference of water of the water permeable membrane, the CO_2 flux, according to the flux equation of Eq. 3-55, is a logarithmic function of the CO_2 partial pressure ratio between the both sides of the membrane, so the CO_2 fluxes are not sensitive to the partial pressure of CO_2. This permeation characteristic enables the possibility of high CO_2 capture from sources even with very low CO_2 concentration using this kind of membrane reactor concept.

Table 6-9 CO STY and CO_2 capture of the CO_2 permeable membrane reactor at 900 °C and 30 bar.

H_2/flue gas / h^{-1}	**CO STY / mol(m^3 s)**	**CO_2 capture rate**
900/900	0.665	39.7%
360/900	0.674	39.7%
900/360	0.608	90.6%
360/360	0.615	90.1%

6.4.2 CO_2 distribution and permeation flux

The distribution of CO_2 molar fraction is shown in Fig. 6-12**.** Here only the cases with different flow rates of flue gas are presented because the H_2 flow rate has little influence on the CO_2 distribution. From the both contours, the area with low CO_2 molar fraction at 360 h^{-1} is larger than that at 900 h^{-1}, as indicated by the blue colors, and most CO_2 is removed. There are no clear boundary layers observed in both contours, as the radius of the flue gas channel is only 7 mm, which is small enough to avoid obvious concentration polarization.

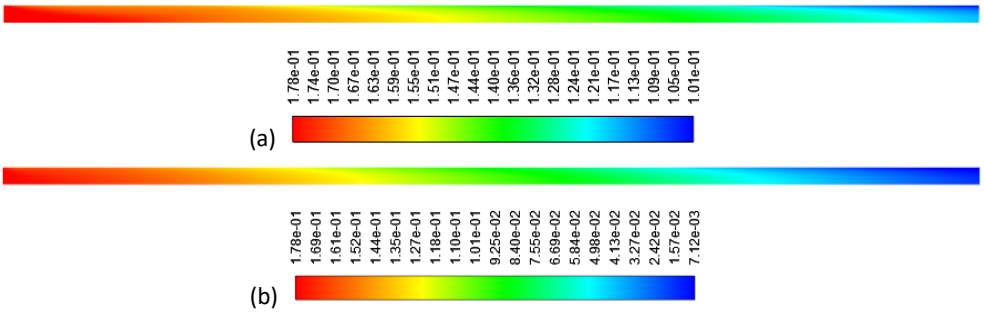

Fig. 6-12 Contours of CO_2 molar fraction of the flue gas: (a) H_2/flue gas=900/900; (b) H_2/flue gas=900/360. The flow direction of flue gas is from left to right.

The CO_2 fluxes along the membrane surface are shown in Fig. 6-13**.** Again, only the fluxes at flue gas GHSVs of 900 and 360 h^{-1} are presented in the figure, and the average CO_2 fluxes are given in Table 6-10. The CO_2 fluxes both increase along the membrane surface in the front end section of the reactor and the two lines are overlapped. After a critical point, the trends of the two lines go differently. The blue line at 900 h^{-1} continues to increase slightly and remains stable for some distance, and it then gradually decreases in the rear end of the reactor. But the yellow line decreases drastically after reaching a maximum point. An overlapping regime and a divergent one are differentiated. In the overlapping regime, the CO_2 fluxes are controlled by the inlet temperature. The inlet temperature of flue gas is lower than the reactor wall temperature and has to be heated by the wall, so the CO_2 fluxes increase in the beginning. This regime corresponds to the areas in red in the above contours. As ever more CO_2 is permeated, the limiting factor becomes the CO_2 concentration in the divergent regime. When the flow rate of flue gas is low, the CO_2 supply is less and its concentration drops very fast. The divergent region corresponds to the areas in blue in the above contours.

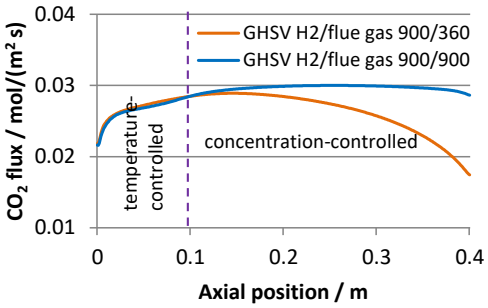

Fig. 6-13 CO_2 fluxes along the membrane surface at different GHSVs of flue gas.

Table 6-10 surface-averaged CO_2 flux at 900 ℃ and 30 bar.

GHSV H_2/flue gas / h^{-1}	**900/900**	**360/900**	**900/360**	**360/360**
CO_2 flux mol/(m^2 s)	0.0289	0.0289	0.0264	0.0262

6.4.3 Effect of the geometry characteristic

The Effects of the geometry characteristic are also investigated by increasing the *A/V* to the value of 79.5. The CO_2 and H_2 conversions are shown in Fig. 6-14**.** Comparing the CO_2 conversions with those in Fig. 6-10, no large difference is observed because the amount of permeated CO_2 is nearly unchanged. But different from the results in Fig. 6-10, the results suggest that the CO_2 conversions are lower at the lower H_2 flow rates. Higher H_2 flow rates shift the reaction equilibrium and increase the CO_2 conversions, although higher H_2 space velocities will take more CO_2 away from the reactor without being reacted. The H_2 conversions are much increased because the H_2 input is less.

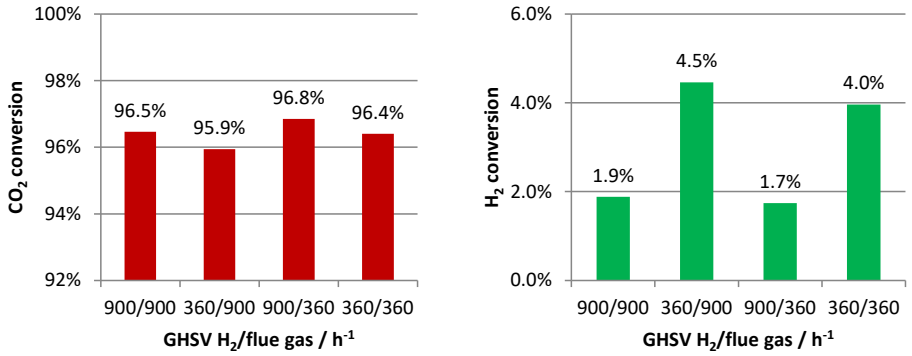

Fig. 6-14 CO_2 and H_2 conversions of the CO_2 permeable membrane reactor at 900 ℃ and 30 bar with *A/V* = 79.5.

The CO STY and CO_2 capture rates are presented in Table 6-11. Compared to the original geometry in Table 6-9, the CO STY with the increased *A/V* is more than tripled as a result of smaller reactor volume, and the design of the reactor is more compact. Overall, the CO_2 capture rates in the table are lower than those with the original geometry. At each H_2 GHSV, the CO_2 capture is slightly decreased because H_2 itself is also the sweep gas and the CO_2 permeation resistance is stronger at a low H_2 sweep velocity.

Table 6-11 CO STY and CO_2 capture of the CO_2 permeable membrane reactor at 900 ℃ and 30 bar with *A/V* = 79.5.

H_2/flue gas / h^{-1}	CO STY / mol(m^3 s)	CO_2 capture rate
900/900	2.20	39.4%
360/900	2.03	36.5%
900/360	2.01	89.8%
360/360	1.87	84.0%

The surface-averaged CO_2 permeation fluxes are calculated and provided in Table 6-12, The values in the table are a little decreased compared to those with the original *A/V* in Table 6-10, as the H_2 input is less and the permeation resistance of CO_2 is increased. In summary, changing the *A/V* can increase the CO STY but cannot improve CO_2 capture rates and conversions for this membrane reactor concept.

Table 6-12 Surface-averaged CO_2 flux at 900 ℃ and 30 bar with *A/V* = 79.5.

GHSV H_2/flue gas / h^{-1}	**900/900**	**360/900**	**900/360**	**360/360**
CO_2 flux mol/(m^2 s)	0.0287	0.0266	0.0261	0.0244

6.5 H_2 permeable membrane reactor concepts for dry reforming of methane

This section compares the performance of the fixed-bed and catalytic membrane reactor concepts in Fig. 6-2 (c) and (d) for the dry reforming of methane. The difference between the fixed-bed membrane reactor and the catalytic membrane reactor lie in the different reaction and mass transport mechanisms, which will be analyzed in detail below. The kinetics of both membrane reactor concepts are calculated based on the rate equations from Eq. 3-40 to Eq. 3-47. The permeation fluxes of H_2 are calculated by Eq. 3-56. The models are first validated and their advantages and disadvantages of each reactor concept are then comprehensively discussed and compared.

6.5.1 Model validation

The models are validated with a fixed-bed reactor from the perspectives of CO_2 and CH_4 equilibrium conversions, as shown in Table 6-13**.** The conversions are obtained by CFD simulations at 450 ℃ and 20 bar with CO_2:CH_4 = 1:1 at various GHSVs. As no experimental data under the same conditions is available for comparisons, the conversions are compared with those by Aspen Plus simulations. Under the same conditions, the CO_2 and CH_4 equilibrium conversions by Aspen Plus simulations are 4.8% and 2.1%, respectively. From the results by CFD simulations, the reaction reaches equilibrium at 270 h^{-1}, at which the conversions are close to those by Aspen Plus simulations. The models can also be validated from a mass transport perspective. A finding by Richardson et al. [155] was that the external mass transport limitations were negligible and the internal effectiveness factor was 0.3 or higher. In this thesis, the external and internal effectiveness factors are calculated to be 0.96 and 0.3, respectively, which are in good agreement with the literature data.

Table 6-13 Comparison of conversions of the dry reforming of methane at 450 ℃ and 20 bar with CO_2:CH_4 = 1:1.

GHSV / h^{-1}	CFD simulation	
	CH_4 conversion	CO_2 conversion
90	4.66%	2.04%
270	4.69%	2.05%
900	4.34%	1.96%

6.5.2 Base case comparison

As mentioned in the boundary conditions in section 6.2.2 and Table 6-1, the operating temperature for the base cases is set to 450 ℃ and the operating pressure in the simulations is fixed at 20 bar. Similar to the water permeable membrane, the analyzed GHSV here also ranges from 90 to 900 h^{-1}. The simulation results are analyzed below.

The CO_2 and CH_4 conversions of the two membrane reactor concepts and the fixed-bed reactor at 450 ℃ and 20 bar with CO_2:CH_4 = 1:1 are shown in Fig. 6-15. The CO_2 and CH_4 conversions of the fixed-bed rector are the same at 90 and 270 h^{-1}, indicating that the reactions have reached equilibrium at 270 h^{-1}. A first finding from the figure is that the CO_2 conversion is always higher than that of CH_4, no matter what the reactor concept is due to the existence of the side reaction of reverse water gas shift, and additional CO_2 is consumed by H_2. For the fixed-bed membrane reactor concept, the CO_2 and CH_4 conversions are both higher than those of the fixed-bed reactor at each GHSV. This is in accordance with the results by Lee et al. that the CO_2 and CH_4 were both increased by removing H_2 [169]. It is easy to explain that the increase of CH_4 conversion is contributed by the shift of the equilibrium of the main reaction. The increase of CO_2 conversion is a result of reaction competition: on the one hand, removing H_2 shifts the equilibrium of the main reaction of dry reforming of methane, but on the other hand, the side reaction is suppressed. So, the overall CO_2 conversions are increased but much more limited than those of CH_4. This also suggests that removing H_2 has a stronger impact on the dry reforming of methane than on the reverse water gas shift because the H_2 stoichiometric coefficient of the main reaction is two while that of the side reaction is only one, which is strong evidence supporting the conclusion made in Chapter 5.

The CO_2 and CH_4 conversions of the catalytic membrane reactor concept decrease much faster with GHSV than the fixed-bed membrane reactor. Only at 90 h^{-1} can the CH_4 conversion be higher compared to the fixed-bed reactor. At the higher GHSVs, the conversions are even lower than equilibrium conversions. This can be explained from the perspectives of reaction and mass transport mechanisms. The reactants and the reactions are located in different places, so the reactants have to be transported to the membrane surface before the reactions take place. The diffusion of reactants is slow and the conversions are very sensitive to GHSV.

In terms of the conversion enhancement, the CO_2 conversion enhancement of the fixed-bed membrane reactor concept is positive, but that of the catalytic membrane reactor concept is negative. The CH_4 conversion enhancement of the fixed-bed membrane reactor concept is higher than the CO_2 conversion enhancement. In the catalytic membrane reactor, the CH_4 conversion enhancement is only positive at 90 h^{-1}, and becomes negative at the higher GHSVs. Although the internal mass transport limitations by catalyst of the catalytic membrane reactor concept is negligible compared to the fixed-bed membrane reactor concept, its external mass transport limitations are much stronger. Such external limitations lead to the formation of concentration polarization of reactants and the deficit of reactants surrounding the membrane makes the conversions lower.

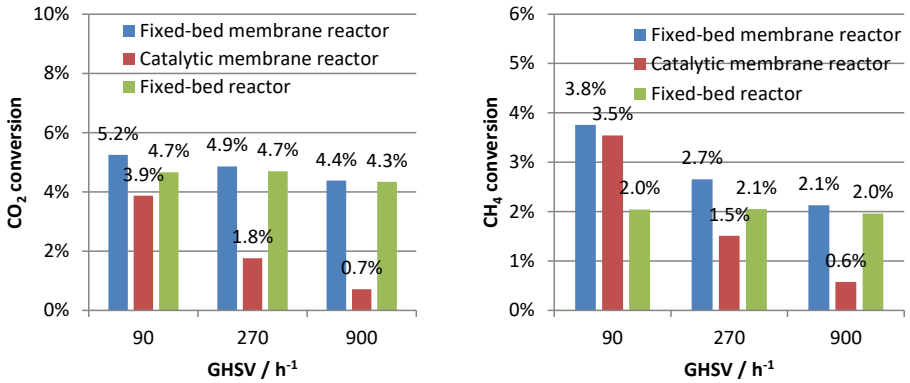

Fig. 6-15 CO_2 and CH_4 conversions of the base cases at 450 °C and 20 bar with CO_2:CH_4 = 1:1.

The CO STY of the fixed-bed membrane reactor is also higher than that both of the catalytic membrane reactor and the fixed-bed reactor at all GHSVs, shown in Table 6-14. The gain in STY is not only contributed by the shift of equilibrium but also by the elevation of the reaction rates. For the fixed-bed reactor, the simulation results show that the reaction rate of

the side reaction is even higher than that of the main reaction, but in the fixed-bed membrane reactor concept, the reaction rate of the main reaction becomes faster due to H_2 removal and the side reaction of reverse water gas shift is much suppressed. The CO STY of the catalytic membrane reactor concept can be only higher than that of the fixed-bed reactor at 90 h^{-1}. The H_2 STY remains higher until 270 h^{-1} but becomes lower at 900 h^{-1}.

Table 6-14 STY of CO and H_2 of base cases at 450 °C and 20 bar with CO_2:CH_4 = 1:1.

GHSV / h^{-1}	Fixed-bed membrane reactor STY / mol/(m^3 s)		Catalytic membrane reactor STY / mol/(m^3 s)		Fixed-bed reactor STY / mol/(m^3 s)	
	CO	H_2	CO	H_2	CO	H_2
90	0.47	0.32	0.39	0.36	0.35	0.08
270	1.18	0.49	0.51	0.44	1.06	0.23
900	3.41	1.06	0.67	0.54	3.31	0.82

From the conversions and STY, the performance of the catalytic membrane reactor concept is even worse than the fixed-bed reactor. A niche of the catalytic membrane reactor concept comes from H_2/CO ratio. The H_2/CO ratios of the fixed-bed reactor concept drop from 0.67 to 0.31 with the increase of GHSV while those of the catalytic membrane reactor concept only from 0.92 to 0.80, as shown in Table 6-15. The H_2/CO enhancement of the catalytic membrane reactor concept is still higher than 200% at 900 h^{-1} but nearly vanishes for the fixed-bed membrane reactor concept. The ability of maintaining high H_2/CO ratios is a unique advantage of the catalytic membrane reactor concept, as it realizes *in-situ* H_2 removal in the true sense. As a result, the H_2 fluxes of the catalytic membrane reactor concept are always higher than those of the fixed-bed membrane reactor concept, and the gaps between them become ever larger with increased GHSV.

The H_2 removal in the catalytic membrane reactor concept is from 92.7% to 76.2% while in the fixed-bed membrane reactor concept it drops quickly from 82.4% to 27.7%. The synchronization between H_2/CO ratio and H_2 removal reveals their direct relationship. Another implicit benefit of H_2 removal is that the selectivities of the reactions are raised. However, removing H_2 from the reaction systems may bring about more severe carbon deposition by methane cracking. According to a study by Kahle et al. [154], H_2 exhibits stronger ability of inhibiting carbon deposition than steam.

Table 6-15 H_2/CO, H_2 removal, and flux of the base cases at 450 °C and 20 bar with CO_2:CH_4 = 1:1.

GHSV / h^{-1}	Fixed-bed membrane reactor			Catalytic membrane reactor			Fixed-bed reactor
	H_2/CO ratio	H_2 removal	H_2 flux / mol/(m^2 s)	H_2/CO ratio	H_2 removal	H_2 flux / mol/(m^2 s)	H_2/CO ratio
90	0.67	82.4%	0.0108	0.92	92.7%	0.0136	0.22
270	0.42	58.5%	0.0118	0.86	84.1%	0.0152	0.22
900	0.31	27.7%	0.0121	0.80	76.2%	0.0168	0.25

6.5.3 Effect of feed ratio and temperature

In order to achieve higher CH_4 utilization, excess CO_2 is fed to the reactor. Overall, the effects of feed ratio and temperature show very similar results to the base cases. The conversions are shown in Fig. 6-16 and the results of STY, H_2/CO ratio, and H_2 removal are provided in Table A-3 and Table A-4 in the Appendix. For the both membrane reactor concepts, decreasing the CH_4:CO_2 molar ratio from 1:1 to 1:2 increases the CH_4 conversion but decreases the CO_2 conversion. Yet the corresponding conversion enhancement of CO_2 and CH_4 is comparable with that of the base cases, suggesting that the contribution of the membrane remains constant. Also, the changes of STY of CO and H_2 are not obvious. A potential benefit of excess CO_2 is that the carbon deposition may be alleviated by the reduction of CO_2. However, the H_2/CO ratios are decreased because more H_2 is consumed by CO_2 through reverse water gas shift, but this should be attributed to the reactions themselves instead of the membrane, as the membrane permeation nearly does not change with the feed condition, as is reflected by the similar H_2 removal and fluxes to the base cases.

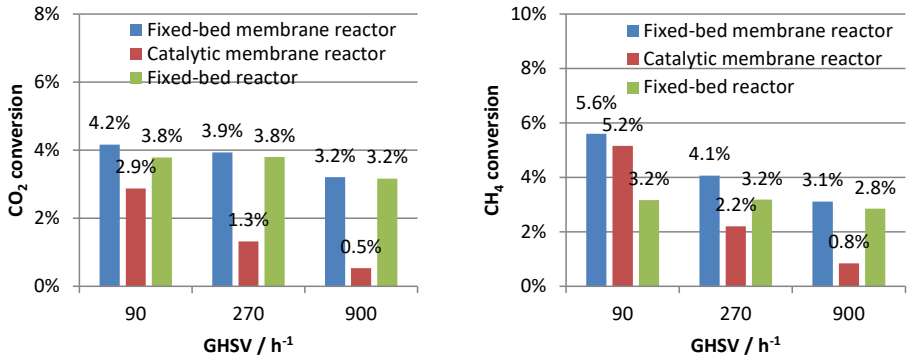

Fig. 6-16 CO_2 and CH_4 conversions at 450 °C and 20 bar with CH_4:CO_2 = 1:2.

Increasing the operating temperature to 500 °C is beneficial to both CH_4 and CO_2 conversions. From the thermodynamic point of view, increasing temperature is a good approach to suppress carbon deposition, but the operating temperature is limited by the Pd membrane, and other H_2 permeable membranes such as dual-phase membranes that can work at high temperatures can be considered. The membrane permeation at the higher temperature is also enhanced that leads to higher conversions. The results of STY, H_2/CO ratio, and H_2 flux at 500 °C are provided in Table A-5 and Table A-6 in the Appendix. As expected, the faster reaction rates at the higher operating temperature make the CO and H_2 STY higher. In addition, the H_2 fluxes are much increased by raising the temperature. Compared to changing the feed ratio, increasing the operating temperature is more effective to the conversion, productivity, and membrane permeation.

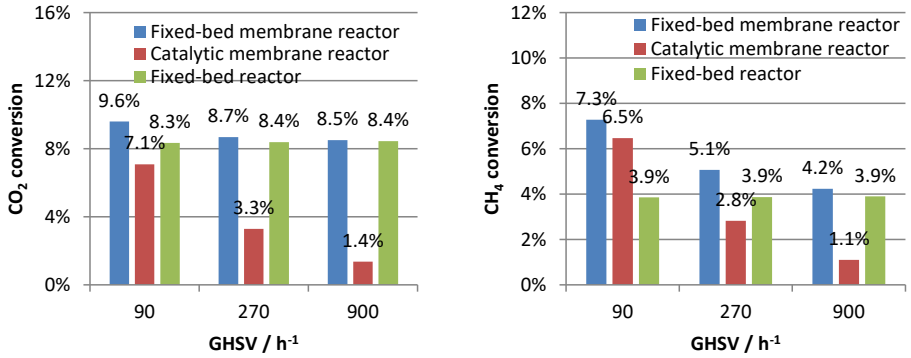

Fig. 6-17 CO_2 and CH_4 conversions at 500 °C and 20 bar with CO_2:CH_4 = 1:1.

6.5.4 Effect of pressure and geometry characteristic

According to the conclusion by Lee et al. [169], the operating pressure 5 bar is a balanced result between conversion and membrane permeation to get higher conversions but maintain efficient H_2 removal. The effects of operating pressure on the CO_2 and CH_4 conversions are shown in Fig. 6-18. As expected, reducing the pressure increases both the CO_2 and CH_4 conversions. Reducing the pressure does not change the equilibrium of the side reaction but shifts that of the main reaction. Comparing the performance of the both membrane reactor concepts, the CO_2 and CH_4 conversions of the catalytic membrane reactor concept at 90 h^{-1} are even higher than those of the fixed-bed membrane reactor concept. These results suggest that reducing the pressure has stronger impacts on the conversions of the catalytic membrane reactor concept.

The results of STY, H_2/CO ratio, and H_2 flux at 5 bar are provided in Table A-7 and Table A-8 in the Appendix. Reducing the operating pressure reduces the STY of CO and H_2, which is a disadvantage of doing this. This is because, on the one hand, reducing the pressure makes the reaction rates slower, and on the other hand, the shift of reaction equilibrium is compromised due to lower H_2 permeation caused by a lower driving force. But compared to the base cases, the STY enhancement of the membrane reactor concepts are both improved. For the fixed-bed membrane reactor concept, the H_2/CO ratios and H_2 removal are strongly increased but the H_2 fluxes remain stable at the reduced pressure. For the catalytic membrane reactor concept, the H_2/CO ratios and H_2 removal are nearly unchanged, but the H_2 fluxes are strongly decreased. At this point, reducing the pressure contributes more to the fixed-bed membrane reactor concept.

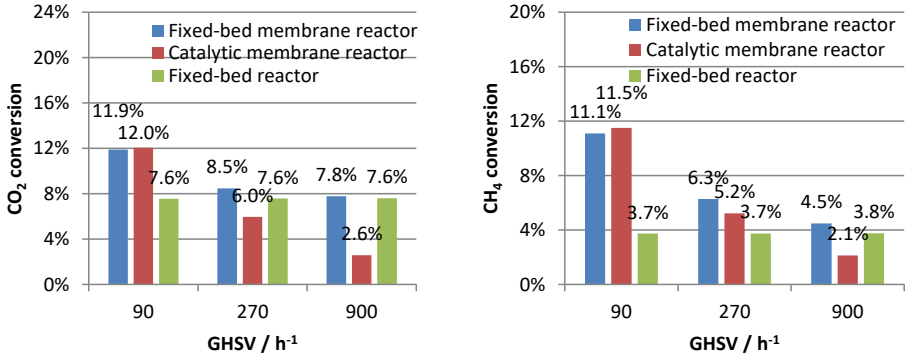

Fig. 6-18 CO_2 and CH_4 conversions at 450 ℃ and 5 bar with CO_2:CH_4 = 1:1.

The CO_2 and CH_4 conversions with different reactor geometry characteristics are shown in Fig. 6-19, which are also realized by increasing the *A/V* to 79.5. The increase of *A/V* does not change the conversions of CO_2 and CH_4 of the fixed-bed reactor but boosts the conversions of the both membrane reactor concepts. For the fixed-bed membrane reactor, the increased *A/V* reduces the mass transport distance of the produced H_2, and for the catalytic membrane reactor concept, the reduced mass transport distance improves the availability of reactants surrounding the membrane.

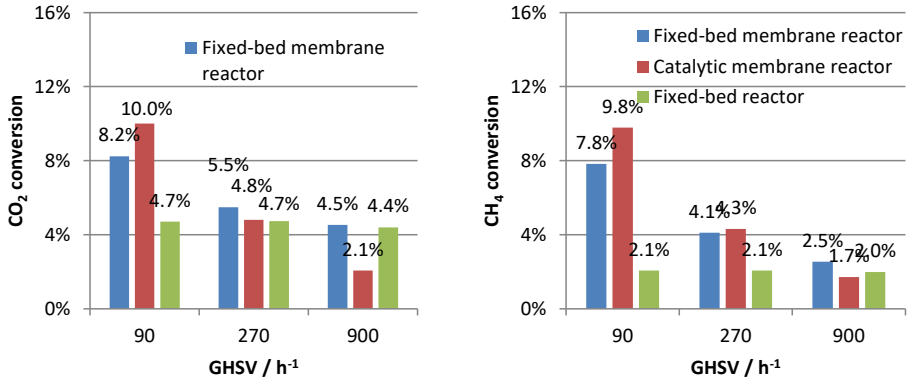

Fig. 6-19 CO_2 and CH_4 conversions 450 °C and 20 bar with CO_2:CH_4 = 1:1 and *A/V*=79.5.

The results of STY, H_2/CO ratio, and H_2 flux with *A/V*=79.5 are provided in Table A-9 and Table A-10 in the Appendix. In addition to the CO_2 and CH_4 conversions, the STY of CO and H_2 also does not change with the *A/V* for the fixed-bed reactor, which is attributed to the equilibrium operations. The increased *A/V* improves the STY of CO and H_2 of the both membrane reactor concepts but more significantly for the catalytic membrane reactor concept. This is because the membrane reactors are more compact and the reactors' space is more efficiently utilized. The increase of *A/V* is also good for the H_2/CO ratio and H_2 removal of the membrane reactor concepts, especially for the fixed-bed membrane reactor because the concentration polarization is much more alleviated. The H_2/CO ratio and H_2 removal improvement of the catalytic membrane reactor are limited because of the H_2 generated on the membrane surface and it is not influenced by the concentration polarization. However, the H_2 fluxes are decreased for both membrane reactor concepts, which is a result of stronger permeation resistance due to the high H_2 extraction.

6.6 Comparison of the membrane reactor concepts

This chapter has developed several membrane reactor concepts for the two reactions that are relevant to Power-to-Fuel applications. Table 6-16 summarizes the performance of each developed membrane reactor concept. The water permeable and CO_2 permeable membrane reactors are both applicable for reverse water gas shift for different purposes. The water permeable membrane reactor concept is effective to improve the conversion of this reaction, but the contradiction between conversion and productivity still exists. The application of CO_2 permeable membranes to reverse water gas shift is a novel idea that integrates CO_2 capture and conversion into one device. This membrane reactor concept does not need to lower the reaction temperature as the water permeable membrane reactor concept does. At present, the productivity is relatively low because of the low CO_2 flux. With the improvement of CO_2 flux, this membrane reactor concept can be applied to more applications such as direct air capture. Summarizing the performance of the two membrane reactor concepts for dry reforming of methane, it is concluded that the catalytic membrane reactor concept is hard to compete with the fixed-bed membrane reactor concept. However, there exists a niche for the catalytic membrane reactor concept that the product ratio of H_2 to CO is always higher, which is also an important advantage for subsequent fuel synthesis reactions.

In the respect of operating condition, increasing temperature is an approach that is both beneficial to the endothermic reactions and membrane permeability, but the limiting temperatures of the membranes are a restricting factor. The effects of pressure depend on the stoichiometric coefficients of reactants and products. The compatibility between reaction and permeation rates should be sufficiently taken into consideration to utilize the membrane potential. Compact designs by increasing surface to volume ratios is a generally applicable way to alleviate the contradiction between conversion and productivity.

Table 6-16 Performance summary of the developed membrane reactor concepts under base case conditions with stoichiometric feed and *A/V* = 79.5

Performance	**Reverse water gas shift**		**Dry reforming of methane**	
Reactor concept	Water permeable membrane reactor	CO_2 permeable membrane reactor	Fixed-bed membrane reactor	Catalytic membrane reactor
Membrane	hydroxy sodalite zeolite	yttria-doped zirconia	Pd-Ag alloy	Pd-Ag alloy
Operating temperature / °C	200 – 250	800 – 900	450 – 500	450 – 500
Conversion / %	5.5 – 15.0	95.9 – 96.8	2.5 – 7.8	1.7 – 9.8[a]
Conversion enhancement / %	3.2 – 103.1	NA	25 - 271	-15 – 367
STY / mol/(m^3 s)	1.39 – 5.04	1.87 – 2.20	0.81 – 1.65	1.02 – 1.62[b]
STY enhancement / %	3.2 – 103.0	NA	101 – 900	98 – 1175
Membrane flux / mol/(m^2 s)	0.0092 – 0.0133	0.0244 – 0.0287	0.0098 – 0.0124	0.0127 – 0.0165
Species removal / %	14.6 – 76.3	39.4 – 89.8	59.7 – 96.5	81.0 – 98.4
Advantage	Effective conversion enhancement	High CO_2 conversion, efficient capture	Higher conversion and productivity	Lower conversion and productivity
Disadvantage	Operating temperature limited	Low H_2 conversion	Low H_2/CO ratio	High H_2/CO ratio

[a]CH_4 conversion, [b]H_2 STY

7 Summary and conclusions

The overall target of this thesis was to develop novel membrane reactor concepts for Power-to-Fuel applications in the background of Process Engineering and Chemical Reaction Engineering. To realize this target, this thesis carried out work at the process level and the equipment level. At the process level, two products of dimethyl carbonate and methyl formate were determined to be prospective ester fuels due to their promising fuel properties. The two esters act as extension of the Power-to-Fuel family and as an addition to methanol-based pathways. Each product can be produced through different pathways from CO_2 and H_2. Starting from process screening, suitable production pathways were first identified with respect to their technical maturities and their compliance with green chemistry principles. The techno-economic feasibility of the selected pathways were then analyzed following the procedures of thermodynamic analysis, process design and simulation as well as energy and cost analyses. Another purpose of process analysis was to identify reactions possible for membrane applications. Reverse water gas shift is a reaction involved in the processes of dimethyl carbonate and methyl formate production that is thermodynamically limited. So it was chosen as a target reaction and two membrane reactor concepts are developed for it. Dry reforming of methane is a reaction similar to reverse water gas shift. It was selected as an alternative reaction to produce syngas and also two membrane reactor concepts were developed accordingly.

Before detailed membrane reactor concept designs, the question of membrane reactor selection and matching was addressed as various membranes and reactor concepts are available now. The mapping relationships among reaction, membrane, and reactor concept were constructed to give an overview of their possible combinations. To deliver deeper insights, two dimensionless numbers of the Damköhler (*Da*) and Péclet (*Pe*) numbers were introduced. The relationship among equilibrium constant, conversion, and the dimensionless numbers was derived in a general manner. This relationship was exemplified through applications to the above two reactions by theoretical calculations. The membrane selection and matching is an important intermediate step between process analysis and reactor development.

The detailed designs of membrane reactors are by ways of CFD simulations. All of the reactor concepts developed in this thesis share the same model geometry, which is a 2D axisymmetric design consisting of two channels. Two reactor concepts using a water permeable membrane and a CO_2 permeable membrane were developed for reverse water

gas shift for different application scenarios. The water permeable membrane reactor is based on the concept of "shift of equilibria" and is for the purpose of conversion enhancement by *in-situ* water removal. The CO_2 permeable membrane reactor is based on the concept of "reactant dosing" to realize the purpose of integrated CO_2 capture and conversion. For dry reforming of ethane, only a H_2 permeable membrane is emplyoed, but two coupling modes of membrane and catalyst were develoeped and compared. The impacts of operating conditions and geometry characteristics on conversion and productivity were comprehensively studied for each membrane reactor concept.

The targets set in the beginning of this thesis have all been realized. The following three aspects are highlighted:

★ DMC and MF can be produced through green pathways that are also technically realistic, energy efficient, and economically viable in the context of the Power-to-Fuel concept.

★ The promising membrane reactor concepts for reverse water gas shift and dry reforming of methane have been identified and their potential has been quantified.

★ CFD models of the $H_2O/CO_2/H_2$ permeable membrane reactors have been developed and the effects of operating conditions and geometry characteristics have been analyzed.

The major findings from this work are specifically summarized as follows:

(1) Oxidative carbonylation of methanol, direct urea methanolysis, and indirect urea methanolysis via ethylene carbonate and propylene carbonate are selected as the four green dimethyl carbonate production pathways for their sound technical maturities. Each pathway is conceptually designed in the context of the Power-to-Fuel concept. Their energy and economic performance is analyzed and compared on the basis of mass and energy balances by process simulations. With the assumed water electrolysis efficiency of 70%, the Power-to-Fuel efficiencies of these pathways correspond to 46.0 - 48.5%. At the assumed H_2 price of 4.6 €/kg, the costs of manufacturing are from 2.29 to 2.42 €/l_{DE}, which are comparable with ethanol and Fischer-Tropsch processes. Using an indicative dimethyl carbonate market selling price of 1000 €/t, these pathways, except for the direct urea methanolysis, are not profitable by net present value and minimum selling price. Applying the same screening criteria to methyl formate, two pathways of carbonylation and dehydrogenation of methanol are determined. Under the same boundary conditions, the process efficiencies range from 48.6% to 52.5% with costs spanning from 2.11 to 2.21 €/l_{DE}. Although the two pathways are slightly profitable for their lower costs, they are vulnerable to market fluctuations and uncertainties.

Methanol synthesis, as a front end processing step that all pathways have in common, is the biggest contributor to capital expenditure instead of the fuel syntheses themselves. The H_2 price is the dominant factor to drive down the costs and improve the economic competitiveness.

(2) The product of the Damköhler (*Da*) and the Péclet (*Pe*) numbers is a very useful dimensionless number group that can guide membrane reactor selection and matching. It correlates to the percentage of species removed by membrane permeation. The relationship among equilibrium constant, conversion, and the dimensionless number group is constructed in a general form and is successfully applied to the reactions of reverse water gas shift and dry reforming of methane by theoretical calculations. It is shown that, beyond the contribution of operating conditions to conversion, the contribution of reaction stoichiometric coefficients should be also effectively leveraged to get higher conversion enhancement. This relationship is helpful for shifting membrane reactor selection and matching from relying on heuristics to dependence on quantified analysis.

(3) The water permeable membrane reactor concept is for the purpose of conversion enhancement for the reaction of reverse water gas shift. The maximum temperature is limited to 250 ℃, which is restricted by the zeolite membrane employed. Two cases with different H_2 to CO_2 molar ratios are simulated. A fixed-bed reactor is first simulated as a reference model, and its equilibrium point is determined to be around 270 h^{-1}. The considered space velocities for the membrane reactor are therefore set between 90 and 900 h^{-1}. The conversions decrease with space velocity, as the water removal rates drop due to shorter permeation time. To achieve effective conversion enhancement beyond 20%, the reaction has to be operated below its equilibrium point, which is at the expense of reduced productivity. Conversion enhancement is directly related to the percentage of water removal, so any approaches that can increase water removal will lead to higher enhancement. Concentration polarization is a key factor that leads to the water flux much lower than its theoretical maximum value. Focus should be put on intensifying mass transport in the membrane reactor, especially in the radial direction, and many approaches can be adopted to realize this, of which increasing membrane area to reactor volume ratios are simple but effective ones.

(4) The CO_2 permeable membrane reactor concept is designed for integrated CO_2 capture and conversion. Compared to the water permeable membrane reactor concept, the preferred high temperature of the reaction does not have to be lowered. This reactor concept can achieve high CO_2 conversions, but the CO_2 flux is the restricting factor to the CO productivity. Another unique advantage of this membrane concept is its ability of capturing

CO_2 from sources with very low concentration, enabled by the permeation characteristics of the dual-phase membrane. This membrane reactor concept will find more applications for CO_2 capture and conversion.

(5) Comparing the performance of the fixed-bed membrane reactor and the catalytic membrane reactor for dry reforming of methane, the former is superior to the latter in terms of conversion and productivity, as the reactants have to be transferred to the membrane surface before the reaction takes place in the catalytic membrane reactor concept. A niche of the catalytic membrane reactor concept is the high H_2/CO ratios contributed by its short H_2 transport distance. The operating pressure is a variable that should be balanced between the conversion and permeation driving force. A higher operating temperature is beneficial to conversion, productivity, and membrane permeation but is limited by the Pd membrane. Membranes that can work at higher temperatures may be more suitable for this reaction. For all membrane reactor concepts developed, increasing membrane area to reactor volume ratio is effective to improve the conversions and productivity.

Throughout the work, a methodological framework that comprises process analysis, theoretical calculations, and CFD simulations can be refined. Process analysis can be used for the techno-economic feasibility of chemical processes and for providing boundary conditions for CFD simulations. Theoretical calculations are a useful tool to guide the selection and matching of reactor concepts and they can also serve as a first check of potential that a reactor concept has. Detailed designs of reactor concepts can be then realized by CFD simulations. These methodologies form an integrated part and can be applied to the development of any other reactor concepts with multilevel analyses.

References

[1] https://www.bundesregierung.de/breg-de/themen/klimaschutz/climate-change-act-2021-1913970 accessed Februry 2022.

[2] International Energy Agency (IEA). Germany 2020 - Energy Policy Review. 2020.

[3] Robinius M, Otto A, Heuser P, Welder L, Syranidis K, Ryberg D, et al. Linking the Power and Transport Sectors—Part 1: The Principle of Sector Coupling. Energies. 2017;10:956.

[4] Carmo M, Fritz DL, Mergel J, Stolten D. A comprehensive review on PEM water electrolysis. International Journal of Hydrogen Energy. 2013;38:4901-34.

[5] Sunfire. SUNFIRE-HYLINK SOEC – TECHNICAL DATA. https://www.sunfire.de/files/sunfire/images/content/Sunfire.de%20(neu)/Sunfire-Factsheet-HyLink-SOEC-20210303.pdf accessed Semptember 2021.

[6] Buttler A, Spliethoff H. Current status of water electrolysis for energy storage, grid balancing and sector coupling via power-to-gas and power-to-liquids: A review. Renewable and Sustainable Energy Reviews. 2018;82:2440-54.

[7] Mondal MK, Balsora HK, Varshney P. Progress and trends in CO2 capture/separation technologies: A review. Energy. 2012;46:431-41.

[8] Wang Y, Zhao L, Otto A, Robinius M, Stolten D. A Review of Post-combustion CO2 Capture Technologies from Coal-fired Power Plants. Energy Procedia. 2017;114:650-65.

[9] Markewitz, Zhao, Ryssel, Moumin, Wang, Sattler, et al. Carbon Capture for CO2 Emission Reduction in the Cement Industry in Germany. Energies. 2019;12:2432.

[10] Zhang X, Witte J, Schildhauer T, Bauer C. Life cycle assessment of power-to-gas with biogas as the carbon source. Sustainable Energy & Fuels. 2020;4:1427-36.

[11] Schorn F, Lohse D, Samsun RC, Peters R, Stolten D. The biogas-oxyfuel process as a carbon source for power-to-fuel synthesis: Enhancing availability while reducing separation effort. Journal of CO2 Utilization. 2021;45:101410

[12] Keith DW, Holmes G, St. Angelo D, Heidel K. A Process for Capturing CO2 from the Atmosphere. Joule. 2018;2:1573-94.

[13] Fasihi M, Efimova O, Breyer C. Techno-economic assessment of CO2 direct air capture plants. Journal of Cleaner Production. 2019;224:957-80.

[14] Sabatino F, Grimm A, Gallucci F, van Sint Annaland M, Kramer GJ, Gazzani M. A comparative energy and costs assessment and optimization for direct air capture technologies. Joule. 2021;5:2047-76.

[15] Kulkarni AR, Sholl DS. Analysis of Equilibrium-Based TSA Processes for Direct Capture of CO2 from Air. Industrial & Engineering Chemistry Research. 2012;51:8631-45.

[16] Sinha A, Darunte LA, Jones CW, Realff MJ, Kawajiri Y. Systems Design and Economic Analysis of Direct Air Capture of CO2 through Temperature Vacuum Swing Adsorption Using MIL-101(Cr)-PEI-800 and mmen-Mg2(dobpdc) MOF Adsorbents. Industrial & Engineering Chemistry Research. 2017;56:750-64.

[17] Schemme S, Samsun RC, Peters R, Stolten D. Power-to-fuel as a key to sustainable transport systems – An analysis of diesel fuels produced from CO2 and renewable electricity. Fuel. 2017;205:198-221.

[18] Schemme S, Breuer JL, Samsun RC, Peters R, Stolten D. Promising catalytic synthesis pathways towards higher alcohols as suitable transport fuels based on H2 and CO2. Journal of CO2 Utilization. 2018;27:223-37.

[19] Burre J, Bongartz D, Mitsos A. Production of Oxymethylene Dimethyl Ethers from Hydrogen and Carbon Dioxide—Part II: Modeling and Analysis for OME3–5. Industrial & Engineering Chemistry Research. 2019;58:5567-78.

[20] Deutz S, Bongartz D, Heuser B, Kätelhön A, Schulze Langenhorst L, Omari A, et al. Cleaner production of cleaner fuels: wind-to-wheel – environmental assessment of CO2-based oxymethylene ether as a drop-in fuel. Energy & Environmental Science. 2018;11:331-43.

[21] Held M, Tönges Y, Pélerin D, Härtl M, Wachtmeister G, Burger J. On the energetic efficiency of producing polyoxymethylene dimethyl ethers from CO2 using electrical energy. Energy & Environmental Science. 2019;12:1019-34.

[22] Rivera-Tinoco R, Farran M, Bouallou C, Auprêtre F, Valentin S, Millet P, et al. Investigation of power-to-methanol processes coupling electrolytic hydrogen production and catalytic CO2 reduction. International Journal of Hydrogen Energy. 2016;41:4546-59.

[23] Herz G, Rix C, Jacobasch E, Müller N, Reichelt E, Jahn M, et al. Economic assessment of Power-to-Liquid processes – Influence of electrolysis technology and operating conditions. Applied Energy. 2021;292:116655.

[24] Schemme S, Breuer JL, Köller M, Meschede S, Walman F, Samsun RC, et al. H2-based synthetic fuels: A techno-economic comparison of alcohol, ether and hydrocarbon production. International Journal of Hydrogen Energy. 2020;45:5395-414.

[25] Bos MJ, Kersten SRA, Brilman DWF. Wind power to methanol: Renewable methanol production using electricity, electrolysis of water and CO2 air capture. Applied Energy. 2020;264:114672.

[26] Marchese M, Buffo G, Santarelli M, Lanzini A. CO2 from direct air capture as carbon feedstock for Fischer-Tropsch chemicals and fuels: Energy and economic analysis. Journal of CO2 Utilization. 2021;46:101487.

[27] König DH, Baucks N, Dietrich R-U, Wörner A. Simulation and evaluation of a process concept for the generation of synthetic fuel from CO2 and H2. Energy. 2015;91:833-41.

[28] Freund H, Sundmacher K. Towards a methodology for the systematic analysis and design of efficient chemical processes: Part 1. From unit operations to elementary process functions. Chemical Engineering and Processing: Process Intensification. 2008;47:2051-60.

[29] Kim Y-h, Park LK, Yiacoumi S, Tsouris C. Modular chemical process intensification: a review. Annual review of chemical and biomolecular engineering. 2017;8:359-80.

[30] Smith R. Chemical Process Design and Integration: John Wiley & Sons Ltd; 2005. pp. 9.

[31] Agahzamin S, Mirvakili A, Rahimpour MR. Investigation and recovery of purge gas streams to enhance synthesis gas production in a mega methanol complex. Journal of CO2 Utilization. 2016;16:157-68.

[32] Schemme S. Techno-economic assessment of processes for the production of fuels from H2 and CO2: RWTH Aachen University; PhD thesis, 2020.

[33] Brynolf S, Taljegard M, Grahn M, Hansson J. Electrofuels for the transport sector: A review of production costs. Renewable and Sustainable Energy Reviews. 2018;81:1887-905.

[34] König DH, Freiberg M, Dietrich R-U, Wörner A. Techno-economic study of the storage of fluctuating renewable energy in liquid hydrocarbons. Fuel. 2015;159:289-97.

[35] Michailos S, McCord S, Sick V, Stokes G, Styring P. Dimethyl ether synthesis via captured CO2 hydrogenation within the power to liquids concept: A techno-economic assessment. Energy Conversion and Management. 2019;184:262-76.

[36] Schorn F, Breuer JL, Samsun RC, Schnorbus T, Heuser B, Peters R, et al. Methanol as a renewable energy carrier: An assessment of production and transportation costs for selected global locations. Advances in Applied Energy. 2021;3:100050.

[37] Böhm H, Zauner A, Rosenfeld DC, Tichler R. Projecting cost development for future large-scale power-to-gas implementations by scaling effects. Applied Energy. 2020;264:114780.

[38] Emets SV, Hoo KV, Mann U. A Modified Hierarchy for Designing Chemical Processes. Industrial & Engineering Chemistry Research. 2006;45:5037-43.

[39] Schmidt-Traub H, Górak A. Integrated Reaction and Separation Operations - Modelling and experimental validation: Springer; 2006. pp. 2-3.

[40] Becka R. CFD-Modelling and Evaluation of Methanol Synthesis Reactors for Power-to-Fuel Application: RWTH Aachen University; Master thesis, 2018.

[41] Pyo S-H, Park JH, Chang T-S, Hatti-Kaul R. Dimethyl carbonate as a green chemical. Current Opinion in Green and Sustainable Chemistry. 2017;5:61-6.

[42] Kaiser D, Beckmann L, Walter J, Bertau M. Conversion of Green Methanol to Methyl Formate. Catalysts. 2021;11:869.

[43] Abdalla A, Liu D. Dimethyl Carbonate as a Promising Oxygenated Fuel for Combustion: A Review. Energies. 2018;11:1552.

[44] Pacheco AM, Marshall LC. Review of Dimethyl Carbonate (DMC) Manufacture and Its Characteristics as a Fuel Additive. Energy & Fuels. 1997;11:2-29.

[45] Maier T, Härtl M, Jacob E, Wachtmeister G. Dimethyl carbonate (DMC) and Methyl Formate (MeFo): Emission characteristics of novel, clean and potentially CO2-neutral fuels including PMP and sub-23 nm nanoparticle-emission characteristics on a spark-ignition DI-engine. Fuel. 2019;256:115925.

[46] Rounce P, Tsolakis A, Leung P, York APE. A Comparison of Diesel and Biodiesel Emissions Using Dimethyl Carbonate as an Oxygenated Additive. Energy & Fuels. 2010;24:4812-9.

[47] Yang J, Jiang Y, Karavalakis G, Johnson KC, Kumar S, Cocker DR, et al. Impacts of dimethyl carbonate blends on gaseous and particulate emissions from a heavy-duty diesel engine. Fuel. 2016;184:681-8.

[48] Durbin DT, Karavalakis G, Johnson CK, Cocker RD, Yang J, Jiang Y, et al. Evaluating the Viability of Dimethyl Carbonate as an Alternative Fuel for the Transportation Sector. 2017.

[49] Delledonne D, Rivetti F, Romano U. Developments in the production and application of dimethylcarbonate. Applied Catalysis A: General. 2001;221:241–51.

[50] Keller N, Rebmann G, Keller V. Catalysts, mechanisms and industrial processes for the dimethylcarbonate synthesis. Journal of Molecular Catalysis A: Chemical. 2010;317:1-18.

[51] Delledonne D, Rivetti F, Romano U. Oxidative carbonylation of methanol to dimethyl carbonate (DMC): a new catalytic system. Journal of Organometallic Chemistry. 1995;488:C15-C9.

[52] Tomishige K, Sakaihori T, Sakai S-i, Fujimoto K. Dimethyl carbonate synthesis by oxidative carbonylation on activated carbon supported CuCl2 catalysts: catalytic properties and structural change. Applied Catalysis A: General. 1999;181:95-102.

[53] Anderson SA, Root TW. Investigation of the effect of carbon monoxide on the oxidative carbonylation of methanol to dimethyl carbonate over Cu+X and Cu+ZSM-5 zeolites. Journal of Molecular Catalysis A: Chemical. 2004;220:247-55.

[54] Li Z, Xie K, Slade RC. High selective catalyst CuCl/MCM-41 for oxidative carbonylation of methanol to dimethyl carbonate. Applied Catalysis A: General. 2001;205:85-92.

[55] Itoh H, Watanabe Y, Mori K, Umino H. Synthesis of dimethyl carbonate by vapor phase oxidative carbonylation of methanol. Greem Chemistry. 2003;5:558-62.

[56] Yang P, Cao Y, Hu J-C, Dai W-L, Fan K-N. Mesoporous bimetallic PdCl2-CuCl2 catalysts for dimethyl carbonate synthesis by vapor phase oxidative carbonylation of methanol. Applied Catalysis A: General. 2003;241:363-73.

[57] Richter M, Fait M, Eckelt R, Schneider M, Radnik J, Heidemann D, et al. Gas-phase carbonylation of methanol to dimethyl carbonate on chloride-free Cu-precipitated zeolite Y at normal pressure. Journal of Catalysis. 2007;245:11-24.

[58] Richter M, Fait MJG, Eckelt R, Schreier E, Schneider M, Pohl MM, et al. Oxidative gas phase carbonylation of methanol to dimethyl carbonate over chloride-free Cu-impregnated zeolite Y catalysts at elevated pressure. Applied Catalysis B: Environmental. 2007;73:269-81.

[59] Matsuzaki T, Nakamura A. Dimethyl carbonate synthesis and other oxidative reactions using alkyl nitrites. Catalysis Surveys of Japan. 1997;1:77-88.

[60] Yamamoto Y, Matsuzaki T, Tanaka S, Nishihira K, Ohdan K, Nakamura A, et al. Catalysis and characterization of Pd-NaY for dimethyl carbonate synthesis from methyl nitrite and CO. Journal of the Chemical Society, Faraday Transactions. 1997;93:3721-7.

[61] Tan H-Z, Chen Z-N, Xu Z-N, Sun J, Wang Z-Q, Si R, et al. Synthesis of High-Performance and High-Stability Pd(II)/NaY Catalyst for CO Direct Selective Conversion to Dimethyl Carbonate by Rational Design. ACS Catalysis. 2019;9:3595-603.

[62] Knifton JF, Duranleau RG. Ethylene glycol—dimethyl carbonate cogeneration. Journal of Molecular Catalysis. 1991;67:389-99.

[63] Knifton JF. Process for cosynthesis of ethylene glycol and dimethyl carbonate. United States Patent. 1987.

[64] Knifton JF. Process for cogeneration of ethylene glycol and dimethyl carbonate. United States Patent. 1993.

[65] Kim D-W, Kim C-W, Koh J-C, Park D-W. Synthesis of dimethyl carbonate from ethylene carbonate and methanol using immobilized ionic liquid on amorphous silica. Journal of Industrial and Engineering Chemistry. 2010;16:474-8.

[66] Yang Z-Z, He L-N, Dou X-Y, Chanfreau S. Dimethyl carbonate synthesis catalyzed by DABCO-derived basic ionic liquids via transesterification of ethylene carbonate with methanol. Tetrahedron Letters. 2010;51:2931-4.

[67] Deng W, Shi L, Yao J, Zhang Z. A review on transesterification of propylene carbonate and methanol for dimethyl carbonate synthesis. Carbon Resources Conversion. 2019;2:198-212.

[68] Ju H-Y, Manju MD, Kim K-H, Park S-W, Park D-W. Chemical fixation of carbon dioxide to dimethyl carbonate from propylene carbonate and methanol using ionic liquid catalysts. Korean Journal of Chemical Engineering. 2007;24:917-9.

[69] Bhanage BM, Fujita S-i, Ikushima Y, Arai M. Synthesis of dimethyl carbonate and glycols from carbon dioxide, epoxides, and methanol using heterogeneous basic metal oxide catalysts with high activity and selectivity. Applied Catalysis A: General. 2001;219:259-66.

[70] Wang M, Wang H, Zhao N, Wei W, Sun Y. High-Yield Synthesis of Dimethyl Carbonate from Urea and Methanol Using a Catalytic Distillation Process. Industrial & Engineering Chemistry Research. 2007;46:2683-7.

[71] Wang M, Wang H, Zhao N, Wei W, Sun Y. Synthesis of dimethyl carbonate from urea and methanol over solid base catalysts. Catalysis Communications. 2006;7:6-10.

[72] Wang M, Zhao N, Wei W, Sun Y. Synthesis of Dimethyl Carbonate from Urea and Methanol over ZnO. Industrial & Engineering Chemistry Research. 2005;44:7596-9.

[73] Zeng G, Wang Y, Gong D, Zhang Y, Wu P, Sun Y. Dual-Role Membrane as NH3 Permselective Reactor and Azeotrope Separator in Urea Alcoholysis. ACS Cent Sci. 2019;5:1834-43.

[74] Bhanage BM, Fujita S-i, Ikushima Y, Arai M. Transesterification of urea and ethylene glycol to ethylene carbonate as an important step for urea based dimethyl carbonate synthesis. Green Chemistry. 2003;5:429.

[75] Li Q, Zhang W, Zhao N, Wei W, Sun Y. Synthesis of cyclic carbonates from urea and diols over metal oxides. Catalysis Today. 2006;115:111-6.

[76] Wang P, Liu S, Zhou F, Yang B, Alshammari AS, Lu L, et al. Two-step synthesis of dimethyl carbonate from urea, ethylene glycol and methanol using acid–base bifunctional zinc-yttrium oxides. Fuel Processing Technology. 2014;126:359-65.

[77] Zhao X, Zhang Y, Wang Y. Synthesis of Propylene Carbonate from Urea and 1,2-Propylene Glycol over a Zinc Acetate Catalyst. Industrial & Engineering Chemistry Research. 2004;43:4038-42.

[78] Wu D, Guo Y, Geng S, Xia Y. Synthesis of Propylene Carbonate from Urea and 1,2-Propylene Glycol in a Monolithic Stirrer Reactor. Industrial & Engineering Chemistry Research. 2013;52:1216-23.

[79] Al-Darwish J, Senter M, Lawson S, Rezaei F, Rownaghi AA. Ceria nanostructured catalysts for conversion of methanol and carbon dioxide to dimethyl carbonate. Catalysis Today. 2020;350:120-6.

[80] Fu Z, Zhong Y, Yu Y, Long L, Xiao M, Han D, et al. TiO2-Doped CeO2 Nanorod Catalyst for Direct Conversion of CO2 and CH3OH to Dimethyl Carbonate: Catalytic Performance and Kinetic Study. ACS Omega. 2018;3:198-207.

[81] Wada S, Oka K, Watanabe K, Izumi Y. Catalytic conversion of carbon dioxide into dimethyl carbonate using reduced copper-cerium oxide catalysts as low as 353 K and 1.3 MPa and the reaction mechanism. Front Chem. 2013;1:8.

[82] Yoshida Y, Arai Y, Kado S, Kunimori K, Tomishige K. Direct synthesis of organic carbonates from the reaction of CO2 with methanol and ethanol over CeO2 catalysts. Catalysis Today. 2006;115:95-101.

[83] Stoian D, Medina F, Urakawa A. Improving the Stability of CeO2 Catalyst by Rare Earth Metal Promotion and Molecular Insights in the Dimethyl Carbonate Synthesis from CO2 and Methanol with 2-Cyanopyridine. ACS Catalysis. 2018;8:3181-93.

[84] Tamboli AH, Chaugule AA, Kim H. Catalytic developments in the direct dimethyl carbonate synthesis from carbon dioxide and methanol. Chemical Engineering Journal. 2017;323:530-44.

[85] Bansode A, Urakawa A. Continuous DMC Synthesis from CO2 and Methanol over a CeO2 Catalyst in a Fixed Bed Reactor in the Presence of a Dehydrating Agent. ACS Catalysis. 2014;4:3877-80.

[86] Honda M, Tamura M, Nakagawa Y, Sonehara S, Suzuki K, Fujimoto K, et al. Ceria-catalyzed conversion of carbon dioxide into dimethyl carbonate with 2-cyanopyridine. ChemSusChem. 2013;6:1341-4.

[87] Stoian D, Bansode A, Medina F, Urakawa A. Catalysis under microscope: Unraveling the mechanism of catalyst de- and re-activation in the continuous dimethyl carbonate synthesis from CO2 and methanol in the presence of a dehydrating agent. Catalysis Today. 2017;283:2-10.

[88] Honda M, Kuno S, Sonehara S, Fujimoto K-i, Suzuki K, Nakagawa Y, et al. Tandem Carboxylation-Hydration Reaction System from Methanol, CO2 and Benzonitrile to Dimethyl Carbonate and Benzamide Catalyzed by CeO2. ChemCatChem. 2011;3:365-70.

[89] Hu X, Cheng H, Kang X, Chen L, Yuan X, Qi Z. Analysis of direct synthesis of dimethyl carbonate from methanol and CO 2 intensified by in-situ hydration-assisted reactive distillation with side reactor. Chemical Engineering and Processing - Process Intensification. 2018;129:109-17.

[90] Eta V, Mäki-Arvela P, Wärnå J, Salmi T, Mikkola J-P, Murzin DY. Kinetics of dimethyl carbonate synthesis from methanol and carbon dioxide over ZrO2–MgO catalyst in the presence of butylene oxide as additive. Applied Catalysis A: General. 2011.

[91] Choi J-C, He L-N, Yasuda H, Sakakura T. Selective and high yield synthesis of dimethyl carbonate directly from carbon dioxide and methanol. Green Chemistry. 2002;4:230-4.

[92] Li C-F, Zhong S-H. Study on application of membrane reactor in direct synthesis DMC from CO2 and CH3OH over Cu–KF/MgSiO catalyst. Catalysis Today. 2003;82:83-90.

[93] Sánchez A, Gil LM, Martín M. Sustainable DMC production from CO2 and renewable ammonia and methanol. Journal of CO2 Utilization. 2019;33:521-31.

[94] Vázquez D, Javaloyes-Antón J, Medrano-García JD, Ruiz-Femenia R, Caballero JA. Dimethyl Carbonate Production Process from Urea and Methanol. Proceedings of the 28th European Symposium on Computer Aided Process Engineering. 2018;43:731-6.

[95] Javaloyes-Antón J, Vázquez D, Medrano-García JD, Caballero JA. Economic Study of the Urea Alcoholysis Process for Dimethyl Carbonate Production. Proceedings of the 28th European Symposium on Computer Aided Process Engineering. 2019.

[96] Chinese Academy of Sciences. http://www.cas.cn/ky/kyjz/201009/t20100926_2974487.shtml. accessed May 2019.

[97] Hsu K-Y, Hsiao Y-C, Chien IL. Design and Control of Dimethyl Carbonate−Methanol Separation via Extractive Distillation Industrial & Engineering Chemistry Research. 2010;49:735-49.

[98] Souza LFS, Ferreira PRR, de Medeiros JL, Alves RMB, Araújo OQF. Production of DMC from CO2 via Indirect Route: Technical–Economical–Environmental Assessment and Analysis. ACS Sustainable Chemistry & Engineering. 2013;2:62-9.

[99] Zhejiang Petrochemical Co. Ltd. http://www.xwchemintl.com/xinwang/show.php?itemid=118. accessed October 2021.

[100] Holtbruegge J, Heile S, Lutze P, Górak A. Synthesis of dimethyl carbonate and propylene glycol in a pilot-scale reactive distillation column: Experimental investigation, modeling and process analysis. Chemical Engineering Journal. 2013;234:448-63.

[101] Holtbruegge J, Kuhlmann H, Lutze P. Process analysis and economic optimization of intensified process alternatives for simultaneous industrial scale production of dimethyl carbonate and propylene glycol. Chemical Engineering Research and Design. 2015;93:411-31.

[102] Holtbruegge J, Leimbrink M, Lutze P, Górak A. Synthesis of dimethyl carbonate and propylene glycol by transesterification of propylene carbonate with methanol: Catalyst screening, chemical equilibrium and reaction kinetics. Chemical Engineering Science. 2013;104:347-60.

[103] Holtbruegge J, Wierschem M, Lutze P. Synthesis of dimethyl carbonate and propylene glycol in a membrane-assisted reactive distillation process: Pilot-scale experiments, modeling and process analysis. Chemical Engineering and Processing: Process Intensification. 2014;84:54-70.

[104] Holtbruegge J, Wierschem M, Steinruecken S, Voss D, Parhomenko L, Lutze P. Experimental investigation, modeling and scale-up of hydrophilic vapor permeation

membranes: Separation of azeotropic dimethyl carbonate/methanol mixtures. Separation and Purification Technology. 2013;118:862-78.

[105] Li Q, Kiss AA. Novel pervaporation-assisted pressure swing reactive distillation process for intensified synthesis of dimethyl carbonate. Chemical Engineering and Processing-Process Intensification. 2021;162:108358.

[106] Huang Z, Li J, Wang L, Jiang H, Qiu T. Novel Procedure for the Synthesis of Dimethyl Carbonate by Reactive Distillation. Industrial & Engineering Chemistry Research. 2014;53:3321-8.

[107] Shi L, Wang S-J, Wong DS-H, Huang K. Novel Process Design of Synthesizing Propylene Carbonate for Dimethyl Carbonate Production by Indirect Alcoholysis of Urea. Industrial & Engineering Chemistry Research. 2017;56:11531-44.

[108] Patraşcu I, Bîldea SC, Kiss AA. Novel eco-efficient process for dimethyl carbonate production by indirect alcoholysis of urea. Chemical Engineering Research and Design. 2020.

[109] Chinese Academy of Sciences. http://www.sxicc.cas.cn/xwzx/zhxw/202007/t20200723_5643699.html. accessed July 2020.

[110] Wu T-W, Chien IL. CO2 Utilization Feasibility Study: Dimethyl Carbonate Direct Synthesis Process with Dehydration Reactive Distillation. Industrial & Engineering Chemistry Research. 2019;59:1234-48.

[111] Ohno H, Ikhlayel M, Tamura M, Nakao K, Suzuki K, Morita K, et al. Direct dimethyl carbonate synthesis from CO2 and methanol catalyzed by CeO2 and assisted by 2-cyanopyridine: a cradle-to-gate greenhouse gas emission study. Green Chemistry. 2021;23:457-69.

[112] Garcia-Herrero I, Cuéllar-Franca RM, Enríquez-Gutiérrez VM, Alvarez-Guerra M, Irabien A, Azapagic A. Environmental Assessment of Dimethyl Carbonate Production: Comparison of a Novel Electrosynthesis Route Utilizing CO2 with a Commercial Oxidative Carbonylation Process. ACS Sustainable Chemistry & Engineering. 2016;4:2088-97.

[113] Yu B-Y, Chen M-K, Chien IL. Assessment on CO2 Utilization through Rigorous Simulation: Converting CO2 to Dimethyl Carbonate. Industrial & Engineering Chemistry Research. 2018;57:639-52.

[114] Kongpanna P, Pavarajarn V, Gani R, Assabumrungrat S. Techno-economic evaluation of different CO2-based processes for dimethyl carbonate production. Chemical Engineering Research and Design. 2015;93:496-510.

[115] Lee SJ, Kim CJ, Kim GY. Methyl formate as a new building block in C1 chemistry. Applied Catalysis. 1990;57:1-30.

[116] He L, Liu H, Xiao C-x, Kou Y. Liquid-phase synthesis of methyl formate via heterogeneous carbonylation of methanol over a soluble copper nanocluster catalyst. Green Chemistry. 2008;10:619.

[117] Rong L, Xu Z, Sun J, Guo G. New methyl formate synthesis method: Coal to methyl formate. Journal of Energy Chemistry. 2018;27:238-42.

[118] Yuan DJ, Hengne AM, Saih Y, Huang KW. Nonoxidative Dehydrogenation of Methanol to Methyl Formate through Highly Stable and Reusable CuMgO-Based Catalysts. ACS Omega. 2019;4:1854-60.

[119] Kishi R, Ogihara H, Yoshida-Hirahara M, Shibanuma K, Yamanaka I, Kurokawa H. Green Synthesis of Methyl Formate via Electrolysis of Pure Methanol. ACS Sustainable Chemistry & Engineering. 2020;8:11532-40.

[120] Zhao H, Lin M, Fang K, Zhou J, Liu Z, Zeng G, et al. A novel Cu–Mn/Ca–Zr catalyst for the synthesis of methyl formate from syngas. RSC Advances. 2015;5:67630-7.

[121] Wu C, Zhang Z, Zhu Q, Han H, Yang Y, Han B. Highly efficient hydrogenation of carbon dioxide to methyl formate over supported gold catalysts. Green Chemistry. 2015;17:1467-72.

[122] Sun R, Kann A, Hartmann H, Besmehn A, Hausoul PJC, Palkovits R. Direct Synthesis of Methyl Formate from CO2 With Phosphine-Based Polymer-Bound Ru Catalysts. ChemSusChem. 2019;12:3278-85.

[123] Scott M, Westhues CG, Kaiser T, Baums JC, Jupke A, Franciò G, et al. Methylformate from CO2: an integrated process combining catalytic hydrogenation and reactive distillation. Green Chemistry. 2019;21:6307-17.

[124] Jens CM, Müller L, Leonhard K, Bardow A. To Integrate or Not to Integrate—Techno-Economic and Life Cycle Assessment of CO2 Capture and Conversion to Methyl Formate Using Methanol. ACS Sustainable Chemistry & Engineering. 2019.

[125] Kaiser P, Unde RB, Kern C, Jess A. Production of Liquid Hydrocarbons with CO2 as Carbon Source based on Reverse Water-Gas Shift and Fischer-Tropsch Synthesis. Chemie Ingenieur Technik. 2013;85:489-99.

[126] Daza YA, Kuhn JN. CO2conversion by reverse water gas shift catalysis: comparison of catalysts, mechanisms and their consequences for CO2conversion to liquid fuels. RSC Advances. 2016;6:49675-91.

[127] Su X, Yang X, Zhao B, Huang Y. Designing of highly selective and high-temperature endurable RWGS heterogeneous catalysts: recent advances and the future directions. Journal of Energy Chemistry. 2017;26:854-67.

[128] Nielsen DU, Hu X-M, Daasbjerg K, Skrydstrup T. Chemically and electrochemically catalysed conversion of CO2 to CO with follow-up utilization to value-added chemicals. Nature Catalysis. 2018;1:244-54.

[129] Chen C-S, Cheng W-H, Lin S-S. Study of iron-promoted Cu/SiO2 catalyst on high temperature reverse water gas shift reaction. Applied Catalysis A: General. 2004;257:97-106.

[130] Pastor-Pérez L, Baibars F, Le Sache E, Arellano-García H, Gu S, Reina TR. CO2 valorisation via Reverse Water-Gas Shift reaction using advanced Cs doped Fe-Cu/Al2O3 catalysts. Journal of CO2 Utilization. 2017;21:423-8.

[131] Kim DH, Han SW, Yoon HS, Kim YD. Reverse water gas shift reaction catalyzed by Fe nanoparticles with high catalytic activity and stability. Journal of Industrial and Engineering Chemistry. 2015;23:67-71.

[132] Sun F-m, Yan C-f, Wang Z-d, Guo C-q, Huang S-l. Ni/Ce–Zr–O catalyst for high CO2 conversion during reverse water gas shift reaction (RWGS). International Journal of Hydrogen Energy. 2015;40:15985-93.

[133] Wolf A, Jess A, Kern C. Syngas Production via Reverse Water-Gas Shift Reaction over a Ni-Al2O3 Catalyst: Catalyst Stability, Reaction Kinetics, and Modeling. Chemical Engineering & Technology. 2016;39:1040-8.

[134] Park S-W, Joo O-S, Jung K-D, Kim H, Han S-H. Development of ZnO/Al2O3 catalyst for reverse-water-gas-shift reaction of CAMERE (carbon dioxide hydrogenation to form methanol via a reverse-water-gas-shift reaction) process. Applied Catalysis A: General. 2001;211:81-90.

[135] Sun Q, Ye J, Liu Cj, Ge Q. In2O3 as a promising catalyst for CO2 utilization: A case study with reverse water gas shift over In2O3. Greenhouse Gases: Science and Technology. 2014;4:140-4.

[136] Daza YA, Kent RA, Yung MM, Kuhn JN. Carbon dioxide conversion by reverse water–gas shift chemical looping on perovskite-type oxides. Industrial & Engineering Chemistry Research. 2014;53:5828-37.

[137] Juneau M, Vonglis M, Hartvigsen J, Frost L, Bayerl D, Dixit M, et al. Assessing the viability of K-Mo2C for reverse water–gas shift scale-up: molecular to laboratory to pilot scale. Energy & Environmental Science. 2020;13:2524-39.

[138] Ernst K-H, Campbell TC, Moretti G. Kinetics of the reverse water-gas shift reaction over Cu(110). Journal of Catalysis. 1992;134:66-74.

[139] Ginés MJL, Marchi AJ, Apesteguía CR. Kinetic study of the reverse water-gas shift reaction over CuO-ZnO-Al2O3 catalysts. Applied Catalysis A: General. 1997;154:155-71.

[140] Ghodoosi F, Khosravi-Nikou MR, Shariati A. Mathematical Modeling of Reverse Water-Gas Shift Reaction in a Fixed-Bed Reactor. Chemical Engineering & Technology. 2017;40:598-607.

[141] Zhang L, Chen L, Xia S, Ge Y, Wang C, Feng H. Multi-objective optimization for helium-heated reverse water gas shift reactor by using NSGA-II. International Journal of Heat and Mass Transfer. 2020;148:119025.

[142] Munera Parra AA, Asmanoglo C, Agar DW. Modelling and optimization of a moving-bed adsorptive reactor for the reverse water-gas shift reaction. Computers & Chemical Engineering. 2018;109:203-15.

[143] Lee J, Park H-G, Hyeon M-H, Kim B-G, Kim SK, Moon S-Y. Low-temperature CO2 hydrogenation overcoming equilibrium limitations with polyimide hollow fiber membrane reactor. Chemical Engineering Journal. 2021;403:126457.

[144] Dzuryk S, Rezaei E. Intensification of the Reverse Water Gas Shift Reaction by Water-Permeable Packed-Bed Membrane Reactors. Industrial & Engineering Chemistry Research. 2020;59:18907-20.

[145] Chen T, Wang Z, Liu L, Pati S, Wai MH, Kawi S. Coupling CO2 separation with catalytic reverse water-gas shift reaction via ceramic-carbonate dual-phase membrane reactor. Chemical Engineering Journal. 2020;379:122182.

[146] Cui X, Kær SK. Thermodynamic Analyses of a Moderate-Temperature Process of Carbon Dioxide Hydrogenation to Methanol via Reverse Water–Gas Shift with In Situ Water Removal. Industrial & Engineering Chemistry Research. 2019;58:10559-69.

[147] Samimi F, Karimipourfard D, Rahimpour MR. Green methanol synthesis process from carbon dioxide via reverse water gas shift reaction in a membrane reactor. Chemical Engineering Research and Design. 2018;140:44-67.

[148] Elsernagawy OYH, Hoadley A, Patel J, Bhatelia T, Lim S, Haque N, et al. Thermo-economic analysis of reverse water-gas shift process with different temperatures for green methanol production as a hydrogen carrier. Journal of CO2 Utilization. 2020;41:101280.

[149] Pakhare D, Spivey J. A review of dry (CO2) reforming of methane over noble metal catalysts. Chemical Society Reviews. 2014;43:7813-37.

[150] Liu X, Wang H, Ye G, Zhou X, Keil FJ. Enhanced performance of catalyst pellets for methane dry reforming by engineering pore network structure. Chemical Engineering Journal. 2019;373:1389-96.

[151] Lin Y, Yang C, Choi C, Zhang W, Machida H, Norinaga K. Lattice Boltzmann simulation of multicomponent reaction-diffusion and coke formation in a catalyst with hierarchical pore structure for dry reforming of methane. Chemical Engineering Science. 2021;229:116105.

[152] Nagaoka K, Okamura M, Aika K-i. Titania supported ruthenium as a coking-resistant catalyst for high pressure dry reforming of methane. Catalysis Communications. 2001;2:255-60.

[153] Nagaoka K, Takanabe K, Aika K-i. Influence of the reduction temperature on catalytic activity of Co/TiO2 (anatase-type) for high pressure dry reforming of methane. Applied Catalysis A: General. 2003;255:13-21.

[154] Kahle LCS, Roussière T, Maier L, Herrera Delgado K, Wasserschaff G, Schunk SA, et al. Methane Dry Reforming at High Temperature and Elevated Pressure: Impact of Gas-Phase Reactions. Industrial & Engineering Chemistry Research. 2013;52:11920-30.

[155] Richardson JT, Paripatyadar SA. Carbon dioxide reforming of methane with supported rhodium. Applied Catalysis. 1990;61:293-609.

[156] Kathiraser Y, Oemar U, Saw ET, Li Z, Kawi S. Kinetic and mechanistic aspects for CO2 reforming of methane over Ni based catalysts. Chemical Engineering Journal. 2015;278:62-78.

[157] Wang H, Duan X, Liu X, Ye G, Gu X, Zhu K, et al. Influence of tubular reactor structure and operating conditions on dry reforming of methane. Chemical Engineering Research and Design. 2018;139:39-51.

[158] Wehinger GD, Eppinger T, Kraume M. Detailed numerical simulations of catalytic fixed-bed reactors: Heterogeneous dry reforming of methane. Chemical Engineering Science. 2015;122:197-209.

[159] Chen X, Wang F, Yan X, Han Y, Cheng Z, Jie Z. Thermochemical performance of solar driven CO2 reforming of methane in volumetric reactor with gradual foam structure. Energy. 2018;151:545-55.

[160] Zhang H, Shuai Y, Pang S, Pan R, Lougou BG, Huang X. Numerical Investigation of Carbon Deposition Behavior in Ni/Al2O3-Based Catalyst Porous-Filled Solar Thermochemical Reactor for the Dry Reforming of Methane Process. Industrial & Engineering Chemistry Research. 2019;58:15701-11.

[161] Fukuda T, Harada MR, Ookawara S, Hamzah AB, Yoshikawa S, Matsumoto H. Double-layered catalytic wall-plate microreactor for process intensification of dry reforming of methane: Reaction activity improvement and coking suppression. Chemical Engineering and Processing - Process Intensification. 2021;164:108406.

[162] Hamzah AB, Fukuda T, Ookawara S, Yoshikawa S, Matsumoto H. Process intensification of dry reforming of methane by structured catalytic wall-plate microreactor. Chemical Engineering Journal. 2021;412:128636.

[163] Paturzo L, Gallucci F, Basile A, Vitulli G, Pertici P. An Ru-based catalytic membrane reactor for dry reforming of methane—its catalytic performance compared with tubular packed bed reactors. Catalysis Today. 2003;82:57-65.

[164] Haag S, Burgard M, Ernst B. Beneficial effects of the use of a nickel membrane reactor for the dry reforming of methane: Comparison with thermodynamic predictions. Journal of Catalysis. 2007;252:190-204.

[165] Leimert J, Karl J, Dillig M. Dry Reforming of Methane Using a Nickel Membrane Reactor. Processes. 2017;5:82.

[166] Caravella A, Brunetti A, Grandinetti M, Barbieri G. Dry Reforming of Methane in a Pd-Ag Membrane Reactor: Thermodynamic and Experimental Analysis. ChemEngineering. 2018;2:48.

[167] Gallucci F, Tosti S, Basile A. Pd–Ag tubular membrane reactors for methane dry reforming: A reactive method for CO2 consumption and H2 production. Journal of Membrane Science. 2008;317:96-105.

[168] García-García FR, Soria MA, Mateos-Pedrero C, Guerrero-Ruiz A, Rodríguez-Ramos I, Li K. Dry reforming of methane using Pd-based membrane reactors fabricated from different substrates. Journal of Membrane Science. 2013;435:218-25.

[169] Lee D, Hacarlioglu P, Oyama ST. The Effect of Pressure in Membrane Reactors Trade-Off in Permeability and Equilibrium Conversion in the Catalytic Reforming of CH4 with CO2 at High Pressure Topics in Catalysis. 2004;29:45-57.

[170] Lee B, Yun S-W, Kim S, Heo J, Kim Y-T, Lee S, et al. CO2 reforming of methane for H2 production in a membrane reactor as CO2 utilization: Computational fluid dynamics studies with a reactor geometry. International Journal of Hydrogen Energy. 2019;44:2298-311.

[171] Coronel L, Múnera JF, Lombardo EA, Cornaglia LM. Pd based membrane reactor for ultra pure hydrogen production through the dry reforming of methane. Experimental and modeling studies. Applied Catalysis A: General. 2011;400:185-94.

[172] Oyama ST, Lim H. An operability level coefficient (OLC) as a useful tool for correlating the performance of membrane reactors. Chemical Engineering Journal. 2009;151:351-8.

[173] Bian Z, Xia H, Wang Z, Jiang B, Yu Y, Yu K, et al. CFD Simulation of a Hydrogen-Permeable Membrane Reactor for CO2 Reforming of CH4: The Interplay of the Reaction and Hydrogen Permeation. Energy & Fuels. 2020;34:12366-78.

[174] Department of Defense. Technology Readiness Assessment (TRA) Guidance, 2011.

[175] European Commission. Technology Readiness Level: Guidance Principles for Renewable Energy Technologies Final Report. Brussels 2017.

[176] Roh K, Bardow A, Bongartz D, Burre J, Chung W, Deutz S, et al. Early-stage evaluation of emerging CO2 utilization technologies at low technology readiness levels. Green Chemistry. 2020;22:3842-59.

[177] Anastas P, Eghbali N. Green chemistry: principles and practice. Chemical Society Reviews. 2010;39:301-12.

[178] Ho M, Wiley D. Liquid absorbent-based post-combustion CO2 capture in industrial processes. Absorption-based post-combustion capture of carbon dioxide: Elsevier; 2016. p. 711-56.

[179] Peters SM, Timmerhaus DK, West ER. Plant Design and Economics for Chemical Engineers fifth edition ed: McGraw-Hill; 2003. pp. 226-275.

[180] Turton R, Bailie R, Whiting W, Shaeiwitz J. Analysis, Synthesis, and Design of Chemical Processes. Third Edition ed: Pearson Education Inc.; 2008. pp. 182-255.

[181] Peters R, Baltruweit M, Grube T, Samsun RC, Stolten D. A techno economic analysis of the power to gas route. Journal of CO2 Utilization. 2019;34:616-34.

[182] Huang K, Miller JB, Huber GW, Dumesic JA, Maravelias CT. A General Framework for the Evaluation of Direct Nonoxidative Methane Conversion Strategies. Joule. 2018;2:349-65.

[183] Jouny M, Luc W, Jiao F. General Techno-Economic Analysis of CO2 Electrolysis Systems. Industrial & Engineering Chemistry Research. 2018;57:2165-77.

[184] Staples MD, Malina R, Olcay H, Pearlson MN, Hileman JI, Boies A, et al. Lifecycle greenhouse gas footprint and minimum selling price of renewable diesel and jet fuel from fermentation and advanced fermentation production technologies. Energy & Environmental Science. 2014;7:1545-54.

[185] Robinius M, Linßen J, Grube T, Reuß M, Stenzel P, Syranidis K, et al. Comparative analysis of infrastructures: hydrogen fueling and electric charging of vehicles. 2018.

[186] Fasihi M, Bogdanov D, Breyer C. Techno-Economic Assessment of Power-to-Liquids (PtL) Fuels Production and Global Trading Based on Hybrid PV-Wind Power Plants. Energy Procedia. 2016;99:243-68.

[187] Detz R, Reek J, Van Der Zwaan B. The future of solar fuels: when could they become competitive? Energy & Environmental Science. 2018;11:1653-69.

[188] Schach M-O, Schneider Rd, Schramm H, Repke J-U. Techno-economic analysis of postcombustion processes for the capture of carbon dioxide from power plant flue gas. Industrial & Engineering Chemistry Research. 2010;49:2363-70.

[189] https://m.made-in-hina.com/search/product?word=Dimethyl%20Carbonate%20Price. accessed August 2019.

[190] http://www.importexportplatform.com/2089_methyl_formate_sellers.html accessed August 2019.

[191] ANSYS Inc. ANSYS Fluent Theory Guide. 2016.

[192] Ergun S. Fluid flow through packed columns. Chemical Engineering Progress. 1952;48:89-95.

[193] Tran A, Aguirre A, Durand H, Crose M, Christofides PD. CFD modeling of a industrial-scale steam methane reforming furnace. Chemical Engineering Science. 2017;171:576-98.

[194] Davis EM, Davis JR. Fundamentals of Chemical Reaction Engineering: McGraw-Hili; 2003. pp. 184-232.

[195] Lommerts JB, Graaf HG, Beenackers ACMA. Mathematical modeling of internal mass transport limitations in methanol synthesis. Chemical Engineering Science. 2000;55:5589-98.

[196] Fuller EN, Schettler PD, Giddings JC. New Method for Prediction of Binary Gas-Phase Diffusion Coefficients. Industrial & Engineering Chemistry. 1966;58:18-27.

[197] Gosiewski K, Bartmann U, Moszczyński M, Mleczko La. Effect of the intraparticle mass transport limitations for the partial oxidation of methane to synthesis gas. Chemical Engineering Science. 1999;54:4589-602.

[198] Li Z, Deng Y, Dewangan N, Hu J, Wang Z, Tan X, et al. High Temperature Water Permeable Membrane Reactors for CO2 Utilization. Chemical Engineering Journal. 2021;420:129834.

[199] Sherman JD. Synthetic zeolites and other microporous oxide molecular sieves. Proceedings of the National Academy of Sciences. 1999;96:3471-8.

[200] Mafra L, Vidal-Moya JA, Blasco T. Structural characterization of zeolites by advanced solid state NMR spectroscopic methods. Annual Reports on NMR Spectroscopy: Elsevier; 2012. p. 259-351.

[201] Asgar Pour Z, Sebakhy KO. A Review on the Effects of Organic Structure-Directing Agents on the Hydrothermal Synthesis and Physicochemical Properties of Zeolites. Chemistry. 2022;4:431-46.

[202] Ceramic Membranes. In: Drioli E, Giorno L, editors. Encyclopedia of Membranes: Springer; 2016. pp. 354.

[203] Korelskiy D. Quality and Performance of Zeolite Membranes: Luleå University of Technology; PhD thesis, 2012.

[204] Gorbe J, Lasobras J, Francés E, Herguido J, Menéndez M, Kumakiri I, et al. Preliminary study on the feasibility of using a zeolite A membrane in a membrane reactor for methanol production. Separation and Purification Technology. 2018;200:164-8.

[205] Wikipedia. https://en.wikipedia.org/wiki/Kinetic_diameter.

[206] Raso R, Tovar M, Lasobras J, Herguido J, Kumakiri I, Araki S, et al. Zeolite membranes: Comparison in the separation of H2O/H2/CO2 mixtures and test of a reactor for CO2 hydrogenation to methanol. Catalysis Today. 2021;364:270-5.

[207] Gallucci F, Paturzo L, Basile A. An experimental study of CO2 hydrogenation into methanol involving a zeolite membrane reactor. Chemical Engineering and Processing: Process Intensification. 2004;43:1029-36.

[208] Gallucci F, Basile A. A theoretical analysis of methanol synthesis from CO2 and H2 in a ceramic membrane reactor. International Journal of Hydrogen Energy. 2007;32:5050-8.

[209] Diban N, Urtiaga AM, Ortiz I, Ereña J, Bilbao J, Aguayo AT. Influence of the membrane properties on the catalytic production of dimethyl ether with in situ water removal for the successful capture of co2. Chemical Engineering Journal. 2013;234:140-8.

[210] Rohde MP, Schaub G, Khajavi S, Jansen JC, Kapteijn F. Fischer–Tropsch synthesis with in situ H2O removal – Directions of membrane development. Microporous and Mesoporous Materials. 2008;115:123-36.

[211] Chung SJ, Park JH, Li D, Ida J-I, Kumakiri I, Lin JYS. Dual-Phase Metal−Carbonate Membrane for High-Temperature Carbon Dioxide Separation. Industrial & Engineering Chemistry Research. 2005;44:7999-8006.

[212] Li Y, Rui Z, Xia C, Anderson M, Lin YS. Performance of ionic-conducting ceramic/carbonate composite material as solid oxide fuel cell electrolyte and CO2 permeation membrane. Catalysis Today. 2009;148:303-9.

[213] Wade JL, Lee C, West AC, Lackner KS. Composite electrolyte membranes for high temperature CO2 separation. Journal of Membrane Science. 2011;369:20-9.

[214] Anderson M, Lin YS. Carbonate–ceramic dual-phase membrane for carbon dioxide separation. Journal of Membrane Science. 2010;357:122-9.

[215] Ortiz-Landeros J, Norton T, Lin YS. Effects of support pore structure on carbon dioxide permeation of ceramic-carbonate dual-phase membranes. Chemical Engineering Science. 2013;104:891-8.

[216] Dong X, Ortiz Landeros J, Lin YS. An asymmetric tubular ceramic-carbonate dual phase membrane for high temperature CO2 separation. Chem Commun (Camb). 2013;49:9654-6.

[217] Dong X, Wu H-C, Lin YS. CO2 permeation through asymmetric thin tubular ceramic-carbonate dual-phase membranes. Journal of Membrane Science. 2018;564:73-81.

[218] Norton TT, Ortiz-Landeros J, Lin YS. Stability of La–Sr–Co–Fe Oxide–Carbonate Dual-Phase Membranes for Carbon Dioxide Separation at High Temperatures. Industrial & Engineering Chemistry Research. 2014;53:2432-40.

[219] Norton TT, Lu B, Lin YS. Carbon dioxide permeation properties and stability of samarium-doped-ceria carbonate dual-phase membranes. Journal of Membrane Science. 2014;467:244-52.

[220] Anderson M, Lin YS. Carbon dioxide separation and dry reforming of methane for synthesis of syngas by a dual-phase membrane reactor. AIChE Journal. 2013;59:2207-18.

[221] Dong X, Lin YS. Catalyst-free ceramic-carbonate dual phase membrane reactor for hydrogen production from gasifier syngas. Journal of Membrane Science. 2016;520:907-13.

[222] Meng L, Ovalle-Encinia O, Lin JYS. Catalyst-Free Ceramic–Carbonate Dual-Phase Membrane Reactors for High-Temperature Water Gas Shift: A Simulation Study. Industrial & Engineering Chemistry Research. 2021;60:3581-8.

[223] Wu H-C, Rui Z, Lin JYS. Hydrogen production with carbon dioxide capture by dual-phase ceramic-carbonate membrane reactor via steam reforming of methane. Journal of Membrane Science. 2020;598:117780.

[224] Adhikari S, Fernando S. Hydrogen Membrane Separation Techniques. Industrial & Engineering Chemistry Research. 2006;45:875-81.

[225] Yun S, Ted Oyama S. Correlations in palladium membranes for hydrogen separation: A review. Journal of Membrane Science. 2011;375:28-45.

[226] Vadrucci M, Borgognoni F, Moriani A, Santucci A, Tosti S. Hydrogen permeation through Pd–Ag membranes: Surface effects and Sieverts' law. International Journal of Hydrogen Energy. 2013;38:4144-52.

[227] Guazzone F, Engwall EE, Ma YH. Effects of surface activity, defects and mass transfer on hydrogen permeance and n-value in composite palladium-porous stainless steel membranes. Catalysis Today. 2006;118:24-31.

[228] Israni SH, Harold MP. Methanol Steam Reforming in Pd−Ag Membrane Reactors Effects of Reaction System Species on Transmembrane Hydrogen Flux. Industrial & Engineering Chemistry Research. 2010;49:10242-50.

[229] Patrascu M, Sheintuch M. On-site pure hydrogen production by methane steam reforming in high flux membrane reactor: Experimental validation, model predictions and membrane inhibition. Chemical Engineering Journal. 2015;262:862-74.

[230] Boon J, Pieterse JAZ, van Berkel FPF, van Delft YC, van Sint Annaland M. Hydrogen permeation through palladium membranes and inhibition by carbon monoxide, carbon dioxide, and steam. Journal of Membrane Science. 2015;496:344-58.

[231] Seidel-Morgenstern A. Membrane Reactors Distributing Reactants to Improve Selectivity and Yield: WILEY-VCH; 2010. pp.4.

[232] Zhang Z, Liguori S, Fuerst TF, Way JD, Wolden CA. Efficient Ammonia Decomposition in a Catalytic Membrane Reactor To Enable Hydrogen Storage and Utilization. ACS Sustainable Chemistry & Engineering. 2019;7:5975-85.

[233] Mengers H, Benes NE, Nijmeijer K. Multi-component mass transfer behavior in catalytic membrane reactors. Chemical Engineering Science. 2014;117:45-54.

[234] Bhatia S, Thien CY, Mohamed AR. Oxidative coupling of methane (OCM) in a catalytic membrane reactor and comparison of its performance with other catalytic reactors. Chemical Engineering Journal. 2009;148:525-32.

[235] Simakov DSA, Sheintuch M. Model-based optimization of hydrogen generation by methane steam reforming in autothermal packed-bed membrane reformer. AIChE Journal. 2011;57:525-41.

[236] Bernstein L, Lund C. Membrane reactors for catalytic series and series-parallel reactions. Journal of Membrane Science. 1993;77:155-64.

[237] Moon WS, Park SB. Design guide of a membrane for a membrane reactor in terms of permeability and selectivity. Journal of Membrane Science. 2000;170:43-51.

[238] Dixon AG. Analysis of intermediate product yield in distributed-feed nonisothermal tubular membrane reactors. Catalysis Today. 2001;67:189-203.

[239] Li G, Kanezashi M, Yoshioka T, Tsuru T. Ammonia decomposition in catalytic membrane reactors: Simulation and experimental studies. AIChE Journal. 2013;59:168-79.

[240] Tsuru T, Yamaguchi K, Yoshioka T, Asaeda M. Methane steam reforming by microporous catalytic membrane reactors. AIChE Journal. 2004;50:2794-805.

[241] Battersby S, Teixeira PW, Beltramini J, Duke MC, Rudolph V, Diniz da Costa JC. An analysis of the Peclet and Damkohler numbers for dehydrogenation reactions using molecular sieve silica (MSS) membrane reactors. Catalysis Today. 2006;116:12-7.

[242] Boutikos P, Nikolakis V. A simulation study of the effect of operating and design parameters on the performance of a water gas shift membrane reactor. Journal of Membrane Science. 2010;350:378-86.

[243] Choi S-W, Jones CW, Nair S, Sholl DS, Moore JS, Liu Y, et al. Material properties and operating configurations of membrane reactors for propane dehydrogenation. AIChE Journal. 2015;61:922-35.

[244] van de Graaf JM, Zwiep M, Kapteijn F, Moulijn JA. Application of a silicalite-1 membrane reactor in metathesis reactions. Applied Catalysis A: General. 1999;178:225-41.

[245] Huang H, Samsun RC, Peters R, Stolten D. Greener production of dimethyl carbonate by the Power-to-Fuel concept: a comparative techno-economic analysis. Green Chemistry. 2021;23:1734-47.

[246] Bussche KV, Froment G. A steady-state kinetic model for methanol synthesis and the water gas shift reaction on a commercial Cu/ZnO/Al2O3Catalyst. Journal of Catalysis. 1996;161:1-10.

[247] Aspen Technology. Aspen Plus Urea Synthesis Loop Model. 2011.

[248] Huang H, Samsun RC, Peters R, Stolten D. Theoretical calculations and CFD simulations of membrane reactor designs. Chemical Engineering Science. 2022;252:117284.

[249] Said SAM, Simakov DSA, Mokheimer EMA, Habib MA, Ahmed S, Waseeuddin M, et al. Computational fluid dynamics study of hydrogen generation by low temperature methane reforming in a membrane reactor. International Journal of Hydrogen Energy. 2015;40:3158-69.

[250] Vandewalle LA, Van de Vijver R, Van Geem KM, Marin GB. The role of mass and heat transfer in the design of novel reactors for oxidative coupling of methane. Chemical Engineering Science. 2019;198:268-89.

Appendix

A. Appendix for chapter 4

Table A-1 Utility consumption of each section for DMC synthesis.

Process	**Oxidative carbonylation**	**Direct urea methanolysis**	**Indirect urea methanolysis via EC**	**Indirect urea methanolysis via PC**
Methanol synthesis	H_2 and CO_2 compression: 6796 kW LP steam: 22809 kW	H_2 and CO_2 compression: 6796 kW LP steam: 22809 kW	H_2 and CO_2 compression: 6796 kW LP steam: 22809 kW	H_2 and CO_2 compression: 6796 kW LP steam: 22809 kW
RWGS and C**O_2** scrubbing	Operating electricity: 13735 kW	0	0	0
Urea synthesis	0	CO_2 compression: 1137 kW LP steam: -19726 kW MP steam: 44678 kW	CO_2 compression: 1137 kW LP steam: -19726 kW MP steam: 44678 kW	CO_2 compression: 1137 kW LP steam: -19726 kW MP steam: 44678 kW
DMC synthesis	Pump: 62 kW LP steam: -88639 kW MP steam: 31344 kW	Pump: 56 kW MP steam: 40157 kW	Pump: 37 kW LP steam: -17913 kW MP steam: 24846 kW	Pump: 45 kW MP steam: 12066 kW
DMC separation	LP steam: 82155 kW	LP steam: 24561 kW	LP steam: 14095 kW HP steam: 26297 kW	LP steam: 24935 kW HP steam: 37749 kW
EC/PC synthesis	0	0	MP steam: 42229 kW	MP steam: 21604 kW

Table A-2 Utility consumption of each section for DMC synthesis.

Process	**Carbonylation of methanol**	**Dehydrogenation of methanol**
Methanol synthesis	H_2 and CO_2 compression: 5105 kW LP steam: 14401 kW	H_2 and CO_2 compression: 9572 kW LP steam: 27282 kW
RWGS and C**O₂** scrubbing	Operating electricity: 13735 kW	0
MF synthesis and separation	Pump and compressor: 744 kW LP steam: 31802 kW	LP steam: 11207 kW MP steam: 68575 kW

B. Appendix for chapter 6

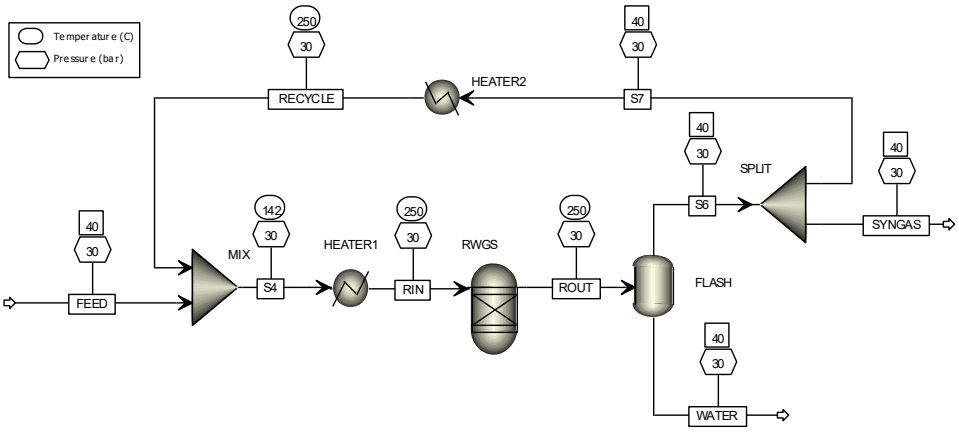

Figure A-1 Aspen Plus simulation flowsheet of reverse water gas shift.

Table A-3 STY of CO and H_2 at 450 and 20 bar with CH_4:CO_2=1:2.

GHSV / h^{-1}	Fixed-bed membrane reactor STY / mol/(m3 s)		Catalytic membrane reactor STY / mol/(m3 s)		Fixed-bed reactor/ STY mol/(m3 s)	
	CO	H_2	CO	H_2	CO	H_2
90	0.49	0.30	0.38	0.34	0.38	0.07
270	1.25	0.46	0.51	0.42	1.13	0.20
900	3.33	1.03	0.67	0.51	3.21	0.78

Table A-4 H_2/CO, H_2 removal and flux at 450 and 20 bar with CH_4:CO_2=1:2.

GHSV / h^{-1}	Fixed-bed membrane reactor			Catalytic membrane reactor			Fixed-bed reactor
	H_2/CO	H_2 removal	H_2 flux	H_2/CO	H_2 removal	H_2 flux	H_2/CO
90	0.61	82.9%	0.0102	0.90	92.8%	0.0131	0.18
270	0.37	60.4%	0.0114	0.83	84.3%	0.0146	0.18
900	0.31	29.1%	0.0124	0.77	76.6%	0.0162	0.24

Table A-5 STY of CO and H_2 at 500 ℃ and 20 bar with CH_4:CO_2=1:1.

GHSV / h^{-1}	Fixed-bed membrane reactor STY / mol/(m3 s)		Catalytic membrane reactor STY / mol/(m3 s)		Fixed-bed reactor STY / mol/(m3 s)	
	CO	H_2	CO	H_2	CO	H_2
90	0.89	0.65	0.71	0.65	0.64	0.17
270	2.17	1.03	0.96	0.82	1.93	0.51
900	6.69	2.22	1.29	1.02	6.47	1.72

Table A-6 H_2/CO, H_2 removal and flux at 500 ℃ and 20 bar with CH_4:CO_2=1:1.

GHSV / h^{-1}	Fixed-bed membrane reactor			Catalytic membrane reactor			Fixed-bed reactor
	H_2/CO	H_2 removal	H_2 flux	H_2/CO	H_2 removal	H_2 flux	H_2/CO
90	0.73	81.8%	0.0218	0.92	91.0%	0.0244	0.27
270	0.48	56.9%	0.0242	0.85	80.6%	0.0272	0.26
900	0.33	26.6%	0.0243	0.79	71.2%	0.0300	0.27

Table A-7 STY of CO and H_2 at 450 ℃ and 5 bar with CH_4:CO_2=1:1.

GHSV / h^{-1}	Fixed-bed membrane reactor STY / mol/(m3 s)		Catalytic membrane reactor STY / mol/(m3 s)		Fixed-bed reactor STY / mol/(m3 s)	
	CO	H_2	CO	H_2	CO	H_2
90	0.30	0.28	0.31	0.30	0.15	0.05
270	0.58	0.41	0.44	0.38	0.45	0.15
900	1.61	0.75	0.62	0.50	1.49	0.49

Table A-8 H_2/CO, H_2 removal and flux at 450 ℃ and 5 bar with CH_4:CO_2=1:1.

GHSV / h^{-1}	Fixed-bed membrane reactor			Catalytic membrane reactor			Fixed-bed reactor
	H_2/CO	H_2 removal	H_2 flux	H_2/CO	H_2 removal	H_2 flux	H_2/CO
90	0.94	92.4%	0.0107	0.96	94.9%	0.0116	0.33
270	0.71	74.2%	0.0126	0.87	82.8%	0.0131	0.33
900	0.47	41.7%	0.0129	0.82	66.6%	0.0138	0.33

Table A-9 STY of CO and H_2 at 450 and 20 bar with CH_4:CO_2=1:1 and *A/V*=79.5.

GHSV / h^{-1}	Fixed-bed membrane reactor STY / mol/(m3 s)		Catalytic membrane reactor STY / mol/(m3 s)		Fixed-bed reactor STY / mol/(m3 s)	
	CO	H_2	CO	H_2	CO	H_2
90	0.84	0.81	1.04	1.02	0.35	0.08
270	1.51	1.09	1.44	1.29	1.07	0.23
900	3.72	1.65	1.98	1.62	3.35	0.82

Table A-10 H_2/CO, H_2 removal and flux at 450 and 20 bar with CH_4:CO_2=1:1 and *A/V*=79.5.

GHSV / h^{-1}	Fixed-bed membrane reactor			Catalytic membrane reactor			Fixed-bed reactor
	H_2/CO	H_2 removal	H_2 flux	H_2/CO	H_2 removal	H_2 flux	H_2/CO
90	0.96	96.5%	0.0098	0.99	98.4%	0.0127	0.22
270	0.72	86.3%	0.0118	0.90	93.2%	0.0152	0.22
900	0.44	59.7%	0.0124	0.82	81.0%	0.0165	0.25

C. User-defined functions

User-defined functions for the water permeable membrane reactor

```
#include "udf.h"
#define NUM_UDM 14
#define membraneID 18

DEFINE_ADJUST(membraneFlux, d)
{
#if !RP_HOST
       real pi = 3.1415926;
       real Diff = 5 * 1E-7;  // mol m-2 s-1 Pa
       real fluxH2O;
       real fluxH2;
       real sum0;
       real sum1;
       real xH2O_0;
       real xH2O_1;

       real Area[ND_ND];
       real volc0;
       real volc1;
       Thread *t0;
       Thread *t1;
       Thread *t;
       cell_t c0;
       cell_t c1;
       face_t f;
       real p_ref = RP_Get_Real("operating-pressure");//unit pascal


       real mw[6];
       mw[0] = 44;
       mw[1] = 2.0;
       mw[2] = 28;
       mw[3] = 18;
       mw[4] = 16;
       mw[5] = 28;

       t = Lookup_Thread(d, membraneID);

       begin_f_loop(f, t)
       {

              F_AREA(Area, f, t);

              c0 = F_C0(f, t);
              t0 = THREAD_T0(t);
              c1 = F_C1(f, t);
              t1 = THREAD_T1(t);

              volc0 = C_VOLUME(c0, t0) * 2 * pi;
              volc1 = C_VOLUME(c1, t1) * 2 * pi;

              sum0 = C_YI(c0, t0, 0) / mw[0] + C_YI(c0, t0, 1) / mw[1] + C_YI(c0, t0,
```

```
2) / mw[2] + C_YI(c0, t0, 3) / mw[3] + C_YI(c0, t0, 4) / mw[4] + C_YI(c0, t0, 5) /
mw[5];
              sum1 = C_YI(c1, t1, 0) / mw[0] + C_YI(c1, t1, 1) / mw[1] + C_YI(c1, t1,
2) / mw[2] + C_YI(c1, t1, 3) / mw[3] + C_YI(c1, t1, 4) / mw[4] + C_YI(c1, t1, 5) /
mw[5];

              xH2O_0 = C_YI(c0, t0, 3) / mw[3] / sum0;
              xH2O_1 = C_YI(c1, t1, 3) / mw[3] / sum1;

              fluxH2O = mw[3] / 1000 * Diff*NV_MAG(Area) * 2 * pi*(-xH2O_1*(C_P(c1, t1)
+ p_ref) + xH2O_0*(C_P(c0, t0) + p_ref));  //kg s-1
              fluxH2 = mw[1] / mw[3] * fluxH2O / 200;

              C_UDMI(c0, t0, 6) = -xH2O_1*(C_P(c1, t1) + p_ref) + xH2O_0*(C_P(c0, t0) +
p_ref);

              C_UDMI(c0, t0, 7) = xH2O_0*(C_P(c0, t0) + p_ref) / 8.314 / C_T(c0, t0);

              C_UDMI(c0, t0, 8) = mw[3] / 1000 * Diff*(-xH2O_1*(C_P(c1, t1) + p_ref) +
xH2O_0*(C_P(c0, t0) + p_ref)) * 1000 / 18;


              if (Area[1]>0)
              {
                     C_UDMI(c0, t0, 0) = (fluxH2O + fluxH2) / volc0;
                     C_UDMI(c1, t1, 0) = -(fluxH2O + fluxH2) / volc1;

                     C_UDMI(c0, t0, 3) = fluxH2 / volc0;
                     C_UDMI(c1, t1, 3) = -fluxH2 / volc1;

                     C_UDMI(c0, t0, 4) = fluxH2O / volc0;
                     C_UDMI(c1, t1, 4) = -fluxH2O / volc1;

                     C_UDMI(c0, t0, 1) = (fluxH2O + fluxH2) / volc0*C_K(c0, t0);
                     C_UDMI(c1, t1, 1) = -(fluxH2O + fluxH2) / volc1*C_K(c0, t0);

                     C_UDMI(c0, t0, 2) = (fluxH2O + fluxH2) / volc0*C_D(c0, t0);
                     C_UDMI(c1, t1, 2) = -(fluxH2O + fluxH2) / volc1*C_D(c0, t0);

                     C_UDMI(c0, t0, 5) = (fluxH2O + fluxH2) / volc0*C_H(c0, t0);
                     C_UDMI(c1, t1, 5) = -(fluxH2O + fluxH2) / volc1*C_H(c0, t0);
              }
              else
              {
                     C_UDMI(c0, t0, 0) = -(fluxH2O + fluxH2) / volc0;
                     C_UDMI(c1, t1, 0) = (fluxH2O + fluxH2) / volc1;

                     C_UDMI(c0, t0, 3) = -fluxH2 / volc0;
                     C_UDMI(c1, t1, 3) = fluxH2 / volc1;

                     C_UDMI(c0, t0, 4) = -fluxH2O / volc0;
                     C_UDMI(c1, t1, 4) = fluxH2O / volc1;

                     C_UDMI(c0, t0, 1) = -(fluxH2O + fluxH2) / volc0*C_K(c1, t1);
                     C_UDMI(c1, t1, 1) = (fluxH2O + fluxH2) / volc1*C_K(c1, t1);

                     C_UDMI(c0, t0, 2) = -(fluxH2O + fluxH2) / volc0*C_D(c1, t1);
                     C_UDMI(c1, t1, 2) = (fluxH2O + fluxH2) / volc1*C_D(c1, t1);
```

```
                    C_UDMI(c0, t0, 5) = -(fluxH2O + fluxH2) / volc0*C_H(c1, t1);
                    C_UDMI(c1, t1, 5) = (fluxH2O + fluxH2) / volc1*C_H(c1, t1);
                }

        }
        end_f_loop(f, t)

#endif

}

DEFINE_SOURCE(mass, c, t, ds, eqn)/*write selected source terms*/
{
#if !RP_HOST
        return C_UDMI(c, t, 0);
#endif
}

DEFINE_SOURCE(energy, c, t, ds, eqn)
{
#if !RP_HOST
        return C_UDMI(c, t, 5);
#endif
}

DEFINE_SOURCE(k, c, t, ds, eqn)
{
#if !RP_HOST
        return C_UDMI(c, t, 1);
#endif
}

DEFINE_SOURCE(epsilon, c, t, ds, eqn)
{
#if !RP_HOST
        return C_UDMI(c, t, 2);
#endif
}

DEFINE_SOURCE(water, c, t, ds, eqn)
{
#if !RP_HOST
        return C_UDMI(c, t, 4);
#endif
}

DEFINE_SOURCE(hydrogen, c, t, ds, eqn)
{
#if !RP_HOST
        return C_UDMI(c, t, 3);
#endif
}


DEFINE_VR_RATE(rwgs, c, t, r, mw, yi, rr, rr_t)

{
```

```
#if !RP_HOST

        real R = 8.314;
        real E1 = 240.1;
        real E2 = 82; //kJ mol-1
        real E3 = 243.9;
        real k1;
        real k2;
        real k3;

        real K_CO;
        real K_H2;
        real K_CH4;
        real K_H2O;

        real dH_CO = -70.65;  //kJ mol-1 enthalpy change
        real dH_H2 = -82.9;
        real dH_CH4 = -38.28;
        real dH_H2O = 88.68;

        real DEN;
        real sum;

        real temp = C_T(c, t);
        real p_ref = RP_Get_Real("operating-pressure");  // unit pascal
        real p_rel = C_P(c, t);
        real p_CO2;
        real p_H2;
        real p_CO;
        real p_H2O;
        real p_CH4;

        real conc_CO2;
        real conc_H2;
        real conc_CO;
        real conc_H2O;

        real Keq1;
        real Keq2;
        real Keq3;
        real rate1;
        real rate2;
        real rate3;

        k1 = 1.842*1E-4*exp(-E1 * 1000 / R*(1 / temp - 1 / 648));
        k2 = 3100 * exp(-E2 * 1000 / R / temp);
        k3 = 2.193*1E-5*exp(-E3 * 1000 / R*(1 / temp - 1 / 648));

        K_CO = 40.91*exp(-dH_CO * 1000 / R*(1 / temp - 1 / 648));
        K_H2 = 0.0296*exp(-dH_H2 * 1000 / R*(1 / temp - 1 / 648));
        K_CH4 = 0.1791*exp(-dH_CH4 * 1000 / R*(1 / temp - 1 / 823));
        K_H2O = 0.4152*exp(-dH_H2O * 1000 / R*(1 / temp - 1 / 823));

        Keq1 = exp(-30.114 + (26830 / temp));
        Keq2 = exp(4.036 - (4400 / temp));
        Keq3 = exp(-26.078 + (22430 / temp));

        sum = yi[0] / mw[0] + yi[1] / mw[1] + yi[2] / mw[2] + yi[3] / mw[3] + yi[4] /
```

```
mw[4];
	p_CO2 = yi[0] / mw[0] / sum*(p_ref + p_rel) / 100000; //bar
	p_H2 = yi[1] / mw[1] / sum*(p_ref + p_rel) / 100000;
	p_CO = yi[2] / mw[2] / sum*(p_ref + p_rel) / 100000;
	p_H2O = yi[3] / mw[3] / sum*(p_ref + p_rel) / 100000;
	p_CH4 = yi[4] / mw[4] / sum*(p_ref + p_rel) / 100000;

	C_UDMI(c, t, 9) = C_YI(c, t, 0) / mw[0] / sum*(p_ref + p_rel);
	C_UDMI(c, t, 10) = C_YI(c, t, 1) / mw[1] / sum*(p_ref + p_rel);
	C_UDMI(c, t, 11) = C_YI(c, t, 2) / mw[2] / sum*(p_ref + p_rel);
	C_UDMI(c, t, 12) = C_YI(c, t, 3) / mw[3] / sum*(p_ref + p_rel);
	C_UDMI(c, t, 13) = C_YI(c, t, 4) / mw[4] / sum*(p_ref + p_rel);

	conc_CO2 = p_CO2 * 100000 / R / temp;
	conc_H2 = p_H2 * 100000 / R / temp;
	conc_CO = p_CO * 100000 / R / temp;
	conc_H2O = p_H2O * 100000 / R / temp;

	DEN = 1 + K_CO * p_CO + K_H2 * p_H2 + K_CH4 * p_CH4 + K_H2O * p_H2O / p_H2;


	rate1 = k1 / pow(p_H2, 2.5) * (pow(p_H2, 3) * p_CO - p_H2O * p_CH4 / Keq1) /
pow(DEN, 2) * 1910 / 3600;  //CO hydrogenation

	rate2 = k2 *(conc_CO2 * pow(conc_H2, 0.3) - conc_CO * conc_H2O / pow(conc_H2,
0.7) / Keq2) * 1910 / 1000 * 0.25; //rwgs

	rate3 = k3 / pow(p_H2, 3.5) * (pow(p_H2, 4) * p_CO2 - p_CH4 * pow(p_H2O, 2) /
Keq3) / pow(DEN, 2) * 1910 / 3600; //CO2 hydrogenation


	if (!strcmp(r->name, "CO-hydrogenation"))
	{
		*rr = rate1;
		*rr_t = rate1;
	}
	else if (!strcmp(r->name, "rwgs"))
	{
		*rr = rate2;
		*rr_t = rate2;
	}
	else if (!strcmp(r->name, "CO2-hydrogenation"))
	{
		*rr = rate3;
		*rr_t = rate3;
	}
	else
	{
		*rr = 0;
		*rr_t = 0;
	}
#endif
}
```

User-defined functions for the CO2 permeable membrane reactor

```
#include "udf.h"
#define NUM_UDM 12
#define membraneID 18

DEFINE_ADJUST(membraneFlux, d)
{
#if !RP_HOST
       real pi = 3.1415926;
       real L = 300E-4; //thickness cm
       real F = 96485;  //Faraday constant
       real porosity = 0.34;
       real CO3 = 3.5; //900C conductivity s cm-1
       real O2 = 0.106; //900C  conductivity s cm-1
       real sum0;
       real sum1;
       real fluxCO2;
       real xCO2_0;
       real xCO2_1;

       real Area[ND_ND];
       real volc0;
       real volc1;
       Thread *t0;
       Thread *t1;
       Thread *t;
       cell_t c0;
       cell_t c1;
       face_t f;
       real p_ref = RP_Get_Real("operating-pressure");//unit pascal


       real mw[6];
       mw[0] = 44;
       mw[1] = 2.0;
       mw[2] = 28;
       mw[3] = 18;
       mw[4] = 16;
       mw[5] = 28;

       t = Lookup_Thread(d, membraneID);

       begin_f_loop(f, t)
       {

              F_AREA(Area, f, t);

              c0 = F_C0(f, t);
              t0 = THREAD_T0(t);
              c1 = F_C1(f, t);
              t1 = THREAD_T1(t);

              volc0 = C_VOLUME(c0, t0) * 2 * pi;
              volc1 = C_VOLUME(c1, t1) * 2 * pi;
```

```
                sum0 = C_YI(c0, t0, 0) / mw[0] + C_YI(c0, t0, 1) / mw[1] + C_YI(c0, t0,
2) / mw[2] + C_YI(c0, t0, 3) / mw[3] + C_YI(c0, t0, 4) / mw[4] + C_YI(c0, t0, 5) /
mw[5];
                sum1 = C_YI(c1, t1, 0) / mw[0] + C_YI(c1, t1, 1) / mw[1] + C_YI(c1, t1,
2) / mw[2] + C_YI(c1, t1, 3) / mw[3] + C_YI(c1, t1, 4) / mw[4] + C_YI(c1, t1, 5) /
mw[5];

                xCO2_0 = C_YI(c0, t0, 0) / mw[0] / sum0;
                xCO2_1 = C_YI(c1, t1, 0) / mw[0] / sum1;

                fluxCO2 = 8.314*C_T(c1, t1) / L / pow(F, 2) / 4 * (porosity*CO3*(1 -
porosity)*O2 / (porosity*CO3 + (1 - porosity)*O2))*NV_MAG(Area) * 2 * pi*pow(10,
4)*(log(xCO2_1*(p_ref + C_P(c1, t1))) - log(xCO2_0*(p_ref + C_P(c0, t0)))) / 1000 *
mw[0];  //kg s-1 8.314*C_T(c1,t1)/4/pow(300,-4)/pow(96485,2)*0.066
                //fluxH2=mw[2]/mw[3]*fluxH2O/200;*/

                C_UDMI(c0, t0, 0) = fluxCO2 / volc0;
                C_UDMI(c1, t1, 0) = -fluxCO2 / volc1;

                C_UDMI(c0, t0, 3) = fluxCO2 / volc0*C_K(c0, t0);
                C_UDMI(c1, t1, 3) = -fluxCO2 / volc1*C_K(c0, t0);

                C_UDMI(c0, t0, 1) = fluxCO2 / volc0*C_D(c0, t0);
                C_UDMI(c1, t1, 1) = -fluxCO2 / volc1*C_D(c0, t0);

                C_UDMI(c0, t0, 2) = fluxCO2 / volc0*C_H(c0, t0);
                C_UDMI(c1, t1, 2) = -fluxCO2 / volc1*C_H(c0, t0);

                C_UDMI(c0, t0, 4) = log(xCO2_1*(p_ref + C_P(c1, t1))) - log(xCO2_0*(p_ref
+ C_P(c0, t0)));

                C_UDMI(c0, t0, 5) = pow(10, 4)*8.314*C_T(c1, t1) / L / pow(F, 2) / 4 *
(porosity*CO3*(1 - porosity)*O2 / (porosity*CO3 + (1 -
porosity)*O2))*(log(xCO2_1*(p_ref + C_P(c1, t1))) - log(xCO2_0*(p_ref + C_P(c0, t0))));

                C_UDMI(c0, t0, 6) = xCO2_0*(C_P(c0, t0) + p_ref) / 8.314 / C_T(c0, t0);


        }
        end_f_loop(f, t)

#endif

}

DEFINE_SOURCE(mass, c, t, ds, eqn)/*write selected source terms*/
{
#if !RP_HOST
        return C_UDMI(c, t, 0);
#endif
}

DEFINE_SOURCE(energy, c, t, ds, eqn)
{
#if !RP_HOST
        return C_UDMI(c, t, 2);
#endif
}
```

```
DEFINE_SOURCE(k, c, t, ds, eqn)
{
#if !RP_HOST
       return C_UDMI(c, t, 3);
#endif
}

DEFINE_SOURCE(epsilon, c, t, ds, eqn)
{
#if !RP_HOST
       return C_UDMI(c, t, 1);
#endif
}


DEFINE_SOURCE(carbon_dioxide, c, t, ds, eqn)
{
#if !RP_HOST
       return C_UDMI(c, t, 0);
#endif
}


DEFINE_SR_RATE(rwgs, f, t, r, mw, yi, rr)

{
#if !RP_HOST

       cell_t c0;
       Thread *t0;

       c0 = F_C0(f, t);
       t0 = THREAD_T0(t);

       real Area[ND_ND];
       F_AREA(Area, f, t);
       real pi = 3.1415926;
       real volc0 = C_VOLUME(c0, t0) * 2 * pi;


       real R = 8.314;
       real E1 = 240.1;
       real E2 = 82; //kJ mol-1
       real E3 = 243.9;
       real k1;
       real k2;
       real k3;

       real K_CO;
       real K_H2;
       real K_CH4;
       real K_H2O;

       real dH_CO = -70.65;  //kJ mol-1 enthalpy change
       real dH_H2 = -82.9;
       real dH_CH4 = -38.28;
       real dH_H2O = 88.68;
```

```
        real DEN;
        real sum;

        real temp = F_T(f, t);
        real p_ref = RP_Get_Real("operating-pressure");  // unit pascal
        real p_rel = F_P(f, t);
        real p_CO2;
        real p_H2;
        real p_CO;
        real p_H2O;
        real p_CH4;

        real conc_CO2;
        real conc_H2;
        real conc_CO;
        real conc_H2O;

        real Keq1;
        real Keq2;
        real Keq3;
        real rate1;
        real rate2;
        real rate3;

        k1 = 1.842*1E-4*exp(-E1 * 1000 / R*(1 / temp - 1 / 648));
        k2 = 3100 * exp(-E2 * 1000 / R / temp);
        k3 = 2.193*1E-5*exp(-E3 * 1000 / R*(1 / temp - 1 / 648));

        K_CO = 40.91*exp(-dH_CO * 1000 / R*(1 / temp - 1 / 648));
        K_H2 = 0.0296*exp(-dH_H2 * 1000 / R*(1 / temp - 1 / 648));
        K_CH4 = 0.1791*exp(-dH_CH4 * 1000 / R*(1 / temp - 1 / 823));
        K_H2O = 0.4152*exp(-dH_H2O * 1000 / R*(1 / temp - 1 / 823));

        Keq1 = exp(-30.114 + (26830 / temp));
        Keq2 = exp(4.036 - (4400 / temp));
        Keq3 = exp(-26.078 + (22430 / temp));

        sum = yi[0] / mw[0] + yi[1] / mw[1] + yi[2] / mw[2] + yi[3] / mw[3] + yi[4] /
mw[4];
        p_CO2 = yi[0] / mw[0] / sum*(p_ref + p_rel) / 100000; //bar
        p_H2 = yi[1] / mw[1] / sum*(p_ref + p_rel) / 100000;
        p_CO = yi[2] / mw[2] / sum*(p_ref + p_rel) / 100000;
        p_H2O = yi[3] / mw[3] / sum*(p_ref + p_rel) / 100000;
        p_CH4 = yi[4] / mw[4] / sum*(p_ref + p_rel) / 100000;

        conc_CO2 = p_CO2 * 100000 / R / temp;
        conc_H2 = p_H2 * 100000 / R / temp;
        conc_CO = p_CO * 100000 / R / temp;
        conc_H2O = p_H2O * 100000 / R / temp;

        DEN = 1 + K_CO * p_CO + K_H2 * p_H2 + K_CH4 * p_CH4 + K_H2O * p_H2O / p_H2;


        rate1 = k1 / pow(p_H2, 2.5) * (pow(p_H2, 3) * p_CO - p_H2O * p_CH4 / Keq1) /
pow(DEN, 2) * 1910 / 3600 * volc0 / (NV_MAG(Area) * 2 * pi);  //CO hydrogenation

        rate2 = k2 *(conc_CO2 * pow(conc_H2, 0.3) - conc_CO * conc_H2O / pow(conc_H2,
```

```
0.7) / Keq2) * 1910 / 1000 * volc0 / (NV_MAG(Area) * 2 * pi); //rwgs

	rate3 = k3 / pow(p_H2, 3.5) * (pow(p_H2, 4) * p_CO2 - p_CH4 * pow(p_H2O, 2) /
Keq3) / pow(DEN, 2) * 1910 / 3600 * volc0 / (NV_MAG(Area) * 2 * pi); //CO2
hydrogenation


	if (!strcmp(r->name, "CO-hydrogenation"))
	{
		*rr = rate1;
	}
	else if (!strcmp(r->name, "rwgs"))
	{
		*rr = rate2;
	}
	else if (!strcmp(r->name, "CO2-hydrogenation"))
	{
		*rr = rate3;
	}
	else
	{
		*rr = 0;
	}
#endif
}
```

User-defined functions for the H2 permeable membrane reactor

```
#include "udf.h"
#define NUM_UDM 12

DEFINE_ADJUST(membraneFlux, d)
{
#if !RP_HOST
	real pi = 3.1415926;
	real R = 8.314;
	real Ea = 6.6; //kJ mol-1
	real A0 = 1.26*1E-3; //mol m-2 s-1 Pa0.5

	real fluxH2;
	real sum0;
	real sum1;
	real xH2_0;
	real xH2_1;

	real Area[ND_ND];
	real volc0;
	real volc1;
	Thread *t0;
	Thread *t1;
	Thread *t;
	cell_t c0;
	cell_t c1;
	face_t f;
```

```
	real p_ref = RP_Get_Real("operating-pressure");//unit pascal

	real mw[7];
	mw[0] = 44;
	mw[1] = 2.0;
	mw[2] = 28;
	mw[3] = 18;
	mw[4] = 16;
	mw[5] = 28;
	mw[6] = 32;

	t = Lookup_Thread(d, 5); //adjacent sweep

	begin_f_loop(f, t)
	{

		F_AREA(Area, f, t);

		c0 = F_C0(f, t);
		t0 = THREAD_T0(t);
		c1 = F_C1(f, t);
		t1 = THREAD_T1(t);

		volc0 = C_VOLUME(c0, t0) * 2 * pi;
		volc1 = C_VOLUME(c1, t1) * 2 * pi;

		sum0 = C_YI(c0, t0, 0) / mw[0] + C_YI(c0, t0, 1) / mw[1] + C_YI(c0, t0,
2) / mw[2] + C_YI(c0, t0, 3) / mw[3] + C_YI(c0, t0, 4) / mw[4] + C_YI(c0, t0, 5) /
mw[5] + C_YI(c0, t0, 6) / mw[6];
		sum1 = C_YI(c1, t1, 0) / mw[0] + C_YI(c1, t1, 1) / mw[1] + C_YI(c1, t1,
2) / mw[2] + C_YI(c1, t1, 3) / mw[3] + C_YI(c1, t1, 4) / mw[4] + C_YI(c1, t1, 5) /
mw[5] + C_YI(c1, t1, 6) / mw[6];

		xH2_0 = C_YI(c0, t0, 1) / mw[1] / sum0;
		xH2_1 = C_YI(c1, t1, 1) / mw[1] / sum1;

		fluxH2 = mw[1] / 1000 * NV_MAG(Area) * 2 * pi*A0*exp(-Ea * 1000 / R /
C_T(c1, t1))*(pow(xH2_1*(C_P(c1, t1) + p_ref), 0.5) - pow(xH2_0*(C_P(c0, t0) + p_ref),
0.5));  //kg s-1

		C_UDMI(c1, t1, 4) = pow(xH2_1*(C_P(c1, t1) + p_ref), 0.5) -
pow(xH2_0*(C_P(c0, t0) + p_ref), 0.5);

		C_UDMI(c1, t1, 5) = mw[1] / 1000 * A0*exp(-Ea * 1000 / R / C_T(c1,
t1))*(pow(xH2_1*(C_P(c1, t1) + p_ref), 0.5) - pow(xH2_0*(C_P(c0, t0) + p_ref), 0.5)) *
1000 / 2;

		C_UDMI(c1, t1, 6) = xH2_1*(C_P(c1, t1) + p_ref) / R / C_T(c1, t1); //not
only H2, all species surface concentration


		if (Area[1]>0)
		{
			C_UDMI(c0, t0, 0) = fluxH2 / volc0;
			C_UDMI(c1, t1, 0) = -fluxH2 / volc1;

			C_UDMI(c0, t0, 3) = fluxH2 / volc0*C_K(c0, t0);
			C_UDMI(c1, t1, 3) = -fluxH2 / volc1*C_K(c0, t0);
```

```
                        C_UDMI(c0, t0, 1) = fluxH2 / volc0*C_D(c0, t0);
                        C_UDMI(c1, t1, 1) = -fluxH2 / volc1*C_D(c0, t0);

                        C_UDMI(c0, t0, 2) = fluxH2 / volc0*C_H(c0, t0);
                        C_UDMI(c1, t1, 2) = -fluxH2 / volc1*C_H(c0, t0);
                }
                else
                {
                        C_UDMI(c0, t0, 0) = -fluxH2 / volc0;
                        C_UDMI(c1, t1, 0) = fluxH2 / volc1;

                        C_UDMI(c0, t0, 3) = -fluxH2 / volc0*C_K(c1, t1);
                        C_UDMI(c1, t1, 3) = fluxH2 / volc1*C_K(c1, t1);

                        C_UDMI(c0, t0, 1) = -fluxH2 / volc0*C_D(c1, t1);
                        C_UDMI(c1, t1, 1) = fluxH2 / volc1*C_D(c1, t1);

                        C_UDMI(c0, t0, 2) = -fluxH2 / volc0*C_H(c1, t1);
                        C_UDMI(c1, t1, 2) = fluxH2 / volc1*C_H(c1, t1);
                }

        }
        end_f_loop(f, t)

#endif

}


DEFINE_SOURCE(energy, c, t, ds, eqn)
{
#if !RP_HOST
        return C_UDMI(c, t, 2);
#endif
}

DEFINE_SOURCE(k, c, t, ds, eqn)
{
#if !RP_HOST
        return C_UDMI(c, t, 3);
#endif
}

DEFINE_SOURCE(epsilon, c, t, ds, eqn)
{
#if !RP_HOST
        return C_UDMI(c, t, 1);
#endif
}

DEFINE_SOURCE(hydrogen, c, t, ds, eqn)
{
#if !RP_HOST
        return C_UDMI(c, t, 0);
#endif
}
```

```
DEFINE_VR_RATE(drm, c, t, r, mw, yi, rr, rr_t)

{
#if !RP_HOST

       real k1;
       real k2;

       real K_CO2_drm;
       real K_CO2_rwgs;
       real K_CH4;
       real K_H2;

       real DEN1, DEN2;
       real sum;

       real temp = C_T(c, t);
       real p_ref = RP_Get_Real("operating-pressure");//unit pascal
       real p_rel = C_P(c, t);
       real p_tot = p_ref + p_rel;
       real p_CO2;
       real p_H2;
       real p_CO;
       real p_H2O;
       real p_CH4;

       real Keq1;
       real Keq2;
       real rate1;
       real rate2;
       real rate_CH4;
       real rate_CO;
       real rate_H2;

       k1 = 1290 * exp(-102065 / 8.314 / temp);
       k2 = 350 * exp(-81030 / 8.314 / temp);

       Keq1 = 6.78E14*exp(-259660 / 8.314 / temp);//exp(8.097-7429.6/temp);
       Keq2 = 56.4971*exp(-36580 / 8.314 / temp);//exp(4.036-(4400/temp));

       K_CO2_drm = 2.61*1E-2*exp(37641 / 8.314 / temp);
       K_CH4 = 2.6*1E-2*exp(40684 / 8.314 / temp);
       K_CO2_rwgs = 0.5771*exp(9262 / 8.314 / temp);
       K_H2 = 1.494*exp(6025 / 8.314 / temp);



       sum = C_YI(c, t, 0) / mw[0] + C_YI(c, t, 1) / mw[1] + C_YI(c, t, 2) / mw[2] +
C_YI(c, t, 3) / mw[3] + C_YI(c, t, 4) / mw[4] + C_YI(c, t, 5) / mw[5] + C_YI(c, t, 6) /
mw[6];
       p_CO2 = C_YI(c, t, 0) / mw[0] / sum*p_tot / 101325; //atm
       p_H2 = C_YI(c, t, 1) / mw[1] / sum*p_tot / 101325;
       p_CO = C_YI(c, t, 2) / mw[2] / sum*p_tot / 101325;
       p_H2O = C_YI(c, t, 3) / mw[3] / sum*p_tot / 101325;
       p_CH4 = C_YI(c, t, 4) / mw[4] / sum*p_tot / 101325;

       C_UDMI(c, t, 7) = C_YI(c, t, 0) / mw[0] / sum*p_tot;
```

```
        C_UDMI(c, t, 8) = C_YI(c, t, 1) / mw[1] / sum*p_tot;
        C_UDMI(c, t, 9) = C_YI(c, t, 2) / mw[2] / sum*p_tot;
        C_UDMI(c, t, 10) = C_YI(c, t, 3) / mw[3] / sum*p_tot;
        C_UDMI(c, t, 11) = C_YI(c, t, 4) / mw[4] / sum*p_tot;

        DEN1 = 1 + K_CO2_drm*p_CO2 + K_CH4*p_CH4;
        DEN2 = 1 + K_CO2_rwgs*p_CO2 + K_H2*p_H2;


        rate1 = k1*K_CH4*K_CO2_drm*p_CO2*p_CH4 / pow(DEN1, 2)*(1 - pow(p_CO,
2)*pow(p_H2, 2) / p_CH4 / p_CO2 / Keq1) * 1750 * 0.29;

        rate2 = k2*K_CO2_rwgs*K_H2*p_CO2*p_H2 / pow(DEN2, 2)*(1 - p_CO*p_H2O / p_CO2 /
(p_H2 + 1E-20) / Keq2) * 1750 * 0.29;


        if (!strcmp(r->name, "drm"))
        {
                *rr = rate1;
                *rr_t = rate1;
        }
        else if (!strcmp(r->name, "rwgs"))
        {
                *rr = rate2;
                *rr_t = rate2;
        }
        else
        {
                *rr = 0;
                *rr_t = 0;
        }

#endif
}
```

List of figures

List of tables

List of symbols

Abbreviations

CAPEX	capital expenditure
CFD	computational fluid dynamics
CGO	gadolinia-doped ceria
CHA	chabazite
COM	cost of manufacturing
DMC	dimethyl carbonate
FAU	faujasite
FCI	fixed-capital investment
GHSV	gas hourly space velocity
H-SOD	hydroxy sodalite zeolite
LHV	lower heating value
LTA	Linde type A
MF	methyl formate
MOR	mordenite
MSP	minimum selling price
NPV	net present value
PEM	polymer electrolyte membrane
SDC	samaria-doped ceria
SoA	state-of-the-art
SOEC	solid oxide electrolyzer cell
STY	space-time yield
TRL	technology readiness level
UDFs	user-defined functions
WC	working capital
YSZ	yttria-doped zirconia

Nomenclature

A	area
C	cost or molar concentration
D	diffusion coefficient
Da	Damköhler number
d_p	catalyst particle diameter
E	energy

E_a	activation energy
e_{CO_2}	specific energy consumption for CO_2 capture
F	Faraday's constant
$\vec{F}$	force
F_p	pressure factor
F_m	material factor
i	interest rate
J_i	diffusion of species
L	reactor length or membrane thickness
$\dot{m}$	mass flow rate
t	time
K_{eq}	equilibrium constant
k_i	kinetic factor of reaction
K_i	adsorption constant
p	pressure
Pe	Péclet number
P_{utility}	utilities consumption
Q_{H_2O}	permeance of water
Re	Reynolds number
r_i	reaction rate
Sc	Schmidt number
Sh	Sherwood number
S_{H_2}	solubility of H_2
S_m / S_h	source term of mass/energy
T	temperature
V	volume
$\vec{v}$	velocity
W_{cat}	catalyst weight
x	molar fraction
X_i	conversion
ΔX_i	conversion enhancement
Y_i	mass fraction of species

Greek letters

α	intrinsic permeance

β	inertial resistance
η_{PtF}	Power-to-Fuel efficiency
η_o	overall effectiveness factor
ξ	reaction extent
ρ	density
μ	fluid viscosity
ε	porosity
ϕ_{TM}	Thiele modulus
τ	tortuosity
σ	ion conductivity

Band / Volume 597
Nanostructures of Transition Metal Sulfides for Anion Exchange Membrane Water Electrolysis
L. Xia (2022), 161 pp
ISBN: 978-3-95806-670-0

Band / Volume 598
Recycling- und Defossilisierungsmaßnahmen der Energieintensiven Industrie Deutschlands im Kontext von CO_2-Reduktionsstrategien
F. Kullmann (2022), XII, 237 pp
ISBN: 978-3-95806-672-4

Band / Volume 599
IEK-14 Report 2022
Research contributions for the energy transition and structural change in the Rhineland
B. Emonts (Ed.) (2022), 83 pp
ISBN: 978-3-95806-676-2

Band / Volume 600
Development of Glass-based Sealants for the Joining of Oxygen Transport Membranes
X. Li (2022), IV, 159 pp
ISBN: 978-3-95806-677-9

Band / Volume 601
High-resolution imaging of transport processes with GPR full-waveform inversion
P. Haruzi (2022), iv, 173 pp
ISBN: 978-3-95806-678-6

Band / Volume 602
Synthesis of optimized cathode materials for all-solid-state lithium batteries
C. Roitzheim (2022), xv, 221 pp
ISBN: 978-3-95806-679-3

Band / Volume 603
Development of components based on Ti_2AlC/fiber composites for aggressive environmental conditions
S. Badie (2023), x, 161 pp
ISBN: 978-3-95806-680-9

Band / Volume 604
Multiregionales Energiesystemmodell mit Fokus auf Infrastrukturen
T. M. Groß (2023), xx, 235 pp
ISBN: 978-3-95806-681-6

Band / Volume 605
Temporal Aggregation Methods for Energy System Modeling
M. A. C. Hoffmann (2023), XXVI, 341 pp
ISBN: 978-3-95806-683-0

Band / Volume 606
Examining transport in the Upper Troposphere – Lower Stratosphere with the infrared limb imager GLORIA
L. Krasauskas (2023), v, 107 pp
ISBN: 978-3-95806-691-5

Band / Volume 607
Sustainable Fabrication of Ceramic Solid Electrolytes for Solid-State Lithium Batteries
R. Ye (2023), vi, 119 pp
ISBN: 978-3-95806-694-6

Band / Volume 608
Improving Nitrogen Retention in Soils Treated with Pig and Cattle Slurry Through the Use of Organic Soil Amendments
X. Cao (2023), XVI, 119 pp
ISBN: 978-3-95806-696-0

Band / Volume 609
Mechanisches Verhalten von Polymer-Elektrolyt-Membran-Elektrolysezellen und -Stacks
S. Holtwerth (2023), x, 251 pp
ISBN: 978-3-95806-697-7

Band / Volume 610
Membrane Reactor Concepts for Power-to-Fuel Processes
H. Huang (2023), VI, 197 pp
ISBN: 978-3-95806-703-5

Energie & Umwelt / Energy & Environment
Band / Volume 610
ISBN 978-3-95806-703-5

Mitglied der Helmholtz-Gemeinschaft

JÜLICH
Forschungszentrum